FABRICATION AND EVALUATION OF NOVEL NON-ENZYMATIC HYDROGEN PEROXIDE AND GLUCOSE SENSORS BASED ON CONDUCTING POLYMER/NANOCOMPOSITES

POORIA MOOZARM NIA

THESIS SUBMITTED IN FULFILMENT OF THE REQUIREMENTS FOR THE DEGREE OF DOCTOR OF PHILOSOPHY

FACULTY OF SCIENCE
UNIVERSITY OF MALAYA
KUALA LUMPUR

2016

UNIVERSITI MALAYA

ORIGINAL LITERARY WORK DECLARATION

Name of Candidate: POORIA MOOZARM NIA (I.C/Passport No: E96078147)
Registration/Matric No: SCH140063
Name of Degree: Doctor of Philosophy (PhD)
Title of Project Paper/Research Report/Dissertation/Thesis ("this Work"):

FABRICATION AND EVALUATION OF NOVEL NON-ENZYMATIC HYDROGEN PEROXIDE AND GLUCOSE SENSORS BASED ON CONDUCTING POLYMER/NANOCOMPOSITES

Field of Study: Polymer Chemistry

I do solemnly and sincerely declare that:

(1) I am the sole author/writer of this Work;
(2) This Work is original;
(3) Any use of any work in which copyright exists was done by way of fair dealing and for permitted purposes and any excerpt or extract from, or reference to or reproduction of any copyright work has been disclosed expressly and sufficiently and the title of the Work and its authorship have been acknowledged in this Work;
(4) I do not have any actual knowledge nor do I ought reasonably to know that the making of this work constitutes an infringement of any copyright work;
(5) I hereby assign all and every rights in the copyright to this Work to the University of Malaya ("UM"), who henceforth shall be owner of the copyright in this Work and that any reproduction or use in any form or by any means whatsoever is prohibited without the written consent of UM having been first had and obtained;
(6) I am fully aware that if in the course of making this Work I have infringed any copyright whether intentionally or otherwise, I may be subject to legal action or any other action as may be determined by UM.

Candidate's Signature Date

Subscribed and solemnly declared before,

Witness's Signature: Date:

Name: **PROFESSOR. Dr. YATIMAH ALIAS**
Designation: **PROFESSOR**

Witness's Signature: Date:

Name: **Dr. WOI PEI MENG**
Designation: **SENIOR LECTURER**

ABSTRACT

This research utilized seven novel nanocomposites as non-enzymatic hydrogen peroxide (H_2O_2) sensor *viz.* glassy carbon electrode (GCE) as substrate. The composites were prepared with various combinations of polypyrrole (Ppy), reduced graphene oxide (rGO), copper and silver nanoparticles (CuNPs and AgNPs) via different electrodeposition processes. Sensors which were prepared by one-step electrodeposition of rGO-CuNPs and rGO-AgNPs showed a linear detection range up to 18 and 24 mmol.L^{-1}, with LOD of 0.601 and 0.016 µmol.L^{-1}, respectively towards H_2O_2. Their good performance is attributed to high surface area and synergetic effect of AgNPs and CuNPs with rGO. Polypyrrole was electrodeposited into the composite as a matrix on which nanometals could embed. The investigations revealed the type of dopants is highly effective in morphology and electrocatalytic performance of sensor. Polypyrrole was fabricated layer-by-layer electrodeposition method in the form of nanofiber when lithium perchlorate was used and showed the best performance. The synergetic effect of rGO, AgNPs and PpyNFs made (rGO-AgNPs)/PpyNFs composite an excellent H_2O_2 sensor with LOD of 1.099 µmol.L^{-1} with the wide linear range up to 90 mmol.L^{-1}. Layer-by-layer electrodeposition of (rGO/PpyNFs/Cu_xO) led to a sensor which showed the best electrocatalytic response to H_2O_2 among all modified electrodes where LOD of 0.030 µmol.L^{-1} and wide linear range detection up to 100 mmol.L^{-1} were recorded. This electrode was further tested as amperometric glucose sensor and showed satisfactory performance with detection range of 0.038 µmol.L^{-1} at the same linear range, which enable it to be used for dual analytes detection. Therefore**,** along with sensing H_2O_2, this sensor was used as detector for glucose. To further look into the effect of rGO on sensor performance, PpyMTs-CuNPs and PpyNFs/AgNPs were prepared via one-step and layer-by-layer electrodeposition, respectively in the absence of rGO. PpyMTs-CuNPs electrode showed good response towards H_2O_2 with LOD of 0.900 µmol.L^{-1} and linear range up to

110 mmol.L^{-1}, whereas PpyNFs/AgNPs showed good electroreduction response to H_2O_2 with LOD of 0.115 µmol.L^{-1} with detection range up to 120 mmol.L^{-1}. It is believed the rGO wrinkle-like morphology was able to increase the surface roughness and consequently acted as an excellent underneath layer. Polypyrrole showed an excellent substrate as a suitable matrix for incorporating nanometals and enhanced speed, sensitivity, selectivity and versatility of the prepared sensors for H_2O_2 detection. Metal nanoparticles (AgNPs and CuNPs) exhibited a narrow size distribution, enhanced electrocatalytic activity and increased electrocatalytic selectivity with wide linear range and the detection of H_2O_2 at low potential. These unique properties of the silver and copper nanoparticles could be ascribed to their excellent electron transfer abilities as well as the ultra-high surface area derived from their nanoscale size.

ABSTRAK

Penyelidikan ini menggunakan tujuh nanokomposit sebagai penderia bukan enzim hidrogen peroksida (H_2O_2) dengan menggunakan elektrod berkaca karbon (GCE) sebagai substrat. Komposit-komposit telah dihasilkan menerusi kombinasi polypyrrole (Ppy), graphene oksida terturun (rGO), nanopartikel tembaga dan perak (CuNPs dan AgNPs) menerusi proses pengelektroenapan yang berbeza. Penderia yang dihasilkan menerusi pengelektroenapan satu-langkah daripada rGO-CuNPs, dan rGO-AgNPs masing-masing menunjukkan julat pengesanan linear sehingga 18 dan 24 $mmol.L^{-1}$, dengan LOD 0.601 dan 0.016 $\mu mol.L^{-1}$, terhadap H_2O_2. Prestasi yang bagus ini adalah disebabkan kawasan permukaan yang luas dan kesan sinergi daripada AgNPs dan CuNPs dengan rGO. Pengelektroenapan polypyrrole ke dalam komposit sebagai matriks membolehkan pembenaman nanologam. Penyiasatan ini mendedahkan pemilihan jenis bahan dop sangat berkesan dalam pembentukan morfologi dan prestasi elektropemangkinan penderia tersebut. Polypyrrole telah difabrikasi menerusi kaedah pengelektroenapan lapisan-demi-lapisan dalam bentuk nanofiber semasa litium perklorat digunakan dan menunjukkan prestasi penderia yang amat baik. Kesan sinergi rGO, AgNPs and PpyNFs menjadikan (rGO-AgNPs)/PpyNFs komposit sebagai penderia H_2O_2 yang cemerlang dengan LOD 1.099 $\mu mol.L^{-1}$ bersama julat linear yang luas sehingga 90 $mmol.L^{-1}$. Pengelektroenapan lapisan-demi-lapisan daripada rGO/PpyNFs/Cu_xO menghasilkan satu penderia yang menunjukkan kesan elektropemangkinan terhadap H_2O_2 yang terbaik di dalam kalangan semua elektrod yang diubahsuai di mana LOD 0.030 $\mu mol.L^{-1}$ dan julat linear yang luas sehingga 100 $mmol.L^{-1}$ telah direkodkan. Elektrod ini telah diuji selanjutnya sebagai penderia amperometrik glukosa dan mempamerkan prestasi yang memuaskan dengan julat pengesanan 0.038 $\mu mol.L^{-1}$ dalam julat linear yang sama, dan ini menunjukkan ia boleh digunakan sebagai penderia dua analit. Oleh itu, bersama penderiaan H_2O_2, penderia ini digunakan untuk mengesan glukosa. Kajian seterusnya dilihat dalam kesan rGO ke atas prestasi penderia selanjutnya, PpyMTs-CuNPs dan PpyNFs/AgNPs masing-masing telah disediakan melalui kaedah pengelektroenapan satu langkah dan lapisan-demi-lapisan, dalam keadaan ketiadaan rGO. Elektrod PpyMTs-CuNPs menunjukkan respons yang baik terhadap H_2O_2 dengan LOD 0.900 µmol.L^{-1} dan julat linear sehingga 110 mmol.L^{-1}, manakala PpyNFs/AgNPs menunjukkan respons pengelektroturunan yang memuaskan terhadap H_2O_2 dengan LOD 0.115 µmol.L^{-1} dan julat pengesanan sehingga 120 mmol.L^{-1}. Morfologi rGO yang kedut dipercayai dapat meningkatkan kekasaran permukaan dan seterusnya bertindak sebagai lapisan bawah yang sangat baik. Polypyrrole telah menunjukkan ia sebagai matriks yang sesuai bagi substrat untuk penggabungan nanologam dan meningkatan kelajuan, sensitiviti, tahap pemilihan bagi penderia yang disediakan untuk mengesan H_2O_2. Nanopartikel logam (AgNPs dan CuNPs) mempamerkan taburan saiz terhad, aktiviti dan pemilihan elektropemangkinan yang telah dipertingkatkan dengan julat linear luas dan pengesanan H_2O_2 pada keupayaan rendah. Ciri-ciri unik yang dipamerkan oleh nanopartikel perak dan tembaga boleh disifatkan sebagai kebolehan pemindahan elektron yang cemerlang serta kawasan permukaan ultra-tinggi yang diperolehi daripada saiz nano mereka.

Acknowledgments

In preparing this dissertation, I am indebted to many people. I would like to express my sincere thanks to my supervisors, **Prof. Dr. Yatimah Binti Alias** and **Dr. Woi Pei Meng**, for their help and guidance throughout the research process. Without their constructive comments and guidance, this dissertation would have not been possible.

I do not have adequate words to express my gratitude to my wonderful family especially **my parents**. Many sincere thanks are given to my supportive wife **Mahtab** who encouraged me throughout the whole process. Without her, this piece of work would have not been written.

To my heroes

My mom and dad

TABLE OF CONTENTS

LIST OF FIGURES

LIST OF SCHEMES

LIST OF TABLES

LIST OF ABBREVIATIONS

ρ	Density
χ^2	Chi-squared
ν	Scan rate
Ag/AgCl	Silver chloride saturated electrode
AgNPs/GCE	Modified glassy carbon electrode with silver nanoparticles
$Ag(NH_3)_2OH$	Silver-ammonia complex
$AgNO_3$	Silver nitrate
AgNPs	Silver nanoparticles
AgNPs-rGO	Silver nanoparticle-reduce graphene oxide
APS	Ammonium persulfate
a_{Ox}	Oxidant chemical activity
a_{Red}	Reductant chemical activity
AsF_5	Arsenic pentafluoride
b	Slope of the calibration curve
C	Capacitance
CA	Chronoamperometry
CP	Conducting polymer
CV	Cyclic voltammetry
D	Diffusion coefficient
d	The spacing of the crystal layers (path difference)
DIW	Deionized water
E	Cell potential
E^o	Standard cell potential
E_g	Band gap
EDX	Energy Dispersive X-ray
EIS	Electrochemical Impedance Spectroscopy
Et_4NBF_4	Tetraethylammonium tetrafluoroborate
F	Faraday’s constant
FET	Field-effect transistors
FESEM	Field Emission Scanning Electron Microscopy
FTIR	Fourier transform infrared spectroscopy
GCE	Glassy carbon electrode
GLC	Glucose
GO	Graphene oxide
GOD	Glucose oxidase
GOx	Glucose oxidase
HCl	Hydrochloric acid
HNO_3	Nitric acid
H_2NaO_4P	Sodium phosphate monobasic
$HNa_2O_4P.2H_2O$	Sodium phosphate dibasic dihydrate
H_2O_2	Hydrogen peroxide
H_3PO_4	Phosphoric acid
H_2SO_4	Sulphuric acid
I_2	Iodine
ITO	Indium tin oxide
KCl	Potassium chloride
$KMnO_4$	Potassium permanganate
LAH	Lithium aluminum hydride
LOD	Limit of detection

LOQ	Limit of qualification
MnO_2	Manganese dioxide
Mn_2O_7	Dimanganese heptoxide
n	Number of electrons transferred per mole
$NaBH_4$	Sodium borohydride
NH_3	Ammonia
$NOPF_6$	Nitrosonium hexafluorophosphate
OxaOx	Oxalate oxidase
PANI	Polyaniline
PBS	Phosphate buffer solution
PPP	Poly-paraphenylene
Ppy	Polypyrroe
PpyMTs	Polypyrrole microtrunks
PpyNFs	Polypyrrole nanofibers
PSD	Position-sensitive detector
Pt	Platinum
PVP	Poly(vinylpyrrolidone)
R_{dif}	Diffusion resistance of electroactive species
RE	Reference electrode
rGO	Reduced graphene oxide
Rs	Cell resistance
s	Solubility
S_B	Standard deviation of the blank solution
S/N	Signal per noise
T	Temperature
t	Time
TEM	Transmission Electron Microscopy
UA	Uric acid
UOx	Urate oxidase
UV-vis	Ultraviolet–visible Spectroscopy
XRD	X-ray diffraction
z	Number of moles of electrons transferred in the cell reaction
Z_{im}	Imaginary impedance
Z_{re}	Real impedance
Zw	Diffusion impedance

CHAPTER 1: INTRODUCTION

An electrochemical biosensor is an analytical tool which, by integrating biological sensing, converts the concentration of an analyte into an electrical signal. Sensors are simple to use, portable and high specificity analytical devices. They have good performances in a variety of fields such as pollution monitoring, health care, pharmacy, agricultural product processing, food, *etc*.

More than 220 million of people around the world are suffering from diabetes which is a highly extensive disease bringing about metabolic disorders. Testing the blood glucose (GLC) is very crucial for diabetic patients and helps to evade the clustering of blood GLC (in the range of 4.4–6.6 mM).

During the last decades, numerous attempts have been done to develop low cost, selective, sensitive and reliable glocuse and hydrogen peroxide sensors because of the importance of measuring the human blood glucose levels (Chen *et al*., 2012). The following reaction shows the reaction in a glucose biosensor used to determine the glucose concentration:

$$\text{Glucose} + O_2 \rightarrow \text{Gluconic acid} + H_2O_2 \qquad \text{(Eq. 1.1)}$$

$$H_2O_2 \rightarrow O_2 + 2H^+ + 2e^- \qquad \text{(Eq. 1.2)}$$

The amount of hydrogen peroxide produced in Eq. 1.1 is commonly measured using an amperometric method as presented in Eq. 1.2 (Shin *et al*., 2010).

For several decades, hydrogen peroxide has exhibited to be an extremely significant analyte as an intermediate in several biological devices as well as in many industrial systems. The unique oxidizing properties make H_2O_2 as an important compound. Decomposition of H_2O_2 leads to formation of hydroxyl radicals, which are employed as oxidizing agents for degradation of organic pollutants from water such as the azo dye materials employed in the textile industry, which are toxic to aquatic life and carcinogenic to humans. H_2O_2 and its derivatives can also be employed as powerful oxidizing agents in the synthesis of many organic compounds (Chen *et al.,* 2012).

In addition, the H_2O_2 decomposition gives an extremely important performance in the production of industrial water electrolyzers, secondary fuel cell and metal-air batteries. Beside its many industrial applications, hydrogen peroxide can also be problematic, its excessive concentration as a product of industrial and atomic power stations affects the environment (Shin, 2010). With respect to medical applications, H_2O_2 plays a main role in reactive oxygen species (ROS) in living organisms and is a central factor in causing several life-threatening human diseases. H_2O_2 is the most valuable marker of oxidative stress, which is connected to aging and severe human diseases such as cancer, cardiovascular disorders, Alzheimer and related neurodegenerative diseases (Shin, 2010). Many enzymatic reactions also create H_2O_2 as a product so its concentration can be used as an indicator of the progress of the reaction. Due to these wide and varied applications, its determination shows a significant analytical issue.

The electrochemical enzymatic sensors have been extremely used in determination of H_2O_2 due to their high sensitivity and their good selectivity. Horseradish peroxide and hemoglobin enzymes have been mostly used for preparation of modified enzymatic electrodes for amperometric determination of H_2O_2 (Shin, 2010). The most unavoidable disadvantage of such modified electrode is chemical and thermal instability, which is inevitable part of the intrinsic nature of the enzymes. This disadvantage has diverted the recent studies to carry out a direct detection of H_2O_2 by using enzyme-less electrodes. Accordingly, studies on the materials for direct detection of H_2O_2 could develop new generation of enzyme-less sensors.

Subsequently, the availability of such systems to both personal health and environmental quality has beneficial impact on society. Thus, the investigation of any technique, which could decrease the development costs and times, reveals other possible system designs and consequently enhances the rate at which new devices are brought to the market, is of utmost importance.

1.1 Background of study

Hydrogen peroxide (H_2O_2) is one of the most important analytes nowadays. Firstly, H_2O_2 is always referred to in different fields including pulp and paper bleaching, cleaning product, textile industry, food processes, pharmaceutical research, biochemistry and minerals processes (Shin, 2010). Secondly, H_2O_2 is involved in many biological events and intracellular pathways and is the byproduct of oxidases such as glucose oxidase, cholesterol oxidase, glutamate oxidase, urate oxidase, lactate oxidase, and also is a substrate for the enzyme horseradish peroxidase (Zhang *et al*., 2013; Das & Prusty, 2013; Jang *et al*., 2013; Kumar & Jampana, 2012; Palanisamy *et al*., 2012). Thirdly, as a powerful oxidizing agent, H_2O_2 can be applied in many organic compound synthesis reactions and is also employed as an oxidant for liquid-based fuel cells (Zhang *et al*., 2013; Das & Prusty 2013; Jang *et al*., 2013; Kumar & Jampana, 2012; Palanisamy *et al*., 2012). Therefore, the reliable, accurate, low-cost, rapid and sensitive determination of hydrogen peroxide has been practically important and widely investigated.

Evolved from the original Clark-oxygen electrode (Clark & Yons, 1962), the oxidation of the analyte at the platinum surface causes the signal from H_2O_2 (Guilbault & Lubrano, 1973). Clark modified his original design by employing a membrane where glucose oxidase (GOD) was immobilized amid a polycarbonate and polyacrylamide membrane and placed on a platinum electrode (Clarke & Santiago, 1977). When the mass transfer of both hydrogen peroxide and glucose is the rate limiting process, a linear dependence of the signal is achieved. Additionally, the linear range of the sensor depends on the oxygen concentration necessary in the enzymatic conversion of glucose by GOD. The most important benefits of the hydrogen peroxide sensor over other kinds of sensors are the relatively easy manufacturing process and the possibility of designing them in small sizes (Wientjes, 2000).

Several analytical methods such as titrimetry, chemiluminscence, chromatography, fluorescence, phosphorescence, spectrophotometry and electrochemical methods have been used for H_2O_2 determination. Nevertheless, most of them present their own technical disadvantages including low sensitivity and selectivity, time consuming, susceptibility to interferences and complicated or expensive instrumentation.

With high sensitivity and selectivity, fast response, practicality, simplicity, low-cost and convenient operation, electrochemical sensors have been an optimal choice to actualize the accurate and sensitive detection of H_2O_2 (Chen, 2012). In recent years, intensive research interest has been put into the design of novel H_2O_2 sensor as well as the improvement of their analysis performances. Various materials have been employed to increase the sensing properties including nanomaterials (Mahmoudian *et al*., 2014), conducting polymers (Kumar & Jampana, 2012), surfactants (Ge *et al*., 2011) and sol–gel materials (Elzanowska *et al*., 2004) and biomaterial such as DNA (Shao *et al*., 2010), fibroin (Lima *et al*., 2016), cellulose (Takahashi *et al*., 2013), eggshell membrane (Li *et* *al*., 2015), chitin and chitosan (Li *et al*., 2014) and so on. Among these materials, nanomaterials especially metal nanoparticles and conducting polymers as well as graphene oxide have been extensively studied and witnessed tremendous growth in the construction of sensors.

With the development of nanoscience, metal nanoparticles have attracted substantial interest and now play an important role in areas such as catalysis, nanosensors, biomedicine, biological labeling, surface enhanced Raman scattering and microelectronics due to their unique electrical, optical, thermal and catalytic properties. Among them, the unique characteristics such as the high surface to volume ratio, high electrical conductivity, favorable biocompatible, excellent catalytic ability and surface reaction activity provide metal nanoparticles enormous possibilities in improving sensor performance (Chen *et al*., 2013).

As illustrated in Eq. 1.1 and 1.2 earlier, hydrogen peroxide monitoring is closely associated to one of the world health issue-Diabetes mellitus. This disease is caused by metabolic disorder which is resulted from deficiency of hyperglycemia and insulin and is expressed by the concentrations of blood glucose lower or higher than the natural range of 80-120 mg/dL (4.4-6.6 mM) (Malhotra *et al*., 2006; Meng *et al*., 2013; Wang, 2008). Diabetes is one of the leading causes of disability and death. The complications of fighting diabetes are numerous such as kidney failure, blindness and higher risks of heart disease. Such complications can be considerably decreased by precise personal control of blood glucose level. Therefore, the management and diagnosis of diabetes needs a stringent observing of blood glucose levels. Subsequently, many of diabetics check their blood glucose levels daily which makes it the main tested analyte. Overall, glucose biosensors give reason for around 85% of the whole market of biosensors. This extremely large market leads to develop new sensing concepts. The enormous economic outlooks associated with the management of diabetes along with the challenge of developing such tight and reliable glycemic control have thus caused to a huge number of interesting research and creative detection systems (Turkmen *et al.*, 2014; Senel & Nergiz, 2012; Dung *et al.,* 2012). Amperometric non-enzymatic modified electrodes, based on conducting polymers, graphene oxide products and nano-sized metals have played a significant role in the development of simple human blood glucose testing and are expected to play a similar role in the move toward continuous glucose monitoring (Zhang *et al.*, 2013; Das & Prusty 2013; Jang *et al.*, 2013; Kumar & Jampana, 2012; Palanisamy *et al.*, 2012). Since 1962 when the initial concept of glucose enzyme electrodes was proposed by Clark and Lyons (Clark, 1962), enormous efforts have been carried out for developing reliable systems for controlling diabetes. Various methods have been investigated in the operation of enzymatic glucose systems. In addition, such systems suggest great promise for other important applications, ranging from food analysis to bioprocess monitoring. The significance of self-control systems has been generated a huge number of publications, the flow of which presents no sign of diminishing. Up until now, although many remarkable developments have been achieved for designing and using of such systems, the promise of tight diabetes management has not covered. Controlling of blood glucose level thus shows the first example of individualized (personalized) medicine (Wang, 2008).

1.2 Sensor characteristics

The performance of a sensor depends upon several static and dynamic parameters, which decides its efficiency towards a particular application. These parameters are listed below:

Sensitivity: It is the measure of the sensors response towards the designed analyte and refers to the change in the amount of sensor signal with the change of concentration of the target substance. Sensitivity of the sensor directly depends upon many factors like receptor and transducer materials, operating conditions, viscosity, and temperature of the measurement medium, *etc*.

Selectivity: It refers to the degree to which a sensor can distinguish target analyte from other species in the sample matrix and especially the substances of related structures. It is the measure of the contribution of the analyte concentration to the total sensor signal as compared to the contribution of concentration of other compounds. It largely depends upon the physical and chemical nature of the analyte and the type of receptor.

Detection limit: This factor is also of prime importance and is the lowest value of a concentration that can be measured by the sensor under given conditions. Generally, a good sensor can respond to the concentration of analyte as low to ppb levels. It directly depends upon the type of receptor and transducer employed and the electronics if circuitry is involved in the built of sensor, in question.

Response time: It is the amount of time required to establish full-scale output from zero concentration to a change in concentration of the analyte or in other words, how long a sensor signal takes time to establish equilibrium value towards a definite concentration. Generally, sensors with short response time are favored for practical applications. Like other characterizing parameters, response time is also affected by the operating conditions and physical factors.

Dynamic range: It is a set of concentration values ranging from the lowest limit to the upper value that can be detected with precision and accuracy. It is necessary for a sensor to cover a wide dynamic range to be applied for practical use.

Stability: Stability characterizes the change in its baseline or sensitivity over a fixed period. It is the ability of a sensor to maintain its activity for a certain period. Usually, drift values are employed to determine the stability of a chemical sensor.

Reproducibility is the accuracy by which the sensor's output can be obtained.

Lifetime is the period in which the sensor can be used without significant deterioration in performance characteristics.

Briefly, an electrochemical sensor, which generates fast, sensitive, selective, precise and accurate response with low response time, high signal to noise ratio and wide dynamic range, is preferred. The electrochemical sensor should be small, cost effective, long-term stable, with good shelf life, and be able to work in harsh environments. All above factors decide the reliability for commercial use.

1.3 Thesis structure

The outline of this thesis is as follows:

Chapter One introduces the background and importance of study and its objectives.

Chapter Two includes a literature review of sensors, conducting polymers, graphene products, nanometals, synthetic methods, applications and relevant research associated with the problem addressed in this study.

Chapter Three presents the methodology and procedures used for data collection and analysis of the four projects:

- Synthesis, morphology, structure and electrochemical properties of electrodeposited polypyrrole.
- Investigation on the effect of two different electrodeposited nanometals (copper and silver) on the sensing properties of hydrogen peroxide.
- Exploration on the effect of graphene oxide and reduced graphene oxide as a substrate on the performance of sensor.
- Optimization of all possible variables including electrodeposition methods (cyclic voltammetry *vs*. amperometry), electrodeposition time, concentrations, pH, scan rate, number of cycles, applied potential, *etc*. to find the best condition for the best performance of the sensor.

Chapter Four presents the results and analysis of the collected data, as well as the discussion on the research findings and implications for practice.

Chapter Five offers a summary and recommendations for future research.

1.4 Objective of study

The overall purpose of this thesis is to optimize the application of polypyrrole as a conducting polymer, metal nanoparticles and graphene (in the form of graphene oxide or reduced graphene oxide) using electrochemical techniques. Particular objectives are as follows:

1. To synthesize various composites including polypyrrole, reduced graphene oxide and nanosized metals and investigate their effect on sensor characteristics toward H_2O_2 and glucose.

2. To study the effect of electrodeposition techniques (cyclic voltammetry *vs*. amperometry) on the structure, morphology and electrochemical properties of polypyrrole and consequently on the sensor performance.
3. To explore the effect of electrodeposited silver and copper nanoparticles on the sensing properties toward H_2O_2 and glucose.
4. To study the effect of pH, concentration, scan rate and number of cycles on the electroreduction and electrodeposition of graphene oxide and consequently on the sensor performance.

CHAPTER 2: LITERATURE REVIEW

The main purpose of a sensor recognition system is to provide the sensor with a high degree of selectivity for analyte measurement. Apart from the inherent catalytic characteristics of a material towards the analyte, its selectivity can be improved by the choice of a suitable electrical potential, by the introduction of a catalytic reaction step, through the addition of perm selective membranes or by further modifications. Many materials have been reported in the literature for electrocatalytic detection of H_2O_2. This section will review the most important materials with particular interest in the analytical parameters of the sensing devices fabricated from them.

2.1 Hydrogen peroxide (H_2O_2)

As a very simple compound found in nature, hydrogen peroxide (H_2O_2) has a huge significance in various applications including mining, clinical, pharmaceutical, environmental, textile and food manufacturing (Tsiafoulis *et al*., 2005). In living organisms, additionally, hydrogen peroxide also plays an important role as signaling molecule in regulating diverse biological processes including vascular remodeling, stomatal closure, apoptosis, immune cell activation and root growth (Laloi *et al*., 2004; Geiszt & Leto, 2004; Goncalves *et al*., 2014). H_2O_2 is also a byproduct produced from some classic biochemical reactions catalyzed by enzymes including urate oxidase (UOx), oxalate oxidase (OxaOx), glucose oxidase, glutamate oxidase, d-amino acid oxidase, alcohol oxidase, lactate oxidase, *etc*. As a result, the investigation on the detection of H_2O_2 is of practical importance for both industrial and academic purposes. Common techniques for H_2O_2 detection including fluorimetry (Lee *et al*., 1990), chemiluminescence (Cinti *et al*., 2014), fluorescence (Gomes *et al*., 2005) and spectrophotometry (Nogueira *et al*., 2005) are costly, complicated and time consuming. In contrast, electrochemistry presents sensitive, rapid, simple and cost-effective ways since H_2O_2 is an electroactive molecule (Wang, 2006).

In electrochemistry, H_2O_2 directly can be either reduced or oxidized at the surface of electrodes. Nevertheless, slow electrode kinetics and high overpotential limit these processes in analytical applications, which will reduce the sensing efficiency and may incur large interferences from other existing electroactive species in real samples such as bilirubin, urate, ascorbate, *etc*. Therefore, the current section on the detection of H_2O_2 principally targets on the materials, methods and synthesize of chemicals, which are usually utilized as sensor.

Various materials including transition metals, dyes, redox proteins, metal oxides, conducting polymers, graphene-based materials and carbon nanotubes have been used to conduct electrocatalytic detection of H_2O_2. On the other hand, in recent years, nanomaterials have drawn huge attention and interest due to their favorable physical, chemical and electronic performances, which are different from bulk compounds.

In addition, the structure and size of nanomaterials can be adjusted for constructing a remarkable sensing platform and increasing sensing performance (Wang, 2005). In view of this fact, some of the as mentioned compounds coupled with nanomaterials have presented specific advantages over ordinary compounds for the detection of H_2O_2 (Bai *et al*., 2011; Zhang *et al*., 2011).

The goal of this part is to give a rundown of the recent improvement and provide an insight into the compounds, which are employed in the electrochemical detection of H_2O_2.

2.2 Types of sensor

2.2.1 Amperometric sensor

Commonly by applying a constant potential, an amperometric sensor records the current produced during the reduction or oxidation of a reactant or product. The electron transfer between catalytic molecules is the most substantial factor, which affects the performance of amperometric sensors. In recent years, numerous attempts have been conducted on the application of electrochemically grown conducting polymer in amperometric sensors. Nanosized metal and metal oxides have been either decorated or entrapped within or on the conducting polymer.

2.2.2 Potentiometric sensor

Potentiometric detection is a rarely employed method in sensors, despite the fact that particular benefits over amperometric detection are shown. Sensors with very slow response and the rate of potential alter instead of steady state potential amounts should be considered as the analytical signal for quantification of the substrate (Gerard *et al.*, 2002). Potentiometric sensors based on conducting polymers can be formed by utilizing pH sensitivity of polymers. The mentioned technique generates some issues, belonging to a critical electrochemical and chemical ability of the polymer because of the similarity of them to the ion-exchange processes and redox equilibria.

2.2.3 Conductometric sensor

This type of sensors records the alterations in the conductivity of the biological material arising amid a couple of metal electrodes. In order to carry out the detection of glucose, hemoglobin/pepsin and urea neutral lipid/lipase, Contractor *et al*. (Contractor *et al*., 1994) have designed sensors, by observing the alteration in the conductivity arising from the changes in pH of the microenvironment and/or redox potential in the conducting polymers.

Additionally, the performance of polyaniline (PANI) films as a glucose biosensor has been studied by Ramanathan and coworkers (Ramanathan *et al*., 1995) via the dielectric spectroscopic measurements of Ppy/glucose biosensor as well (Ramanathan *et al*., 2000).

2.2.4 Optical sensor

The emitted or absorbed light as a result of a biochemical reaction is the main measurement technique in the optical sensors. In this category of sensors, suitable detectors are used to guide light waves by means of optical fibers. The optical sensors have been employed for O_2, pH and CO_2 detection.

2.2.5 Piezoelectric sensor

This type of sensor functions on the rule of creating electric dipoles on subjecting an anisotropic natural crystal to mechanical stress. The mass of the crystal is enhanced because of the adsorption of an analyte, which results in changed frequency of oscillation.

This kind of sensors has been used for the detection of nitrous oxide, carbon monoxide, ammonia, methane, hydrogen and other organophosphorus materials (Gerard, 2002).

2.3 Materials used for electrochemical H_2O_2 sensor

2.3.1 Conducting polymers

Recently, electrochemical sensors have drawn a huge attention due to having applications in environmental monitoring, food freshness, clinical diagnostics and bioprocess monitoring (Dobson, 2011; Shin & Kameoka, 2012). A number of materials such as graphene-based materials, conducting polymers (CPs) and nanosized metals have been employed to increase the stability in the fabrication of the desired sensors. In this situation, conducting polymers have developed the materials of choice for recent technological advances in biotechnology (Malhotra, 2006).

For a long time, polymers have been used as insulators. In fact, not many years ago, any polymer's electrical conduction - mainly because of weak bound ions- was ordinarily expected as an unacceptable property. Even though, over the last few decades, the ionic conductivity of polyelectrolytes (macromolecules with ionizable functionalities) and polymer electrolytes (macromolecular solvents containing low molar mass ions) have been extensively used in electrochemical systems such as power sources, sensors and development of solid-state electrochemical systems, the developments of CPs have caused a typical alteration in scientists' understanding and emerged a new outline in physics and chemistry (Inzelt, 2011).

The background of conducting polymers dates back to the 1970s when, unintentionally, a unique type of polymer was discovered with high electronic conductivity (conducting polymers) in the partially oxidized state (or less generally, in the reduced state). Heeger, MacDiarmid and Shirakawa, had important roles in this discovery that awarded them the Nobel Prize in Chemistry in 2000 for "the discovery and development of electronically conductive polymers" (Shirakawa *et al.*, 1977; Shirakawa, 2001; Ito *et al.*, 1974). As it happened many times in the science history, to this discovery, there were various precursors containing theoretical forecasting made by quantum chemists and physicists and various CPs that had already been developed. For example, in 1862, by the anodic oxidation of aniline, Henry Letheby was able to prepare polyaniline which was conductive and presented electrochromic performance (Bidan *et al*., 1999). However, the development of polyacetylene by Shirakawa and his colleagues and the finding of the considerable enhance its conductivity after “doping” by the group led by Heeger and MacDiarmid which had indeed opened this new field of research.

Electrochemistry plays an important role in the characterization and development of conducting polymers. Electrochemical methods are particularly appropriate to the controlled synthesis of these materials and for the tuning of a well-defined oxidation state. The fabrication, application and characterization of electronically conducting polymeric systems are still in the center of scientists and researchers’ attention in electrochemistry. At least two main reasons for this extreme interest exist. Firstly, the intellectual curiosity of researchers focusing on finding out the performance of these systems, especially on the charge transfer mechanism and the processes of charge transport occurring among redox reactions of conducting polymers. Secondly, a wide range of promising applications of these materials in the fields of organic electrochemistry, electrocatalysis, energy storage, corrosion protection, microsystem technologies, electrochromic displays, sensors, electronic devices, microwave screening, *etc*.

With respect to the conducting polymers development and their applications, numerous excellent reviews have been published (Inzelt, 2011; Heinze *et al*., 2010; Cosnier & Karyakin, 2010). Beside these comprehensive reviews, surveys of specific groups of polymers (Stejskal & Sapurina, 2005), techniques of characterization (Barbero, 2005; Buck *et al.*, 2004), or areas of application (Rubinson & Kayinamura, 2009; Deshpande *et al.*, 2014) have also been presented.

During the past 30 years, the basic nature of charge propagation is principally figured out (Sabouraud *et al.*, 2000); *i.e.*, the electron transportation can be expected to take place through an electron exchange reaction (electron hopping) between neighboring redox sites in redox polymers and by the movement of delocalized electrons through conjugated systems in the case of so-called intrinsically conducting polymers (*e.g.*, polypyrrole, polyaniline).

As a matter of fact, various mechanisms of conduction, including fluctuation induced tunneling and variable range electron hopping have been presented. Practically in every case, by the movement of electro-inactive ions, the charge is also carried, which means these compounds constitute mixed conductors. Based on the complexity and diversity of mentioned systems -note the polymeric properties (segmental and chain, alterations in the morphology, slow relaxation) and chemical alterations (dimerization, cross-linking, ion-pair formation, *etc*.) connected with them- the discovery of new system leads new issues to be solved. Further investigation is required to obtain a precise knowledge of all of the processes related to the static and dynamic characteristics of different interacting molecules confined in a polymer network. Even though the conductivity of CPs is an attractive and usable feature in itself, their most significant property is the variability of their conductivity, *i.e.*, the ease with which the materials can be reversibly switched between their conducting and insulating forms.

Unusual electronic properties of conducting polymers such as low energy optical transitions, electrical conductivity, high electron affinity and low ionization potential are due to π-electron backbone. The extended π-conjugated structure of the conducting polymers has single and double bonds changing along the chain of polymer. High values of the electrical conductivity achieved in such polymers has caused the name “synthetic metals” (Kopecka *et al.*, 2014). Many researchers have studied the applications of conducting polymers such as biosensing devices and analytical chemistry (Karami & Nezhad, 2013; Gerard, 2002; Gangopadhyay & De, 2000; Badhulika *et al.*, 2014).

In the recent years, novel approaches have been started by researchers. The contemporary trend is based on the design of composites such as nanocomposites of polymers and other materials including graphene-based materials, carbon nanotubes or inorganic compounds which have specific properties and structure.

In different fields of sensors (amperometric, voltammetric, potentiometric, conductometric and impedimetric), CPs are employed as active sensing, or catalytic layers; nevertheless, in various number of applications, conducting polymers serve as matrices which entrap enzymes or other biologically active materials.

In future, hybrid materials and nanocomposites based on CPs, mainly will be mainly significant compounds. There is a huge anticipation concerning electro conducting nanomaterials including nanorods, nanotubes, nanofibers and other nanostructures based upon the supramolecular self-assembly of CPs.

The behaviors of both the CP-based transistors and electrochemical cells may be improved by manipulation of their microstructures. CPs are comparatively cheap compounds, nevertheless, the particularly enhanced features can give more improvement regarding the mass production making the products much less expensive (Suarez-herrera, 2009).

2.3.1.1 Background of conducting polymers

In 1975, immediately after the discovery of poly(sulphur nitride), research on conducting polymers (Greene & Street, 1975). By simple doping with oxidizing agents (p-doping) such as $NOPF_6$, AsF_5 and I_2 or reducing agents such as sodium napthalide (n-doping), they could increase the conductivity of polyacetylene (10^{-9} S.cm^{-1}) by various times (10^5 S.cm^{-1}). This has attracted much more interest of the scientists and researchers to the discovery and investigation of new conducting polymers. Ivory and his colleague (Ivory *et al.*, 1979), have synthesized poly-paraphenylene (PPP) which produces high conducting charge transfer complexes with both oxidized and reduced (p- and n-doping) conditions. Conductivity increases from 10^{-5} to 500 cm^{-1} by using AsF_5 dopant. Electron spin-resonance measurements and theoretical models reveal that the PPP's charge transport is a polaron/bipolaron.

Discovery of poly-paraphenylene was especially impressive, since its solution processability and paved the way for potentially achieving commercially applicable conducting plastics (Rabolt *et al.*, 1980). One of the most studied polymers among various poly-hetrocyclines is polypyrrole (Ppy). Pyrrole can be electrochemically oxidized in aqueous solution (*e.g.* H_2SO_4) on platinum electrode. The resulted material is a CP, which is known as "pyrrole black". Coherent layers of polypyrrole (conductivity of 100 S.cm^{-1}) presented superior stability in the air were produced by Kanazawa and his team (Kanazawa *et al.*, 1979).

Insolubility of polypyrrole in any organic solvents is the major drawback of its processability. Many other conducting polymers including polyaniline, polycarbazole, polyindole, polyfuran, *etc*. have also been prepared. Figure 2.1 shows the structure of some typical CPs.

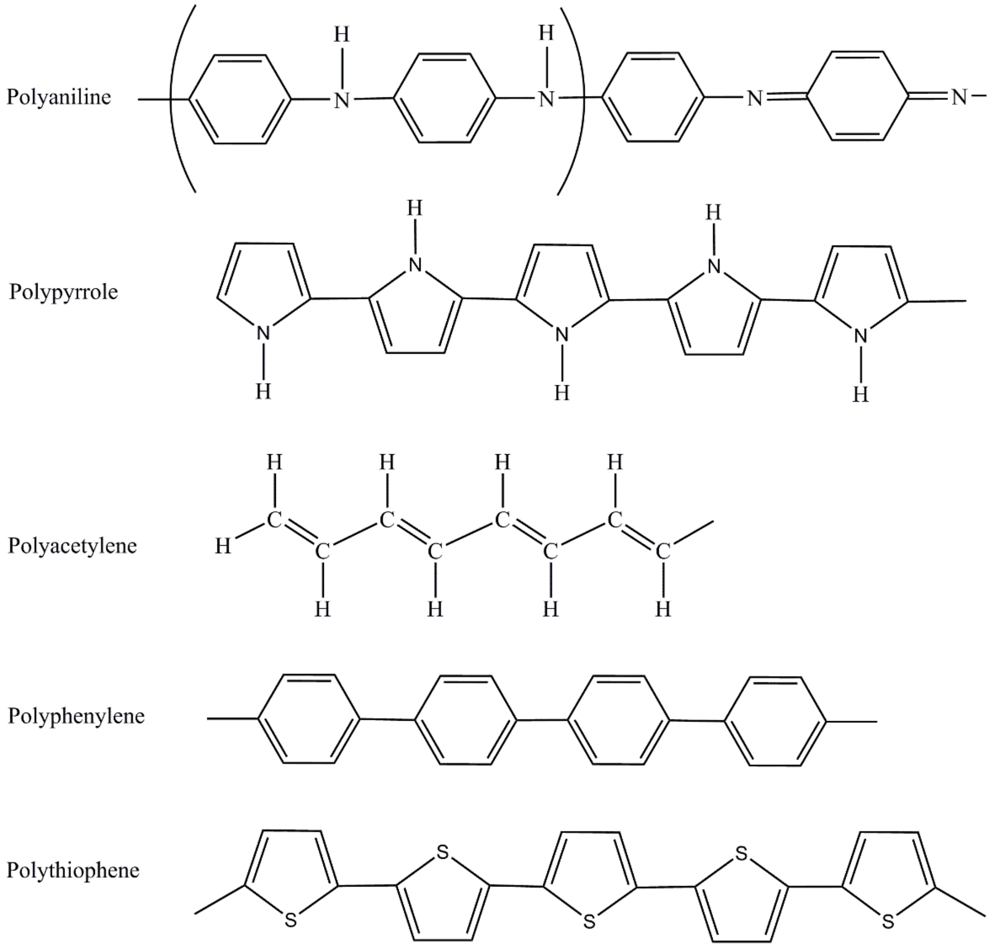

Figure 2.1: Chemical structures of typical CPs usually employed in sensor applications.

2.3.1.2 Mechanism of conduction

The conduction mechanism in aforementioned polymers is complicated since this type of polymer shows conductivity in a wide range and involved various mechanisms within different systems. CPs present increased conductivity by various times of magnitude of doping. By employing the concept of solitons, polarons and bipolarons, the electronic phenomena in these systems has been explained (Gerard, 2002).

A variety of factors such as polaron and conjugation length, the overall chain length and charge transfer to adjacent molecules have influenced the conductivity in conducting polymers (Suarez-herrera, 2009). These are described by several models based on intersoliton hopping, the hopping between localized states assisted by intra-chain hopping of bipolarons, lattice vibrations, variable range hopping in 3-dimensions and charging energy limited tunneling among conducting domains.

2.3.1.3 Conducting polymers synthesis

Several techniques are used for the synthesis of CPs. Nevertheless, the most frequently employed method is the oxidative coupling including the oxidation of monomers to generate a cation radical followed by coupling to form di-cations and the repetition leads to the polymer. Due to its simplicity and reproducibility, electrochemical method has been rapidly becoming the favored common technique for fabricating electrically CPs. One of the major benefits of electrochemical polymerization is that the reactions can be performed at room temperature. The film thickness can be easily adjusted by varying either the current or potential with time. Electropolymerization of this type of polymers is commonly achieved by:

- Constant potential (potentiostatic method)
- Constant current (galvanostatic method)
- Potential scanning or sweeping techniques.

It should be mentioned that as early as in 1983, Fauvarque and his team (Fauvarque *et al.*, 1983) reported the synthesis of poly(*p*-phenylene) film by electroreduction-assisted catalysis by Ni(0) complex. In the first part, electropolymerization is explained in the context of π-conjugated polymers. Four eras have been identified in this saga: the “era of physicists”, the “era of electrochemists”, the “era of polymerists” and the “era of molecular electronics” (Cosnier, 2010). This division appears a little artificial, since the progress in each of these generations let from mutual enrichment among these scientific communities. The “era of electrochemists” starts in the 1980s with the early use of electropolymerization.

The second part presents the major milestones reached by the process of electropolymerization in the light of the functionalization of surfaces for the electrodeposition of increasingly sophisticated conjugated architectures endowed with specific functionalities from sensors to active photovoltaic layers. This part, the “era of electrochemists”, began with the electropolymerization of aromatic heterocycles and derivatives. In addition to the ‘‘easy-to-handle effect’’ which has been previously illustrated by *(CH)x*, electropolymerization is based on a new concept of oxidative condensation through the generation of radical cations. Early work in 1916 and 1937 (Cosnier, 2010) on chemically-prepared “*neri di pirrolo*” had not been aware of the electronic properties of these powders of poly(oxipyrrole). Chemical oxidation of aniline, reported by De Surville and coworkers in 1968 (De Surville *et al*., 1968), and of pyrrole, reported by Hautiere Christofini in 1973 (Cosnier, 2010), were recognized to provide electrically conductive materials. Electropolymerization allowed handling of polypyrrole, polyaniline and poly(*p*-phenylene) films, resulting in completely new polymers films. Consequently, in early 1980s, the electrochemist community came up to the idea to use electrochemistry not only as a tool to prepare CP films but also as a methodology to investigate the doping/dedoping process electrochemically tuned with the associated movements of ionic dopants and the concomitant evolution of the electronic structure. The first electropolymerization experiment reported in 1968 by Dall’oxlio (Suarez-herrera, 2009) on pyrrole in water medium was not the trigger event; as a matter of fact, except for aniline in acidic media, pristine pyrrole and, as reported later, for thiophene and derivatives in micellar medium (Kone *et al*., 2005; Tamburri *et al*., 2009), few heterocycles are soluble and able to electropolymerize in aqueous media. The first determining event was the electropolymerization in an organic medium of pyrrole (0.06 M) in acetonitrile (1% aqueous) containing 0.1 M Et_4NBF_4, reported in the article of Diaz and co-authors. in 1979 (Diaz *et al*., 1979).

The route then opened for the screening of electrochemical synthesis of conducting polymers by anodic oxidative condensation of aromatic heterocycles. Over the next 10 years, electropolymerization of polythiophene, poly(*p*-phenylene), polynaphthalene, polyanthracene, polypyrene, polyindole, polyazulene, polyfluorene and polycarbazole were reported (Clergereaux *et al*., 2000). Polyaniline, which was first chemically synthesized and considered as early as in 1968 by De Surville and coworkers (De Surville, 1968) as a semiconductor whose redox properties can be tuned by the pH, was electrosynthesized by Diaz in 1980 (Diaz & Logan, 1980), and then rediscovered around 1985 in the light of the new concepts of conjugated structures (Lang *et al*., 2006).

An important step towards the functionalization of surfaces was the inclusion of a functional dopant during electrodeposition. Electrodeposition of conducting polymer films at the surface of an electrode has opened a new field at the convergence between two rich domains: electrochemistry of modified electrode (Cosnier, 2010) and conjugated systems (Suarez-herrera, 2009). Consequently, applications of modified electrodes in electrocatalysis, electrochromism, energy storage, electroanalysis and sensors have been enriched by the specific properties of intrinsically conducting polymers (CPs), for example, electrochemically tunable doping and dedoping (equivalent to adjustable redox states), polymeric matrix affording electrical wiring, uses as immobilized redox mediators, and the capacity to induce new functionalities by the use of specific gratings. Reciprocally, electrochemistry has opened up the route to easy-to-handle polymer films in a manner similar to the way that polyacetylene, $(CH)x$, prepared as a film by a modification of the Natta reaction (Suarez-herrera, 2009), resulted in the discovery, in 1977, of the doping effect as presented by Shirakawa and coworkers (Shirakawa *et al.*, 1977). In addition, this cross-fertilization enlarged the panel of new CP-based materials, such as electrogenerated composites and strengthened or brought in new applications such as energy conversion and storage, electrotriggered drug delivery, soft actuators, chemical and electrochemical sensors, biocompatible films and artificial muscles (Jang, 2006). Applications of pristine polyheterocycles were limited to the exploitation of their redox properties (batteries and supercapacitors) and related modulations in conductivity (electrochemical transistors), color (electrochromism) and volume changes (actuators). Functionalization by the inclusion of specific dopants (Figure 2.2) soon appeared as a straightforward route (Inzelt, 2011), since no specific chemistry on the heterocycle is required. The inclusion of the functional dopant present in the electrolyte during electropolymerization was preferred over the exchange of classical nonfunctional dopants (perchlorate, chloride, tetrafluoroborate, *etc*.) after the electrodeposition just by dipping in a solution containing the functional dopant. In fact, the reverse reaction, that is, the retrodiffusion of the functional dopant in a renewed solution cannot be avoided, even though it had been exploited in a certain manner for the electrocontrolled release of species. Use of a bulky dopant (*i.e.*, with a diameter more than 5–6 Å) during electrodeposition allows an almost irreversible trapping in the polymeric matrix due to the entanglement of the polymeric chains around the dopant. The shape of the dopant is also a determining factor and for linear dopants, such as alkylsulfonates, the retention starts from chain length of C10 (Cosnier, 2010). In this case, other holding factors such as hydrophobicity of the dopant chain must be considered. When the anionic dopant is immobilized, the dedoping results in the insertion of a cation to insure the electroneutrality (Schab-balcerzak, 2011).

This cationic pseudodoping is also performed when the anionic dopant, usually sulfonate, is directly grafted on the conjugated polymer skeleton (self-doped polymers) (Rickert *et al*., 2008)) or is a pending group of an ionomeric polymer (Cosnier, 2010).

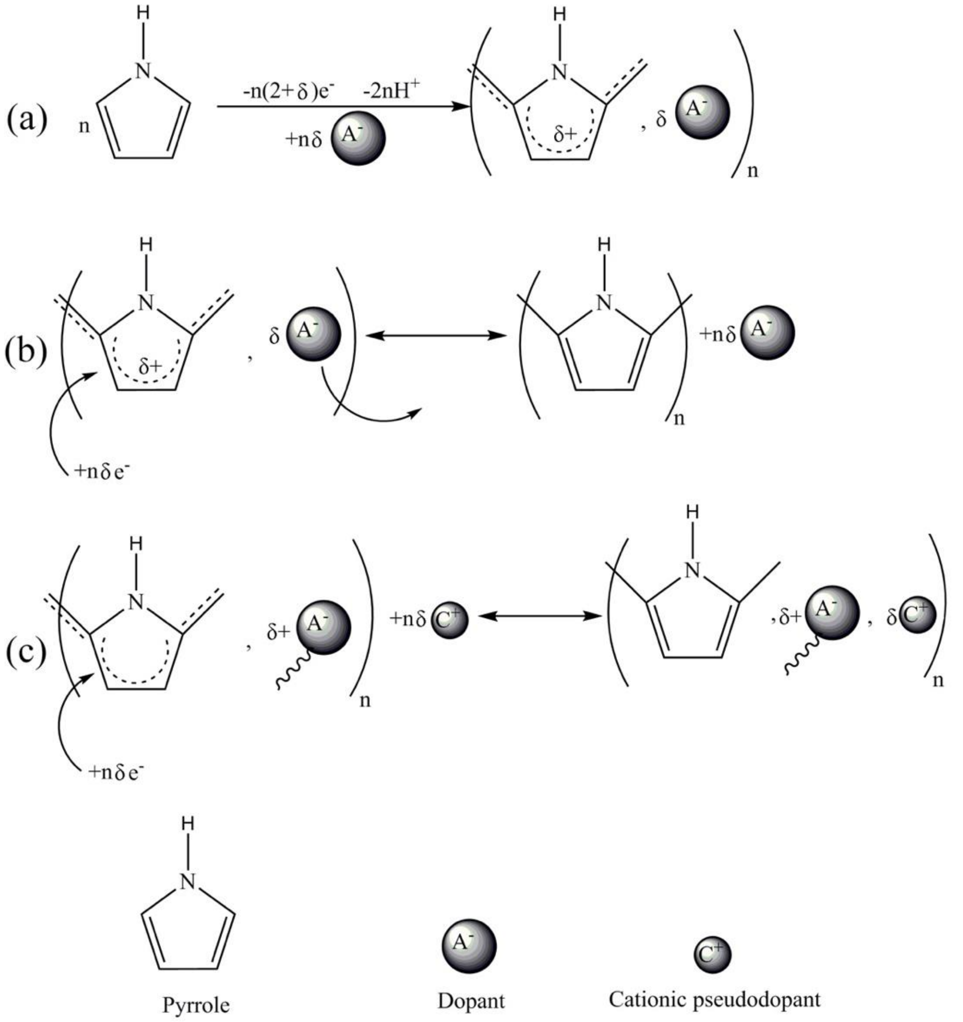

Figure 2.2: Electropolymerization with functional dopant. (a) The function is introduced during the electrodeposition, using a specific dopant A^- entrapped into the polymeric backbone; (b) When the dopant is small, the anionic dopants A^- are mobile and mainly expelled during the dedoping by electroreduction; (c) Provided that the anionic dopants are immobilized (the wavy line symbolizes this immobilization), the dedoping results mainly in the entrance of a cationic “pseudodopant” C^+ and *vice versa* during doping.

2.3.1.4 Conducting polymers application

The synthesis and production of nanoscale conducting polymers has become popular because they are promising materials for the fabrication of next-generation sensors. Furthermore, CPs like polypyrrole (Ppy) and polyaniline (PANI) have received considerable interest in the last few years because of their applications as sensor and biosensors due to their polymer chain structure, high conductivity, environmental stability and low cost (Shahnavaz *et al*., 2014). The conducting polymers have drawn much attention mainly due to their excellent performances in electrochromic devices, solar cells, molecular electronic devices, lightweight batteries, corrosion and sensors. By electrodeposition of polypyrrole on the reduced graphene oxide surface, polymeric heterojunctions, solar cells have been fabricated (Ramasamy *et al*., 2015). In order to fabricate electrode materials for rechargeable batteries, many conducting polymers including polypyrrole, polyindole, polyacetylene, polyaniline, polythiophene, polyindole, *etc*. have been reported (Guerfi *et al*., 2014; Aradilla *et al*., 2014; Huang & Yang, 2014; Liu *et al*., 2014; Holze & Wu, 2014; Li *et al*., 2014). Researchers have employed Ppy films as a drug release system (Seyfoddin *et al*., 2015). The potential for CPs is huge in the field of photonics and electronics (nonlinear optics) and has been utilized to prepare capacitors, diodes, printed circuit boards and field-effect transistors (FET). Polyaniline or PEDOT nanofiber sensors commonly present a shorter response time and higher sensitivity due to high surface areas (Long *et al*., 2011). It was found that the response times of the polyaniline nanofiber sensors exposed to trimethylamine, chloroform and toluene were two times faster, with the current variations up to 4 times higher than of the bulk polyaniline sensors.

2.3.1.5 Characteristics of polypyrrole

As one of the most important members in conducting polymer family, polypyrrole has its own unique characteristics different from the other conducting polymers, recognized by its high conductivity, electrochemical activity, stability, and biocompactibility (Kopecka, 2014). Polypyrrole has been under extensive investigation for its application in electronic and electroactive materials, such as field effect transistors, electroluminescent diodes and electromagnetic shielding layers. On the other hand, polypyrrole has also been fabricated in various types of advanced form, such as selfassemble monolayers (SAM), Langmuir-Blodgett films and nano architectures, in order to study the morphology-dependent properties of polypyrrole and possibly precise control of the polymer properties through alternating morphologies. However, polypyrrole has also been subject to be one of the components of various composite and electrode materials, functioning from the conductive substrate, biological binders, to protective layers. In general, polypyrrole could be referred to the polymers formed through the polymerization of pyrrole or its derivatives. The most common polypyrrole produced solely from pristine pyrrole and pyrrole derivatives are barely used in practical production of pyrrole, only if certain special application requirements have been specific (solubility, meltability, dispersibility, *etc*.). Polypyrrole could be produced through varying kinds of methods including electrochemical, oxidation, plasma and irradiation polymerization, among of which the electrochemical and oxidation methods are the most frequently utilized (Sabouraud, 2000). The polymerization of pyrrole majorly follows the free radical cationic mechanism, which is generally composed of three synthetic steps namely initiation, propagation and termination (Sabouraud, 2000). When an electron is taken from the pyrrole monomer by the oxidants or current flow, a pyrrole radical cation would form, and it would initiate the polymerization through the coupling with another pyrrole monomer. This coupling process would continue generating radical dimers, trimers, tetramers with active chain ends, which would eventually lead to the formation of the long-chain polypyrrole. The thus-formed polypyrrole is majorly composed of polymer backbones with alternating single and double bonds, which are normally referred to as the π conjugated system. Excessive amount of oxidative dopants are normally required to create oxidation defects along the polymer backbone, which would result in the formation of polarons and bipolarons localized within certain distorted chain portions composed of four pyrrole rings. Quinoid-like pyrrole rings also exist within the distorted portions in order to link the charge components of the polarons/bipolarons together. The existence of polarons/bipolarons within the polymer backbones would create a new electronic state for the polymer, located between the valence band and conduction band, which enables charge transfer through these states and facilitates the conducting properties of the polymer backbone. Furthermore, the conductivity of polypyrrole could be controlled by varying the oxidation state of the polymer backbones, on the basis of not deteriorating their conjugated conformation. Higher oxidation state would create more polarons/bipolarons as well as increasing the energy range of the electronic states, which would eventually lead to a new band formation and enhances the conductivity substantially (Liu, 2011). Based on the conductivity, compounds are categorised into three groups: conductors, semiconductors and non-conductors/insulators. Two energy bands exist. Valence band which relates to the electronic energy levels where they are occupied and the second one is conductance band which is the unoccupied energy levels (Figure 2.3). The band gap, E_g, is the difference in energy between the top of the outermost valence band and the bottom of the conduction band. Conductivity occurs when the electrons travel from the valence band to the conductance band. The valence band in conductors overlaps with the conduction band, *i.e.*, $E_g \approx 0$ eV, and the electrons fill up the conduction band partially. The gap between the valence and conduction bands is small in semiconductors, where $E_g \approx 1.0$ eV; therefore, the electrons have this ability to be excited from the valence band into the conduction band at room temperature. However, for insulators, the gap between the valence and conduction bands is large, where $E_g \geq 10$ eV, and as a result, the excitation of the electrons from the valence band into the conduction band is very difficult. However, conducting polymers in the region of 1.0 eV were considered as semiconductors according to the Bredas and Street' establishment but this band theory model fails to explain the conductivity associated with conducting polymers. It is now generally accepted that the conducting nature of the polymers arises from the formation of various redox states upon the oxidation of the conjugated backbone. This is due to the formation of mobile charge carriers, which are termed as polarons and bipolarons (Molapo *et al*., 2012; Dai, 2004).

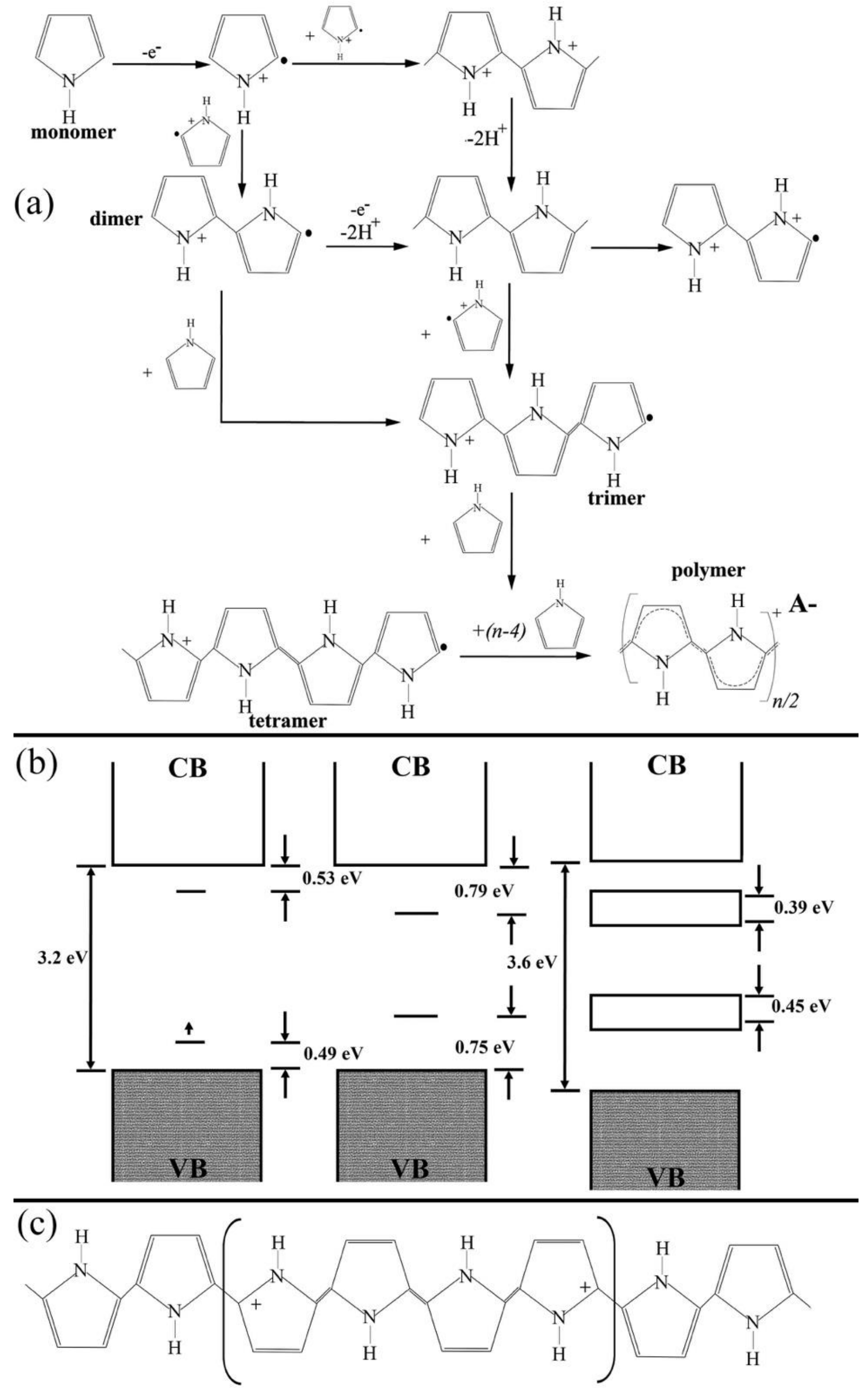

Figure 2.3: (a) Polymerization mechanism of polypyrrole; (b) Polypyrrole structure upon doping. From left to right: low doping level, polaron formation; moderate doping level, bipolaron formation; high doping level (33 mol%), formation of bipolaron bands; (c) Molecular structure of polypyrrole.

2.3.2 Graphene

In recent years, due to particular physical and chemical properties and several potential applications, graphene-based materials have drawn a huge attention in both technological and scientific areas (Shao, 2010). Compared to carbon nanotubes (CNTs), graphene-based materials present significant preferences of ease of processing, safety and low cost (Chen, 2012). In contrast with CNTs, graphene-based materials are free from the contamination of transition metals which leads it to be an excellent platform for electrochemical applications.

Enormous scientific activity has initiated soon after the report of a technique to prepare individual graphene sheets by Geim *et al.* in 2004 (Geim & Novoselov, 2007; Novoselov *et al*., 2004). Graphene is a two-dimensional (2D) crystal that is stable at room temperature. Extraordinary electronic characteristics including the anomalous quantum Hall effect give graphene an astonishing electronic structure (Novoselov *et al*., 2007) and special high carrier mobility at almost high charge carrier concentrations under ambient conditions (Bolotin *et al*., 2008; Novoselov, 2004). As a new material, the applications of graphene-based materials are drawing huge attention since several attractive properties such as electrical (Orlita *et al*., 2008), thermal (Balandin *et al*., 2008) and mechanical (Lee *et al*., 2008) properties have been described to support the dominance of graphene based materials to traditional ones (Gao, 2015). Based on this tendency, graphite oxide, firstly emerged over 150 years ago, (Schafhaeutl, 1840) has rediscovered as an extreme attractive material because of its importance as a pioneer for the economical and mass production of graphene-based materials. The layered structure of graphite oxide and graphite are similar, but in graphite oxide, the plane of carbon atoms is heavily decorated by oxygen functionalities, expanding the interlayer distance and making the atomic-thick layers hydrophilic. Consequently, under mild ultrasonication, these oxidized sheets can be exfoliated in water. As a result of this exfoliation, graphene oxide (GO) consists of only one or few layers of carbon atoms like graphene. The most appealing feature of graphene oxide is that by eliminating the oxygen-containing groups with the recovery of a conjugated structure, GO can be partially reduced to graphene-like sheets. Most of the time, the reduced graphene oxide (rGO) layers are known as one type of chemically derived graphene. Functionalized graphene, chemically converted graphene, reduced graphene and chemically modified graphene are some other names which have also been used for reduced graphene oxide (Eda & Chhowalla, 2010). The most straightforward target of each of reduction way is to create graphene like materials which is very much alike to the pristine graphene achieved from direct mechanical exfoliation (such as Scotch tape method) of singular sheets of graphite both in properties and structure. Although many attempts have been done, the ultimate goal is far away to be achieved. Defects and residual functional groups seriously change the carbon plane structure. Therefore, for this reason, it is not suitable to mention as rGO, still, easily as graphene since the characteristics are considerably different. Graphene oxide has two significant properties:

1. As raw material, graphite is an inexpensive material and also the synthesize process is cost-effective chemical methods with a high yield.
2. It is highly hydrophilic and can form stable aqueous colloids to facilitate the assembly of macroscopic structures by simple and cheap solution processes, both of which are important to the large-scale uses of graphene.

Consequently, graphene oxide and reduced graphene oxide are still in the center of attention in the research and development of graphene, chiefly concentrating on their mass applications. Hence, the reduction of GO is certainly an important subject and various processes of reduction produce different characteristics which consequently influence the ultimate performance of materials or devices. Although the ultimate goal to obtain appropriate graphene is not easy to achieve, scientific attempts have gradually made it closer (Pei & Cheng, 2012).

Graphene-based materials have shown high level performance in many applications including solar cells (Yin *et al*., 2014), batteries (Mahmood *et al*., 2014; Wu *et al*., 2015), fuel cells (Paneri *et al*., 2014), electronics (Mabrook & Zeze, 2015), supercapacitors (Ruoff, 2014; Shao *et al*., 2015) and biosensors (Mahmoudian *et al*., 2015; Ghadimi *et al*., 2015) due to its particular physical and chemical properties such as excellent thermal and electric conductivity, high surface area (theoretically 2630 m^2/g for single-layer graphene) and high mechanical strength.

Graphene-based materials have presented remarkable performance in terms of macroscopic scale conductivity and electrocatalytic activity than materials based on carbon nanotubes. Regarding this fact, in electrochemistry, opportunities happened upon by carbon nanotubes maybe applicable for graphene-based materials. In compare to carbon nanotubes, ease of processing, high surface area, low cost and safety are the potential advantages of graphene-based material. Because of high purity (in contrast with carbon nanotubes, transition metals such as Ni, Fe, *etc*. are not present in graphene from reduction of GO), it gives an excellent platform to investigate the electrochemical properties of carbon materials. It is anticipated that, in many applications, graphene-based material is increasingly competing with carbon nanotubes. Graphene-based material shows superior electron transfer which promotes the ability for some analyte and great electrocatalytic performance toward small biomolecules including hydrogen peroxide making graphene-based material greatly appealing for non-enzymatic electrochemical sensors.

2.3.2.1 Electrochemistry of graphene

In electrochemistry, for the potential application of a specific type of carbon compound, the fundamental electrochemical properties should be investigated to understand different significant factors of carbon electrodes (Jia *et al.*, 2007; Niwa *et al.*, 2006; McCreery, 2008): redox potentials, electron transfer rate, electrochemical potential window, *etc*. Zhou shows that in 0.1 M phosphate buffer solution (PBS) in pH 7.0, graphene presents a broad electrochemical potential window of *ca.* 2.5 V (Zhou *et al.*, 2009), which is almost similar to glassy carbon electrode (GCE), graphite and even boron-doped diamond electrodes (McCreery, 2008; Palanisamy, 2012). The AC impedance spectra shows that the charge transfer resistance of graphene is much lower than graphite and GC electrodes (Palanisamy, 2012). By employing cyclic voltammetry (CV) of redox couples including $[Fe(CN)_6]^{3-/4-}$ and $[Ru(NH_3)_6]^{3+/2+}$, the electron transfer behavior of graphene is studied which shows well-defined redox peaks (Yang *et al.*, 2009; Lin *et al.*, 2009). Cathodic and anodic peak currents in the cyclic voltammetry are linear with the square root of the scan rate, suggesting that the redox mechanisms on graphene-based electrodes are mainly diffusion controlled (Lin, 2009). The peak to peak potential separations (ΔE_p) in cyclic voltammetries for most one electron transfer redox couples are totally low, near to the ideal amount of 59 mV, as an example, 61.5 to 73 mV(10 mV/s) for $[Fe(CN)_6]^{3-/4-}$ (Wang *et al.*, 2009; Tang *et al.*, 2009; Lin, 2009) and 60 to 65 mV (100 mV/s) for $[Ru(NH_3)_6]^{3+/2+}$ (Tang, 2009), much smaller than GC electrode (McCreery, 2008). The ΔE_p is linked to the electron transfer (ET) coefficient (Shao, 2010), and a low peak to peak potential separations value showing a fast electron transfer for a single electron electrochemical reaction (Shang *et al.*, 2008) on graphene-based material. To investigate the electrochemical activity of graphene based material to various types of oxidation-reduction systems, Tang *et al*. (Tang *et al.*, 2009) studied three typical redox pairs systematically: $[Ru(NH_3)_6]^{3+/2+}$, $[Fe(CN)_6]^{3-/4-}$ and $Fe^{3+/2+}$. As it is known, $[Ru(NH_3)_6]^{3+/2+}$ is an almost ideal outer-sphere oxidation / reduction system that it does not have sensitivity to most surface defects or impurities and can serve as a practical benchmark in compare with electron transfer of several carbon electrodes. Ferricyanide-ferrocyanide, $[Fe(CN)_6]^{3-/4-}$ is surface-sensitive but not oxide-sensitive; and $Fe^{3+/2+}$ is both surface-sensitive and oxide-sensitive (Shao, 2010). The electron transfer rate constants (k_0) determined from cyclic voltammetry's curves of graphene and GC electrodes are 0.18 $cm.s^{-1}$ and 0.055 $cm.s^{-1}$ for $[Ru(NH_3)_6]^{3+/2+}$, respectively (Tang, 2009). This shows that the graphene particular electronic structure, especially the high density of the electronic states over a wide energy range endows graphene with fast electron transfer (McCreery, 2008). The electron transfer rate constants (k_0) for GCE and $[Fe(CN)_6]^{3-/4-}$ on graphene were measured to be 0.029 $cm.s^{-1}$ and 0.49 $cm.s^{-1}$, respectively, and the ET rates for $Fe^{3+/2+}$ at graphene electrode are several times higher than GCEs (Tang, 2009). These show that the surface, the physicochemistry and electronic structure of graphene are favorable for ET (Tang, 2009; Chen, 2012; Shao, 2010).

2.3.2.2 Preparation and characteristics of graphene oxide

For the first time, Schafhaeutl (Schafhaeutl, 1840) in 1840 and Brodie (Brodie, 1859) in 1859 reported GO. Dreyer and his colleanges (Dreyer *et al.*, 2010), Compton and Nguyen (Compton & Nguyen, 2010) have widely reviewed the evolution history of synthesis techniques and chemical structure of GO. Currently, the prevalent method of preparing GO is based upon the technique which is suggested by Offeman and Hummers (Hummers & Offeman, 1958) in 1958, in which the oxidation of graphite to graphite oxide is performed by treating graphite with a water-free solution containing sodium nitrate, potassium permanganate and sulfuric acid. Although various modification has been suggested (Hirata *et al*., 2004; Kovtyukhova *et al*., 1999; Wu *et al*., 2009; Zhao *et al*., 2010), the main strategy is unchanged. Consequently, these techniques are generally called as modified Hummers methods.

Although this technique has been proposed for over a century, due to partial amorphous character and consequently the complexity of GO, the exact chemical structure is still not fully understood. Many early studies have developed various structures of graphene oxide with a common lattice composed of discrete repeat units (Szab *et al*., 2006). The extensively preferred model of GO proposed by Lerf *et al.,* (Lerf *et al*., 1998; He *et al*., 1998) is a non-stoichiometric model (Figure 2.4) where the carbon sheet is functionalized by epoxy (1,2-diether) and alcohol functionalities. Carbonyl functional groups exist as well, possibly as carboxylic acids at sheet edge as well as organic carbonyl defects within the sheet. Recently, the nuclear magnetic resonance (NMR) spectroscopy investigations (Gao *et al*., 2009; Cai *et al*., 2008) of graphene oxide have proposed little modifications to the recommended structural model such as the existence of 5- and 6-membered lactose on the periphery of graphitic sheets and also the existence of tertiary alcohols and esters on the surface, while epoxy and hydroxyl functional groups are still dominant (Gao, 2015). A perfect plane of graphene is flat and consists of only trigonally bonded sp^2 carbon atoms (Lui *et al*., 2009) apart from microscopic ripples (Stolyarova *et al*., 2007). The heavily decorated graphene oxide planes compose partially of tetrahedrally bonded sp^3 carbon atoms, which are slightly displaced below or above graphene sheet (Schniepp *et al*., 2006). Because of the deformation of the structure and existence of covalently bonded functionalities, graphene oxide planes are atomically rough (Parades *et al*., 2008; Paredes *et al*., 2009; Mkhoyan *et al*., 2009). Mkhoyan and co-authors investigated the distribution of oxygen groups on a graphene oxide monolayer by employing high-resolution annular dark field (ADF) imaging in a scanning transmission electron microscopy (STEM) (Mkhoyan, 2009). The obtained data shows that the oxidation fluctuates degree at the nanometer scale, proposing the existence of *sp*^{3} and *sp*^{2} carbon clusters of a few nanometers. Various researchers (Gómez-Navarro *et al*., 2007; Gómez-Navarro *et al*., 2010; Paredes, 2009; Kudin *et al*., 2008) have investigated the graphene oxide surface with scanning tunneling microscopy (STM) and discovered highly defective areas, possibly because the existence of oxygen and other regions are almost intact. Notably, Pandey *et al.* reveals that the graphene-like honeycomb lattice in graphene oxide is preserved, although with disorder, that is, the carbon atoms attached to functional groups are slightly displaced but the overall size of the unit cell in graphene oxide remains similar to that of graphene (Pandey *et al*., 2008). Accordingly, graphene oxide can be explained as an oxidized regions random distribution with oxygen functionalities, linked with non-oxidized areas where majority of the carbon atoms preserve *sp*^{2} hybridization. In the graphitic lattice, the long-conjugated network plays a critical role in the conductivity of graphene (Kaiser, 2001; Kopelevich & Esquinazi, 2007). Functionalization localizes π-electrons and damages the conjugated structure, resulting in a decrease of carrier concentration as well as mobility. However, conjugated regions exist in the graphene oxide, long range (> l m) conductivity is blocked by the absence of percolating pathways among *sp*^{2} carbon clusters to allow classical carrier transport to take place. Subsequently, as-prepared graphene oxide layers are commonly insulating, showing a charge transfer resistance of 10^{12} Ω/sq. or higher (Wu, 2009; Zhao, 2010).

The bonded functional groups and lattice defects restore the graphene’s electronic structure and represent strong scattering centers affecting the electrical transport. As a result, the graphene oxide reduction is related to eliminating the oxygen functionalities attached to the graphene and eliminating other atomic-scale lattice defects, as well as aiming at restoring the conjugated network of the graphitic lattice. These structure alterations lead to restoring of conductivity and other graphene properties (Pei, 2012).

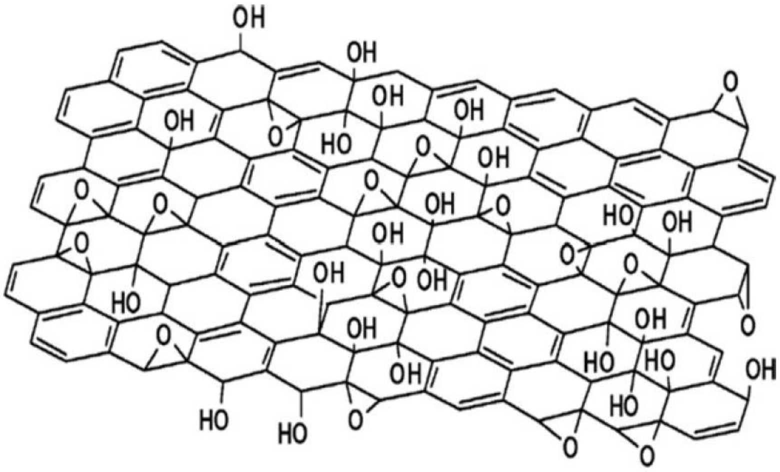

Figure 2.4: Lerf–Klinowski model of GO.

2.3.2.3 Reduction of graphene oxide

Due to disrupted *sp*^{2} bonding structures, graphene oxide is an electrically insulating material. Since by recovering the π-network, the electrical conductivity can be recovered as well. Therefore, the process of reduction is one of the most significant reactions of GO. Chemically reduced graphene oxide (CRGO), reduced graphene oxide (rGO) and graphene are the most relevant names of the product of this reaction. The two mentioned products are usually mixed up but the differences of the structure can be important which make the use of separate terms appropriate. Additionally, it should be considered that there is a difference between graphene oxide and graphite oxide. In the case of chemical, graphene oxide and graphite oxide are similar, but structurally they are not the same. Instead of maintaining a stacked structure, the material is exfoliated into monolayers or few-layered stacks. Due to its hydrophilicity, the surface functionality (especially in basic solution) considerably weakens the platelet–platelet interactions. To exfoliate graphite oxide to graphene oxide, a variety of mechanical and thermal techniques can be employed, although stirring and sonicating graphite oxide in water are the most relevant rout. Sonicating polar organic solution such as water, even though is much faster than mechanical stirring, has a considerable negative effect which causes significant destruction to the graphene oxide sheets (Parades, 2008). Instead of owning an average size of various microns per side, the dimensions decreased to various hundred nanometers and the final production includes a markedly larger size distribution (Becerril *et al.*, 2008; Gómez-Navarro, 2007). Graphitic structure can be broken by the oxidation process into smaller fragments as well (Becerril *et al*, 2008; Gómez-Navarro, 2007). The solvent and the extent of surface functionalization imparted during oxidation are the factors which affect the maximum dispersibility of GO, which is significant for processing and further derivatization. Based on our best knowledge, it is clear that the higher surface polarity causes the higher dispersibility. Typically, in the water, the dispersibilities are approximately 1 to 4 $mg.mL^{-1}$ (Si & Samulski, 2008). AFM investigations of graphene oxide sheets revealed sonication leading to almost a complete exfoliation of the graphene oxide (Parades, 2008) due to the similarities between pristine graphene and reduced graphene oxide. Therefore, the reduction process is one of the most significant reactions of GO. In order to use graphene in large-scaled applications, the most desirable method to produce large quantities of graphene-like materials is chemical reduction of graphene oxide. These conversion techniques can be obtained via thermal, electrochemical or chemical reduction route. All of these reduction methods produce resemble pristine graphene products in different degrees, especially regarding to their thermal, mechanical and electrical properties, as well as their surface morphology.

2.3.2.3.1 Chemical reduction

In order to reduce graphene oxide, various chemicals can be used. Hydrazine monohydrate was one of the first reported chemicals (Stankovich *et al.*, 2007). Due to its stability against reactivity with water, hydrazine monohydrate draws a huge attention for reducing aqueous dispersions of GO. Because of the side reactions with solvents which usually are employed for dispersing graphene oxide (such as water), its reduction with highly strong reducing agents including lithium aluminum hydride (LiAH) is still challenging. Producing graphene-like materials is highly similar to the pristine graphene which is obtained from straightforward mechanical exfoliation such as Scotch tape technique of singular graphite layers that is the main target of any technique of reduction (Novoselov, 2004). Despite the fact that the reduction mechanism of how hydrazine reacts with graphene oxide remains not clear, at least one mechanism has been proposed as depicted in Scheme 2.1 (Stankovich *et al.*, 2006). Based on previous information about the reduction pathway of hydrazine in different systems, it may lead to educated predictions for the case of GO.

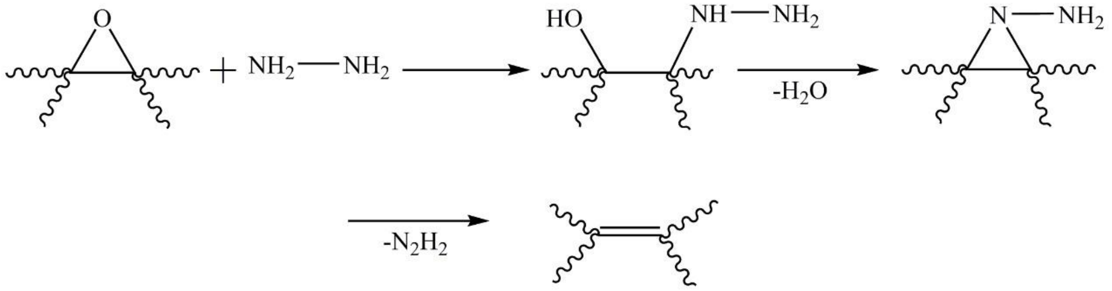

Scheme 2.1: A reaction way for epoxide reduction by hydrazine.

Hydrazine is a moderate reagent which is usually employed for the alkenes reduction (Gao, 2015). The mentioned procedure generally takes place via *syn* addition of hydrogen across the alkene, merged with N_2 extrusion. This procedure is mild enough to leave other functional groups including nitro and cyano groups, untouched. Few valuable experiments exist for characterizing the features of starting material and produced products. The first experiment is an analysis of the Brunauer–Emmett–Teller (BET) surface area. In short, by measuring the gas amount (generally N_2) physisorbed to a surface, BET quantifies the material surface area (Gao, 2015). Other methods of characterization such as Raman, where the D and G bands (related to the order or disorder of the system and an index of the stacking structure, respectively) are the main vibrational techniques detected in graphitic structures. The intensity ratios of D and G bands (D/G) are usually employed as a means of determining the number of layers in a graphene sample and its overall stacking behavior; high ratios of D/G suggest a high degree of exfoliation/disorder (Das *et al.*, 2008).

2.3.2.3.2 Thermal reduction

Chemical reduction is certainly, the most frequently used technique for graphene oxide reduction, but it is not the only technique. Findings have shown on the thermal reduction and exfoliation of graphene oxide (Schniepp, 2006; McAllister *et al.*, 2007). Instead of employing a chemical reductant to eliminate the oxygen-containing groups, by directly heating graphene oxide, it may form carbon oxide species which are thermodynamically stable (Gao, 2015). Heating GO to 1050 °C leads to extrusion of carbon dioxide and consequently, exfoliation of the stacked structure occurs. High pressure within the stacked layers is created by high temperature gas. Based on state equations, a pressure of 40 MPa is generated at 300 °C, while as much as 130 MPa is generated at 1000 °C (McAllister *et al.*, 2007). Based on calculation of the Hamaker, a pressure of 2.5 MPa is essential for separating two platelets of stacked graphene oxide (McAllister *et al.*, 2007). The structural damage is a meaningful effect of thermal exfoliation which releases of carbon dioxide (Kudin, 2008). Roughly 30% of GO mass decreased throughout the exfoliation process, leaving behind vacancies and topological defects throughout the reduced graphene oxide sheets (Park *et al.*, 2009). Defects inevitably affect the electronic properties of the product by decreasing the ballistic transport path length and introducing scattering sites. In spite of structural defects, although, bulk conductivities of 1000–2300 $S.m^{-1}$ were achieved, demonstrating effective overall restoration and reduction of the plane electronic structure.

2.3.2.3.3 Electrochemical reduction

The electrochemical elimination of the oxygen containing groups is another technique which presents good ability for the graphene oxide reduction. Recently electroreduction has been employed to change the graphene oxide structure or graphene itself (Zhou *et al*., 2009). Principally, electrochemical method could reduce dangerous reductants usage such as hydrazine and the demand to dispose of the by-products. A variety of substrates such as ITO, glassy carbon electrode, plastic, *etc.* were used for depositing thin films of graphene oxide. The modified electrodes were located at opposite ends of the film and linear sweep voltammetry was run in a sodium phosphate buffer. By using an aqueous buffer solution at ambient condition, electrochemical reduction of graphene oxide layers or films can be conducted in a regular electrochemical cell. Usually, no specific chemical agent is needed for the electrochemical reduction, and is chiefly caused by the electron exchange between graphene oxide and electrodes. Ramesha and Sampath figured out the process of graphene oxide reduction by using cyclic voltammetry and in the range of 0 to -1 V *vs.* SCE which started at -0.6 V and reached a maximum at -0.87 V in a 0.1 M KNO_3 solution (Ramesha & Sampath, 2009). In this scanning voltage range, the process is electrochemically irreversible and the reduction can be obtained by only one cycle. Zhou presented the best reduction result by employing an electrochemical approach (Zhou, 2009). Elemental investigation of the prepared reduced graphene oxide presented a C/O ratio of 23.9 and the film conductivity was calculated to be approximately 85 $S.cm^{-1}$. He also figured out that the reduction potential is controlled by the buffer solution pH. A low pH value is appropriate for graphene oxide reduction, therefore, the authors suggested that H^+ ions take part in the reaction. In order to prepare GO films, An *et al.* employed electrophoretic deposition (EPD). They figured out that graphene oxide layers could also be reduced on the anode surface amid electrophoretic deposition, which is in contrast with the general opinion that in an electrochemical cell, oxidation takes place at the surface of anode (An *et al*., 2010). The simultaneous electroreduction and electrodeposition might be useful for many electrochemical applications (Pei, 2012), however the mechanism of reduction is still not clear. Scheme 2.2 proposed the reaction process which highlights the critical role of H^+ ions in the buffer solution.

In spite of the fact that this shows to be totally effective (and yet mild) at reducing of oxide functionality, and it prohibits the using of hazardous chemical reactants and their byproducts, electroreduction has not been showed on a large sample. The deposition of reduced graphene oxide on the surface of electrodes is probably to make bulk electroreduction difficult on a preparative scale. Scalability is a principal necessity of a valuable synthetic protocol if graphene oxide is to be widely utilized (Gao, 2015).

$$\begin{array}{c}\text{Graphene}\\\text{Oxide}\end{array} + aH^+ + be^- \longrightarrow \begin{array}{c}\text{Reduced Graphene}\\\text{Oxide}\end{array} + cH_2O$$

Scheme 2.2: Proposed reaction for the electrochemical reduction of graphene oxide in a sodium phosphate buffer.

2.3.2.4 H_2O_2 detection by graphene based materials

H_2O_2 is a common enzymatic product of oxidases and a substrate of peroxidases, which is significant in sensor development and biological processes (Zhou, 2009). H_2O_2 is a significant mediator in pharmaceutical, food, industrial, environmental and clinical analysis as well. Decreasing the oxidation-reduction over potentials is an important task for developing sensor for hydrogen peroxide detection. Various types of carbon materials, such as carbon nanotubes (Wang & Lin, 2008; Wang, 2005), have been investigated in order to fabricate sensors for hydrogen peroxide detection. The electrochemical performance of H_2O_2 detection on chemically reduced graphene oxides (CR-GO) was investigated by Zhou *et al.*, which presented a significant enhance in electron transfer rate as compared with graphite/GC and bare GC electrodes (Zhou *et al.*, 2009). The linear relationship of hydrogen peroxide at the applied potential of -0.2 V is 0.05–1500 mM, which is wider than the formerly reported results for carbon nanotubes (Zhou *et al.*, 2009). The sensor presenting much lower applied potential of hydrogen peroxide oxidation-reduction started at 0.2/0.1 V compared to graphite and bare electrode. The high density of edge-plane-like defective sites on the graphene, providing several active sites for electron transfer, is attributed for this wide range (Banks & Compton, 2005; Banks *et al.*, 2004; Banks *et al.*, 2005). This great increased electrochemical behavior of graphene-based sensors for hydrogen peroxide detection may lead to high selectivity and sensitivity of electrochemical sensors. The promising electrochemical behavior of CR-GO sensor is ascribed to the high density of edge-plane-like defective sites on CR-GO (Banks *et al.*, 2004; Banks *et al.*, 2005). PVP-protected graphene-polyethylenimine functionalized ionic liquid (PFIL) sensor was characterized by Shan *et.al* for detection of H_2O_2 (Shan *et al.*, 2009). The more positive reduction potential (at 0 V) and more reduction current confirmed that the graphene-based sensor had much better electrochemical behavior for H_2O_2 detection than the PFIL. Moreover, Shan *et al.*, employed chitosan as a matrix for combining graphene and gold nanoparticles (AuNPs) to fabricate a glucose biosensor (Shan *et al*., 2010). The prepared biosensor showed the highest electrochemical performance to hydrogen peroxide than chitosan, graphene/chitosan and AuNPs/chitosan biosensors. The synergistic effect of graphene and AuNPs is the main reason for this increased electrochemical performance (Li *et al*., 2007).

2.3.3 Metal and metal oxide

Metal nanoparticles have attracted extensive research attention within decades for their unique electronic, catalytic and sensory properties. They may serve as interconnections for nanodevices (Shen *et al*., 2009), substrate for high performance catalysts (Chandra & Xu, 2007) and active species for sensory materials (Varghese & Grimes, 2003). The unique properties of the metal nanoparticles could be ascribed to their excellent electron transfer abilities inherent from the bulk counterpart as well as the ultra-high surface area derived from their nanoscale size (Rao *et al*., 2000). Among various kinds of metal nanoparticles, the ones of noble metals, such as Pt, Pd, Au, Ag are under close scientific investigation due to their outstanding environmental stability and catalytic properties toward a diversity of reactions (Okumura *et al*., 2003). Nanocrystals including nanoparticles, rods, wires, cubes, octahedrons of these noble metals have been numerously synthesized and their catalytic properties upon various species and analytes have also been shown (Wiley *et al*., 2007).

Besides noble metals, base metals such as Cu, Ni, Co, Mo and Re also possess distinguished catalytic activities for many specific reactions and analytes (Astruc, 2008). Compared to noble metals, these base metals have indeed have the advantages of bearing high efficiency for specific chemical reactions, ease of chemical modification and relative low price (Farmer & Campbell, 2010).

Transition metals have been recognized as excellent catalysts not only due to their ability to have various oxidation states, but to adsorb other materials and activate them in the process. However, nanometals can exhibit particular benefits of high effective surface area, increased mass transport, size controlled optical, chemical and electrical features and effective usage of expensive compounds (Lu *et al*., 2008). Due to high ratio of surface atoms with free valences to the cluster of total atoms, transition metals nanoparticles can be made excellent catalysts (Hrapovic *et al*., 2004). Large number of transition metal nanoparticles such as platinum (Pt) (Ghadimi *et al.*, 2015), palladium (Pd) (An *et al*., 2015; Momeni & Nabipour, 2015), copper (Cu) (Deng *et al*., 2015; Mani *et al*., 2015), rhodium (Rh) (Gatselou *et al*., 2015), iridium (Ir) (Limshan *et al*., 2015) and ferrum (Fe) (Qi & Zheng, 2015; Jakubec *et al*., 2015) have been successfully employed for electrocatalytic determination of hydrogen peroxide. Au (in different shapes and structures such as nanowire) is one of the most investigated transition metals (Chen *et al*., 2015; Guo *et al*., 2009), nanoporous Au (Meng *et al*., 2011), Au nanocages (Zhang *et al.*, 2011) and Au nanoparticles (Ma *et al*., 2015; Okawa *et al*., 2015) have been investigated for electrocatalytic determination of H_2O_2 reduction. It seems that Au nanocage (Zhang *et al.*, 2011) and nanoporous Au (Meng *et al.*, 2011) had a slightly better performance than the others. Due to high conductivity, surface area and electrocatalytic activity, carbon-based nanomaterials such as graphene-based materials were largely employed as supporting materials in order to reserve high catalytic activities and obtain high loading for transition metal nanoparticles. A large number of investigations have been carried out based upon this approach for determination of H_2O_2 though the strategies may slightly vary (Lorestani *et al*., 2015; Tajabadi *et al*., 2015; Ma, 2015; Cui *et al*., 2015). Other transition metals including Pd nanoparticles (Zhang *et al*., 2016) and Ag nanoparticles (Lorestani *et al*., 2015) also have been employed with graphene base materials for electrocatalytic determination of H_2O_2.

Transition metal oxides including manganese oxide, (Xu *et al*., 2010; Mahmoudian *et al*., 2014) cobalt oxide (Parnell *et al*., 2015; Li *et al*., 2015), titanium dioxide (Leonardi *et al*., 2014; Wang *et al*., 2014), copper oxide (Bin *et al*., 2014; Gao & Liu, 2015) and iridium oxide (Elzanowska, 2004) have been proposed to present electrocatalytic activity toward hydrogen peroxide. Nevertheless, many of them were based on the electrocatalytic oxidation of H_2O_2 in which high potentials were applied on the working electrode.

As an example, at an applied potential of +0.65 V *vs*. SCE, a modified electrode of nanoparticle of MnO_2 and dihexadecyl hydrogen phosphate composite film was employed for H_2O_2 determination (Yao *et al*., 2006) and in another study, in order to perform H_2O_2 determination at an applied potential of +0.4 V, a TiO_2/MWCNT modified electrode was used (Jiang & Zhang, 2009). Based on the application viewpoint, the operation potentials of the mentioned sensors are quite high to be applied to real biological samples.

Xu and the team (Xu *et al.*, 2010) reported the MnO_2/MWCNT sensor for determination of hydrogen peroxide which presented high anti-interference feature without any permselective membranes against ascorbic acid, citric acid and uric acid in spite of the high operation potential of 0.45 V. Bai *et al.* (Bai *et al*., 2007) figured out that nanoparticle of MnO_2 sensors present bi-direction electrocatalytic activity to the H_2O_2 oxidation/reduction. The interference from ascorbic acid significantly decreased when this sensor was operated at 0 V in the reduction of H_2O_2.

Copper oxide shows a significant performance for H_2O_2 sensing. Luque *et al.* revealed that the CuO/carbon paste electrode presented a superior electrocatalytic ability to the reduction and oxidation of H_2O_2. -0.1 V was selected as the operated potential for this sensor for detection of glucose (Luque *et al*., 2005). A CuO nanoparticle/nafion sensor was constructed for detection of H_2O_2 by Miao *et al*. (Miao *et al*., 2008). At an applied potential of -0.3 V and in the range of 0.15–9.00 mM, this sensor presented a detection limit of 0.06 mM in 0.1 M NaOH.

Magnetite properties has also been reported to have excellent electrocatalytic ability to the H_2O_2 detection. Lin and Len (Lin & Leu, 2005) fabricated a Fe_3O_4/chitosan modified electrode for a hydrogen peroxide sensor with particular properties of electrocatalytic reduction as well as interference elimination. This sensor showed the benefits of low applied potential (-0.2 V *vs*. Ag/AgCl), rapid response, low background current and long shelf-life (9 months at room temperature).

In order to fabricate a glucose sensor, Comba and his colleges (Comba *et al*., 2010) employed electrosynthesized Fe_3O_4 nanoparticles within a carbon paste electrode. Because of the low operation potential at -0.1 V, this sensor exhibited no response to 0.4 mM uric acid and 0.1 mM ascorbic acid with the detection limit of 3.0×10^{-4} M and sensitivity of 32±4 $\mu A.M^{-1}$.

2.3.3.1 Silver nanoparticles based H_2O_2 sensor

As typical nanomaterials, Ag nanoparticles have been widely employed to construct non-enzymatic H_2O_2 due to their excellent catalytic activity for the reduction of H_2O_2.

Among different methods utilized to synthesize Ag nanoparticles, electrochemical deposition has attracted much attention since it has proven to be the least expensive, highly productive and readily adoptable (He *et al*., 2004).

Blanco *et al.* (Blanco *et al*., 2013) and Safavi *et al.* (Safavi *et al*., 2009) have developed an electrochemical sensing of H_2O_2 by electrodepositing Ag nanoparticles on indium tin oxide conducting glass (ITO) substrate and carbon ionic liquid electrode (CILE), respectively.

Wu *et al.* prepared the Ag–DNA hybrid nanoparticles using electrodeposition with DNA as a template. The hybrid nanoparticles showed a narrow size distribution and a favorable catalytic ability to the reduction of H_2O_2 (Wu *et al.*, 2006).

Bui and co-workers (Bui *et al.*, 2010) reported a H_2O_2 sensor based on Ag nanoparticles which were patterned on flexible and transparent single-walled carbon nanotube (SWCNT) films using the electrochemical deposition method.

Besides, electrodepositing Ag nanoparticles on the ZnO (Wang & Zheng, 2010), chitosan/graphene oxide nanocomposites/cysteamine (Wang *et al.*, 2012), poly(o-phenylenediamine) (PoPD) (Mu, 2011), poly[3,4-ethylenedioxythiophene] (PEDOT) (Balamurugan & Chen, 2009) and natural nano-structure attapulgite (Chen *et al.*, 2011) modified electrode was also constructed to perform sensing H_2O_2, respectively.

Yi *et al.* prepared novel nanoporous Ag particles through hydrothermal process for electroreduction of H_2O_2 in alkaline media (Yi *et al.*, 2011). Sun *et al.* prepared well-stable Ag nanoparticles (AgNPs) with diameter of 5 nm from an aqueous solution of $AgNO_3$ and poly [(2-ethyldimethylammonioethyl methacrylate ethyl sulfate)-co-(1-vinylpyrrolidone)] (PQ11) using the facile hydrothermal synthesis method without extra introduction of other reducing agents and protective agents (Sun *et al.*, 2011).

It was found that such dispersion can form stable AgNPs-embedded films on bare electrode surfaces and these nanoparticles exhibit remarkable catalytic performance for hydrogen peroxide (H_2O_2) detection.

Recently, through the chemical reduction of silver ion, a variety of Ag nanoparticles-based nanocomposites was prepared to fabricate H_2O_2 sensor, including graphene-AgNPs (Lorestani *et al.,* 2015), polypyrrole-AgNPs (Mahmoudian *et al.,* 2014), polyaniline-AgNPs (Lorestani *et al.,* 2015), hyper branched copolymer-AgNPs (Yao *et al*., 2011), Ag@PMPD–Ag (Tian *et al*., 2011), MWCNT-AgNPs, single-walled carbon nanotubes- AgNPs (Lin *et al*., 2014).

Lu *et al.* (Lu *et al*., 2012) reported an interesting work in which that supramolecular microfibrils of *o*-phenylenediamine (OPD) dimmers were prepared based on the oxidation of OPD monomers by $FeCl_3$. Such microfibrils were treated with $AgNO_3$ aqueous solution to transform into nanofibers decorated with spherical AgNPs with sizes in the range of 5~20 nm, leading to a non-enzymatic H_2O_2 sensor.

He and his colleagues (He *et al*., 2010) used $Na_2Ti_3O_7$ nanowires as 3D frames for loading Ag nanoparticles to construct H_2O_2 sensing.

Wang *et al.* (Wang *et al*., 2012) reported the synthesis of monodisperse polydopamine (PDA)–Ag hybrid hollow microspheres through self-polymerization of dopamine on ZnO microspheres as sacrificial templates. Many other methods have been applied to prepare Ag nanoparticles, such as UV irradiation method (Lin *et al*., 2010), microwave-assisted reduction method (Liu *et al*., 2011), chemical plating method (Zhai & Gao, 2010) and green synthesis of nano-Ag (Shukla *et al*., 2012).

All of these works exhibited the feasibility of the non-enzymatic H_2O_2 sensors. Table 2.1 showed the analytical performance of Ag nanoparticles based on non-enzymatic H_2O_2 sensors.

As seen in Table 2.1, Ag-modified electrodes exhibited favorable catalysis effect with wide linear range and achieved the detection of H_2O_2 at low potential.

Table 2.1: Examples of non-enzymatic H_2O_2 sensors based on Ag nanoparticles.

Modified electrode	**Performance**		**Ref.**
	LOD (µmol.L^{-1})	**Linear range** (mmol.L^{-1})	
Ag-DNA/GCE	0.6	0.0025 ~ 0.002	(Wu *et al.*, 2006)
AgPs-SWCNT electrode	2.76	0.00016 ~1.8	(Bui *et al.*, 2010)
Ag NPs/ZnO/GCE	0.42	0.02~ 5.5	(Wang *et al.*, 2010)
AgNPs/CHIT-GO/cysteamine/Au	7	0.006 ~18	(Wang *et al.*, 2012)
AgNPs/PoPD	1.5	0.006 ~ 673	(Wang *et al.*, 2012)
Ag NPs/ATP/GCE	2.4	0.0001 ~ 215	(Chen *et al.*, 2011)
Ag/GC electrode	0.1	0.04 ~ 9000	(Singh & Pandey, 2011)
PQ11-AgNPs/GCE	33.9	0.1 ~ 1800	(Lu *et al.*, 2011)
Ag/GN-R/GCE	28	0.1 ~ 40	(Liu *et al.*, 2010)
Ag@PMPD-Ag/GCE	2.5	170 ~1000	(Tian *et al.*, 2011)
SWCNT/AgNPs/CCE	0.2	0.1 ~ 8	(Habibi *et al.*, 2012)
Ag-3D/graphite electrode	1	0.05 ~ 2.5	(He *et al.*, 2010)
Polydopamine-Ag Hollow/GCE	1.97	0.92 ~ 20	(Wang *et al.*, 2012)
Ag/graphene/GCE	0.5	10 ~100	(Liu *et al.*, 2011)

Furthermore, the non-enzymatic H_2O_2 sensors obtained relatively higher stability than enzyme biosensors. However, the non-enzymatic H_2O_2 sensors generally hold the detection limits of 0.1~10 µM, which is not as low as 0.01~ 0.1 µM as compared to enzymatic H_2O_2 sensors.

2.3.3.2 Copper based H_2O_2 sensor

Copper (Cu) nanoparticles has gained particular interest because of its distinctive properties including natural abundance, low production cost, high stability and good electrical properties, which make it one of the most promising catalysts for applications in H_2O_2 sensors (Qiu *et al.*, 2009).

Selvaraju and Ramaraj investigated the electrocatalytic activity of Cu nanoparticles towards the reduction of H_2O_2, which was deposited electrochemically on GC electrode (Selvaraju & Ramaraj, 2009). Kumar and the team (Kumar *et al.*, 2009) synthesized the Cu nanoparticles/poly (*o*-phenylenediamine) film modified electrode, which was used to analyze H_2O_2 and nitrite. Meng prepared the polypyrrole nanowire-Cu nanocomposite and fabricated a non-enzymatic H_2O_2 sensor employing the obtained materials (Meng, 2013). Tsai *et al.* (Tsai *et al.*, 2011) deposited Cu nanoparticles and Cu hexacyanoferrate (CuNPs-CuHCF) hybrid electroactive polynuclear films on electrode surfaces. The advantages of CuNPs-CuHCF films demonstrated sensitive response to H_2O_2. Annamalai *et al.* (Annamalai *et al.*, 2012) proposed H_2O_2 sensors by employing Cu nanoparticle/ functionalized multi walled carbon nanotube/chitosan nanocomposites for H_2O_2 detection. Table 2.2 showed the analytical performance of Cu nanoparticles based non-enzymatic H_2O_2 sensors.

Table 2.2: Examples of Cu based non-enzymatic H_2O_2 sensors based Cu nanoparticles.

Modified electrode	Performance		Ref.
	LOD (μmol.L^{-1})	**Linear Range** (mmol.L^{-1})	
NM-PdCu/GCE	0.1	up to 8	(Liu *et al.*, 2011)
CopperNPs-CuHCF/PEDOT/GCE	0.1	0.001 ~ 0.54	(Tsai, 2011)
CuO/OPpy/MWCNTs/CCE	500	Up to 0.02	(Yu *et al.*, 2015)
Sandwich-structured CuO	1	Up to 0.032	
Cu/Psi-CPE	27	500-3780	(Ensafi *et al.*, 2014)
CuO/MWCNTs/OPpy	5 0.5	Up to 0.01 Up to 2×10^{-6}	(Yu, 2015)
Cu-MWCNTs	1	Up to 0.075	(Yang *et al.*, 2010)
Ppy-copper/Au	2.3	0.007 ~ 4.3	(Zhang *et al.*, 2008)

2.3.3.3 Bimetallic nanoparticles based H_2O_2 sensor

Bimetallic nanoparticles have attracted significant attention as electrocatalysts, since the addition of the second metal brings about vitally strategic variations in particle shape, size, surface morphology, chemical and physical properties (Chen *et al*., 2012). Compared with the corresponding metal nanoparticles, bimetallic exhibited higher catalytic activity, better resistance to deactivation, and greater catalytic selectivity (Yu *et al*., 2011). These bimetallic nanostructures are usually in forms of alloys, core shell structures, and mixed monometallic nanoparticles (Chen *et al*., 2012). Most recently, the bimetallic nanoparticles have been applied for constructing H_2O_2 sensors. Different forms of Au-Ag bimetallic nanoparticles have been prepared to catalyze H_2O_2. Wang *et al.* (Wang *et al*., 2010) and Tsai *et al.* (Tsai *et al*., 2010) fabricated Au-Ag alloy nanoparticles through the reduction of Ag on the Au nanoparticles modified film and electrodeposition process, respectively, for the detection of H_2O_2. Manivannan and Ramaraj (Manivannan & Ramaraj, 2009) synthesized the core shell $Au_{100-x}Ag_x$ bimetallic nanoparticles embedded in methyl functionalized silicate (MTMOS) network and investigated their electrocatalytic activity towards the reduction of H_2O_2. Beside Au-Ag bimetallic nanoparticles, Au-Pt alloy nanoparticles were also under the research focus of common used materials (Kang *et al*., 2008). Yu *et al.* prepared a series of room-temperature ionic liquids (RTILs) containing different functional groups, which were utilized as electrodeposition substrate for depositing Au/Pt nanostructures (Yu *et al*., 2011). Meanwhile, Au/Pt nanoparticles provide a facile way to construct a third-generation H_2O_2 sensor. Guo and coworkers (Guo *et al*., 2009) reported an interesting work concerning that the ultra-high-density Au/Pt core shell nanoparticles supported on coaxial nanocables (UASCN) which could be used as an enhanced material for constructing H_2O_2 electrochemical devices with high performance. Niu *et al.* (Niu *et al*., 2012) developed snowflake-like Pt/Pd bimetallic clusters modified screen-printed gold electrode for glucose and H_2O_2 sensing. In addition, bimetallic nanoparticles such as Pt/Ir (Chang *et al*., 2014), Au/Ag (Li, 2014), Pd/Cu (Uzunoglu *et al*., 2015), Pt/Pd (Zhang *et al*., 2016), Rh/Pd (Rajkumar *et al*., 2011) and Ru/Rh (Chen, 2013) were employed for fabricating an electrochemical sensing platform for H_2O_2 determination.

CHAPTER 3: EXPERIMENTAL & PROCEDURE

This chapter emphasizes on the materials, techniques and experimental methods that were used in this research to fabricate and characterize the sensors. They include electrochemical techniques (cyclic voltammetry, amperometry and Electrochemical Impedance Spectroscopy), microscopic (Transmission Electron Microscopy, Scanning Electron Microscopy), Fourier Transform Infrared Spectroscopy, Raman spectroscopy, Atomic Force Microscopy (AFM) and X-ray diffraction. The measurements were performed in three-electrode system. For electrochemical studies, depending on the system under investigation, different composites served as the working electrode, a coiled platinum wire was used as the auxiliary (counter) electrode and the reference electrode used was saturated calomel electrode (SCE), unless mentioned elsewhere.

3.1. General

In this chapter, the synthesis and characterization of seven novel nanocomposites were described. Their experimental procedure for activity towards hydrogen peroxide detection is included in this chapter. In order to differentiate the composites which were synthesized by one-step procedure from those synthesized through layer-by-layer deposition, two different styles of presentation have been used. Symbol of “-” was used for the composites which were synthesized by one step electrodeposition and symbol of “/” was employed for those synthesized through layer-by-layer deposition.

3.2. Chemicals

In this thesis, AR grade chemicals with high purity were used and listed in Table 3.1. Deionized water (resistivity of 18.2 MΩ.cm at 25 °C) was used throughout the studies.

Table 3.1: List of chemicals used in this work.

Chemical compounds	**Molecular formula**	**Brand**	**Purity (%)**
Ammonia solution	NH_4OH	Sigma Aldrich	25.0
Copper chloride	$CuCl_2$	Sigma Aldrich	>99
Ethanol	C_2H_6O	Sigma Aldrich	>99.8
Silver nitrate	$AgNO_3$	Sigma Aldrich	>99.7
Pyrrole	C_4H_5N	Sigma Aldrich	≥98
Sodium nitrate	$NaNO_3$	Sigma Aldrich	≥99
Phosphoric acid	H_3PO_4	Sigma Aldrich	≥85
Potassium permanganate	$KMnO_4$	Sigma Aldrich	≥99
Sodium hydroxide	$NaOH$	Sigma Aldrich	≥98
Hydrochloric acid	HCl	Fluka	≥99
Sucrose	$C_{12}H_{22}O_{11}$	Sigma	≥99.5
Fructose	$C_6H_{12}O_6$	Sigma	≥99.5
Uric acid	$C_6H_{14}O_6$	Sigma	>99
Ascorbic acid	$C_6H_8O_6$	Sigma	>99
Nitric Acid	HNO_3	Sigma	>99
Sulfuric acid	H_2SO_4	Fluka	≥99
Glucose	$C_6H_{12}O_6$	Sigma	>88
Phosphoric acid	H_3PO_4	Fluka	≥97.5
Disodium phosphate	Na_2HPO_4	Fluka	≥97.5
Monosodium phosphate	NaH_2PO_4	Sigma Aldrich	≥99
Potassium ferricyanide(III)	$K_3Fe(CN)_6$	Sigma Aldrich	≥99
Potassium chloride	KCl	Sigma Aldrich	≥99
Graphite flakes	C	Ashbury Inc	
Hydrogen peroxide	H_2O_2	Sigma Aldrich	30%(w/w)

3.3. Cell setup and synthesis

3.3.1. Cell configuration

Figure 3.1 shows the conventional three-electrode electrochemical cell setup in which a glassy carbon (3 mm diameter) (GCE), a saturated calomel electrode (SCE) and a coiled platinum wire are used as working, reference and counter electrode, respectively. These electrodes were purchased from BASi Company. The cyclic voltammetry (CV), Electrochemical Impedance Spectroscopy (EIS) and amperometry (AMP) measurements were carried out using Autolab model PGSTAT 302N.

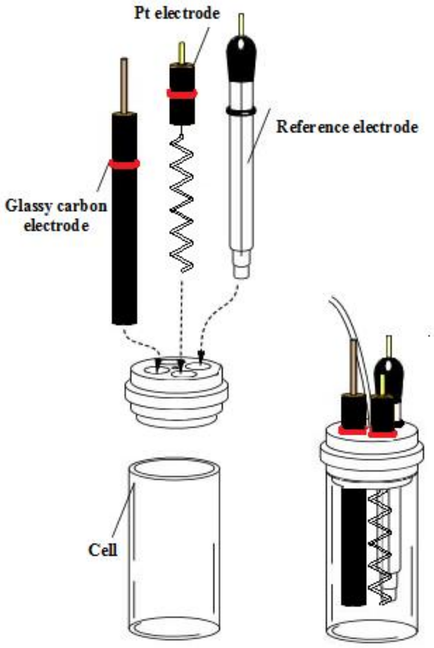

Figure 3.1: Conventional three-electrode electrochemical cell setup.

3.3.2. Pre-treatment of the electrode

Prior to fabrication, the surface of bare glassy carbon electrode (3.0 mm diameter) must be polished to eliminate any traces, which affect the rate of electron transfer. The most common method is via mechanical polishing in which pads are used with 1, 0.1 and 0.05 mm alumina polish powder. The electrode is held in a vertical position while making figure-8 motions on the polishing pad (Figure 3.2). The clean GCE was polished to a mirror and the electrode surface is rinsed with distilled water to remove all the traces of the polishing material and then is sonicated in distilled water for few minutes to ensure complete removal of the alumina particles. To be ready for use, it was dried under high purity N_2 gas flow.

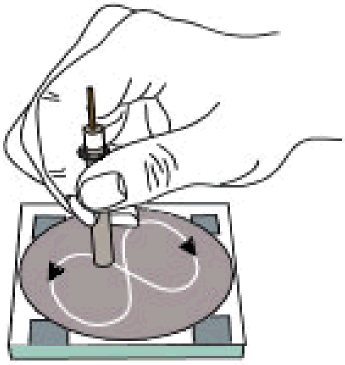

Figure 3.2: Electrode polishing process.

3.3.3. Preparation of polypyrrole (Ppy)

The polypyrrole layer was electrodeposited by amperometry method on the glassy carbon electrode (GCE) at different potential values (0.5–1 V) under high-purity nitrogen atmosphere. The electropolymerization was conducted in a solution containing 0.1 M monomer and 0.1 M of different concentrations of one kind of supporting electrolyte: lithium perchlorate ($LiClO_4$), sodium dodecyl sulfate (SDS), para toluene sulfonic acid (PTSA), or copper chloride ($CuCl_2$). The electrodeposited polypyrrole on the surface of GCE was rinsed with deionized water. The electrochemical synthesis was carried out at room temperature, in a one-compartment cell with a platinum (Pt) counter electrode and a saturated calomel reference electrode (SCE). Before electrodeposition process, the solutions were deoxygenated with N_2.

Polymers were formed through cyclic voltammetry (0 to 0.8 V at 1 mVs^{-1} *vs*. SCE) and amperometry method (at 0.5-1 V *vs*. SCE for 800 s). In order to eliminate residual monomers and oligomers present in the polypyrrole, the modified electrode was transferred to a monomer-free 0.1 M phosphate buffer solution (PBS) and scanned by using cyclic voltammetry technique with potential ranging from 0 to 0.8 V at 50 mV s^{-1}.

The general electrochemical synthesis of polypyrrole can be presented as in Figure 2.2, where A^- is the counter ion, which influences the polymerization process. To give charge balance, the charged polypyrrole must include anion and electrons in which anion is essential for the formation of a polypyrrole in an oxidized form and electrons for moving through the polymer. The *n* value was measured to be 2.2–2.4. Depending on the charge and type of the anion, the polypyrrole oxidation level should be 0.25~0.32 per pyrrole unit. In order to obtain electroneutrality, one anion is used for every 3–4 pyrrole units and this makes up 30~40% of the final weight of the polymer (Figure 2.2) (Khalkhali, 2005; Shea, 1999).

3.3.4. Preparation of graphene oxide (GO)

GO was prepared by a modified Hummers' method (Huang *et al*., 2011). Graphite flakes (Aldrich) was used for preparation of graphene oxide. 3 g of graphite flakes was first oxidized by reacting with concentrated phosphoric acid (H_3PO_4) and sulphuric acid (H_2SO_4) in 1:9 volume. The reaction vessel was immersed in an ice bath, and 18 g potassium chlorate was added gradually. The reaction was allowed to go on for three days during stirring to fully oxidize graphite into graphite oxide (GO), then added 30% H_2O_2

(200 ml) and was left over 10 min to complete the oxidization. GO was centrifuged and washed with 1 M HCl for 3 times (4000 rpm, 10 min). The GO was further centrifuged and filtered by deionized water to remove metal ions. If gel form is obtained, centrifuge at 96000 rpm will able to remove the gel. If it is not in the gel form, 4000 rpm of centrifuge setup can be used. The graphene oxide can be exfoliated by applying mild sonication for 5 min to obtain yellow brown suspension (Figure 3.3).

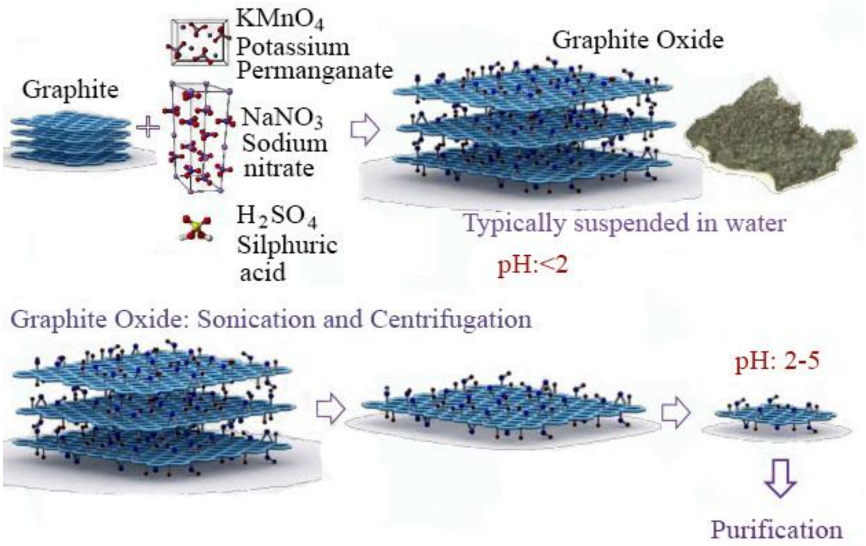

Figure 3.3: Procedure of synthesizing GO by modified Hummer method.

The exfoliated GO could be reduced to graphene by refluxing the GO solution with hydroquinone for 20 h. The final products were then centrifuged, washed, and finally vacuum-dried (Figure 3.3).

To remove any extra salts and acids from the prepared GO, 0.05 wt% of GO suspension in water was sonicated for 3h before being dialyzed for another 6 h in doubled-distilled water. The obtained dialyzed GO was then centrifuged for 20 min at 3000 rpm for removing un-exfoliated GO, and it was then dried for 24 h at 50 °C. Figure 3.4 shows GO free film and suspension.

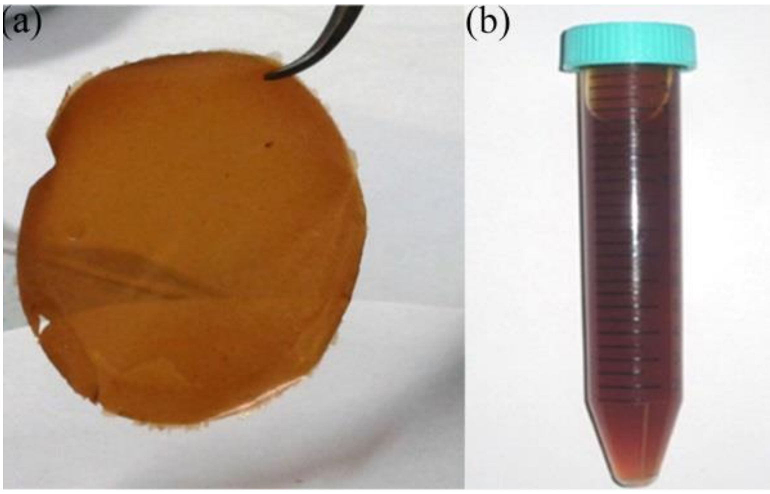

Figure 3.4: (a) Graphene oxide free film; (b) graphene oxide suspension.

3.3.5. Preparation of phosphate buffer solution (PBS)

0.1 M phosphate buffer solution (PBS) was prepared from 1.0 M monopotassium phosphate (KH_2PO_4) and 1.0 M dipotassium phosphate (K_2HPO_4) in deionized water making a solution with approximately pH 6.5 and 7.2.

3.3.6. Preparation of Ag solution

The solution of silver-ammonia [$Ag(NH_3)_2OH$] was made by adding ammonia (1 wt%) to the silver nitrate (50 mM) solution until the precipitates were completely dissolved. The synthesized $Ag(NH_3)_2OH$ concentration was around 40 mM (Moradi *et al*., 2013). Figure 3.5 shows the procedure of preparing Ag solution.

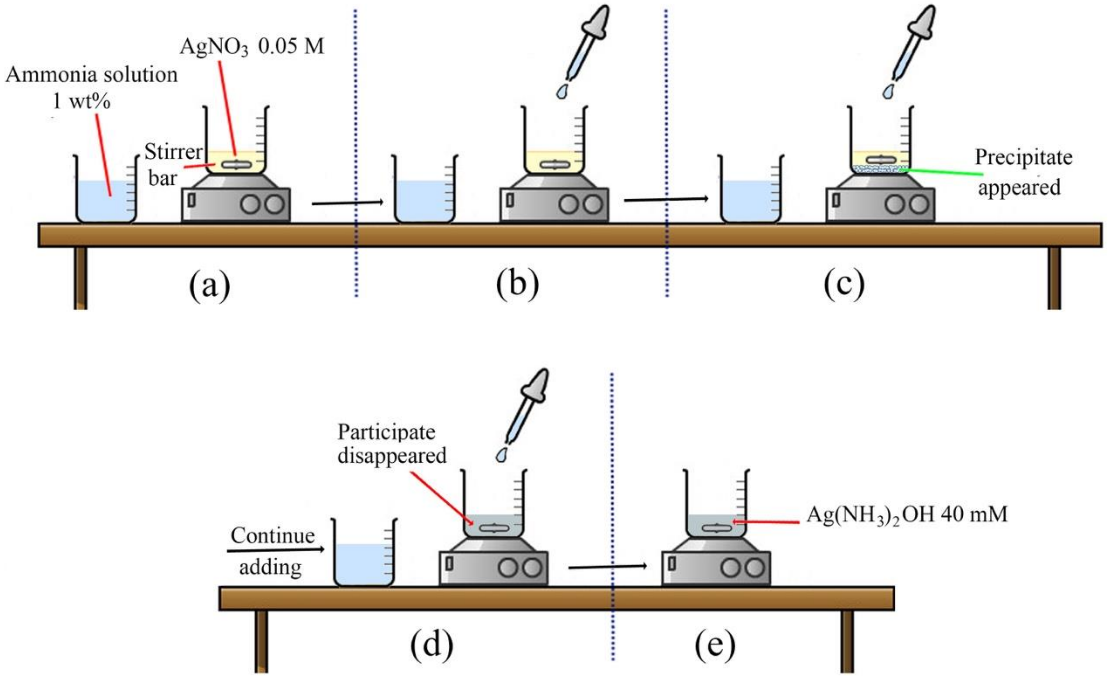

Figure 3.5: Procedure for preparing silver-ammonia solution.

3.3.7. Preparation of rGO-AgNPs composite

The prepared GO powder was exfoliated by ultrasonication to form a 0.1 mg mL^{-1} GO colloidal dispersion. Then, three different concentrations of [$Ag(NH_3)_2OH$] as a source of silver were mixed by GO solution. The solution of GO was mixed with the concentration of 1, 5 and 10 mM of [$Ag(NH_3)_2OH$]. The solutions were stirred for 30 min. The mixture solutions were nominated into rGO-AgNPs-1, rGO-AgNPs-2 and rGO-AgNPs-3, respectively. In order to investigate the effect of silver solution, one electrode was prepared with $AgNO_3$ solution, which was nominated into rGO-AgNPs-4.

3.3.8. Preparation of rGO-CuNPs composite

The prepared GO powder was exfoliated by ultrasonication to form a 0.1 mg mL^{-1} GO colloidal dispersion. Then, three different concentrations of $CuCl_2$ as a source of copper were mixed by GO solution. The solution of GO was mixed with the concentrations of 1, 5 and 10 mM of $CuCl_2$. The solutions were stirred for 30 min. The mixture solutions were nominated into rGO-CuNPs-1, rGO-CuNPs–2 and rGO-CuNPs-3, respectively. In order to electrodeposit the CuNPs decorated reduced graphene oxide electrode, two different routes were used: cyclic voltammetry was carried out at a potential of 0 to −1.5 V (*vs*. SCE) at scan rate of 10 mV/s for 3 cycles in the as-prepared solutions with N_2 bubbling (CV-rGO-CuNPs). In the second way, an amperometry technique was employed at a constant potential of -0.4 V (*vs*. SCE) for 420 s (AMP-rGO-CuNPs) (Luo *et al*., 2012).

Each method was nominated as AMP- and CV-. In order to investigate the effect of oxidation of copper, the modified electrodes were placed in NaOH 1 M solution and scanned for 40 cycles at potential window of -0.5 to 0.3 at 50 mVs^{-1} and consequently copper oxide was formed.

3.3.9. Preparation of rGO/PpyNFs/Cu_xO composite

The prepared graphene oxide was deposited and reduced simultaneously on the glassy carbon surface via CV by scanning repetitively from 0 to -1.5 V *vs*. SCE at scan rate of 1 mVs^{-1} in a solution composed of 7 mgL^{-1} graphene oxide and 0.1 M phosphate buffer (PBS) at pH 7.2.

The electropolymerization of Ppy nanofibers on the surface of coated GCE with rGO was performed in two different methods: First, by cyclic voltammetry in a single compartment cell, with the applied potential ranging from 0.0 to 0.8 V at a scan rate of 1 mVs^{-1}, the electropolymerization was performed in four voltammetric cycles on the surface of rGO. Second, amperometry was used for the electrodeposition of polypyrrole on the surface of rGO at the constant potential of 0.8 V *vs.* SCE for 800 s. The monomer solution for both methods contains mixed electrolytes in a 0.1 M phosphate buffer solution (pH 7.2), 0.1 M pyrrole monomer and 0.1 M $LiClO_4$.

Before oxidization by CV scan, in a solution containing 0.1 M KCl and four different concentrations of $CuCl_2$ (10, 30, 60, 90 mM), the Cu nanoparticles were electrodeposited on the surface of modified electrode at the constant potential of -0.6 V. Right after this stage, in order to permit the Cu nanoparticles to enter the oxidation form (Cu_xO), CV was performed in 0.1 M NaOH solution at the applied range of -0.5 to 0.3 V *vs*. SCE at a scan rate of 50 mVs^{-1} for 40 cycles (Meng *et al.,* 2013; Le & Liu, 2009). Figure 3.6 shows the process of the modified electrode schematically.

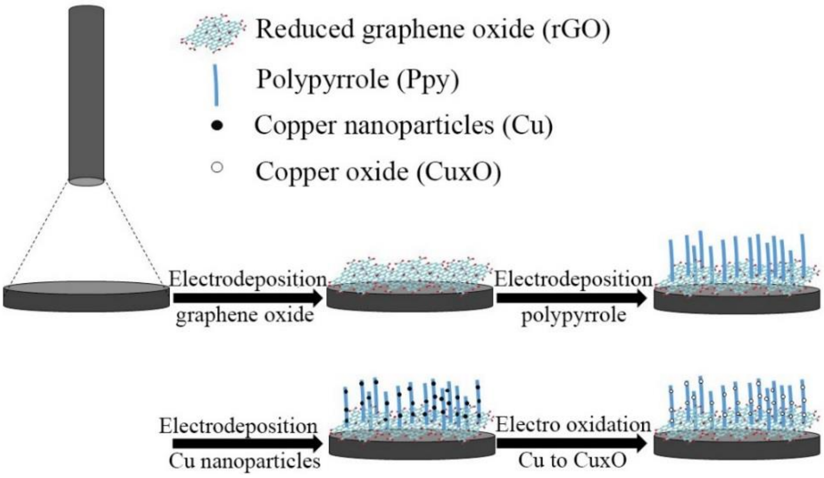

Figure 3.6: Schematic diagram of the electrode fabrication process for rGO/PpyNFs/Cu_xO.

3.3.10. Preparation of rGO/Ppy/AgNPs composite

rGO Was electrodeposited on the surface of GCE as described in section 3.3.9. The electropolymerization of Ppy nanofibers on the surface of coated GCE with rGO was performed via an amperometry method at the constant potential of ranging from 0.5 to 1 V *vs*. SCE for 800 s. The monomer solution contains mixed electrolytes in a 0.1 M phosphate buffer solution (pH 7.2), 0.1 M pyrrole monomer and three different kinds of counterions ($LiClO_4$, $LiNO_3$, SDS) with concentration of 0.1 M. One was carried out without adding counterion and in the blank solution. AgNPs solutions were prepared using the solution of $AgNO_3$ at three concentrations *i.e.* 1 mM, 5 mM and 10 mM, which were then called AgNPs-1, AgNPs-2 and AgNPs-3, respectively.

3.3.11. Preparation of (rGO-AgNPs)/PpyNFs composite

GO-AgNPs was prepared by mixing the solution of $Ag(NH_3)_2OH$ with GO solution at three different volume ratios *i.e.* 3:1, 6:1 and 12:1 under stirring for 4 hours, which were then called GO-AgNPs-1, GO-AgNPs-2 and GO-AgNPs-3, respectively.

The obtained precipitate was then filtered and dried overnight at 50 °C. Previously, $AgNO_3$ was used as the source of AgNPs for most nanocomposites (Campbell & Compton, 2010; Gao *et al*., 2013).

To check the effect of using $Ag(NH_3)_2OH$ instead of $AgNO_3$, the composite GO-AgNPs has been prepared by adding GO to 0.04 M $AgNO_3$ with the volume ratio of 6:1, which was then labeled as GO-AgNPs-4. The prepared AgNPs-GO at different ratio were carefully dropped in 5 different volumes (5, 10, 15, 20, 25 µL) on the surface of GCE in order to find the best ratio and volume, respectively.

Two separate methods were used for synthesizing (rGO-AgNPs)/PpyNFs. In the first method, cyclic voltammetry was chosen for reducing graphene oxide and polymerization of pyrrole in a compartment cell in one-step process. CV was scanned at the applied potential ranged from -1.5 to 0.8 V *vs*. SCE, in order to conduct the reduction and polymerization process (CV-(rGO-AgNPs)/PpyNFs) in a solution containing mixed electrolytes in a 0.1 M phosphate buffer solution (pH 7.2), 0.1 M pyrrole monomer and 0.1 M $LiClO_4$. In the second method, at first, GO-AgNPs was reduced through amperometry method. Seven different potentials (-1.0, -1.1, -1.2, -1.3, -1.4, -1.5, -1.6 V *vs*. SCE) for 500 s were used for reduction process in a solution containing 0.1 M phosphate buffer solution (pH 7.2) in order to find the best potential. Then, the electrode was carefully washed and rinsed with distilled water. In the second step, polymerization was done on the surface of rGO-AgNPs electrode through amperometry method at a constant potential of 0.8 V for 800 s in a solution containing 0.1 M pyrrole monomer and 0.1 M $LiClO_4$ (AMP-(rGO-AgNPs)/PpyNFs.) N_2 was purged before each process for 10 min in order to eliminate O_2 from electrolyte. Figure 3.7 shows the process schematically.

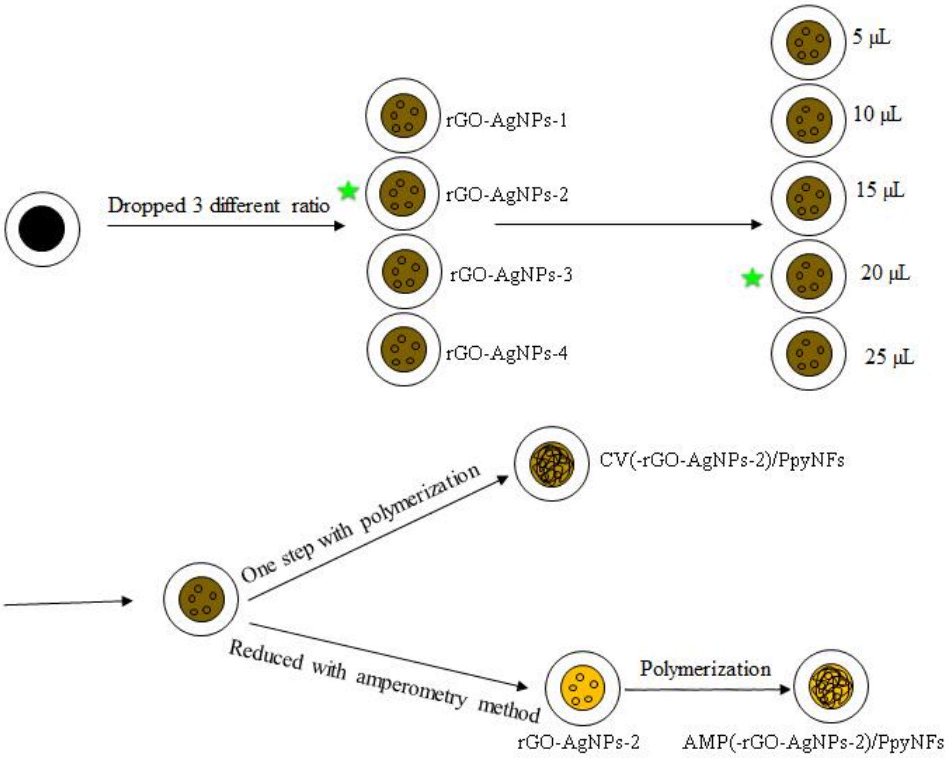

Figure 3.7: Schematic diagram of the electrode fabrication process for (rGO-AgNPs)/PpyNFs.

3.3.12. Preparation of PpyNFs/AgNPs composite

AgNPs solutions were prepared using the solution of [$Ag(NH_3)_2OH$] at three concentrations *i.e.* of 1 mM, 5 mM and 10 mM, which were then called AgNPs-1, AgNPs-2 and AgNPs-3, respectively. To check the effect of using [$Ag(NH_3)_2OH$] compared to $AgNO_3$, the solution of AgNPs has been prepared by the concentration of 1 mM $AgNO_3$ which was then labeled as AgNPs-4.

Through cyclic voltammetry (CV) method, the electrodeposition of silver nanoparticles on the polypyrrole surface was carried out with the potential ranging from 0.6 to -0.3 V *vs*. SCE and in $Ag(NH_3)_2OH$ solution at different concentrations (1, 5 and 10 mM). The initial potential for all silver electrodeposition was 0.6 V. AgNPs-Ppy was prepared by using solution of $Ag(NH_3)_2OH$ at three different concentrations *i.e.* 1 mM, 5 mM and 10 mM, which were then nominated to AgNPs-1-Ppy and AgNPs-2-Ppy and AgNPs-3-Ppy, respectively. Figure 3.8 shows the process schematically.

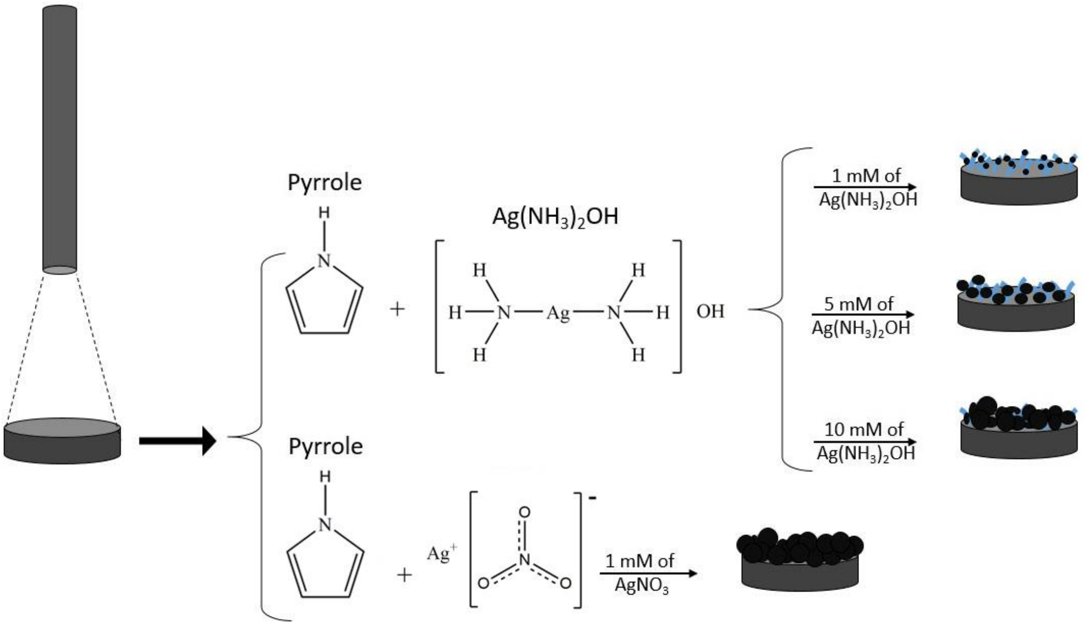

Figure 3.8: Schematic diagram of the electrode fabrication process for PpyNFs/AgNPs.

3.3.13. Preparation of PpyNFs-CuNPs composite

The synthesis solutions contained 0.1 M pyrrole monomer and one of the investigated supporting electrolytes, including $LiClO_4$, SDS, PTSA and $CuCl_2$, with a given concentration.

Before electrodeposition process, the solutions were deoxygenated with N_2. Polymers were formed through cyclic voltammetry (-0.6 to 0.8 V at 1 mVs^{-1} *vs*. SCE) and by amperometry method (at 0.8 V *vs*. SCE). Figure 3.9 shows the process schematically.

Table 3.2 shows the features of the prepared composites.

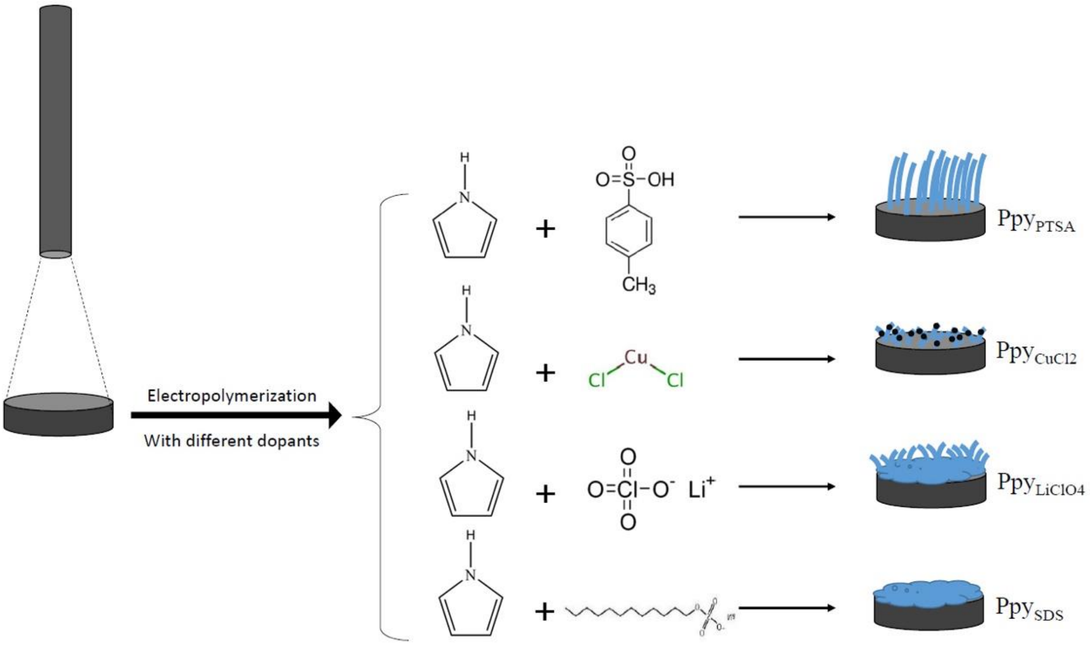

Figure 3.9: Schematic diagram of the electrode fabrication process for PpyNFs-CuNPs.

To ease the reading, Table 3.2 features all the prepared composites in this work, together with their methods of preparation.

Table 3.2: List of the prepared composites in this work.

Abbreviation	**Modification**	**Sample preparation**
rGO-AgNPs	rGO is decorated by AgNPs	One-step electrodeposition process by amperometry method
CV-rGO-CuNPs	rGO is decorated by CuNPs	One-step electrodeposition process by cyclic voltammetry method
AMP-rGO-CuNPs	rGO is decorated by CuNPs	One-step electrodeposition process by amperometry method
rGO/PpyNFs/Cu_xO	Cu_xO is decorated on Ppy on the surface of rGO	Layer-by-layer electrodeposition process
rGO/PpyNFs/AgNPs	AgNPs are decorated on Ppy on the surface of rGO.	Layer-by-layer electrodeposition process
CV-(rGO-AgNPs)/PpyNFs	Ppy is deposited on the surface of AgNPs and rGO.	Layer-by-layer electrodeposition process through cyclic voltammetry method.
AMP-(rGO-AgNPs)/PpyNFs	Ppy is deposited on the surface of AgNPs and rGO.	Layer-by-layer electrodeposition process through amperometry method.
PpyNFs/AgNPs	AgNPs are decorated on the surface of Ppy.	Layer-by-layer electrodeposition process
CV-PpyMTs-CuNPs	CuNPs are decorated on the surface of Ppy.	One-step electrodeposition process through cyclic voltammetry method.
AMP-PpyMTs-CuNPs	CuNPs are decorated on the surface of Ppy.	One-step electrodeposition process through amperometry method.

3.4. Instrumentation

The morphologies of the composites were investigated by Field Emission Scanning Electron Microscopy (FESEM Quanta 200F) and the weight percentage of the composites were verified using Energy Dispersive X-ray Spectroscopy (EDX). The structures were analyzed by X-ray Diffraction (XRD). A Fourier Transform Infrared Spectroscopy (FTIR) was used to obtain FTIR spectra of the sample. The electrochemical measurements were recorded using a potentiostat/galvanostat (Model PGSTAT-302N from Autolab). All of the measurements were taken at room temperature and all the electrochemical test were carried out three times.

3.4.1. Electrochemical studies

Autolab PGSTAT-302N potentiostat/galvanostat has been used for investigation and determination of the modified electrodes' electrochemical activity for H_2O_2 detection. The NOVA software is included in Autolab PGSTAT-302N. This software can run some useful DC techniques such as cyclic voltammetry, chronoamperometry (CA), chronopotentiometry (CP) and *etc*. The cyclic voltammetry technique was used for the detection of H_2O_2 and electropolymerization of nanocomposites and chronoamperometry were used for determination of linear range, limit of detection (LOD), limit of qualification (LOQ), selectivity and sensitivity of modified H_2O_2 sensors.

3.4.1.1. Amperometry (AMP)

In this technique, a constant potential is applied to a working electrode and the current is measured as a function of time. The constant potential is commonly selected (based on the CV experiments) such that the resulting current is mass transport limited, thus at steady state, it represents a concentration of the electro-active species, which is the analyte of interest or can be correlated to its concentration. Amperometry is based on study of the sensor response to a change of substrate concentration, which is referred as titration. It involves the current measurements of a sensor under constant polarisation immersed in a buffer solution, while changing the analyte concentration (stepwise). The results were plotted on a current versus time curve. The time between the changes of analyte concentration is determined by the properties of the sensor, namely by the time required for the current to reach equilibrium state. Solution was stirred to provide faster convective transport of the analyte to the electrode surface.

3.4.1.2. Cyclic voltammetry (CV)

Cyclic voltammetry (CV) is one of the important and sensitive electroanalytical methods to study the redox processes, understanding reaction intermediates and obtaining stability of reaction products. Cyclic voltammetry provides crucial information regarding the thermodynamics and kinetics of redox processes based on varying the applied potential in both forward and reverse directions while monitoring the current. The peak potentials and peak currents of the cathodic and anodic peaks are two important parameters in a cyclic voltammogram. If the electron transfer process is fast when compared to other processes (such as diffusion), the reaction is said to be electrochemically reversible and the peak separation is:

$$\Delta E_{\mathrm{p}} = E_{\mathrm{pa}} - E_{\mathrm{pc}} = 2.303\, RT / nF \qquad \text{(Eq. 3.1)}$$

In this work, the electrochemical performance of modified electrodes based on different composites was examined using cyclic voltammetry method in the presence of H_2O_2 in 0.1 M PBS (pH 6.5) using Autolab PGSTAT 302N.

3.4.1.3. Electrochemical Impedance Spectroscopy (EIS)

The electrochemical impedance spectroscopy is a more general concept of resistance and has become very popular nowadays as a complementary technique for the characterization of electrode processes at complex interfaces. Electrochemical impedance spectroscopy is measured by applying AC potential with small amplitude (5 to 10 mV) to an electrochemical cell and measuring the current flowing through the working electrode. An electrode-solution interface undergoing an electrochemical reaction is treated as an electronic circuit consisting of a combination of resistors and capacitors (Tlili *et al.*, 2006). By using this useful technique, the study of any intrinsic material property or specific processes that could influence the conductivity/resistivity or capacitivity of an electrochemical system is possible.

For electrochemical sensing, impedance techniques are useful to observe changes in electrical properties arising from biorecognition events at the surfaces of modified electrodes. For example, changes in the conductance of the electrode can be measured as a result of protein immobilization and antibody-antigen reactions on the electrode surface (Bakker, 2004; Janata, 2002). In this work, this technique was used to analyse different modified electrodes with a frequency ranging from 0.1 to 1×10^5 Hz in 0.1 M KCl solution containing 1.0 mM $Fe[(CN)_6]^{3-/4-}$(1:1).

3.4.2. Field Emission Scanning Electron Microscopy (FESEM)

Field Emission scanning electron microscopy (FESEM) is an extremely useful tool for the surface study of the samples which offers a better resolution of surface samples images than the optical microscopy. The FESEM measurements were done on a high resolution FEI Quanta 200F model instrument. This powerful tool is used widely in materials science field for examining and interpreting materials structure. The filament (electron gun) is heated by a current to generate an electron beam and this beam is collimated by electromagnetic condenser lenses and scanned across the surface of the sample by electromagnetic detection coils. Secondary electrons (SE) and backscattered electrons (BSE) signals are mostly used to generate SEM images.

3.4.3. Energy Dispersive X-Ray (EDX)

Energy Dispersive X-Ray (EDX) analysis is widely used for chemical analysis and characterizations. The EDX measurements were done on an EDX INCA Energy 400 model instrument. The intensity of backscattered electrons generated by electron bombardment can be correlated to the atomic number of the element within the sampling volume. Hence, qualitative elemental information can be determined. The characteristic X-rays emitted from the sample serve as fingerprints and give elemental information for the samples, including semi-quantitative and quantitative information, as well as the line profiling and spatial distribution of elements (elemental/chemical mapping).

3.4.4. Fourier Transform Infrared Spectroscopy (FTIR)

Fourier Transform Infrared Spectroscopy (FTIR) is an analytical technique based on the vibrations of the atoms within a molecule and measures the absorption of various infrared light wavelengths by the material of interest to specify molecular components and structures. An interferogram will collect the infrared spectra of a sample and measures all infrared frequencies simultaneously. FTIR spectrometer acquires and digitizes the interferogram, performs the FT function and outputs the spectrum. Sensitivity is one of the advantages of FTIR which makes the identification of even the smallest of contaminants possible. The very little possibility of mechanical breakdown is another advantage of this technique. These advantages, along with several others, make this tool a very reliable, extremely accurate and reproducible technique. In this work, FTIR spectra of the samples were recorded at ~293 K on a Magna-IR 560 spectrometer with 2 cm^{-1} resolutions by averaging 128 scans at a weight ratio in the 4000 – 400 cm^{-1} region.

3.4.5. X-Ray Diffraction (XRD)

The X-ray diffractometer is one of the non-destructive tools for the analysis of crystalline materials. A Siemens D5000 XRD unit, with an X-ray source having wavelengths of Kα = 1.5406 Å was used to record the data. The fingerprint characterization of these materials and a determination of their structure can be gained by using X-ray the device patterns. The basic of XRD analyses are based on Bragg's law. When X-rays of wavelength λ are incident at an angle θ on a crystal lattice, a portion of these beams will be scattered in all directions. The necessary and sufficient condition for constructive interference is known as Bragg's law. According to the law, scattered waves originating from each atom will be in phase with each another. Scheme 3.1 shows the geometric requirements for this condition. Bragg's law is follows:

$$n\lambda=2d_{hkl}\sin\theta \qquad \text{(Eq. 3.7)}$$

where,

λ = the wavelength of the X-ray

d = the spacing of the crystal layers (path difference)

θ = the incident angle (the angle between incident ray and the scatter plane)

n = an integer

The principle of Bragg’s law is applied in the construction of instruments such as Bragg spectrometer, which is often used to study the structure of crystals and molecules. All aspects of this formula are introduced in Scheme 3.1 dhkl as the interplanar spacing as a function of the Miller indices (h, k, and l) as well as the lattice parameters.

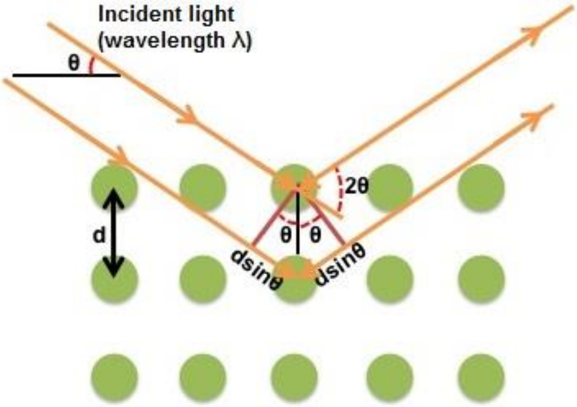

Scheme 3.1: Schematic of the diffraction of an X-rays beam by parallel atomic crystalline material.

Usually, diffraction experiments were applied at a fixed wavelength; therefore, measurement of the diffraction angles enables the calculation of the associated dhkl and then the lattice constants.

3.4.6. Transmission Electron Microscopy (TEM)

Transmission Electron Microscopy (TEM) is a technique in which a beam of electrons is based onto an ultrathin specimen and transmitted through it interacting with the specimen as it passes through. Because of this interaction, an image is formed. The image is magnified and focused on an imaging device, such as a layer of photographic film or a fluorescent screen, or is detected using a sensor (*e.g.*, CCD camera). The magnified transmitted signal can be observed through direct electron imaging or electron diffraction. Electron diffraction patterns are applied to determine the crystallographic structure of the materials. The cantilever is usually made up of silicon or silicon nitride with a tip radius of curvature about nanometers. When the tip is reached into proximity of a sample surface, forces between the tip and the sample cause a deflection of the cantilever according to Hooke’s law. Transmission Electron Microscopy images were captured using Philips PW 6061 TEM system (model CM 200, Eindhoven, Netherlands) to analyze the samples.

3.4.7. Atomic Force Microscopy (AFM)

Atomic Force Microscopy (AFM, PSIA XE-100) measurements were utilized to analyze the structures and surface morphology. The most applied method for cantilever deflection measurements is the beam deflection method. In this method, laser light from a solid-state diode is reflected off the back of the cantilever and collected by a photodiode detector (PSD) consisting of two closely spaced photodiodes whose output signal is collected by a differential amplifier.

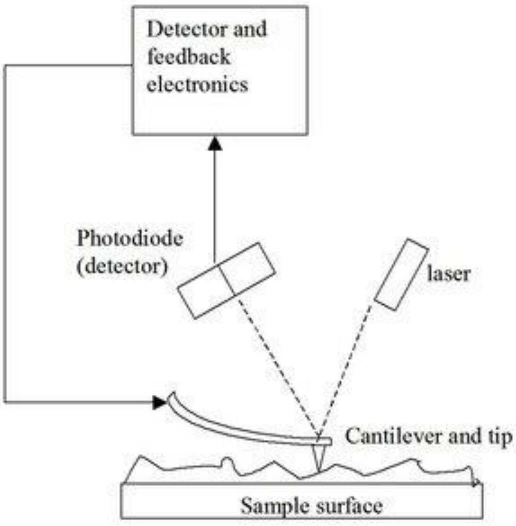

Scheme 3.2: Schematic of the AFM beam deflection method.

Angular displacement of the cantilever results in one photodiode collecting more light than the other photodiode, producing an output signal (the difference between the photodiode signals normalized by their sum), which is proportional to the deflection of the cantilever. It detects cantilever deflections <10 nm (thermal noise limited). A long beam path (several centimeters) amplifies changes in beam angle (Scheme 3.2).

3.4.8. Raman spectroscopy

Raman spectroscopy is a spectroscopic technique used to observe vibrational, rotational and other low-frequency modes in a system. Raman spectroscopy is commonly used to provide a fingerprint by which molecules can be identified. It relies on inelastic scattering or Raman scattering of monochromatic light, usually from a laser in the visible, near infrared, or near ultraviolet range. The laser light interacts with molecular vibrations, phonons or other excitations in the system, resulting in the energy of the laser photons being shifted up or down. The shift in energy gives information about the vibrational modes in the system.

Typically, a sample is illuminated with a laser beam. Electromagnetic radiation from the illuminated spot is collected with a lens and sent through a monochromator. Elastic scattered radiation at the wavelength corresponding to the laser line (Rayleigh scattering) is filtered out, while the rest of the collected light is dispersed onto a detector by either a notch filter or a band pass filter. Spontaneous Raman scattering is typically very weak and as a result, the main difficulty of Raman spectroscopy is separating the weak inelastically scattered light from the intense Rayleigh scattered laser light. Historically, Raman spectrometers used holographic gratings and multiple dispersion stages to achieve a high degree of laser rejection. In the past, photomultipliers were the detectors of choice for dispersive Raman setups, which resulted in long acquisition times. However, modern instrumentation almost universally employs notch or edge filters for laser rejection and spectrographs either axial transmissive (AT), Czerny–Turner (CT) monochromator, or FT (Fourier transform spectroscopy based), and CCD detectors.

The Raman spectra were obtained using a CRM200 Confocal Raman Microscope (WITec GmbH, Ulm, Germany) employing a 532 nm excitation wavelength to confirm the reduction of graphene oxide. Excitation was provided by a HeNe laser (Melles Griot). The exciting laser radiation was coupled into a Zeiss microscope through a wavelength-specific single mode optical fiber. The incident laser beam was collimated via an achromatic lens and passes a holographic band-pass filter before it was focused onto the sample through the microscope objective. The sample is located on a piezo-electrically driven microscope scanning stage with an x, y resolution of ca. 3 nm and a repeatability of ± 5 nm, and *z* resolution of ca. 0.3 nm and ± 2 nm repeatability. The Raman back-scattered radiation was detected by a back-illuminated deep depletion, 1024×128 pixel charge-coupled device camera operating at -82℃.

CHAPTER 4: RESULTS & DISCUSSION

This chapter reports the fabrication of seven novel non-enzymatic sensors and associated characterization in order to develop the new electrochemical sensors. The rGO was electrodeposited to enhance the electrochemical performance of the sensor. The effect of different dopants and electropolymerization methods on the performance of polypyrrole were investigated. Silver and copper nanoparticles were electrodeposited and characterized in order to improve the performance of non-enzymatic sensor.

4.1. rGO-AgNPs composite

4.1.1. Fourier Transform Infrared Spectroscopy (FTIR)

The FTIR spectrum of the GO and rGO are shown in Figure 4.1, respectively. For GO, the broad peak centered at 3389 cm^{-1} is assigned to the O-H stretching vibrations while the peaks at 1731 cm^{-1}, 1630 cm^{-1} and 1490 cm^{-1} are attributed to C=O stretching, sp^2-hybridized C=C group and O-H bending, C-OH stretching (Basirun *et al*., 2013).

In addition, the peak at 1142 cm^{-1} can be attributed to C-O vibration of epoxy or alkoxy groups. The peak at 3391 cm$^{−1}$ in the rGO spectra is related to O–H groups and the bands at 1685 cm^{-1} and 1321 cm$^{−1}$ are related to C-O and C-OH, respectively (Figure 4.1(a)).

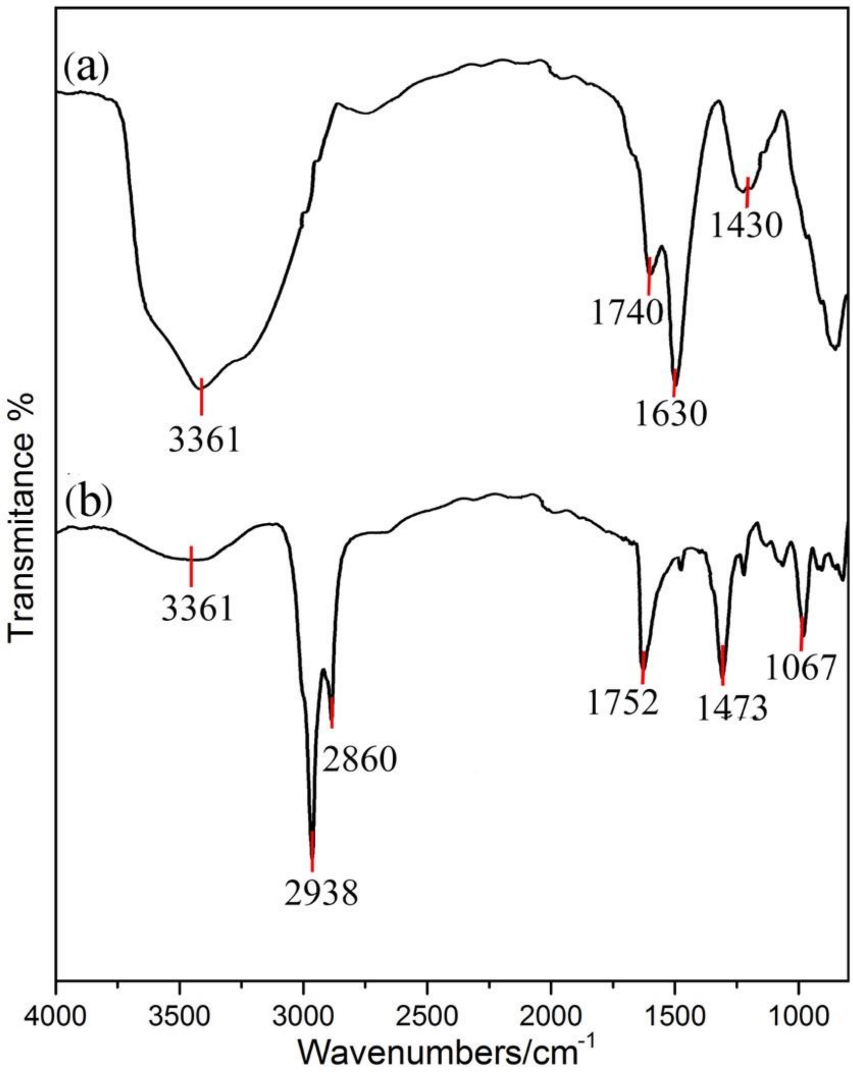

Figure 4.1: FTIR spectra for (a) GO, (b) rGO.

The peaks at 1260 cm^{-1} and 1016 cm^{-1} in the rGO spectrum are recognized as the C-O stretching vibration of the epoxy and alkoxy groups, respectively (Mahmoudian *et al*., 2012). The peaks at 2925 cm^{-1} and 2857 cm^{-1} in the rGO spectrum are related to the CH_2 asymmetric and symmetric stretching vibrations, respectively.

4.1.2. X-ray Powder Diffraction (XRD)

The XRD patterns of the GO and rGO-AgNPs-1 nanocomposite are presented in Figure 4.2.

The existence of the peak at 12.4° (Figure 4.2(a)) showed that graphene oxide was successfully synthesized (McAllister *et al.*, 2007; Zhou *et al*., 2010). In Figure 4.2, peak at 12.4° is related to GO characteristic peak (McAllister *et al.*, 2007; Zhou *et al.*, 2010), while the small peak appeared at ~23° is assigned to the elimination of surface oxygen - containing groups (Mayavan *et al*., 2012).

The small hump in rGO-AgNPs-1 nanocomposite at ~11° shows that the GO had been successfully reduced to rGO via electrochemical reduction. Meanwhile, the prominent peaks at 38.6°, 43.9°, 64.1°, and 77.4° for rGO-AgNPs-1 nanocomposites in Figure 4.2 are related to the (111), (200), (220), and (311) crystallographic planes of face-centered cubic nanoparticles of silver, respectively (Zainy *et al*., 2012). The sharp peak located at 37.9° is related to crystalline silver nanoparticles, affirmed the formation of high purity as-synthesized crystalline silver (Xie *et al*., 2012; Teo *et al*., 2012).

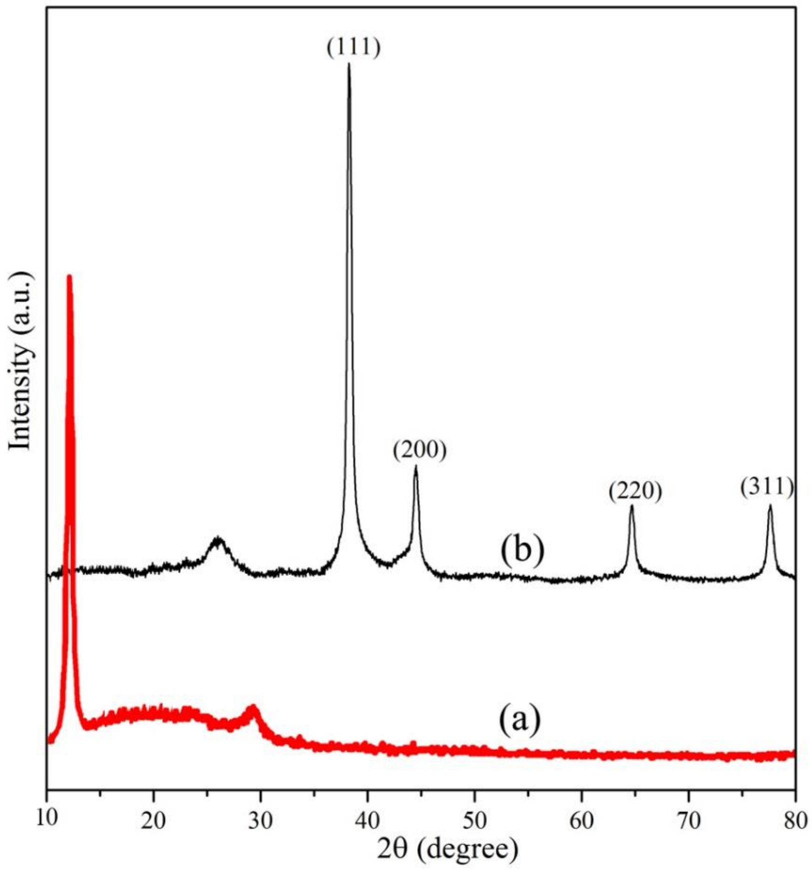

Figure 4.2: XRD spectra of (a) GO and (b) rGO-AgNPs-1

4.1.3. Raman spectroscopy

As shown in Figure 4.3, the rGO-AgNPs-1 nanocomposite fabricated by employing the one-step electrochemical technique was characterized by Raman spectroscopy.

For comparison, Figure 4.3(b) shows the Raman spectrum of graphene oxide. Both the graphene oxide and rGO present a strong D peak (defect peak because of intervalley scattering) at 1345 cm^{-1} and a strong G peak (the graphene peak) at 1607 cm^{-1} (Ferrari, 2007). Nevertheless, the ratio of D/G of the rGO (1.87) is higher than that of graphene oxide (1.17), showing an increase in the number of smaller graphene domains upon reduction of graphene oxide (Ferrari & Robertson, 2000). Additionally, 2D and 2G bands located at 2634 and 2919 cm^{-1}, respectively appeared after electrochemical reduction. The mentioned spectrum reveals that GO has been successfully reduced to rGO (Luo, 2012).

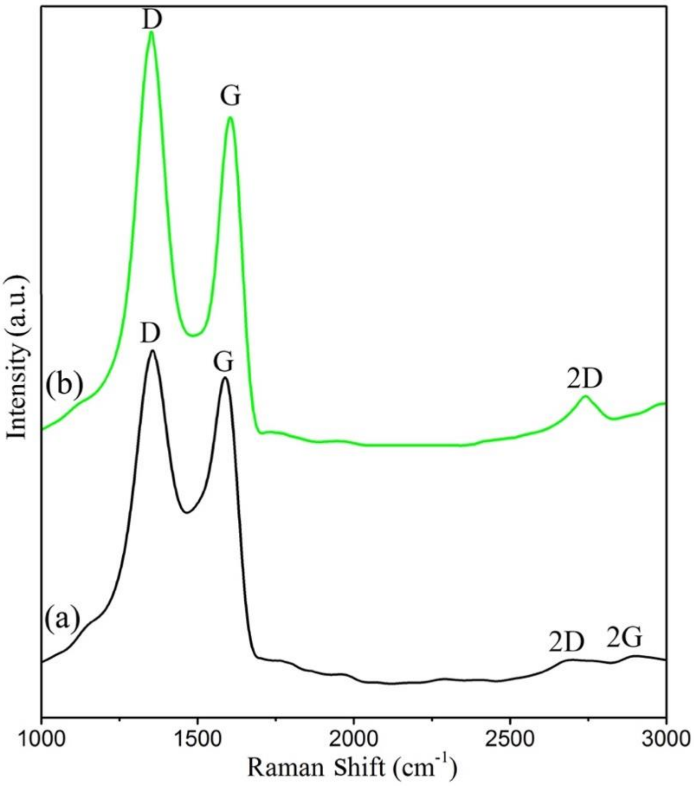

Figure 4.3: Raman spectrum of (a) rGO-AgNPs-1 and (b) GO.

4.1.4. Field Emission Scanning Electron Microscopy (FESEM)

A FESEM and particle size distribution of the rGO-AgNPs-1, rGO-AgNPs-2, rGO-AgNPs-3 and rGO-AgNPs-4 are shown in Figure 4.4.

As depicted in Figure 4.4(a, b), the AgNPs with an average size of 30 nm and particle size with a narrow distribution have been decorated, uniformly dispersed on the reduced graphene oxide surface and anchored on most parts of the reduced graphene oxide surface.

As can be seen in Figure 4.4(c-f), as the concentration of $Ag(NH_3)_2OH$ increased, the average size of particles increased and consequently the particle size distribution of deposited Ag become widened.

As previously reported, the size and coverage density of electrodeposited silver nanoparticles on the reduced graphene oxide surface are affected by the types of Ag precursors (Moradi *et al.*, 2013).

The average particle size is increased to 820 nm and the particle size distribution widened, when $AgNO_3$ was used as a precursor of Ag as shown in Figure 4.4(e, f).

The plausible reason is that $Ag(NH_3)_2OH$ has a higher stability than $AgNO_3$ and has resistance to reduction, preventing the growth of Ag into large particles (Moradi *et al.*, 2013; Kaniyankandy *et al.*, 2007).

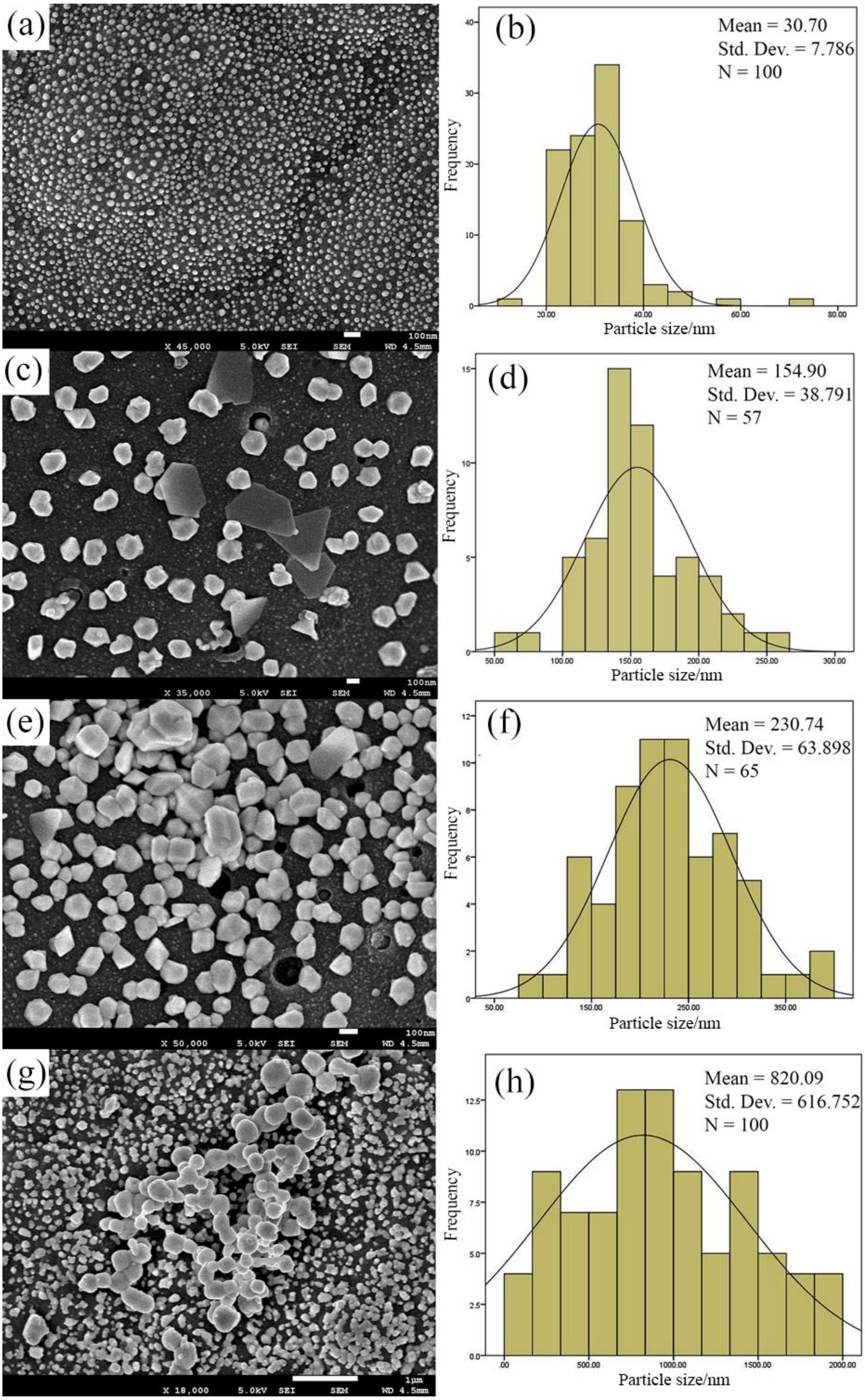

Figure 4.4: FESEM images and particle size distribution of (a, b) rGO-AgNPs-1, (c, d) rGO-AgNPs-2, (e, f) rGO-AgNPs-3 and (g, h) rGO-AgNPs-4.

4.1.5. Cyclic voltammetry (CV)

Electrocatalytic reduction of rGO-AgNPs-1, 2, 3 and rGO-AgNPs-4 is shown in Figure 4.5. The catalytic activities of rGO-AgNPs-1, rGO-AgNPs-2 and rGO-AgNPs-3 electrodes are markedly better than rGO-AgNPs-4. The comparison between rGO-AgNPs-1, rGO-AgNPs-2 and rGO-AgNPs-3 which were synthesized in the $Ag(NH_3)_2OH$ solution, shows that the rGO-AgNPs-1 has the highest electrocatalytic activity which is mainly due to higher available surface area.

In comparison with rGO-AgNPs-1, although the particle density of rGO-AgNPs-2, 3 are much higher, but particle size of AgNPs increased which led to lower surface area. FESEM (Figure 4.4) images support the results of CVs. For all the modified electrodes, in the absence of hydrogen peroxide, the CV curve is quite similar to the bare electrode (not shown). However, as can be seen in Figure 4.5, with the addition of hydrogen peroxide, a reduction peak centered at about -0.05 V appeared, corresponds to the reduction of hydrogen peroxide. This suggests that AgNPs and rGO played a major role in the electroreduction of hydrogen peroxide.

The enhanced electrocatalytic performance of rGO-AgNPs-1 as compared to other modified electrodes is probably due to fast electron transfer provided by reduced graphene sheets as well as high conductivity and the large surface area (Luo, 2012), confirming the important role of the reduced graphene oxide plays in the electrocatalytic performance towards hydrogen peroxide reduction.

As can be obtained from the mentioned results, it can be concluded that the rGO-AgNPs-1 shows a synergistic combination of reduced graphene oxide sheets and silver nanoparticles on the electrochemical reduction of hydrogen peroxide.

Finally, it can be concluded that after addition of H_2O_2 to the solution, silver nanoparticles which are decorated on the surface of the rGO react chemically with H_2O_2 according to the following equations:

$$\mathrm{rGO - AgNPs(0) + H_2O_2 \rightarrow rGO - AgNPs(I) - OH} \qquad \text{(Eq. 4.1)}$$

$$\mathrm{rGO - AgNPs(I) - OH + 2H^+ + 2e^- \rightarrow rGO - AgNPs(0) + 2H_2O} \qquad \text{(Eq. 4.2)}$$

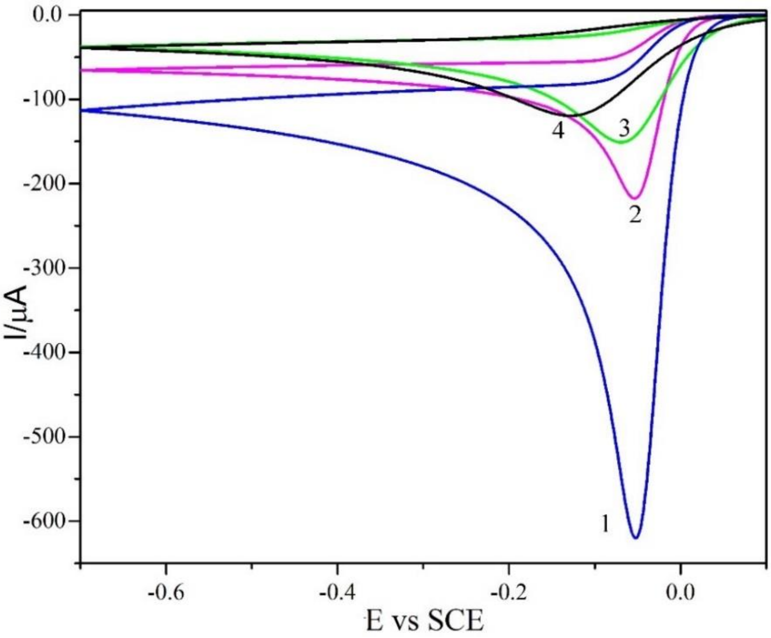

Figure 4.5: CVs of (1) rGO-AgNPs-1, (2) rGO-AgNPs-2, (3) rGO-AgNPs-3 and (4) rGO-AgNPs-4 in the presence of 1 mM H_2O_2 in 0.1 M PBS (pH 6.5) at scan rate of 50 mV s^{-1}.

4.1.6. Electrochemical Impedance Spectroscopy (EIS)

In order to analyze the impedance changes of the modified electrode, Electrochemical Impedance Spectroscopy was employed. Figure 4.6 depicts the Nyquist plots in 0.1 M KCl solution containing 1 mM $\mathrm{Fe(CN)_6^{-3/-4}}$ (1:1).

The Nyquist plot of impedance spectra consists of semicircle portion which at higher frequencies correlates to the electron transfer limited process, while on the other hands, a linear portion at lower frequencies correlates to the diffusion process. The electron transfer resistance (R_{ct}) can be evaluated by using the semicircle diameter.

As previously discussed, by increasing the concentration of $Ag(NH_3)_2OH$ solution, the size of the electrodeposited AgNPs increased and consequently, agglomeration takes place.

Moreover, by increasing the density of electrodeposited AgNPs, the charge transfer resistance (R_{ct}) of the modified electrodes decreases. This can be attributed to the low resistance properties of AgNPs. The comparison between the semicircle diameters from the Nyquist diagrams of rGO-AgNPs-1 (681 Ω), rGO-AgNPs-2 (1051 Ω) and rGO-AgNPs-3 (1265 Ω) shows the direction of R_{ct}:

GCE > rGO-AgNPs-3 > rGO-AgNPs-2 > rGO-AgNPs-1

In order to figure out the impedance parameters, the NOVA 1.11 software is employed in the simulations. The $R_s(CPE[R_{ct}W])$ equivalent circuit model was employed in the simulation of the impedance behavior of all the modified electrodes, from the experimentally gained impedance data.

By exploiting the series components, the model was developed. The first component is ohmic resistance of the solutions (R_s) and the second one is a set of constant phase elements (CPE) and the resistance of layer (R_{ct}).

R_{ct} indicates the conductivity of the samples that are in the parallel position with CPE. Additionally, from the diffusion impedance, W which stands for the Warburg element is a series connection to R_{ct}. Table 4.1 shows the obtained data of all modified electrodes.

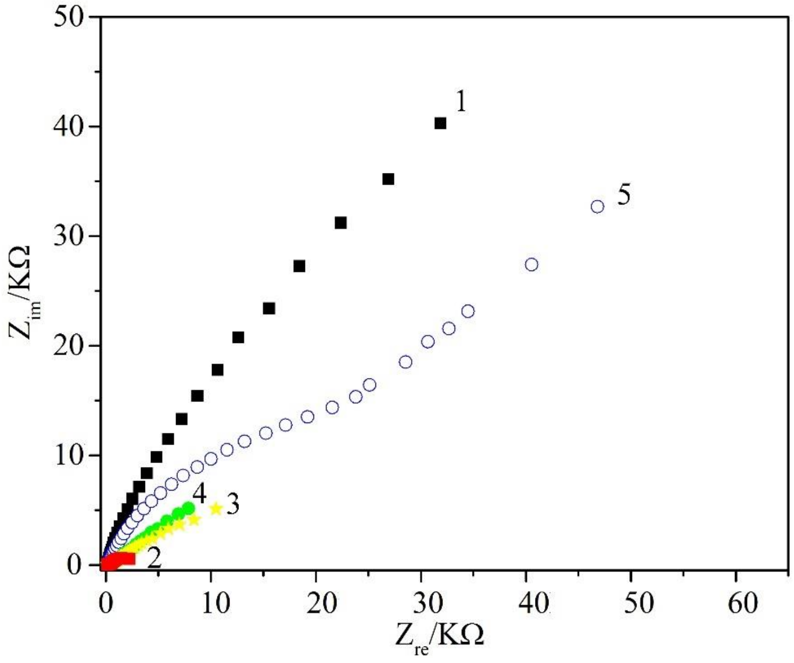

Figure 4.6: Nyquist plots of (1) bare electrode, (2) rGO-AgNPs-1, (3) rGO-AgNPs-2, (4) rGO-AgNPs-3 and (5) rGO-AgNPs-4 in 0.1 M KCl solution containing 1 mM $Fe(CN)_6^{3-/4-}$ (1:1).

Table 4.1: EIS parameters achieved by equivalent circuits modified electrodes in 0.1 M KCl solution containing 1 mM $Fe(CN)_6^{3-/4-}$ (1:1).

Electrode	**R_{s1} (Ω)**	**R_{ct1} (Ω)**	**Q_1 (μMho)**	**W (mMho)**	**n_1**	**R_{ct2} (Ω)**	**Q_2 (μMho)**	**n_2**
Bare electrode	183	290×10^3	-	11.8	0.88	-	-	-
rGO-AgNPs-1	182	681	0.624	-	0.92	11695	108	0.55
rGO-AgNPs -2	185	1051	0.751	-	0.91	12547	111	0.56
rGO-AgNPs-3	198	1265	1.04	-	0.94	12285	154	0.64
rGO-AgNPs-4	189	105×10^3	0.864	12.5	0.85	-	-	-

4.1.7. Sensor optimization

The mentioned experimental results confirm that H_2O_2 can electrochemically be reduced in the presence of rGO-AgNPs-1 on the surface of GCE. To develop the performance of the sensor, various factors influencing the current response of the sensor were investigated. In order to investigate the influence of operating potential on the amperometric response of the rGO-AgNPs-1, the reduction current studied under batch conditions ranging from 0.0 to -0.2 V in a solution containing 1 mM H_2O_2 in 0.1 M phosphate buffer solution (pH 6.5). The potential value of -0.05 V was determined as the operating potential.

4.1.7.1. Amperometric detection of H_2O_2

Amperometric i–t curve is the regularly utilized technique to assess the electrocatalytic activities of electrochemical sensors. Figure 4.7 shows the amperometric responses of the rGO-AgNPs-1 electrode at -0.05 V versus SCE as a result of the successive addition of H_2O_2 to the continuously stirred 0.1 M phosphate buffer solution (pH 6.5) at 25 °C. The experiments were carried out with freshly prepared electrode. As shown in Figure 4.7, the rGO-AgNPs-1 was very sensitive to the changes in the concentration of H_2O_2 and responded rapidly. The response time was fast (less than 3 s) and with increasing the concentration of H_2O_2 from 0.1 mM to 24 mM, the current increased linearly. In calibration curve, the sensor shows linear section for the response to H_2O_2 with the linear regression equation of $I = 435\ (\mu A.mM^{-1}) + 58.2$ ($R^2 = 0.9997$). The limit of quantification (LOQ) and the limit of detection (LOD) of rGO-AgNPs-1 were determined by using the following equations:

$$LOQ = \frac{10S_B}{b} \qquad \text{(Eq. 4.3)}$$

$$LOD = \frac{3S_B}{b} \qquad \text{(Eq. 4.4)}$$

where b is the slope of the calibration curve and S_B is the standard deviation of the blank solution as shown in Figure 4.7 (inset). The LOD and LOQ (S/N = 3) are calculated to be 0.0165 and 0.055 µM, respectively.

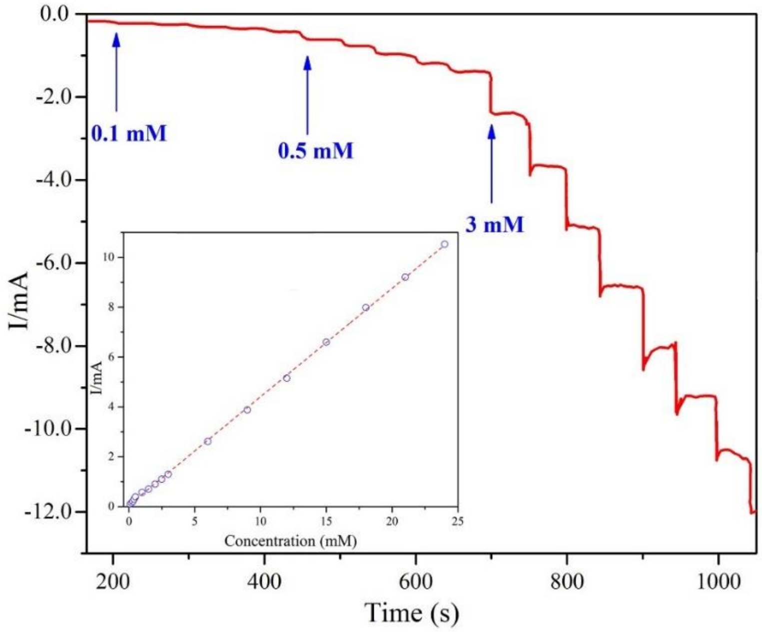

Figure 4.7: Current–time responses of rGO-AgNPs-1 with the subsequent addition of H_2O_2 into 0.1 M PBS (pH 6.5) at -0.05 V; (Inset) Calibration curve.

As listed in Table 4.2, the detection limit and the linear range of rGO-AgNPs-1 are better and wider than most of the other modified electrodes based on reduced graphene oxide and silver nanoparticles.

Table 4.2: Comparison between LOD and linear range of different non-enzymatic H_2O_2 sensors with rGO-AgNPs-1.

Modified electrode	**Performance**		**Ref.**
	LOD (μmol.L^{-1})	**Liner range** (mmol.L^{-1})	
Ag NPs-NFs/GCE	62	0.1–80	(Tian *et al.*, 2010)
Ag NP-CPNBs	0.9	0.1-70	(Luo *et al.*, 2011)
Graphene–AgNPLs	3	0.02–10	(Zhong *et al.*, 2013)
ERGO-Ag/GCE	1.6	0.1–100	(Moradi *et al.*, 2013)
AgNP/rGO-benzylamine	31.3	0.1–100	(Liu *et al.*, 2011)
Ag NPs-MWCNT/Au	0.5	0.05–17	(Zhao *et al.*, 2009)
PQ11-AgNPs/GCE	33.9	0.1–180	(Lu *et al.*, 2011)
Ag NPs/PPy/Fe3O4/GCE	1.7	0.005–11.5	(Qi *et al.*, 2015)
PDDA-rGO/AgNPs/GCE	35	0.1–41	(Liu *et al.*, 2013)
rGO-AgNPs	0.016	0.1-24	This work

4.1.7.2. Repeatability, reproducibility and stability

The repeatability, reproducibility and stability of the prepared sensor were studied. Five modified electrodes were prepared under the same condition and relative standard deviation (RSD) of the current response toward 1 mM H_2O_2 was found to be 1.81%, confirming that the results can be reproducible. The repeatability of one sensor to determine 1 mM H_2O_2 was fairly good. The RSD was 3.65% for 10 successive assays. In order to investigate the stability of rGO-AgNPs-1 electrode, the modified electrode was stored in ambient condition and the current was periodically monitored for 21 days (Figure 4.8). The current response did not have considerable decrease by the first week, and as can be seen from Figure 4.8, the sensor retains around 89% of its initial response after three weeks (I_0 and I are the response current in the first and following days, respectively). The overall performance concluded that rGO-AgNPs-1 shows a good repeatability, reproducibility and stability.

4.1.7.3. Interference study

Figure 4.8 (inset) demonstrates the selectivity and anti-interference advantages by comparing the amperometric responses of relevant electroactive species. The amperometric response of the rGO-AgNPs-1 towards the successive addition of 1 mM H_2O_2 was measured and this is followed by glucose, ascorbic acid, ethanol and uric acid into 0.1 M PBS at pH 6.5 at a working potential of -0.05 V *vs*. SCE. As can be seen, the current response of the mentioned electroactive interfering species is quite negligible which confirms that rGO-AgNPs-1 has a superior selectivity towards H_2O_2. The good ability of anti-interference is largely attributed to the low working potential of -0.05 V used in the determination of H_2O_2 (Wang, 2010).

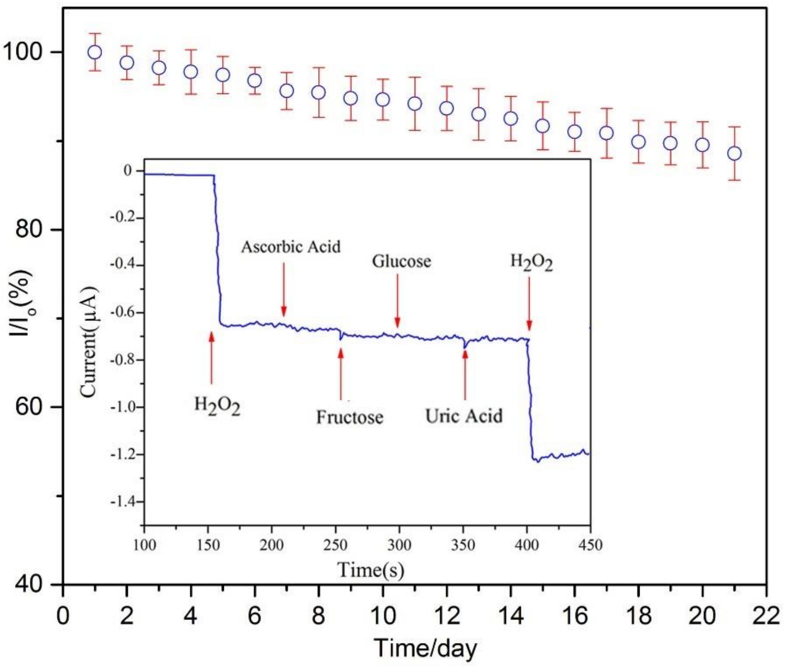

Figure 4.8: Long term stability of the rGO-AgNPs-1 studied in three weeks, and (Inset) shows amperometric response of rGO-AgNPs-1- upon the successive addition of 1 mM uric acid, glucose, ascorbic acid and fructose into 0.1 M PBS (pH 6.5) with an applied potential -0.05 V.

To prove the accuracy of the sensor, a lens-cleaning solution was used for performing the detection of H_2O_2. The H_2O_2 determination in the samples of the mentioned solution was carried out on the modified sensor employing standard addition method. The dilution of samples has been done through using phosphate buffer solution (pH 6.5) prior to determining the current response. Later, H_2O_2 solutions were successively added to the system in order to determine the current response through standard addition method.

All the measurements were carried out four times. Table 4.3 lists the average recoveries. According to Table 4.3 and considering the relative standard deviation (RSD) values and calculated recovery, it can be observed that the developed sensor holds possible applications for evaluating specific concentration range of H_2O_2.

Table 4.3: H_2O_2 determination in real samples by using rGO-AgNPs-1.

Sample	Added (mM)	RSD%	Measured by sensor (mM)	Recovery%
1	0.1	1.209	0.0979	97.96
2	1	1.766	0.972	97.26
3	5	3.640	4.935	98.5
4	15	3.313	15.174	101.16
5	20	3.284	19.986	99.93

The performance of rGO-AgNPs-1 electrode towards glucose was investigated. Figure 4.9 shows the CV recorded by the electrode in presence of glucose at 1 mM. As can be seen, the prepared nanocomposite did not show significant performance as no obvious redox response was recorded thus suggesting that in this potential window, rGO-AgNPs-1 nanocomposite is not suitable to be used for dual detection of glucose and hydrogen peroxide.

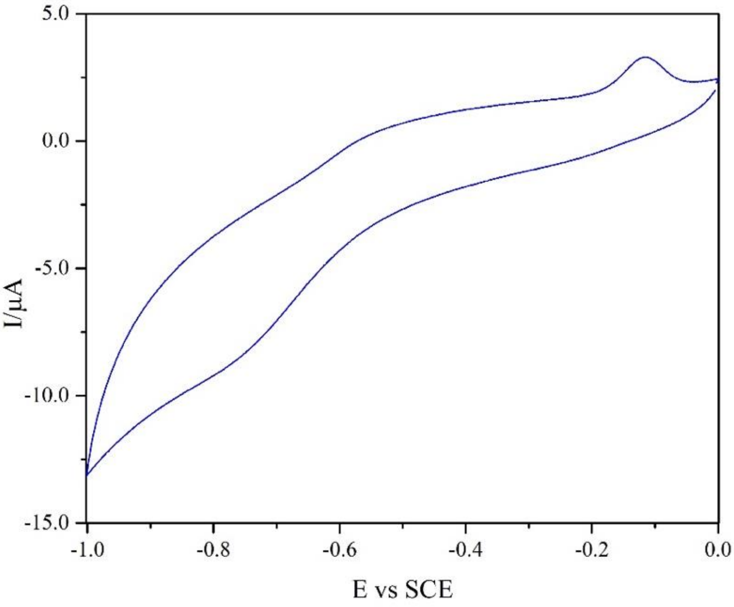

Figure 4.9: CV of rGO-AgNPs-1 electrode in a 0.1 M phosphate buffer solution (pH 7.2) and 1 mM glucose, scanned at 50 mVs^{-1} scan rate.

4.2. rGO-CuNPs composite

4.2.1. Fourier Transform Infrared Spectroscopy (FTIR)

The FTIR spectrum of the GO and rGO are shown in Figure 4.10, respectively. For GO, the broad peak centered at 3389 cm^{-1} is assigned to the O-H stretching vibrations while the peaks at 1731, 1630 and 1490 are attributed to C=O stretching, *sp*^{2}-hybridized C=C group and O-H bending, C-OH stretching (Basirun *et al.*, 2013). In addition, the peak at 1142 cm^{-1} can be attributed to C-O vibration of epoxy or alkoxy groups. The peak at 3391 cm^{-1} in the rGO spectra is related to O–H groups and the bands at 1685 and 1321 cm^{-1} are related to C-O and C-OH, respectively (Figure 4.10(a)). The peaks at 1260 and 1016 cm^{-1} in the rGO spectrum are recognized as the C-O stretching vibration of the epoxy and alkoxy groups, respectively (Mahmoudian *et al.*, 2012). The peaks at 2925 and 2857 cm^{-1} in the rGO spectrum are related to the CH_2 asymmetric and symmetric stretching vibrations, respectively.

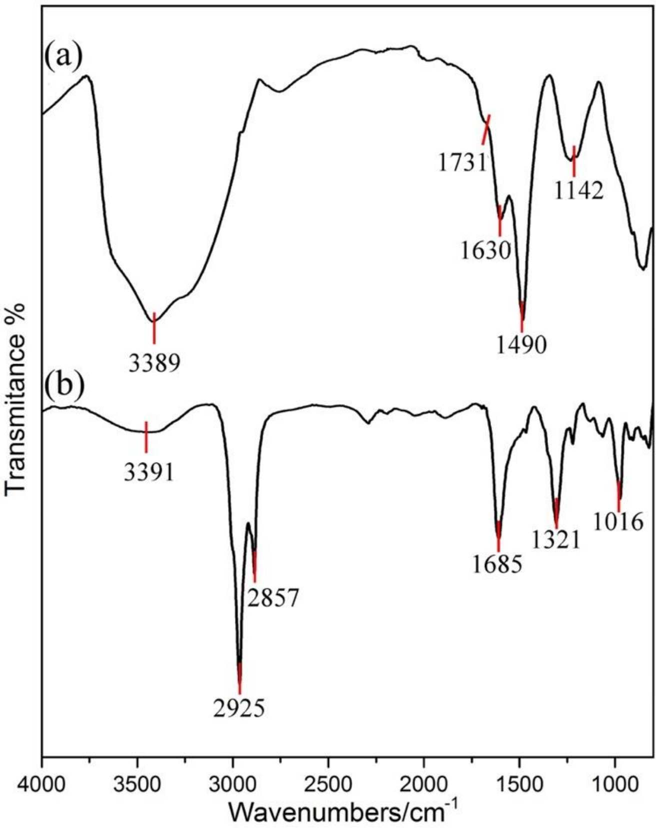

Figure 4.10: FTIR spectra for (a) GO, (b) rGO.

4.2.2. X-ray Powder Diffraction (XRD)

The XRD patterns of the GO and rGO-CuNPs nanocomposite are presented in Figure 4.11. The existence of the peak at 13.4° (Figure 4.11(a)) showed that graphene oxide was successfully converted to rGO (McAllister *et al.*, 2007; Zhou, 2010). As can be seen in the XRD pattern of CV-rGO-CuNPs-2 nanocomposite (Figure 4.11(b)), the broad peak at 24° is corresponded to the diffraction of loosely stacked graphene (Zhang *et al.*, 2010).

The distinctive peaks centered at 43.5, 50.5 and 74.5° are attributed to the (111), (200) and (220) facets of the face-centered cubic structures of Cu crystal, respectively (Luo *et al.*, 2012; Yang *et al.*, 2010).

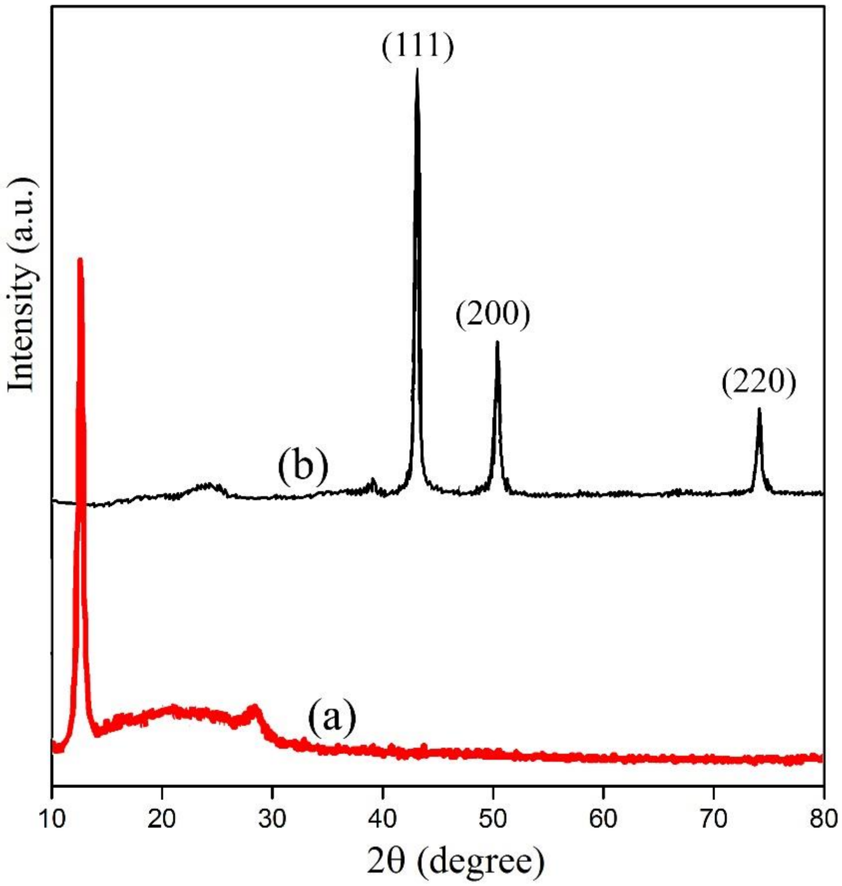

Figure 4.11: XRD spectra of (a) GO and (b) CV-rGO-CuNPs-2.

4.2.3. Raman spectroscopy

As shown in Figure 4.12, the CV-rGO-CuNPs-2 nanocomposite fabricated by employing the one-step electrochemical technique was characterized by Raman spectroscopy. For comparison, Figure 4.12(b) shows the Raman spectrum of graphene oxide. Both the graphene oxide and rGO present a strong D peak (defect peak because of intervalley scattering) at 1340 cm^{-1} and a strong G peak (the graphene peak) at 1600 cm^{-1} (Ferrari, 2007). Nevertheless, the ratio of D/G of the rGO (1.38) is higher than that of graphene oxide (1.17), showing an increase in the number of smaller graphene domains upon reduction of graphene oxide (Ferrari, 2000). Additionally, 2D and 2G bands located at 2637 and 2915 cm^{-1}, respectively appeared after electrochemical reduction. The mentioned spectrum reveals that GO has been successfully reduced to rGO (Luo *et al.*, 2012).

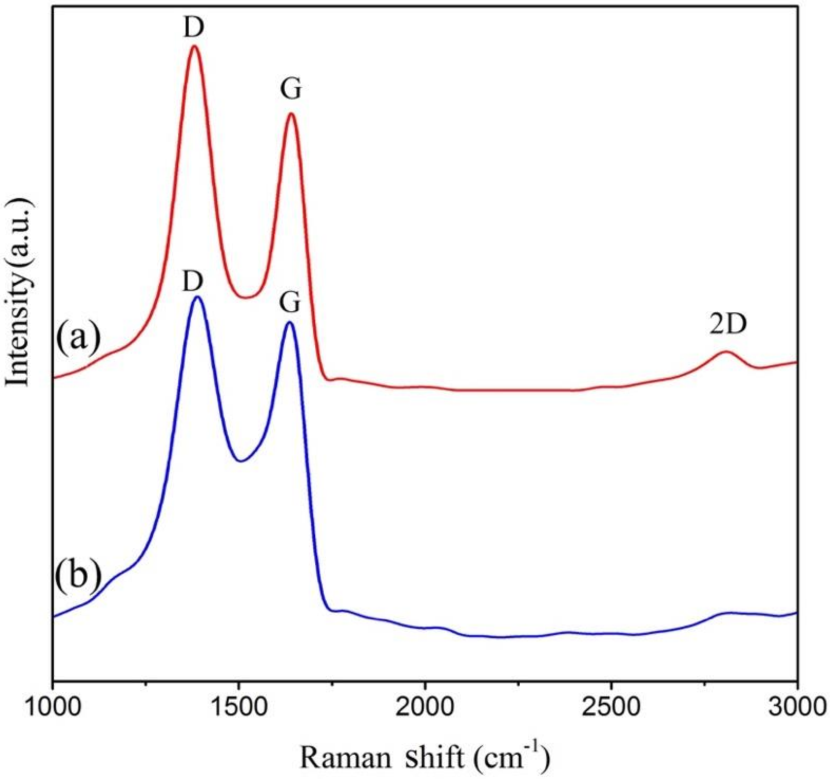

Figure 4.12: Raman spectrum of (a) GO and (b) CV-rGO-CuNPs-2.

4.2.4. Field Emission Scanning Electron Microscopy (FESEM)

FESEM of all modified electrodes are shown in Figure 4.13. As depicted in Figure 4.13(a, b), in the lower concentration of Cu, small amount of Cu has been deposited on the surface of reduced graphene oxide.

In the amperometry method (Figure 4.13(a)), the small amount of copper particles with high particle size were decorated, otherwise, in the cyclic voltammetry method and at the same concentration (Figure 4.13(b)), there is no sign of existence of copper. The main reason might be due to low concentration of copper.

On the other hand, with increasing the concentration of copper, Cu particles which decorated reduced graphene oxide have emerged.

As can be seen in Figure 4.13(c, d), as the concentration of Cu increased, much more Cu particles were electrodeposited on the surface of rGO. In the amperometry method and at concentration of 5 mM of $CuCl_2$ (Figure 4.13(c)), due to the agglomeration of Cu particles, particle size increased to more than 1 μm.

On the other hand, in the cyclic voltammetry method (Figure 4.13(d)), CuNPs which uniformly decorated wrinkled rGO were electrodeposited.

The main reason for agglomeration in amperometry method might be the fact that in this method, the electrodeposition was carried out at copper electrodeposition potential which leads to electrodeposition of high amount of Cu, otherwise in cyclic voltammetry and in the selected potential window, there is a lower chance for agglomeration.

As can be seen in Figure 4.13(d), CuNPs with particle size less than 100 nm which growth with reduced graphene oxide were electrodeposited on the surface of GCE. With increasing the concentration, the average size of particles increased as well.

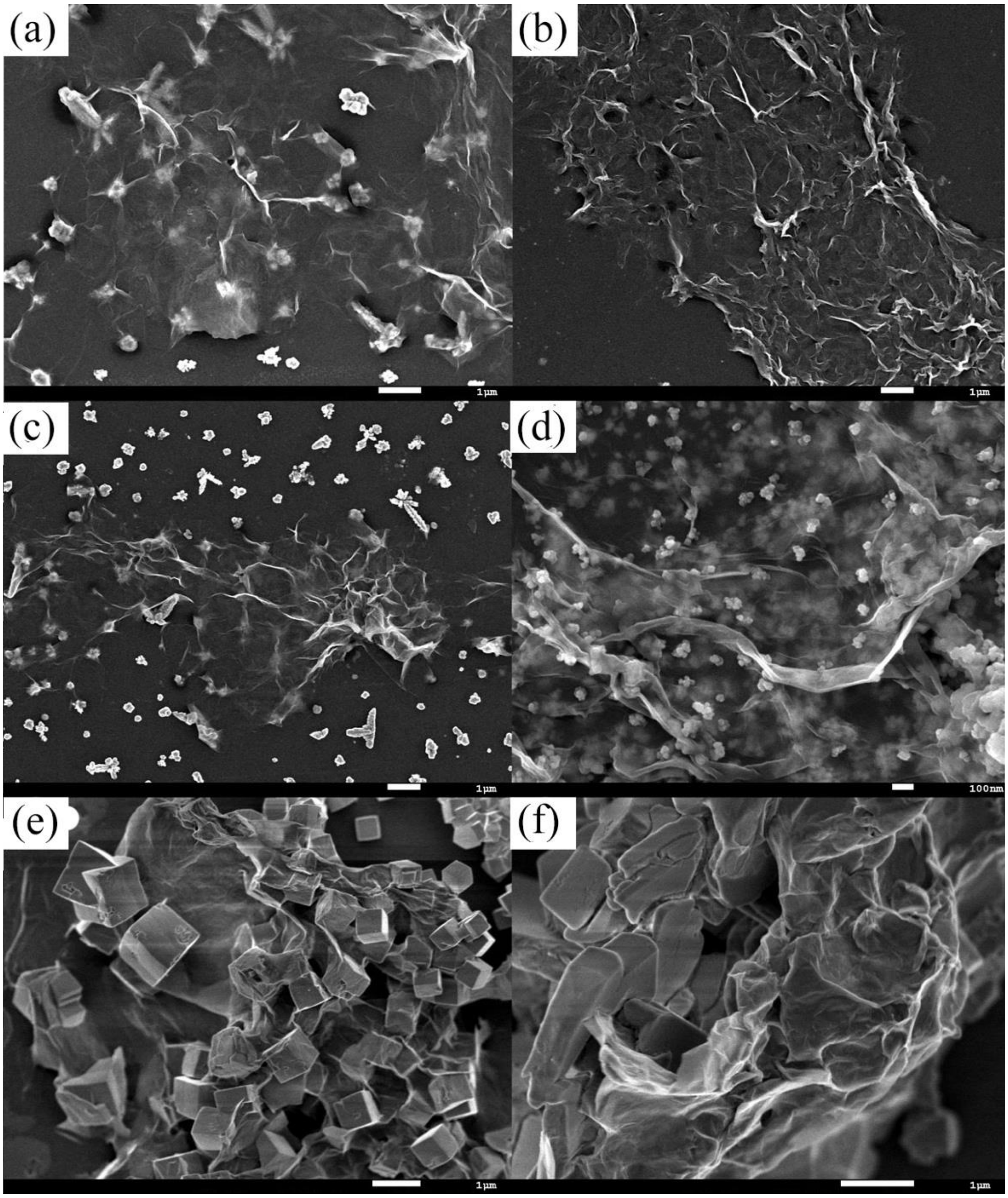

Figure 4.13: FESEM images of (a) AMP-rGO-CuNPs-1, (b) CV-rGO-CuNPs-1, (c) AMP-rGO-CuNPs-2, (d) CV-rGO-CuNPs-2, (e) AMP-rGO-CuNPs-3 and (f) CV-rGO-CuNPs-3.

4.2.5. Cyclic voltammetry (CV)

Electrocatalytic reduction of AMP-rGO-CuNPs-1, 2, 3/GCE and CV- rGO-CuNPs-1, 2, 3 and their copper oxide forms are shown in Figure 4.14. The catalytic activities of almost all CV- rGO-CuNPs are markedly better than AMP-rGO-CuNPs.

Figure 4.14 shows that the CV-rGO-CuNPs-2 exhibits the highest electroreduction activity towards H_2O_2 at -0.2 V *vs*. SCE. In comparing between CV- and AMP-rGO-CuNPs-3, the particle density of CV- and AMP-rGO-CuNPs-2 is higher and although particle density for CV- and AMP-rGO-CuNPS-2 is lower than CV- and AMP-rGO-CuNPs-3, the particle size of Cu particles increased which led to a lower surface area. FESEM images approve the results of CVs. For CV-rGO-CuNPs-2, in the absence of hydrogen peroxide, the CV curve is quite similar to the bare electrode (not shown).

However, as can be seen in Figure 4.14, with the addition of hydrogen peroxide, a reduction peak centered at about -0.2 V appeared, corresponds to the reduction of hydrogen peroxide. This suggests that CuNPs played a major role in the electroreduction of hydrogen peroxide. In order to figure out the role of copper in the form of its oxides, Cu_xO-rGO was synthesized and its electrocatalytic response to hydrogen peroxide is also investigated as shown in Figure 4.14.

The Cu_xO-rGO showed weak hydrogen peroxide peak. It is obviously observed that CV-rGO-CuNPs-2 exhibited much higher current than AMP-rGO-CuNPs-2 which might be due to the well distribution and smaller particle size of copper nanoparticles. The enhanced electrocatalytic performance of CV-rGO-CuNPs-2 as compared to other modified electrodes is probably due to high conductivity and the large surface area as well as fast electron transfer provided by reduced graphene sheets (Luo *et al.*, 2012), confirming the important role of the reduced graphene oxide plays in the electrocatalytic performance towards hydrogen peroxide reduction. As can be obtained from the mentioned results, it can be concluded that the CV-rGO-CuNPs-2 shows a synergistic combination of reduced graphene oxide sheets and copper nanoparticles on the electrochemical reduction of hydrogen peroxide.

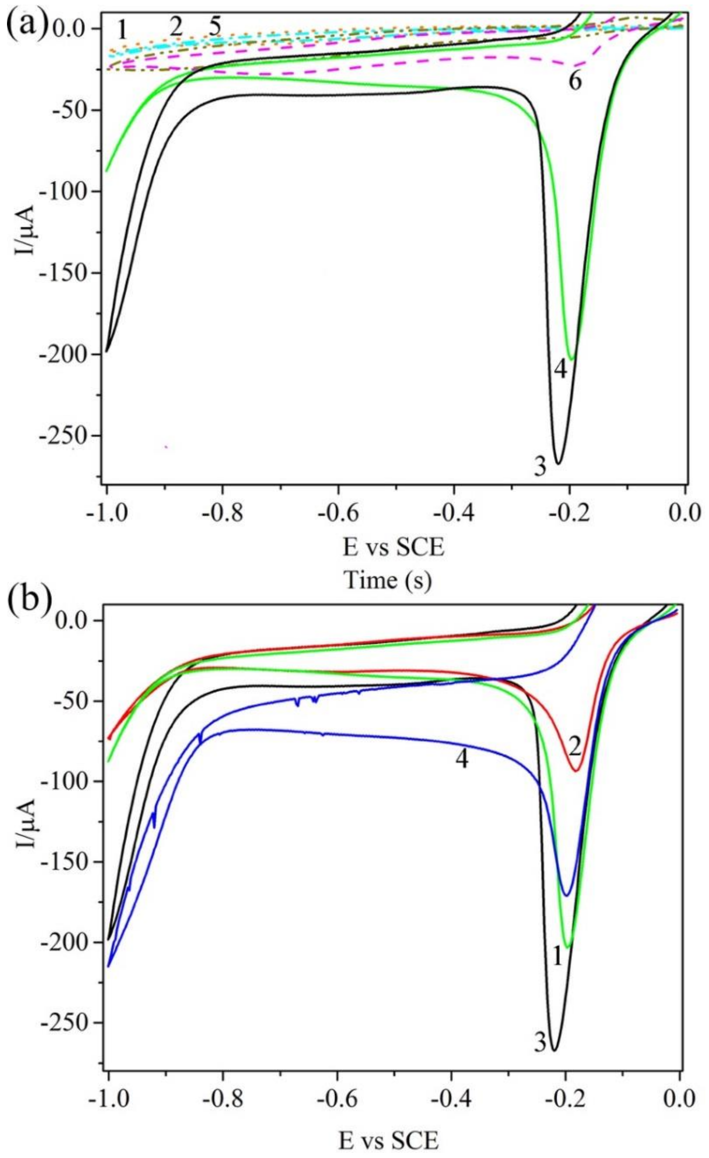

Figure 4.14: (a) CVs of different modified electrodes: (1) CV-rGO-CuNPs-1, (2) AMP-rGO-CuNPs-1, (3) CV-rGO-CuNPs-2, (4) AMP- rGO-CuNPs-2, (5) CV- rGO-CuNPs-3 and (6) AMP- rGO-CuNPs-3 in 0.1 M PBS (pH 6.5) with adding 1 mM H_2O_2. (b) CVs of (1) AMP-rGO-CuNPs-2, (2) AMP-rGO-Cu_xO-2, (3) CV- rGO-CuNPs-2 and (4) CV-rGO-Cu_xO-2 in the presence of 1 mM H_2O_2 in 0.1 M PBS (pH 6.5) at scan rate of 50 mV s^{-1}.

In a possible electrocatalytic mechanism for the H_2O_2 reduction, Cu(II) was first electrochemically oxidize to Cu(II), reacting chemically with H_2O_2 and resulting in the conversion of H_2O_2 into OH^- and regeneration of the catalyst, as shown in the following equations (Mahmoudian *et al*., 2014; Zhang *et al.*, 2008):

$$\text{rGO-CuNPs(0)} + H_2O_2 \rightarrow \text{rGO-CuNPs(II)} + 2OH^- \qquad \text{(Eq. 4.5)}$$

$$\text{rGO-CuNPs(II)} + 2e^- \rightarrow \text{rGO-CuNPs(0)} \qquad \text{(Eq. 4.6)}$$

4.2.6. Electrochemical Impedance Spectroscopy (EIS)

As can be seen in Figure 4.15, the Nyquist plot of all modified electrodes in the frequency range of 0.1 Hz to 100 kHz, almost presents a semicircle with different diameters, indicating their different conductivities.

For rGO-CuNPs in higher concentrations, another semicircle is observed suggesting that the smaller one is due to CuNPs and the bigger one is as a result of reduced graphene oxide.

By fitting the data and in high frequency area, it can be observed that the sequence of R_{ct} values for different electrodes is:

CV-rGO-CuNPs-2 < CV-rGO-CuNPs-3 < CV-rGO-CuNPs-1< CV-rGO-Cu_xO-2

This shows that the rGO-CuNPs nanocomposite develops a synergistic effect of reduced graphene oxide sheets and Cu nanoparticles. In the electron transfer process, CuNPs act as an electron mediator.

In other words, by incorporating Cu nanoparticles, the heterogeneous electron transfer capacity of reduced graphene oxide has been considerably increased (Luo *et al*., 2012; Ye *et al*., 2005).

The main reason for increasing the charge transfer in CV-Cu_xO-rGO as compared with CV-rGO-CuNPs-2 is that Cu_xO is a p-type semiconductor which has poor conductivity (Yuan *et al*., 2013; Meng *et al.,* 2013).

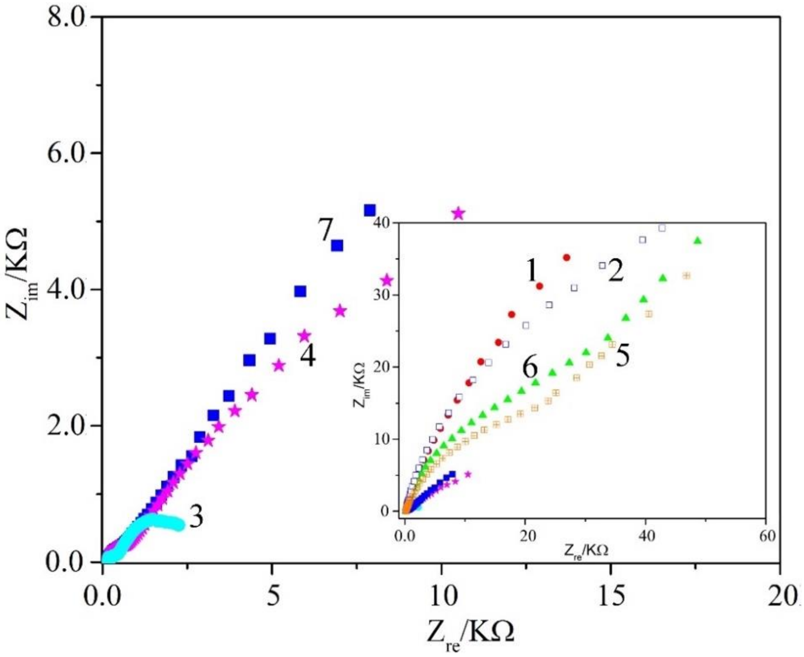

Figure 4.15: Nyquist plots of (1) CV-rGO-CuNPs-1, (2) AMP-rGO-CuNPs-1, (3) CV-rGO-CuNPs-2, (4) AMP-rGO-CuNPs-2, (5) CV-rGO-CuNPs-3, (6) AMP-rGO-CuNPs-3 and (7) CV-rGO-Cu_xO-2.

Table 4.4: EIS parameters achieved by equivalent circuits modified electrodes in 0.1 M KCl solution containing 1 mM $Fe(CN)_6^{3-/4-}$ (1:1).

Electrode	R_s (Ω)	R_{ct1} (Ω)	Q_1 (μMho)	W (μMho)	n_1	R_{ct2} (Ω)	Q_2 (μMho)	n_2
CV-rGO-CuNPs-1	175	83762	6.95	11.9	0.82	-	-	-
AMP-rGO-CuNPs-1	167	77432	5.42	10.4	0.85	-	-	-
CV-rGO-CuNPs-2	212	195	1.54	-	0.96	2228	135	0.62
AMP-rGO-CuNPs-2	182	443	0.615	-	0.93	12468	110	0.52
CV-rGO-Cu_xO-2	166	24771	3.45	24.1	0.76	-	-	-
CV-rGO-CuNPs-3	170	36005	2.26	18.2	0.83	-	-	-
AMP-rGO-CuNPs-3	170	48708	6.73	10.5	0.83	-	-	-

4.2.7. Sensor optimization

To investigate the performance of the H_2O_2 sensor, various factors influencing the current response of the sensor were investigated. Figure 4.16 shows the influence of operating potential on the amperometric response of the CV-rGO-CuNPs-2 and the reduction current studied under batch conditions ranging from −0.1 to −0.3 V *vs*. SCE in a solution containing 1 mM H_2O_2 in 0.1 M phosphate buffer solution (pH 6.5).

As can be seen in Figure 4.16(a)(inset), the potential value of −0.2 V was determined as the operating potential.

4.2.7.1. Amperometric detection of H_2O_2

Amperometric i–t curve is the regularly utilized technique to assess the electrocatalytic activities of electrochemical sensors.

Figure 4.16(a) displays the current response of CV-rGO-CuNPs-2 with successive addition of H_2O_2 into PBS at pH 6.5 under the applied potential of −0.2 V in the stirring condition (2000 rpm).

The response time was fast (less than 3 s) and as the concentration of H_2O_2 increases from 0.1 to 18 mM, the current increased linearly. In calibration curve (Figure 4.16(b)), the sensor shows linear section for the response to H_2O_2 with the linear regression equation of $I = 119.75\ (\mu A.mM^{-1}) + 134.47$ ($R^2 = 0.987$).

Based on the Eq. 4.3 and Eq. 4.4, the LOD and LOQ (S/N = 3) are calculated to be 0.601 and 2.00 µM, respectively.

As listed in Table 4.5, the detection limit and the linear range of CV-rGO-CuNPs-2 are better and wider than most of the other modified electrodes based on reduced graphene oxide and copper.

Table 4.5: Comparison between LOD and linear range of different non-enzymatic H_2O_2 sensors with CV-rGO-CuNPs-2.

Modified electrode	**Performance**		**Ref.**
	LOD ($\mu mol.L^{-1}$)	**Linear range** ($mmol.L^{-1}$)	
CuO@Cu_2O–NWs/PVA	0.35	3-10	(Chirizzi *et al*., 2016)
Cu/chitosan/CNTs	20	0.5–120	(Wang *et al*., 2008)
Cu@CuO/GCE	0.21	0.003–8	(Song *et al*., 2015)
CuSHNs/RGO/GCE	3.0	0.005–4.0	(Wang *et al*., 2015)
CuS|rGO	0.3	0.01-10	(Yang *et al*., 2014)
Cu_2O/Cu NCs	33.9	0.0004–10	(Luo *et al*., 2014)
Cu-MWCNTs	1	Up to 7.5	(Yang *et al*., 2010)
Cu/Psi-CPE	0.27	0.0005-3.78	(Ensafi *et al*., 2014)
ERGO-Ag/GCE	1.6	0.1–100	(Moradi *et al*., 2013)
Go/MnO_2	0.8	5-600 µM	(Li *et al*., 2010)
CV-rGO-CuNPs-2	0.601	0.1-18	This work

4.2.7.2. Repeatability, reproducibility and stability

By measuring the current response towards hydrogen peroxide after three weeks, the stability of the prepared electrode was studied and only 12% loss in the current signal was recorded (Figure 4.17), which indicates an acceptable stability of the sensor. The reproducibility was studied for five identically-made electrodes with a relative standard deviation (RSD) of 4.56%, which indicates the process reliability.

A set of five measurements for a single electrode were made upon the addition of 1 mM hydrogen peroxide in 0.1 M PBS with RSD of 3.54%, demonstrating excellent reproducibility. These results confirm that the CV-rGO-CuNPs-2 has an excellent reproducibility and acceptable stability which make it suitable for practical use.

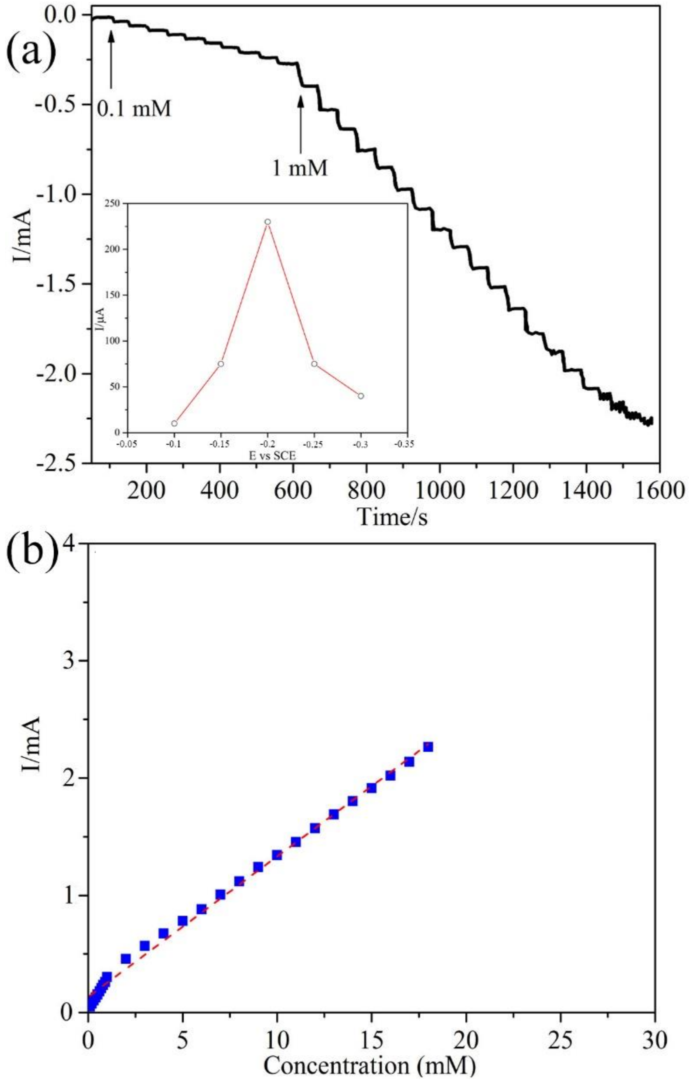

Figure 4.16: (a) Current–time responses of CV-rGO-CuNPs-2 with successive increasing H_2O_2 concentration at -0.2 V *vs*. SCE and (b) Dependence of the current response *vs*. H_2O_2 concentration.

4.2.7.3. Interference study

The effect of electroactive interfering species on modified electrode was evaluated. Figure 4.17(inset) shows the amperometric response of the CV-rGO-CuNPs-2 towards the successive addition of 1 mM H_2O_2 and this is followed by glucose, ascorbic acid, fructose, uric acid and lactose into 0.1 M PBS at pH 6.5. As can be seen, the current response of the mentioned electroactive interfering species is quite negligible, which confirms that CV-rGO-CuNPs-2 has a superior selectivity towards H_2O_2.

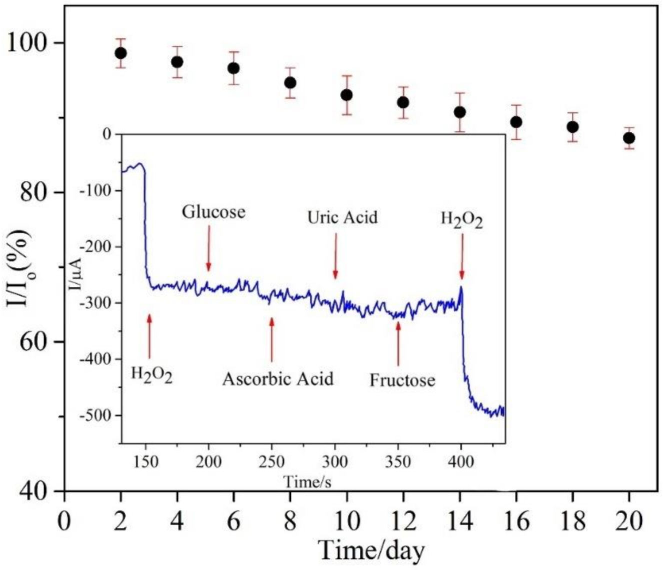

Figure 4.17: Stability of the sensor stored at 4 °C over 3 weeks in PBS with addition of 1 mM H_2O_2 at -0.2 V *vs*. SCE and the inset shows amperometric response of CV-rGO-CuNPs-2 upon the successive addition of 1 mM H_2O_2, glucose, ascorbic acid, fructose and uric acid into 0.1 M PBS (pH 7.2) with an applied potential -0.2 V.

To prove the accuracy of the sensor, a lens-cleaning solution was used for performing the detection of H_2O_2. The H_2O_2 determination in the samples of the mentioned solution was carried out on the modified sensor employing standard addition method. The dilution of the samples has been done through using phosphate buffer solution (pH 6.5) prior to determining the current response. Later, H_2O_2 solutions were successively added to the system in order to determine the current response through standard addition method. All the measurements were carried out four times. Table 4.6 lists the average recoveries.

According to Table 4.6 and considering the relative standard deviation (RSD) values and calculated recovery, it can be observed that the developed sensor holds possible applications for evaluating specific concentration range of H_2O_2.

Table 4.6: H_2O_2 determination in real samples by using CV-rGO-CuNPs-2.

Sample	Added (mM)	RSD%	Measured by sensor (mM)	Recovery%
1	0.1	0.810	0.097	97.45
2	1	1.655	0.964	96.48
3	5	6.296	5.129	102.58
4	10	1.890	9.605	96.05
5	50	1.517	48.628	97.25

In order to study the performance of CV-rGO-CuNPs-2 electrode towards glucose cyclic voltametry was carried out. As shown in Figure 4.18, the prepared nanocomposite did not show significant performance at the presence of glucose, indicating that in this potential window, CV-rGO-CuNPs-2 nanocomposite cannot be used as a sensor for GLC detection. The residual oxygen-containing groups remained at the surface of rGO are responsible for the small redox peaks around -0.6 V which are neglectable.

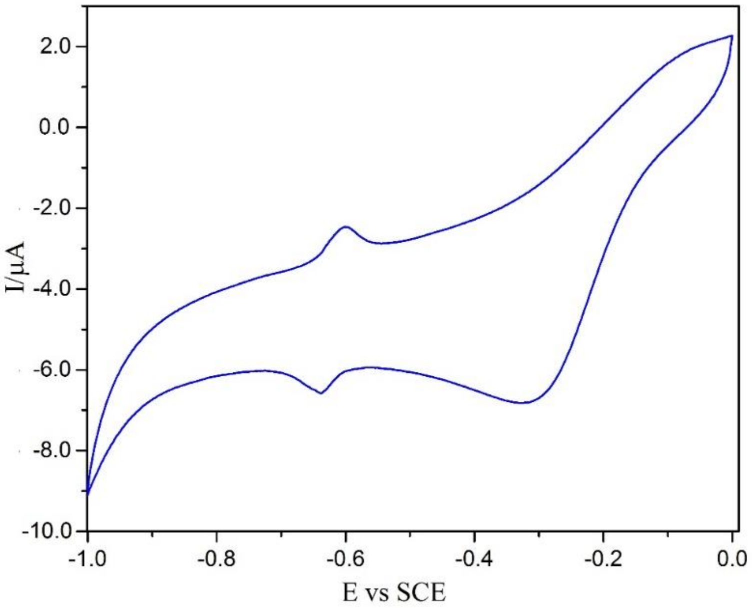

Figure 4.18: CV of CV-rGO-CuNPs-2 electrode in a 0.1 M phosphate buffer solution (pH 7.2) and 1 mM glucose, scanned at 50 mVs^{-1} scan rate.

4.3. rGO/PpyNFs/Cu$_x$O composite

4.3.1. Electrodeposition of rGO, PpyNFs and Cu$_x$O

Figure 4.19(a) shows the first cycle among the four cycles of the electrochemical deposition of rGO layer. As can be seen and also mentioned in the previous studies (Zhang *et al.*, 2013; Zhou *et al.*, 2009), one anodic and two cathodic peaks can be recognized. The electrochemical reduction of GO which is reversible is responsible for the cathodic current peak III. In contrast, the oxidation reduction pair of some electrochemically active oxygen-containing groups on graphene planes is responsible for anodic peak I and cathodic peak II.

These active oxygen-containing groups cannot be eliminated by cyclic voltammetry method from the graphene sheets (Chen *et al.*, 2011; Liu *et al.*, 2011). The FESEM image (Figure 4.19(b)) confirms the formation of rGO film on GCE. The image of FESEM displays that the surface of GCE electrode with modified rGO is wrinkled and rough due to the formation of rGO. This can be justified as in the course of electrodeposition, when the electrode potential decreased to negative, GO was electrochemically reduced to form rGO which is extremely hydrophobic (Takahashi *et al.*, 2013).

The electropolymerization of Ppy nanofibers (PpyNFs) has been performed with two methods with the same materials. Figure 4.19(c) shows the first four successive cyclic voltammograms of the rGO on glassy carbon electrode. The process of monomer oxidation starts as the potential increases to 0.65 V *vs*. SCE, in the anodic scan of the first cycle on the surface of rGO with mixed electrolyte is composed of 0.1 M phosphate buffer solution, 0.1 M pyrrole monomers and 0.1 M $LiClO_4$ at the scan rate of 1 mVs^{-1}.

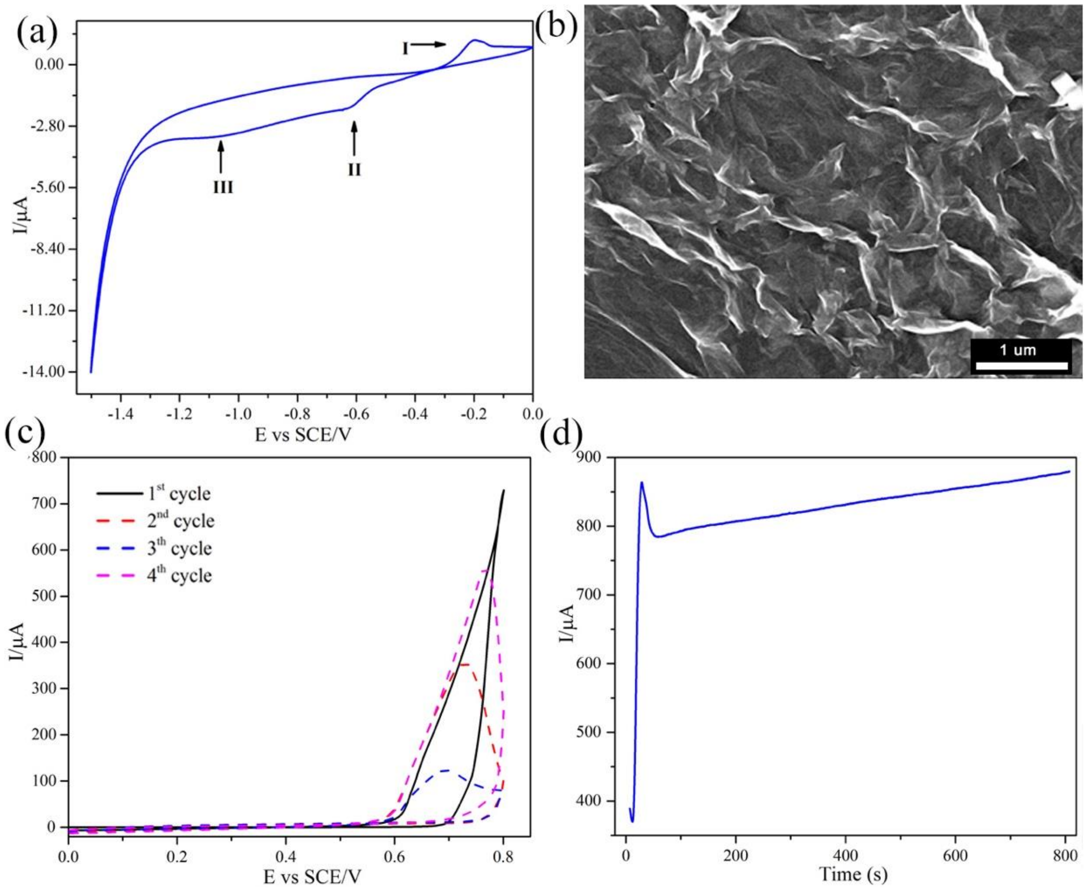

Figure 4.19: (a) Electrodeposition of rGO on GCE in an aqueous solution of 0.7 mg.L^{-1} GO and a 0.1 M phosphate buffer solution at the scan rate of 1 mV s^{-1}. (b) FESEM of rGO/GCE (c) CVs of CV-PpyNFs electropolymerization on the surface of rGO and (d) amperometry electropolymerization of PpyNFs on the surface of rGO/GCE from an aqueous solution containing 0.1 M pyrrole, 0.1 M phosphate buffer solution and 0.1 M $LiClO_4$ constant potential of 0.8 V for 800 s.

The faster scan rate will lead to a shorter reaction time for each scan cycle and thus the increment of the film’s radius in a faster scan cycle is less than that of a slower scan cycle (Li *et al*., 2013). Figure 4.19(d) shows the electropolymerization process with amperometry method. As can be seen, as electropolymerization process starts, a noticeable increase in the current is observed suggesting that a conductive polypyrrole has been formed and after around 50 s, the current reaches the steady state condition.

4.3.2. Fourier Transform Infrared Spectroscopy (FTIR)

The FTIR spectrum of the GO, rGO, AMP-PpyNFs and AMP-rGO/PpyNFs are shown in Figure 4.20. For GO, the broad peak centered at 3363 cm^{-1} is assigned to the O-H stretching vibrations while the peaks at 1740, 1630 and 1431 are attributed to C=O stretching, *sp*^{2}-hybridized C=C group and O-H bending, C-OH stretching (Basirun *et al*., 2013).

In addition, the peak at 1050 cm^{-1} can be attributed to C-O vibration of epoxy or alkoxy groups. The peaks at 3299 and 3295 cm^{-1} in the AMP-PpyNFs and AMP-rGO/PpyNFs spectra (Figure 4.20(c, d)) are attributed to N–H stretching vibrations of the pyrrole ring. The peak at 3361 cm^{-1} in the rGO spectra is related to O–H groups and the bands at 1753 and 1477 cm^{-1} are related to C-O and C-OH, respectively (Figure 4.20(b)). The peaks at 1260 and 1067 cm^{-1} in the rGO spectrum are recognized as the C-O stretching vibration of the epoxy and alkoxy groups, respectively (Mahmoudian *et al.*, 2012).

The peaks at 2938 and 2860 cm^{-1} in the rGO spectrum are related to the CH_2 asymmetric and symmetric stretching vibrations, respectively. The peaks at 1703 and 1653 cm^{-1} are related to C-N-C bond in the AMP-PpyNFs and AMP-rGO/PpyNFs spectra in Figure 4.20(c, d), respectively.

The bands at 1570 and 1510 cm^{-1} are related to the C–C and C–N in the AMP-PpyNFs and AMP-rGO/PpyNFs spectra, respectively (Sahoo *et al*., 2012). The peaks at 1471 and 1421 cm^{-1} are recognized as typical Ppy ring vibrations (Figure 4.20(c, d)), respectively. The aliphatic C-H peaks (at 2866 and 2930 cm^{-1} in the AMP-rGO-PpyNFs spectrum) and the peaks representing the C-O stretching vibration of the epoxy (at 1270 and 1052 cm^{-1}) and alkoxy groups (at 1268 and 1063 cm^{-1}) in AMP-rGO/PpyNFs spectra, respectively, confirm the existence of rGO.

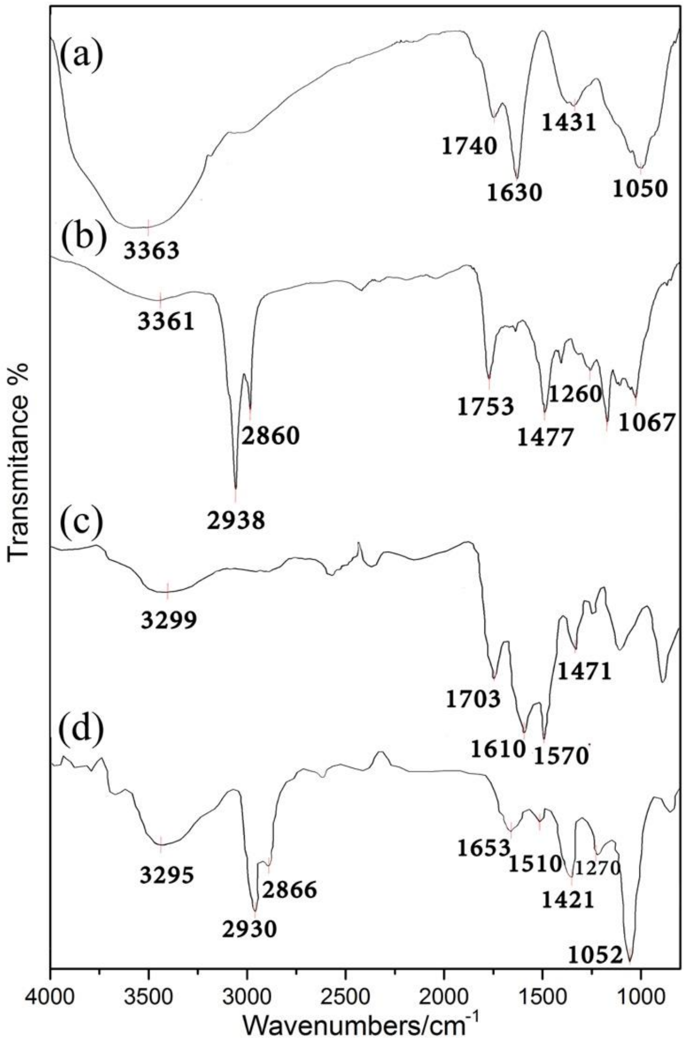

Figure 4.20: FTIR spectra for (a) GO, (b) rGO, (c) AMP-PpyNFs and (d) AMP-rGO/PpyNFs

4.3.3. Energy-dispersive X-ray spectroscopy (EDX)

EDX analysis was employed to prove the elemental composition at various stages. Figure 4.21 displays the EDX spectra of AMP-rGO/PpyNFs and AMP-rGO/PpyNFs/Cu$_x$O. Elemental Cu is detected in AMP-rGO/PpyNFs/Cu$_x$O, although it is not present in the unmodified AMP-rGO/PpyNFs. This supports the point that Cu was able to be successfully deposited onto Ppy nanofibers.

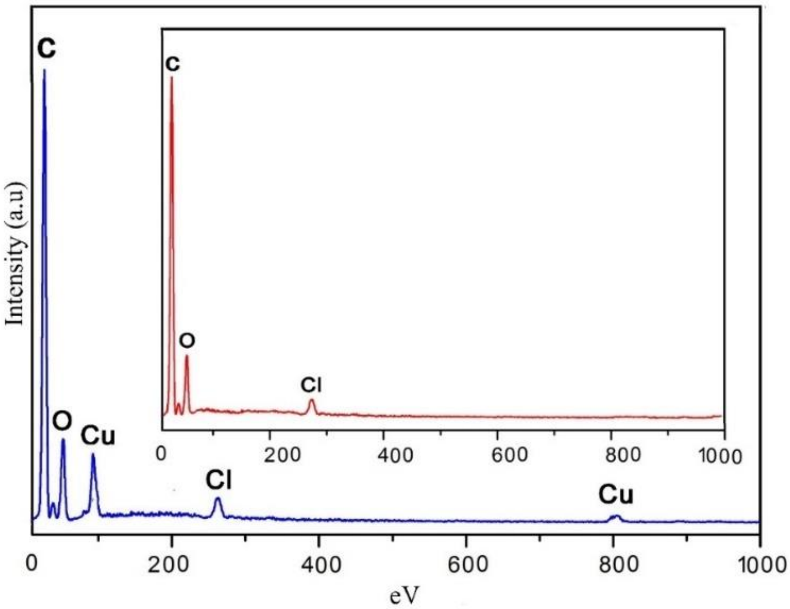

Figure 4.21: EDX spectra of AMP-rGO/PpyNFs and AMP-rGO/PpyNFs/Cu_xO.

4.3.4. X-ray Diffraction (XRD)

XRD analysis was employed to affirm the composition of CuxO electrodeposited on the surface of Ppy nanofibers. Figure 4.22 presents the XRD patterns of the AMP-rGO/PpyNFs/CuxO.

The diffraction peaks which have been obtained for AMP-rGO/PpyNFs/Cu_xO are in the same manner with the preceding recorded standards (Sun *et al.*, 2015; Cherevko & Chung, 2010). No peak has been observed for Cu which shows that the Cu deposited on Ppy was fully changed into CuO and Cu_2O composite (Cao & Gong, 2012).

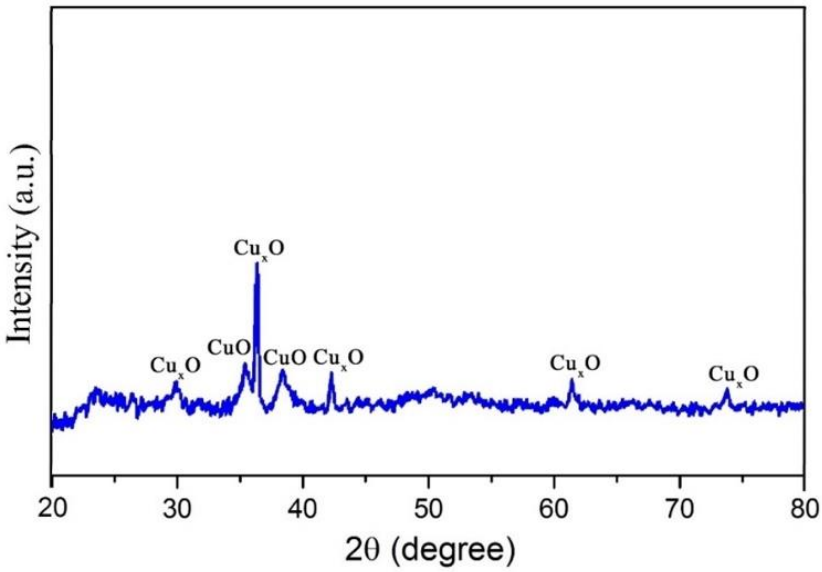

Figure 4.22: XRD spectrum of AMP-rGO/PpyNFs/Cu$_x$O.

4.3.5. Raman spectra

Raman spectra is generally employed to characterize graphene samples. Figure 4.23(a-d) displays Raman spectra of GO, rGO, AMP-PpyNFs and AMP-rGO/PpyNFs composite. For GO (Figure 4.23(a)) and rGO (Figure 2.23(b)), the Raman spectra hold the high intensity of G band at 1595 cm^{-1} and D band at 1342 cm^{-1}, caused by the in-plane optical vibration and first-order zone boundary phonons, respectively. Moreover, a 2D band at 2701 cm^{-1} is detected in the Raman spectra of rGO, which is matched with the second-order zone boundary phonons (Zhu *et al*., 2010). The broad peaks near 1341 cm^{-1} and 1591 cm^{-1} are similar to ring stretching mode of the polymer backbone and conjugated structure, respectively (Mikat *et al*., 2001). Although, in the Raman spectra of AMP-rGO/PpyNFs composite, the new peak can indexed at 2699 cm^{-1} which should be 2D peak of rGO in composite (Rao *et al*., 2009). The extensive 2D band in the Raman spectra of AMP-rGO/PpyNFs (Figure 4.23(d)) shows that rGO in composite may be a structure with various layers (Wang *et al*., 2012).

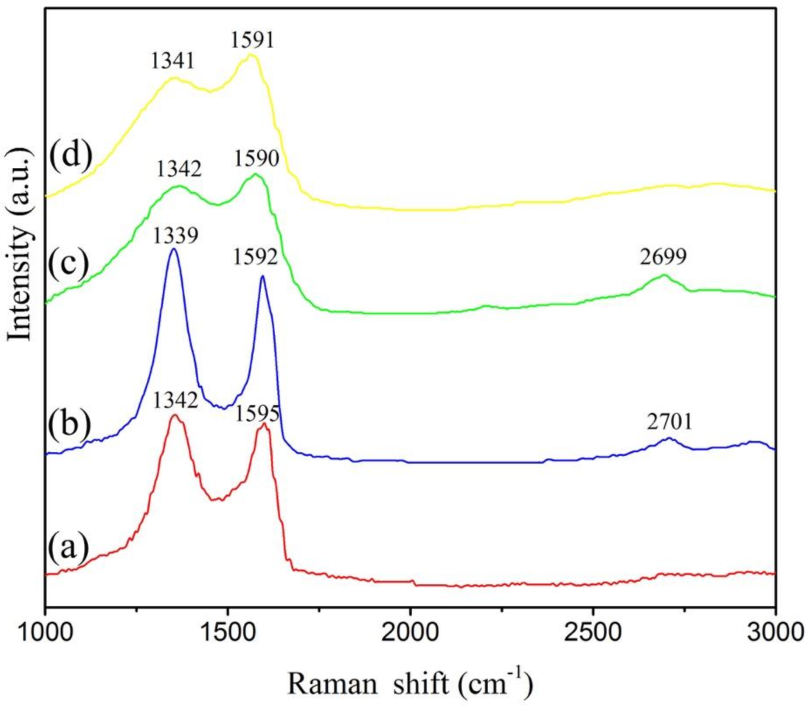

Figure 4.23: Raman spectra of (a) GO, (b) rGO, (c) AMP-PpyNFs and (d) AMP-rGO/PpyNFs.

4.3.6. Field Emission Scanning Electron Microscopy (FESEM)

As can be seen in FESEM Figure 4.24(a, b), the surface morphologies of the amperometry Ppy nanofibers matrix and cyclic voltammetry PpyNFs were characterized. Figure 4.24(b) presents clear and comparatively smooth amperometry Ppy nanofibers in diameter of ~100 nm, more stretched than cyclic voltammetry Ppy.

Figure 4.24(a) shows that a larger surface area can be detected in amperometry method. The amperometry Ppy nanofibers have a well-arranged polymer chain structure with greatly high ratio of surface-to-volume that is useful for the decorating by Cu_xO particles.

The FESEM of CV-PpyNFs (Figure 4.24(a)) indicates that as a result of the variation of applied potential, the film formation is not homogenous. Besides, the existence of non-homogeneous polypyrrole confirms that the conditions of polymerization highly influence the morphology of the film (Li *et al.,* 2013).

The reason for homogeneity of AMP-PpyNFs is not similar to CV method. In CV method monomers meet a wider potential range which are not necessarily the oxidation potential of the monomer oxidation, then polymers with various lengths are made and apparently, they are not uniformed, whereas in amperometry method, monomers are exposed to oxidation potential at a very short time.

The morphologies of the AMP-rGO/PpyNFs/Cu_xO composites with various concentrations of Cu nanoparticles are displayed in Figure 4.24(c, d, e, and f). It can be seen that 10 mM concentration of Cu is the best compared with the others in which Cu_xO particles are uniformly attached on the surface of Ppy nanofibers. These morphological features provide several beneficial properties, such as, active sites that are more available, high catalysis properties and large surface area of AMP-rGO/PpyNFs/Cu_xO for hydrogen peroxide reduction.

The FESEM also confirms that the agglomeration of CuxO took place among with the increasing of Cu nanoparticle. It should be mentioned that different scales were used to show how much agglomeration occurred in each concentration. As can be seen in Figure 4.24(b), the diameter of each fiber is almost 100 nm. Figure 4.24(c) is also in the same scale and shows that the copper oxide particles uniformly covered each Ppy nanofiber.

With increasing concentration (Fig. 4-24(d, e)), wider scales were chosen in order to show that the agglomerated particles were becoming bigger compared with Ppy nanofibers. In Figure 4.24(f), all the copper oxide particles completely covered the surface so that there is no Ppy nanofiber to be distinguished.

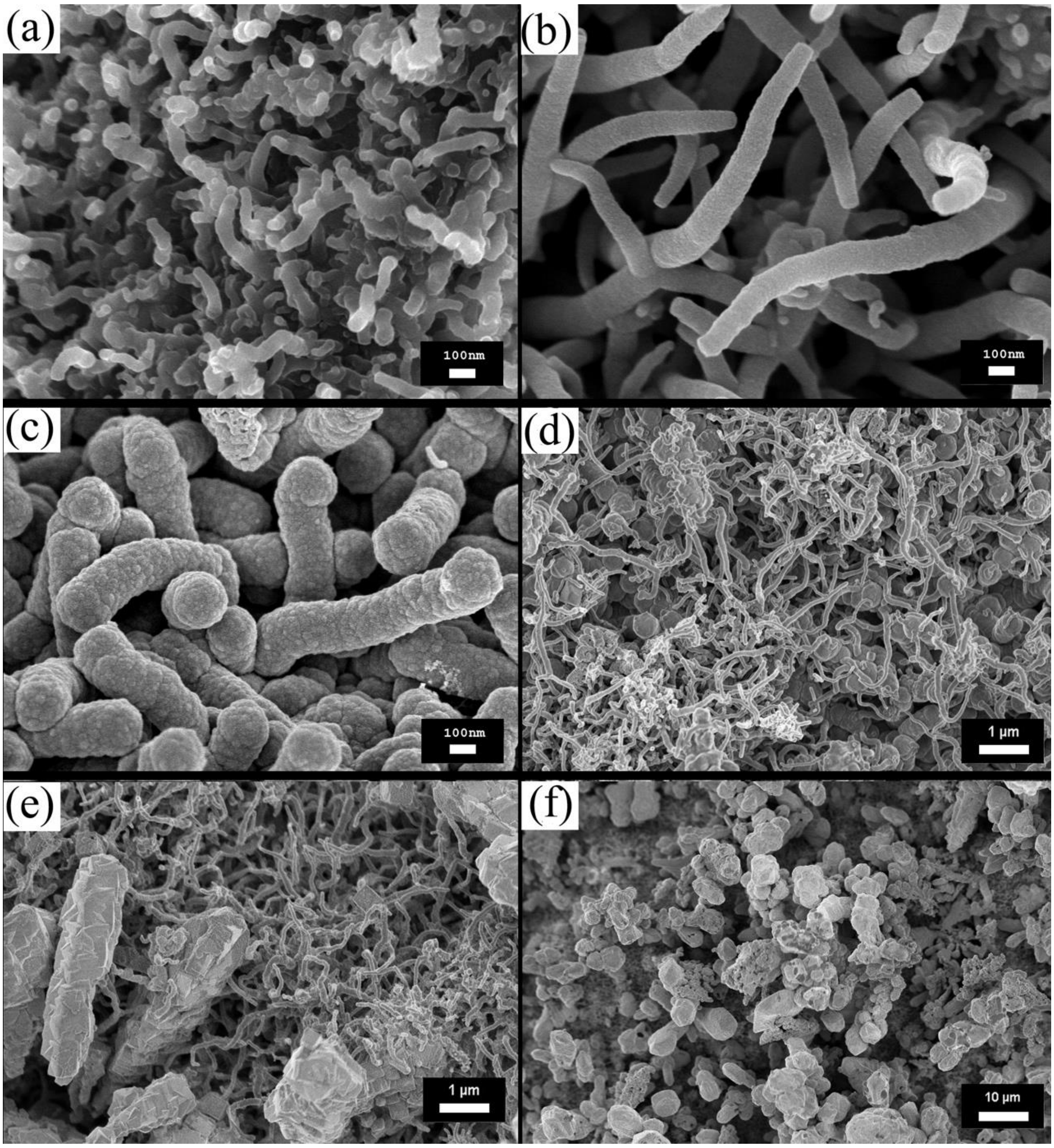

Figure 4.24: FESEM of (a) CV-rGO/PpyNFs, (b) AMP-rGO/PpyNFs, (c) AMP-rGO/PpyNFs/Cu_xO (10 mM), (d) AMP-rGO/PpyNFs/Cu_xO (30 mM), (e) AMP-rGO/PpyNFs/Cu_xO (60 mM) and (f) AMP-rGO/PpyNFs/Cu_xO (90 mM).

4.3.7. Electrochemical Impedance Spectroscopy (EIS)

In order to analyze the impedance changes of the modified electrode, electrochemical impedance spectroscopy was employed. Figure 4.25(a) depicts the Nyquist plots in 0.1 M KCl solution containing 1 mM $Fe[(CN)_6]^{3-/4-}$ (1:1). The Nyquist plot of impedance spectra consists of semicircle portion which at higher frequencies correlates to the electron transfer limited process while on the other hands, a linear portion at lower frequencies correlates to the diffusion process.

The electron transfer resistance (R_{ct}), by using the diameter of the semicircle diameter can be evaluated. The results confirmed that the alteration of GCE by reduced graphene oxide makes the resistance of charge transfer extremely reduced which can be interpreted due to the fact that the rGO layer protects various small band gaps which are agreeable for the electron conduction (Stankovich *et al.*, 2006). Moreover, the comparison between the semicircle diameters from the Nyquist diagrams of AMP-rGO/PpyNFs/Cu_xO (1529 Ω), AMP-rGO/PpyNFs (429 Ω), CV-rGO/PpyNFs (2341 Ω) and rGO (19781 Ω) shows the direction of R_{ct}:

(R_{ct}): GCE> rGO> CV-rGO/PpyNFs> AMP-rGO/PpyNFs-Cu_xO > AMP-rGO/PpyNFs

The main reason for increasing the charge transfer in AMP-rGO/PpyNFs/Cu_xO compared with AMP-rGO/PpyNFs is that Cu_xO is a p-type semiconductor which has poor conductivity. In order to figure out the impedance parameters, the Nova 1.11 software is employed in the simulations.

By exploiting the series components, the model was developed. The first component is ohmic resistance of the solutions of the electrolyte R_s and the second one is a set of constant phase elements (CPE) and the resistance of layer which indicates the conductivity of the sample (R_{ct}) that are in the parallel position. In addition, from the diffusion impedance, W for the Warburg element is a series connection to R_{ct}.

The $R_s(CPE[R_{ct}W)])$ equivalent circuit model was employed in the simulation of the impedance behavior of all the modified electrodes, from the experimentally gained impedance data. Figure 4.25(b) shows the Bode plot that is in agreement with results obtained from Nyquist plot.

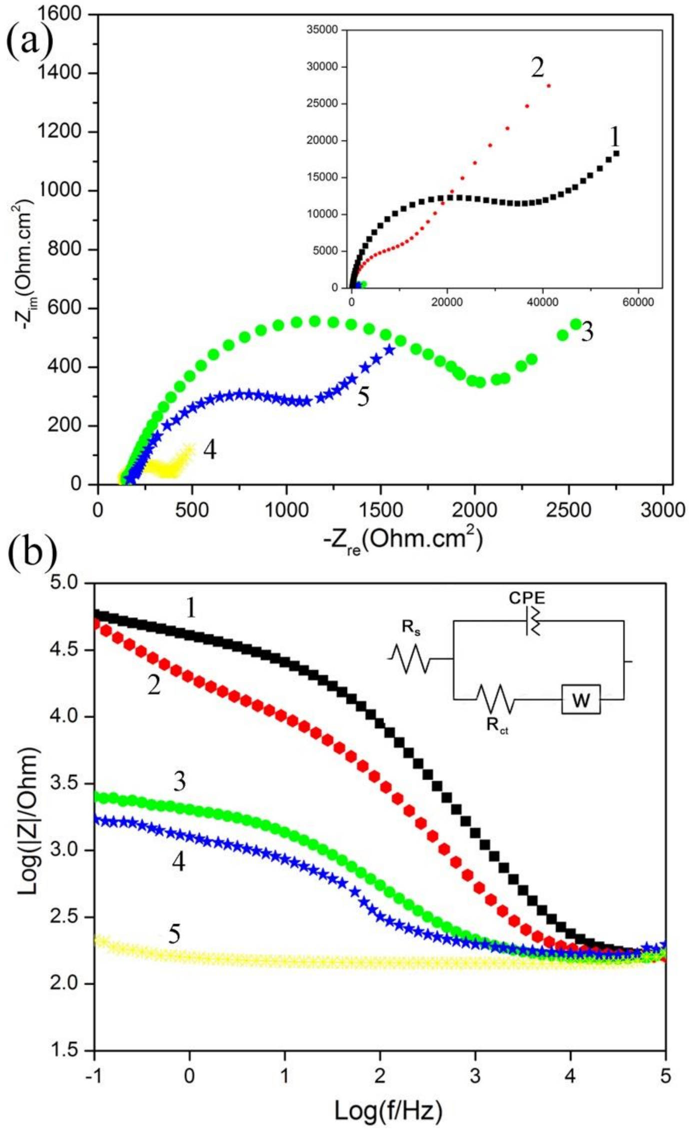

Figure 4.25: (a) Nyquist plots of (1) bare electrode, (2) rGO, (3) CV-rGO/PpyNFs, (4) AMP-rGO/PpyNFs and (5) AMP-rGO/PpyNFs/Cu_xO (10 mM) (b) Bode plots of (1) bare electrode, (2) rGO, (3) CV-rGO/PpyNFs, (4) AMP-rGO/PpyNFs and (5) AMP-rGO/PpyNFs/Cu_xO (10 mM).

4.3.8. Detection of H_2O_2

4.3.8.1. Cyclic voltammetry (CV)

In order to investigate the electrochemical performance of the prepared electrode towards H_2O_2, CV of all modified electrodes was carried out in a 0.1 M phosphate buffer solution (PBS) at pH 6.5 in the presence and absence of 1 mM H_2O_2. For the AMP-rGO/PpyNFs electrode (Figure 4.26), a wide and low current response were recorded under the presence of H_2O_2 at the selected potential range.

When Cu_xO are electrodeposited on the surface of PpyNFs, the modified electrodes show a remarkable electrocatalytic behavior toward H_2O_2 reduction. PpyNFs decorated with Cu_xO is different from individual Ppy, not only in the synergistic amplification effect between PpyNFs and Cu_xO but also in the electroreduction effect of Cu_xO toward hydrogen peroxide.

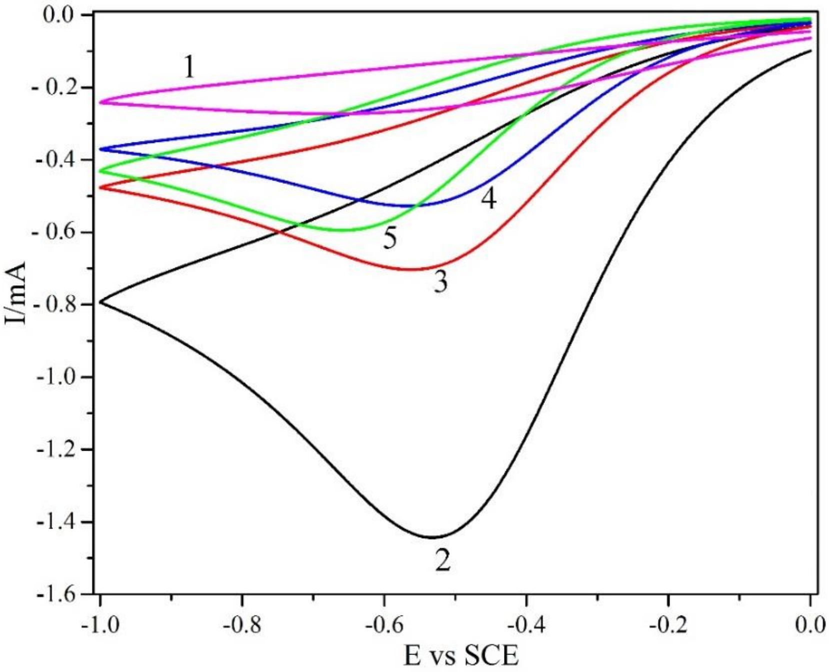

Figure 4.26: CVs of (1) AMP-rGO/PpyNFs, (2) AMP-rGO/PpyNFs/Cu_xO (10 mM), (3) AMP-rGO/PpyNFs/Cu_xO (30 mM), (4) AMP-rGO/PpyNFs/Cu_xO (60 mM) and (5) AMP-rGO/PpyNFs/Cu_xO in 0.1 M phosphate buffer solution (pH 6.5) and 1 mM H_2O_2, scanned at applied potential ranged from 0 to -1 V *vs*. SCE at 50 mVs^{-1} scan rate.

A highly increased reduction peak at AMP-rGO/PpyNFs/Cu_xO (10 mM) electrode in the presence of H_2O_2 revealed the synergistic effect of Cu_xO, rGO and polypyrrole which can greatly improve the electrocatalytic reduction of H_2O_2. With increasing the concentration of Cu_xO solution, the particle size increased and consequently the agglomeration takes place leads to the reduction of H_2O_2.

4.3.8.2. Sensor optimization

In order to find the best potential, the relationship between the reduction current of H_2O_2 and the applied potential was measured. To find proper potential for amperometric response, the applied potential of the AMP-rGO/PpyNFs/Cu_xO was evaluated over the range of -0.4 to -0.6 V *vs*. SCE. Finally, -0.5 V was selected as the optimized potential.

Figure 4.27(a) indicates the amperometric responses at -0.5 V of AMP-rGO/PpyNFs/Cu_xO electrode with subsequently adding in H_2O_2 concentration from 0.1 to 100 mM. The comparable calibration curve is shown in Figure 4.27(a) (inset). The relationship between the current and the concentration which is linear, is settled in the concentration range from 0.1 to 100 mM.

The linear part increases from 0.1 mM to 100 mM with a linear regression equation of $I = 141.5\ (\mu AmM^{-1}) + 99.94$ ($R^2 = 0.996$). By employing Eq. 4.3 and Eq. 4.4, the LOD and LOQ (S/N of 3) are estimated to be 0.036 μM and 0.12 μM for the linear part, respectively.

4.3.8.3. Stability, reproducibility and repeatability

The studied sensor shows a good stability, with a loss of only 12.1% in current response after two weeks at 4°C (Figure 4.27(b)). By measuring the response to 1 mM H_2O_2 over one month, the long term stability of sensor was studied.

The sensor was kept in the atmosphere and for 10 first days, it was tested every day and the next 20 days, every five days, measurement was taken.

The results indicate that the response was relatively the same over the entire examination days, suggesting that the sensor can be used in long term applications.

It should be added that for five electrodes which have been made identically with a relative standard deviation (RSD) of 3.54% the reproducibility was explored, while 10 measurements for the same electrode were carried out by adding 1 mM H_2O_2 with RSD of 4.6%, showing high repeatability.

4.3.8.4. Interference study

Successive addition of 1 mM H_2O_2, fructose, ascorbic acid, uric acid and lactose into 0.1 M phosphate buffer solution (pH 6.5) was used for AMP-rGO/PpyNFs/Cu_xO in order to study the effect of common interfering species (Figure 4.27(b) (inset)).

As can be seen, the current of these interfering species does not reveal an obvious additional signal which indicates that this modified electrode has a good selectivity towards H_2O_2.

There is a comparison between the performance of the AMP-rGO/PpyNFs/Cu_xO and those of previously reported non-enzymatic H_2O_2 sensors based on Cu_xO, Ppy and rGO in Table 4.7.

The linear range of prepared sensor (0.1–100 mM) is considerably greater than that of other Cu_xO, Ppy and rGO, making AMP-rGO/PpyNFs/Cu_xO high potential for industrialization.

The high sensitive catalytic performance, the wide linear range and low detection limit can be attributed to the nature of Cu_xO based on Ppy nanofibers and the existing rGO as a substrate for upper layer which increase the conductivity of the system. Comparing the Cu_xO modified electrode and CuO/Cu_2O-modified electrode, it was found that due to the synergic effect of CuO and Cu_2O (Cu_xO), the latter has a wider linear detection range towards electrocatalytic oxidation of GLC (Huang *et al*., 2010).

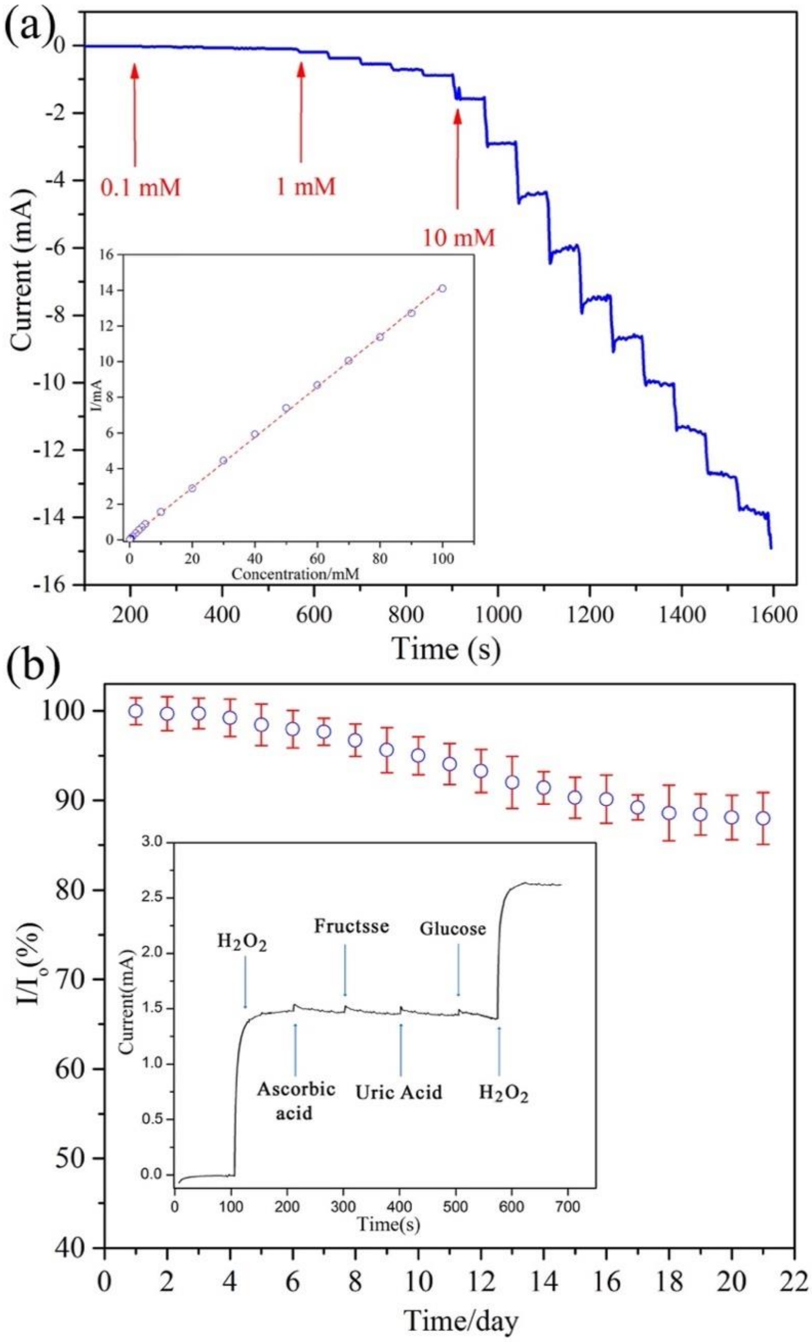

Figure 4.27: (a) Current–time responses of AMP-rGO/PpyNFs/Cu_xO with the subsequent addition of H_2O_2 into 0.1 M PBS (pH 6.5) at -0.5 V and (Inset) calibration curve in the range of 0.1-100 mM, (b) Long term stability of the AMP-rGO/PpyNFs/Cu_xO studied in three weeks, and (inset) shows amperometric response of AMP-rGO/PpyNFs/Cu_xO upon the successive addition of 1 mM uric acid, glucose, ascorbic acid and fructose into 0.1 M PBS (pH 6.5) with an appliedpotential -0.5 V.

Table 4.7: Comparison between LOD and linear range of different non-enzymatic H_2O_2 sensors with AMP-rGO/PpyNFs/Cu_xO.

Modified electrode	**Performance** **LOD** (µmol.L^{-1})	 **Linear range** (mmol.L^{-1})	**Ref.**
CuO/OPpy/MWCNTs/CCE	0.05	Up to 2	(Yu *et al*., 2015)
Sandwich-structured CuO	~1	Up to 3.2	(Meher & Rao, 2013)
Cu_xO/Ppy/Au	6.2	Up to 8.0	(Meng *et al*., 2013)
Porous Cu–NiO	0.5	0.5-5	(Zhang *et al*., 2011)
NA/NiONF-rGO/GCE	0.77	0.002-0.6	(Zhang *et al*., 2012)
Cu_2O/NiO_x/GO/GC	0.4	0.87–2.95	(Yuan *et al*., 2013)
Porous CuO	0.14	0.001-2.5	(Cherevko *et al*., 2010)
AMP-rGO/PpyNFs/Cu_xO	0.03	0.1-100	This work

Furthermore, Cu_xO particles can finely cover the Ppy nanofibers and the Cu_xO can highly raise the electrocatalytic active areas and enhance electron transfer. Additionally, the Ppy nanofibers can provide larger surface area for H_2O_2 molecules to be detected, adequately enhanced electrons.

To prove the accuracy of the sensor, a lens-cleaning solution was used for performing the detection of H_2O_2. The H_2O_2 determination in the samples of the mentioned solution was carried out on the modified sensor employing standard addition method. The dilution of samples has been done through using phosphate buffer solution (pH 6.5) prior to determining the current response. Later, H_2O_2 solutions were successively added to the system in order to determine the current response through standard addition method.

All the measurements were carried out four times. Table 4.8 lists the average recoveries. According to Table 4.8 and considering the relative standard deviation (RSD) values and calculated recovery, it can be observed that the developed sensor holds possible applications for evaluating specific concentration range of H_2O_2.

Table 4.8: Determination of H_2O_2 in real samples of AMP-rGO/PpyNFs/Cu_xO.

Sample	Added (mM)	RSD%	Measured by sensor (mM)	Recovery%
1	0.1	1.079	0.098	98.45
2	0.5	3.199	0.504	100.91
3	1	6.165	1.010	101.04
4	5	3.677	4.986	99.72
5	50	0.748	49.468	98.93

AMP-rGO/PpyNFs/Cu_xO electrode is found to have the lowest LOD and LOQ as compared to other composites. Therefore, in order to further investigate the sensing performance of AMP-rGO/PpyNFs/Cu_xO electrode, the behavior towards glucose was also studied.

4.3.9. Detection of glucose (GLC)

4.3.9.1. Cyclic voltammetry (CV)

Figure 4.28(a) displays the cyclic voltammetry of the bare GCE (inset), rGO (inset), AMP-rGO/PpyNFs, CV-rGO/PpyNFs, in a 0.1 M phosphate buffer solution (pH 7.2) and 1 mM concentration of GLC. Compared to the bare GCE, the rGO indicates a rise in the anodic and cathodic current.

Mahmoudian and his co-workers presented that the presence of rGO increases the conductivity of the system (Mahmoudian *et al.*, 2012). The CVs of CV-rGO/PpyNFs and

AMP-PpyNFs reveal a redox couple in the anodic and also cathodic scans. The doping/dedoping process of Ppy nanofibers is responsible for the peaks. When a positive potential is employed, the counter ions are occupied (doping) and later the anions make the positive charges of Ppy nanofibers balanced. In contrary, when a sufficient negative potential is used for the polymer, the counter ions are freed (de-doping). Figure 4.28(a) indicates the influence of the electropolymerization method on the electrocatalytic activity of the PpyNFs towards GLC oxidation. By comparing the CVs of CV-rGO/PpyNFs with AMP-rGO/PpyNFs, it will be approved that compared with CV method, synthesizing PpyNFs with amperometry shows much more sensitivity towards GLC. Figure 4.28(b) displays the CVs of different concentrations of Cu_xO on the surface of AMP-rGO/PpyNFs in a 0.1 M phosphate buffer solution (pH 7.2) and 1 mM GLC, scanned at applied potential ranged from 1 to -1 V at scan rate of 50 mVs^{-1}. As can be seen, 10 mM concentration of Cu is the best compared with the others. FESEM images (Figure 4.24) also confirmed the result.

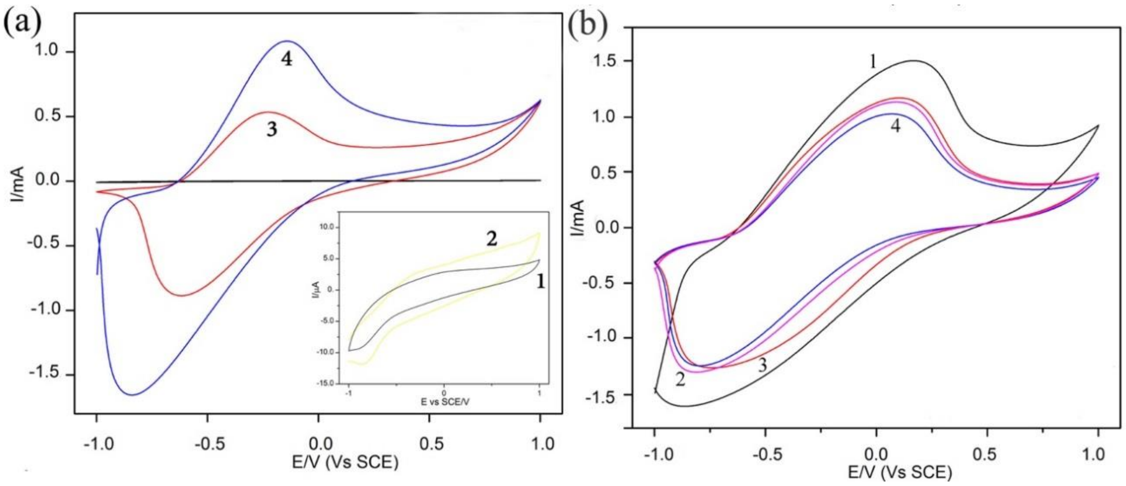

Figure 4.28: (a) CVs of (1) the bare GCE (inset), (2) rGO (inset), (3) CV-rGO/PpyNFs, (4) AMP-rGO/PpyNFs and (b) CVs of different concentrations of Cu_xO on the surface of AMP-rGO/PpyNFs in a 0.1 M phosphate buffer solution (pH 7.2) and 1 mM glucose, scanned at applied potential ranged from 1 to -1 V at 50 mVs^{-1} scan rate.

4.3.9.2. Sensor optimization

In order to find the best potential, the relationship between the oxidation current of glucose (GLC) and the applied potential was measured. To find proper potential for amperometric response, the applied potential of the AMP-rGO/PpyNFs/Cu$_x$O was evaluated over the range of -0.2 to 0.4 V *vs*. SCE. Finally, +0.2 V was selected as the optimized potential. Figure 4.29 indicates the amperometric responses at +0.2 V of AMP-rGO/PpyNFs/Cu$_x$O electrode with subsequently adding in GLC concentration from 0.1 to 100.0 mM. The comparable calibration curve is shown in Figure 4.29(inset). The relationship between the current and the concentration which is linear, is settled in the concentration range from 0.1 to 100 mM by a linear regression equation of I = 141.21 (µAmM^{-1}) + 114.32 (R^2=0.996). Limit of detection (LOD) and the limit of quantification (LOQ) of AMP-rGO/PpyNFs/Cu$_x$O were calculated based on Eq. 4.3 and Eq. 4.4. The LOD and LOQ (S/N of 3) are estimated to be 0.03 µM and 0.11 µM for the linear part, respectively.

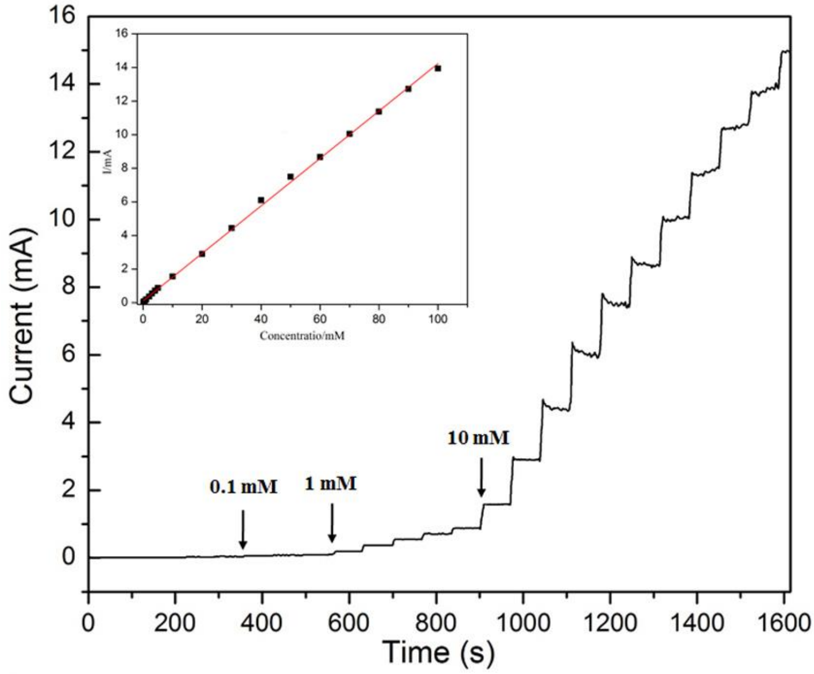

Figure 4.29: Current–time responses of AMP-rGO/PpyNFs/Cu$_x$O with successive increasing GLC concentration at +0.2 V *vs*. SCE and the inset shows the dependence of the current response *vs*. GLC concentration.

4.3.9.3. Stability and interference study

The modified electrode presents an excellent stability, with a loss of only 13.2% in current response after two weeks at 4°C (Figure 4.30). Successive addition of 1 mM GLC, fructose, ascorbic acid, uric acid and lactose into 0.1 M phosphate buffer solution (pH 7.2) was used for AMP-rGO/PpyNFs/Cu_xO in order to study the effect of common interfering species (Figure 4.30(inset)).

As can be seen, the current of these interfering species does not reveal an obvious additional signal which indicates that this modified electrode has a good selectivity towards GLC.

The linear range of the sensor (0.1 –100 mM) is considerably greater than that of other Cu_xO, Ppy and rGO, making AMP-rGO/PpyNFs/Cu_xO high potential for industrialization. The wide linear range, low detection limit and the high sensitive catalytic performance can be attributed to the nanocomposite nature of Cu_xO based on Ppy nanofibers and moreover the existing rGO as a substrate for upper layer which increase the conductivity of the system.

Compared with CuO or Cu_2O-modified electrode, the Cu_xO (CuO and Cu_2O composite)-modified electrode has a wider linear detection range towards electrocatalytic oxidation of GLC due to the synergic effect of CuO and Cu_2O.

Furthermore, Cu_xO particles can finely cover the Ppy nanofibers and the Cu_xO can highly raise the electrocatalytic active areas and enhance electron transfer. Additionally, the Ppy nanofibers can provide larger surface area for GLC molecules to be detected, adequately enhanced electrons.

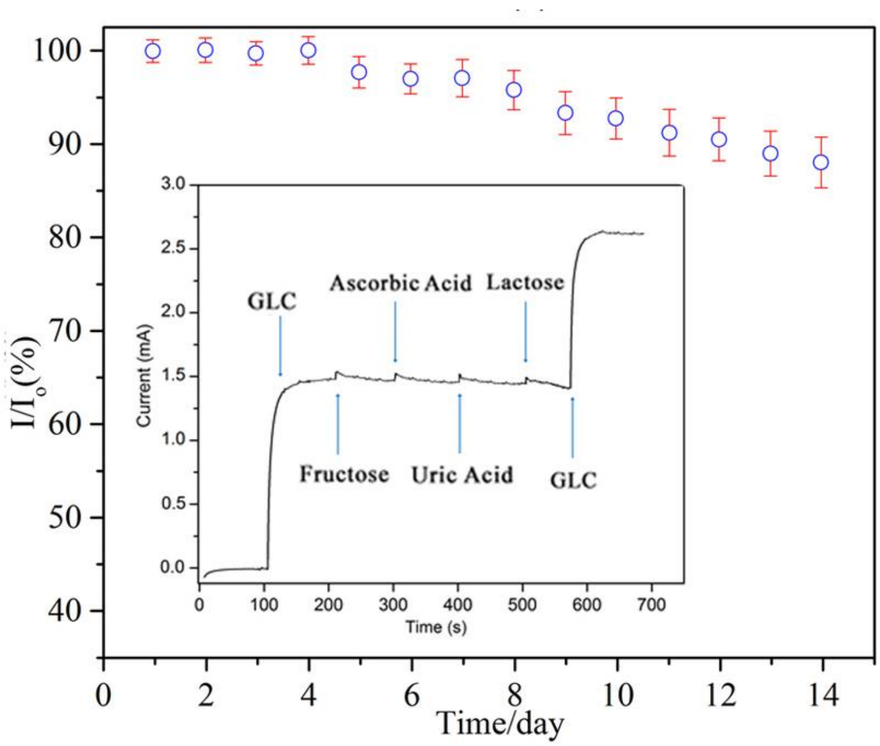

Figure 4.30: Stability of the sensor stored at 4°C over two weeks in PBS with addition of 1 mM GLC at +0.2 V *vs*. SCE and the inset shows amperometric response of AMP-rGO/PpyNFs/Cu_xO upon the successive addition of 1 mM GLC, ascorbic acid, fructose, uric acid and lactose into 0.1 M PBS (pH 7.2) with an applied potential +0.2 V *vs*. SCE.

In order to find out the accuracy of the sensor, the sensor was applied to real blood serum samples for determination of GLC.

By employing standard addition method, GLC in human blood was determined on the modified sensor. Before the current response measurement, the samples were diluted by using phosphate buffer solution (pH 7.2) and then GLC solutions were added one after another to the system. All the measurements were carried out five times and the results are listed in Table 4.9.

The calculated recovery and relative standard deviation (RSD) values from Table 4.9 show that the prepared sensor possesses potential applications in determining certain concentration range of GLC.

Table 4.9: Determination of GLC in real samples by using AMP-rGO/PpyNFs/Cu_xO.

Sample	Added (mM)	RSD%	Measured by sensor (mM)	Recovery%
1	0.1	0.872	0.098	98.25
2	0.5	1.239	0.459	97.92
3	1	0.995	0.983	98.63
4	5	0.968	4.936	98.72
5	50	1.036	49.408	98.81

4.4. rGO/Ppy/AgNPs composite

4.4.1. Field Emission Scanning Microscopy (FESEM)

rGO was prepared separately via electrodeposition method. The FESEM and TEM images of rGO are shown in Figure 4.31. The transparency of rGO is due to reduction of it by electrochemical way.

The image of FESEM displays that the surface of rGO is wrinkled and rough. This can be justified as in the course of electrodeposition, when the electrode potential decreased to negative, GO was electrochemically reduced to form rGO which is extremely hydrophobic (Takahashi *et al.*, 2013).

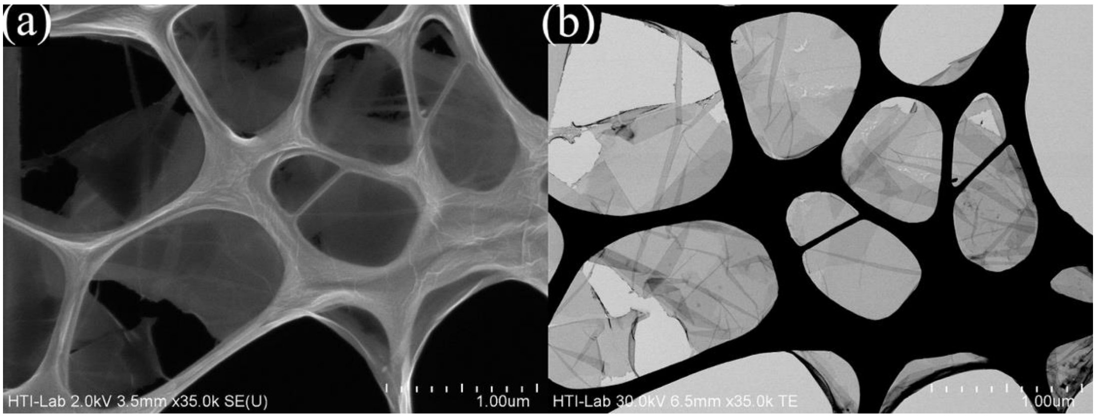

Figure 4.31: (a) FESEM image of rGO, (b) TEM image of rGO.

4.4.2. Atomic Force Microscopy (AFM)

AFM is needed to establish the thickness and surface roughness of single sheets. As shown in Figure 4.32(a), the AFM image of GO sheets gives the largest apparent height of ∼120 nm, indicating the multilayer structure. After being reduced, rGO has a much rougher surface, harvests more active sites, and shows lower film thickness ∼20 nm (Figure 4.32(b)). The decrease in the thickness is mainly due to the removal of functional group from the basal plane of graphene (Kudin, 2008; Tung *et al*., 2009).

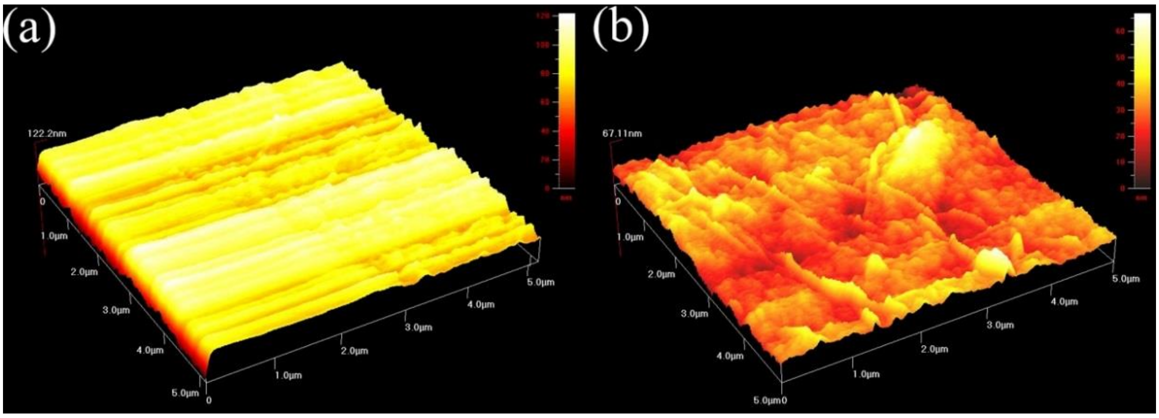

Figure 4.32: AFM of (a) GO and (b) rGO.

4.4.3. X-ray Diffraction (XRD)

Figure 4.33 shows the X-ray diffractions of rGO/Ppy/AgNPs deposited on GCE. As can be seen, a broad peak exists at 24–27°, due to the periodically aligned polypyrrole chains (Zha *et al*., 2013).

The intense peaks at 38.2°, 44.3°, 65.0° and 76.8° correspond to (111), (200) and (220) planes of cubic phase of silver, respectively (Moradi *et al*., 2013; Panigrahi & Srivastava, 2015). The diffractograms of Ppy/AgNPs composites presented the peaks due to the existence of Ppy and silver nanoparticles.

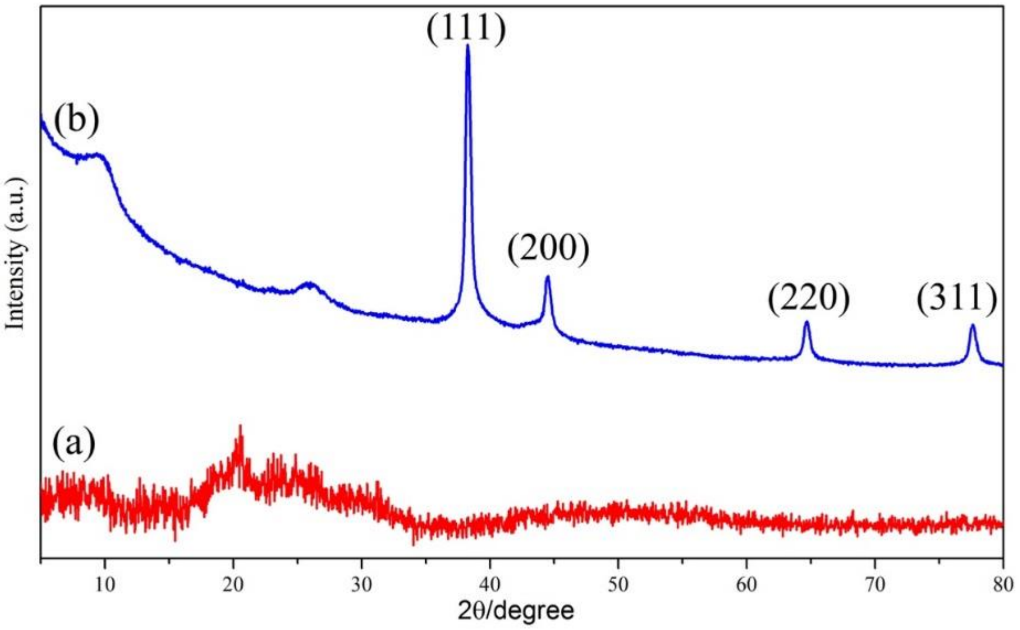

Figure 4.33: XRD spectra of (a) Ppy and (b) rGO/Ppy/AgNPs-1.

4.4.4. Cyclic voltammetry (CV)

rGO was electrodeposited on the surface of GCE with the same procedure which explained in the section 4.3.1. Three distinctive peaks were observed which confirmed the formation of rGO. Figure 4.34 shows the electrodeposition curve of pyrrole in the absence of any counterions.

As can be seen, by increasing the applied potential, there is no significant difference in current value which suggests that in the absence of counterion, electropolymerization cannot initiate.

Figure 4.35 shows the electropolymerization process via amperometry method with different counterions at applied potential ranging from 0.5 to 1 V *vs*. SCE for 800 s.

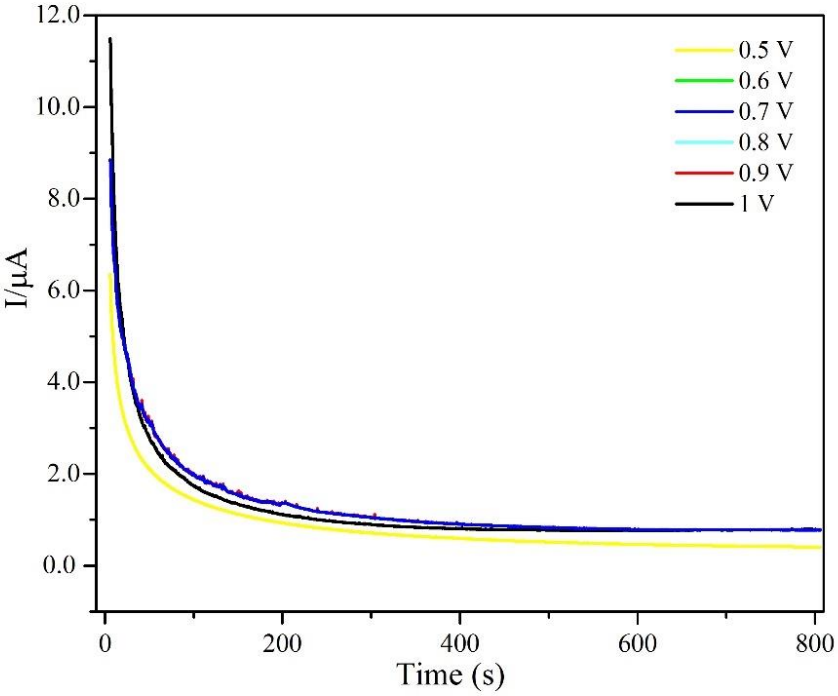

Figure 4.34: Amperometry electropolymerization of Ppy from an aqueous solution containing 0.1 M pyrrole, 0.1 M phosphate buffer solution at constant potential of 0.5 to 1 V for 800 s.

Under the presence of various dopants (Figure 4.35(a, c, e)), at lower constant potential (0.5 to 0.7 V), there is no increasing in the current which suggests that these potentials are not suitable for starting of polymerization.

On the other hand, as can be seen in Figure 4.35(b, d, f), in higher potentials (0.8 to 1 V), as electropolymerization process starts, a noticeable increase in the current is observed suggesting that a conductive polypyrrole has been formed and the current reaches the steady state condition.

This data shows that dopant do help in triggering the process of electropolymerization at lower potential compared to the absence of dopants.

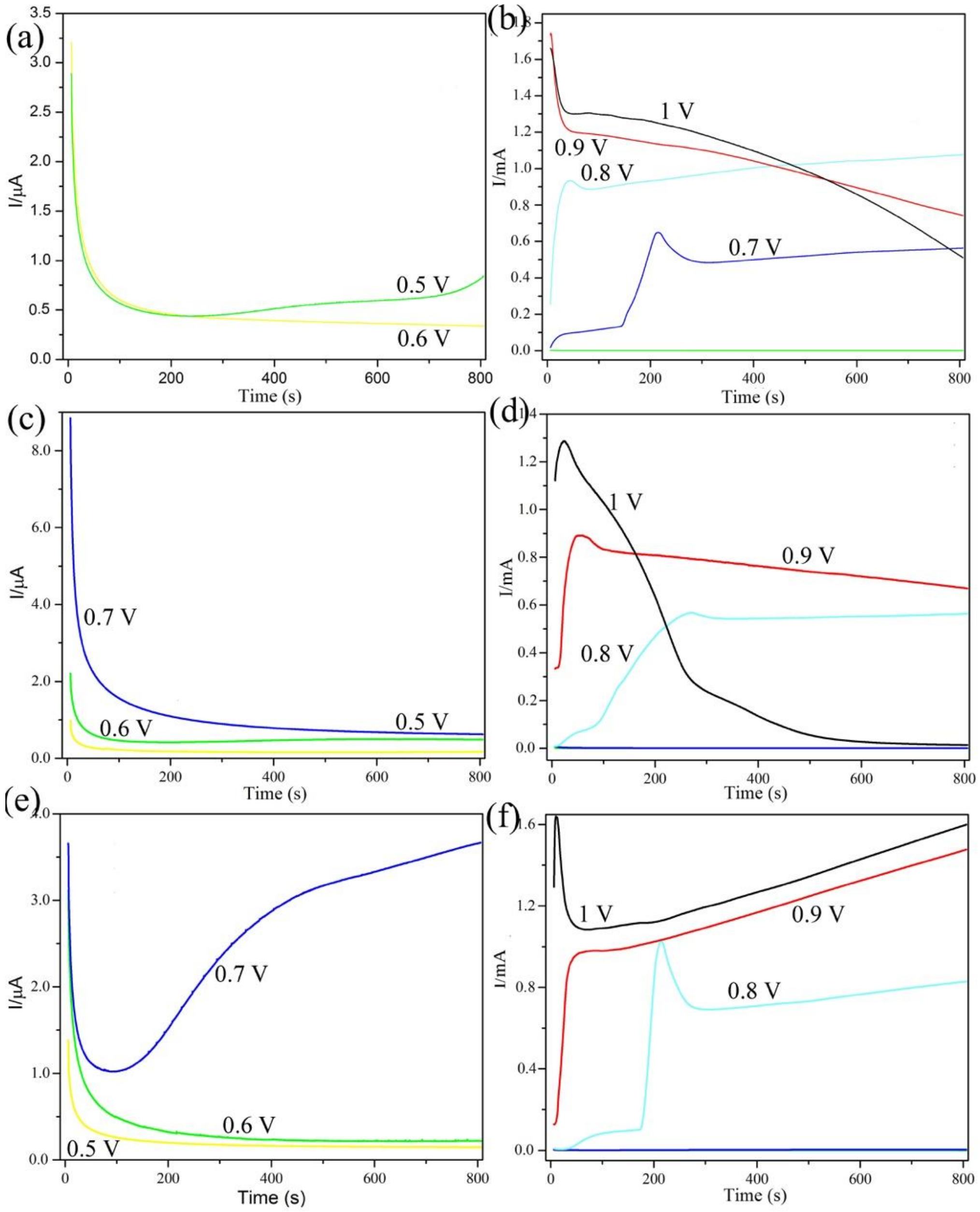

Figure 4.35: Amperometry electropolymerization of Ppy from an aqueous solution containing 0.1 M pyrrole, 0.1 M phosphate buffer solution and (a, b) 0.1 M $LiClO_4$, (c, d) 0.1 M $LiNO_3$ and (e, f) 0.1 M SDS at constant potential of 0.5 to 1 V for 800 s.

Figures 4.36 and 4.37 show the comparison of electrocatalytic activity of various modified electrodes (with and without dopant) toward H_2O_2 reduction. Generally, for Ppy which synthesized at low applied potential (0.5 to 0.7) V *vs*. SCE, the electrodes did not have a distinct reduction peak. With potential to 0.8 and 0.9 V, a dramatic change in the current was observed which confirmed that these potentials are not only suitable for initiating the polymerization, but it also shown the response towards H_2O_2. In the case of 1 V, the current suddenly dropped which can be due to the overoxidation of Ppy, which explains the negative response towards H_2O_2.

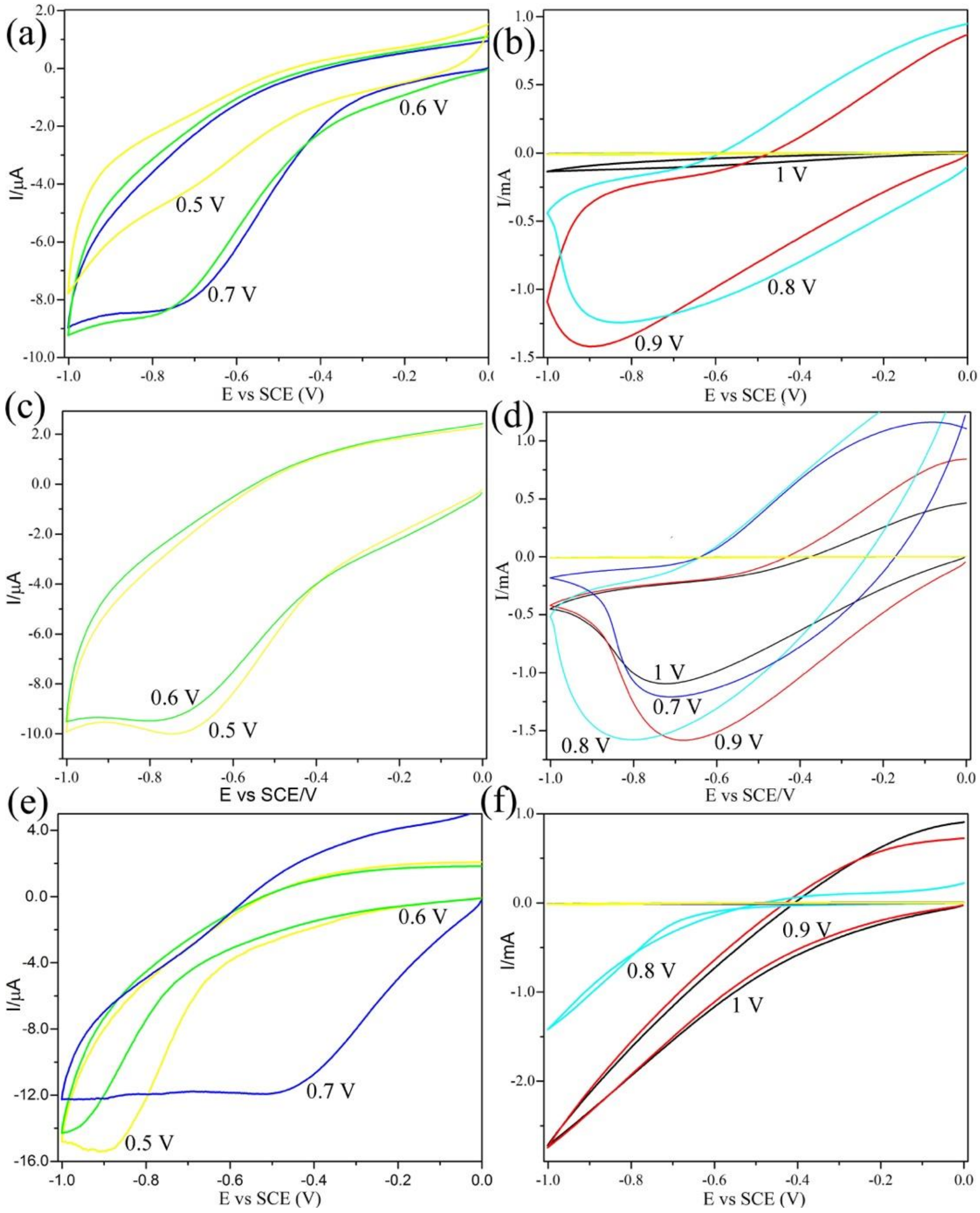

Figure 4.36: Cyclic voltammograms of (a, b) Polypyrrole with $LiClO_4$ counterion, (c, d) Polypyrrole with $LiNO_3$ counterion and (e, f) Polypyrrole with SDS counterion at different constant potential in the presence of 1 mM H_2O_2 in phosphate buffer solution (pH 6.5) at scan rate of 50 mVs^{-1}.

The possible reduction mechanism is proposed as follow:

$2Ppy_{(s)} + H_2O_{2(l)} \rightarrow 2Ppy^{+}_{(s)} + 2OH^{-}_{(aq)}$ (Eq. 4.7)

$Ppy^{+}_{(s)} + e^{-}$ (applied potential) $\rightarrow Ppy_{(s)}$ (Eq. 4.8)

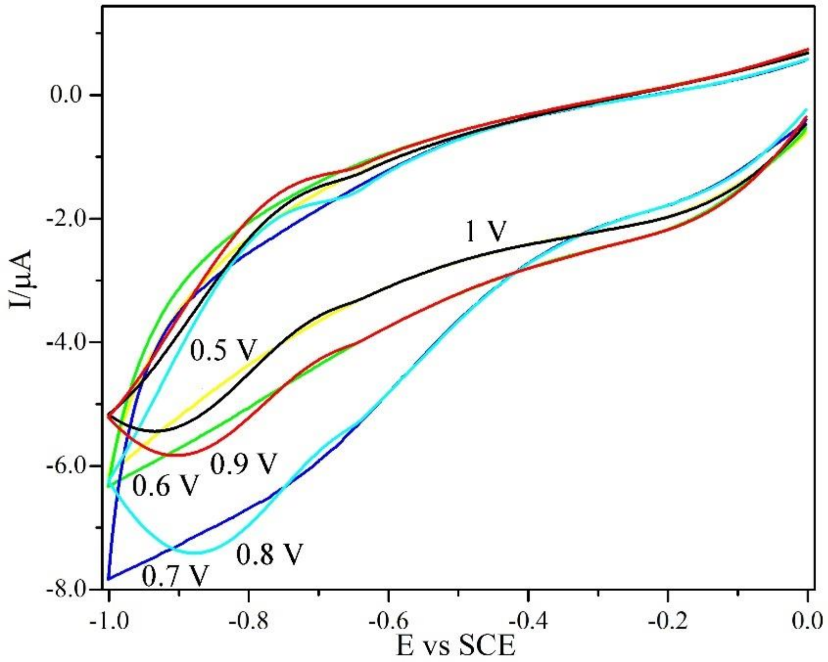

Figure 4.37: Cyclic voltammograms of polypyrrole without adding counterion at different constant potential in the presence of 1 mM H_2O_2 in phosphate buffer solution (pH 6.5) at scan rate of 50 mVs^{-1}.

Figure 4.38 summarized the best behavior of each modified electrode under the same potential towards H_2O_2 in 0.1 M phosphate buffer solution (PBS) at pH 6.5. It is obviously seen that rGO/Ppy/AgNPs electrodes, showed weak peaks in compared with rGO/Ppy. This is primarily due to the electrodeposition of big size silver particles. As previously shown (Moradi *et al.*, 2013), electrodeposition of silver by $AgNO_3$ solution, leads to agglomeration of particles and consequently, lower surface area which reduces electrocatalytic activity.

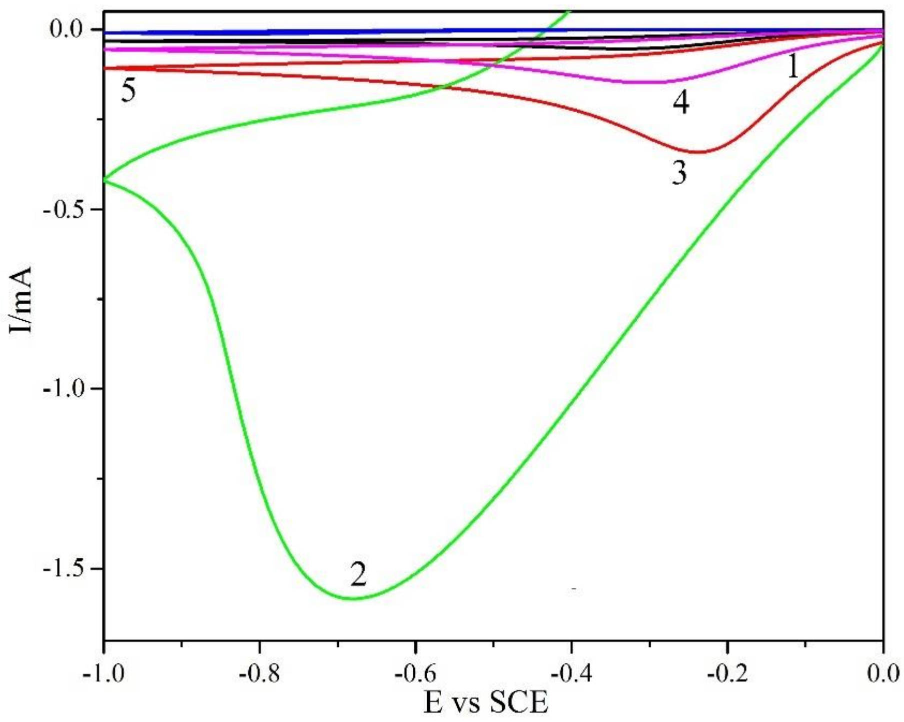

Figure 4.38: Cyclic voltammograms of (1) rGO, (2) rGO/Ppy, (3) rGO/Ppy/AgNPs-1, (4) rGO/Ppy/AgNPs-2 and (5) rGO/Ppy/AgNPs-3 in the presence of 1 mM H_2O_2 in phosphate buffer solution (pH 6.5) at scan rate of 50 mVs^{-1}.

4.4.5. Electrochemical Impedance Spectroscopy (EIS)

In order to analyze the impedance changes of the modified electrodes, electrochemical impedance spectroscopy was carried out. Figure 4.39 shows the Nyquist and Bode plots in 0.1 M KCl solution containing 1 mM $Fe[(CN)_6]^{3-/4-}$ (1:1).

The Nyquist plot of impedance spectra consists of semicircle portion which at higher frequencies correlates to the electron transfer limited process while on the other hands, a linear portion at lower frequencies correlates to the diffusion process. The electron transfer resistance (R_{ct}), by using the diameter of the semicircle diameter can be evaluated.

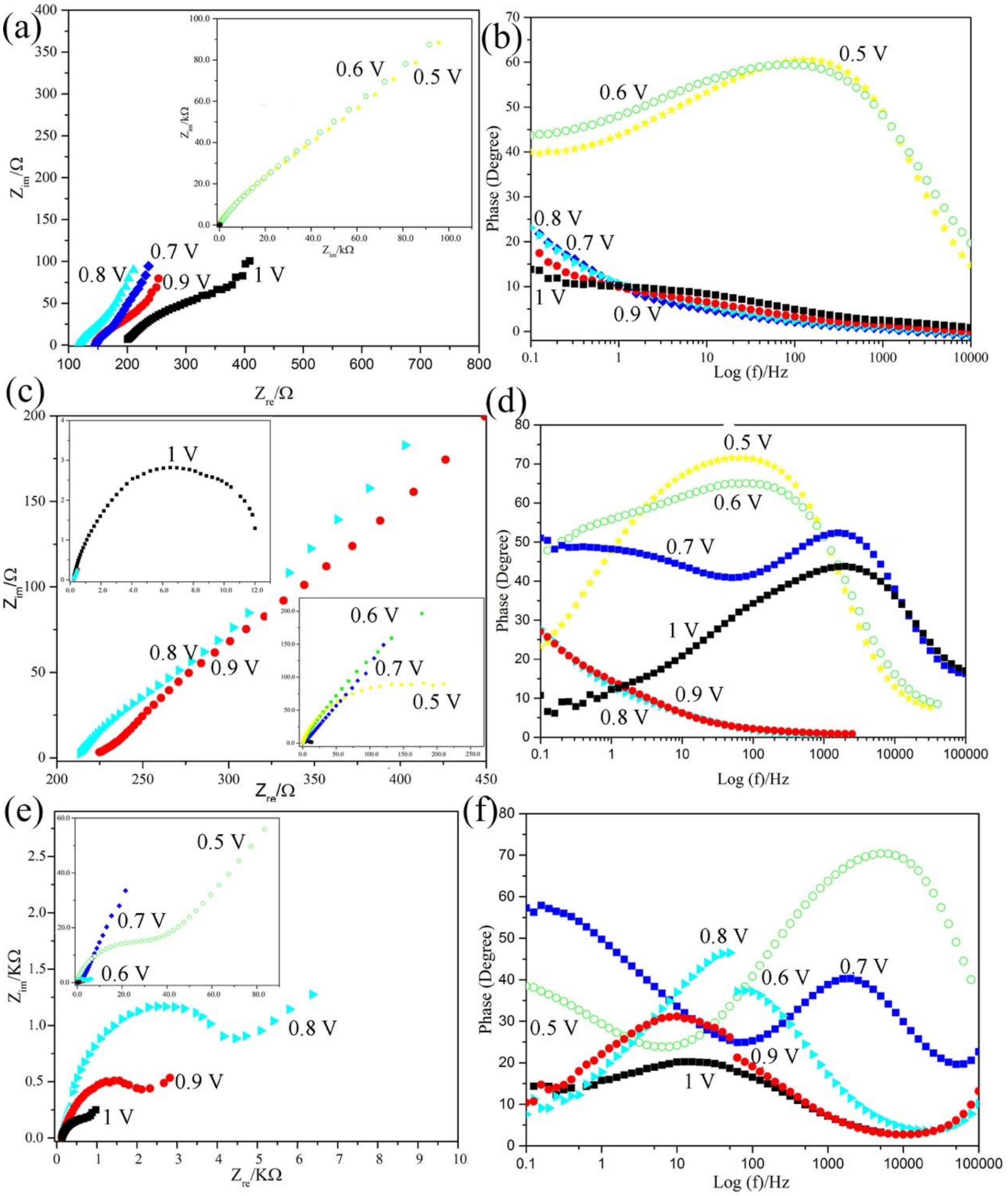

Figure 4.39: EIS data of (a) polypyyrole with $LiClO_4$ counterion, (b) polypyyrole with $LiNO_3$ counterion and (c) polypyyrole with SDS counterion at diferent constant potential in the presence of 1 mM H_2O_2 in in 0.1 M KCl solution containing 1 mM $Fe(CN)_6^{3-/4-}$(1:1).

As can be seen, in the electropolymerization process, by increasing applied potential, the semi-circle diameter of the modified electrodes reduces which confirms that at higher potentials, polypyrrole owns higher conductivity. Moreover, the comparison between the semicircle diameters from the Nyquist diagrams shows the direction of R_{ct}:

(R_{ct}): Ppy (0.5V)> Ppy (0.6 V)> Ppy (0.7 V)> Ppy(0.8 V) > Ppy (0.9 V) > Ppy (1 V)

In order to figure out the impedance parameters, the Nova 1.11 software is employed in the simulations. The $R_s(CPE[R_{ct}W)])$ equivalent circuit model was employed in the simulation of the impedance behavior of all the modified electrodes, from the experimentally gained impedance data. By exploiting the series components, the model was developed. The first component is ohmic resistance of the solutions of the electrolyte R_s and the second one is a set of constant phase elements (CPE) and the resistance of layer which indicates the conductivity of the sample (R_{ct}) that are in the parallel position. In addition, from the diffusion impedance, W for the Warburg element is a series connection to R_{ct}.

4.4.6. Sensor optimization

To check the possible concentration range of the H_2O_2 detection, the amperometric study is carried out. The outcome of amperometric response of the rGO/Ppy/AgNPs composite with a constant potential at -0.5 V by adding different concentration of H_2O_2 in 0.1 M phosphate buffer solution (pH 6.5) is presented in Figure 4.38(a). The current of working electrode increased dramatically up to 95% steady-state current within 3 s manifestly a fast amperometric response behavior. The steady-state calibration plot over the concentration range has been prepared from the amperometric response, as shown in Figure 4.40 (b). The plot of H_2O_2 concentration range from 0.1 mM up to 30 mM shows almost nonlinear behavior towards peak currents and the R^2 value is unsatisfactory. The performance of rGO/Ppy/AgNPs composite was not impressive, therefore further improvement is needed.

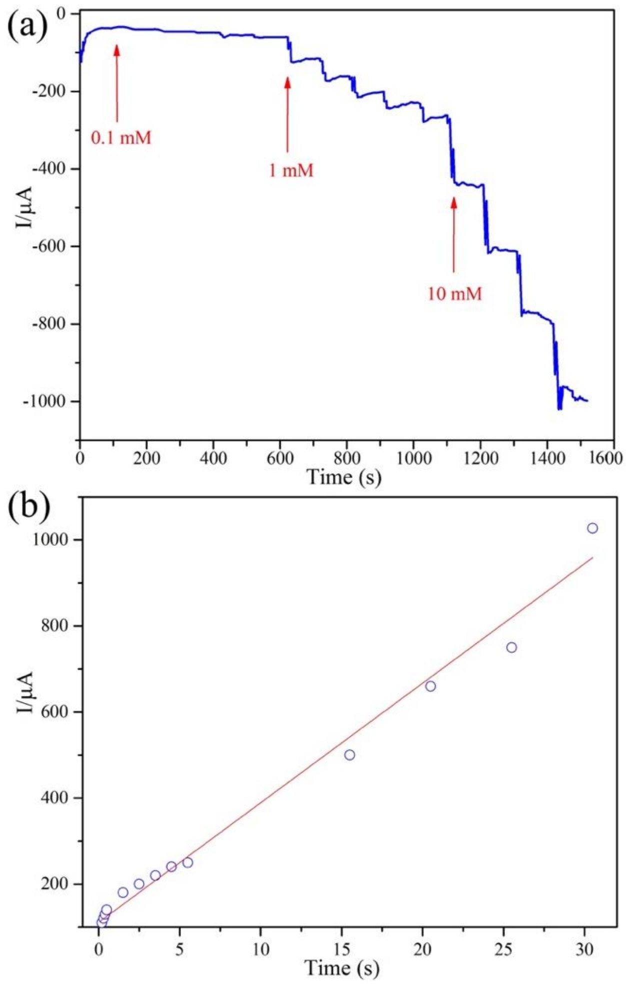

Figure 4.40: (a) Current–time responses of rGO/Ppy/AgNPs-1 with the subsequent addition of H_2O_2 into 0.1 M PBS (pH 6.5) at −0.5 V and (b) Calibration curve rGO/Ppy/AgNPs.

The electrolatalytic activity of rGO/Ppy/AgNPs-1 electrode towards glucose was studied. The prepared nanocomposite did not show significant performance as no obvious oxidation response was recorded, thus suggesting that in this potential window, rGO-AgNPs-1 nanocomposite is not suitable to be used for dual detection of glucose together with hydrogen peroxide.

4.5. (rGO-AgNPs)/PpyNFs composite

Figure 4.41 shows the reduction and polymerization process by cyclic voltammetry in one-step process. In the negative potentials, GO was reduced to rGO.

When potential reaches to the positive values, polymerization takes place. Peaks I and II confirms that GO successfully was reduced to rGO (Moradi *et al.*, 2013; Guo *et al.*, 2009). Moreover, as potential sufficiently increases to pyrrole oxidation potential (+0.6 V), radical polymerization starts (Brânzoi *et al.*, 2004; Mahmoudian *et al.*, 2012). This process was repeated for four cycles in order to make sure reduction and polymerization process were successfully performed.

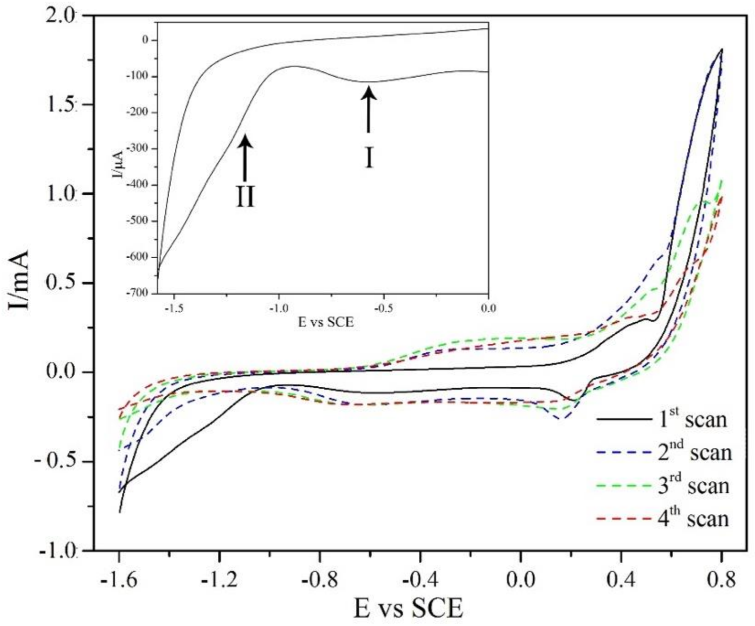

Figure 4.41: One-step electrodeposition and reduction process in a solution containing 0.1 M phosphate buffer, 0.1 $LiClO_4$ and 0.1 pyrrole at the scan rate of 25 mVs^{-1}.

4.5.1. Fourier Transform Infrared Spectroscopy (FTIR)

Figure 4.42 displays the FTIR spectrum of GO, AMP-(rGO-AgNPs-2) and AMP-(rGO-AgNPs-2)/PpyNFs composites, respectively. For graphene oxide, the peaks at 1740, 1620 and 1380 are related to stretching C=O, *sp*^{2}-hybridized C=C group and O-H bending, C-OH stretching and C-O-C stretching, respectively while the broad peak centered at 3253 cm^{-1} is responded to the stretching vibrations of O-H groups (Cheng *et al.*, 2013). In addition, the peaks at 1155 and 1043 cm^{-1} can be assigned to C-O vibration of alkoxy or epoxy (Pham *et al*., 2011). For AMP-(rGO-AgNPs-2), the peaks located at 1691, 1442, 2835 and 2930 cm^{-1} are attributed to the sp^2 hybridized C=C group and O-H bending, O-H deformation and stretching vibration of CH_2 (symmetric and asymmetric) groups, respectively (Moradi *et al.*, 2013). For GO, the peak located at 1740 cm^{-1} cannot be seen for (rGO-AgNPs), showing that the group of carbonyl was eliminated by the electrochemical reduction (Guo *et al.*, 2009). The broad peak at 3334 cm^{-1} for (rGO-AgNPs) is likely to be assigned to the O-H stretching vibration of absorbed water molecules.

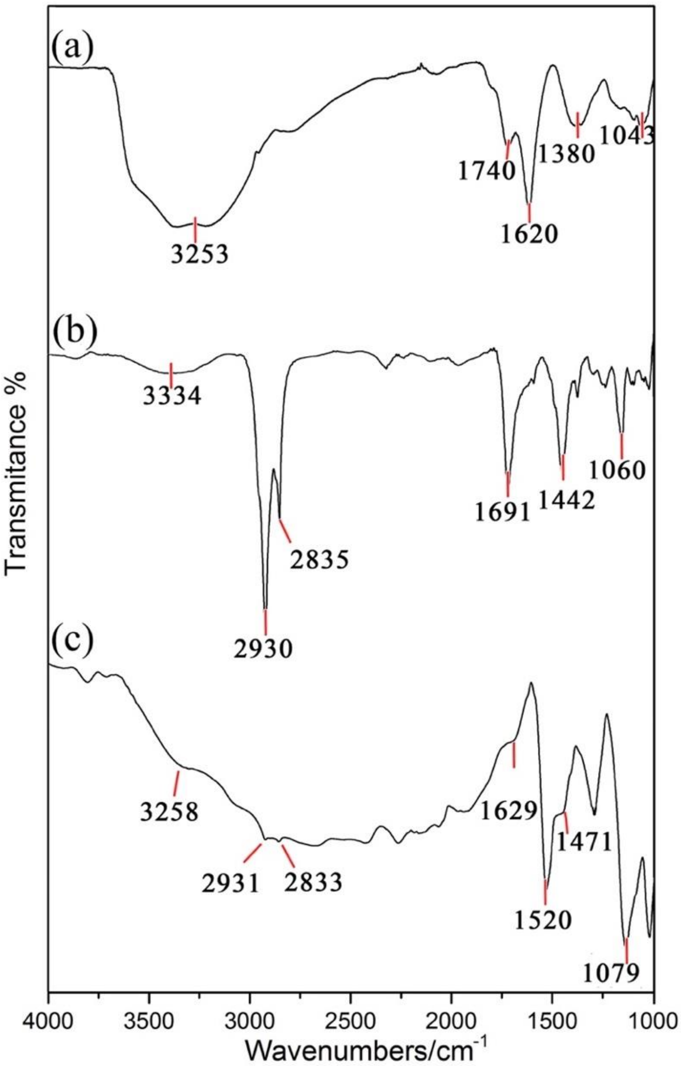

Figure 4.42: FTIR spectrum of the (a) GO, (b) AMP-(rGO-AgNPs-2) and (c) AMP-(rGO-AgNPs-2)/PpyNFs.

Figure 4.42(c) shows the FTIR spectra of AMP-(rGO-AgNPs-2)/PpyNFs which includes the bands at 1471, 1520 and 3258 cm^{-1}, corresponding to the stretching vibrations of C-N, C-C and N-H in the pyrrole ring, respectively (Jang & Oh, 2005).

The peaks located at 2833 and 2931 cm^{-1} were attributed to the symmetric and asymmetric vibrations of CH_2. The peaks centered at 1253 and 1079 cm^{-1} responded to the C-N stretching and C-H deformation vibrations of PpyNFs (Ishpal & Kaur, 2013; Lin *et al.*, 2013).

4.5.2. X-ray Diffraction (XRD)

Figure 4.43 shows the X-ray diffraction (XRD) patterns confirm the formation of GO and AMP-(rGO-AgNPs). In Figure 4.43(a), peak at 10.5° is related to GO characteristic peak, while the small peak appeared at ~23° is assigned to the elimination of surface oxygen -containing groups (Mayavan *et al.*, 2012).

The small hump in AMP-(rGO-AgNPs-2) nanocomposite at ~11° shows that the GO had been successfully reduced to rGO via electrochemical reduction. Meanwhile, the prominent peaks at 38.1°, 44.3°, 64.5° and 77.5° for AMP-(rGO-AgNPs-2) nanocomposites in Figure 4.43(b) are related to the (111), (200), (220), and (311) crystallographic planes of face-centered cubic nanoparticles of silver, respectively (Zainy *et al.*, 2012).

The sharp peak located at 38.5° is related to crystalline silver nanoparticles, affirmed the formation of high purity as-synthesized crystalline silver (Xie *et al.*, 2012; Teo *et al.*, 2012).

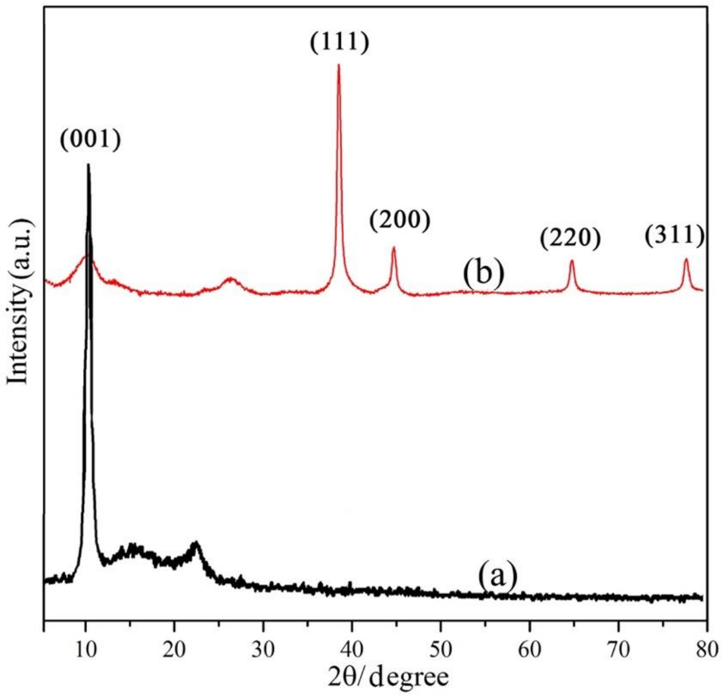

Figure 4.43: XRD data of (a)GO and (b) AMP-(rGO-AgNPs-2).

4.5.3. Field Emission Scanning Electron Microscopy (FESEM)

FESEM images along with the size distribution diagram for different AMP-(rGO-AgNPs) ratios prepared by volume ratio of 3 (a, b), 6 (c, d), 12 (e, f) and the solution with GO to $AgNO_3$ volume ratio of 6 (g, h) are displayed in Figure 4.44.

As shown in Figure 4.44(a-f), with increasing the $Ag(NH_3)_2OH$ concentration, the average of particle size and total particles' numbers also raised, and the size distribution was widened. As can be seen in Figure 4.44(b, c), the nano-sized silver particles with an average size of 19.3 nm and a narrow particle size distribution have been well distributed on the surface of graphene nanosheets. In higher ratio of AgNPs (12:1), as can be seen in Figure 4.44(e, f), the agglomeration of silver particles takes place.

Figure 4.44(g, h) shows the effect of silver precursor types on the coverage density and particle size on surface of graphene.

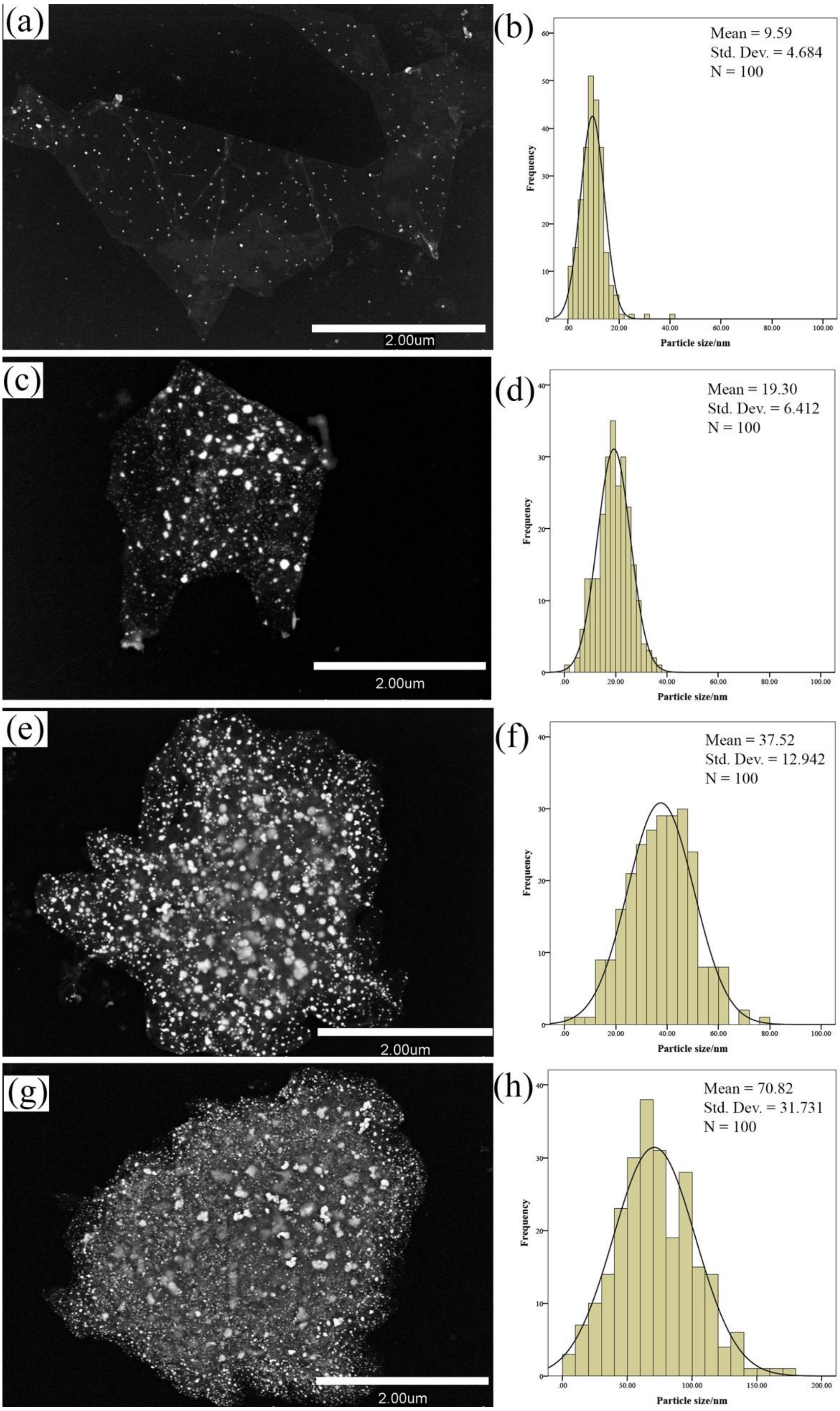

Figure 4.44: FESEM images and particle size distribution of (a, b) (rGO-AgNPs-1), (c, d) (rGO-AgNPs-2), (e, f) (rGO-AgNPs-3) and (g, h) (rGO-AgNPs-4).

With using $AgNO_3$ solution, the average particle size raised up to 70 nm and broadened the size distribution which is mainly due to the fact that compared with $AgNO_3$, $Ag(NH_3)_2OH$ has a higher stability and resists reduction, preventing the growth of large Ag particles (Kaniyankandy *et al*., 2007).

Figure 4.45 shows FESEM images of PpyNFs prepared in two different methods. As can be seen, electropolymerization with amperometry leads to synthesize polypyrrole with larger and clear nanofibers which generates higher surface area.

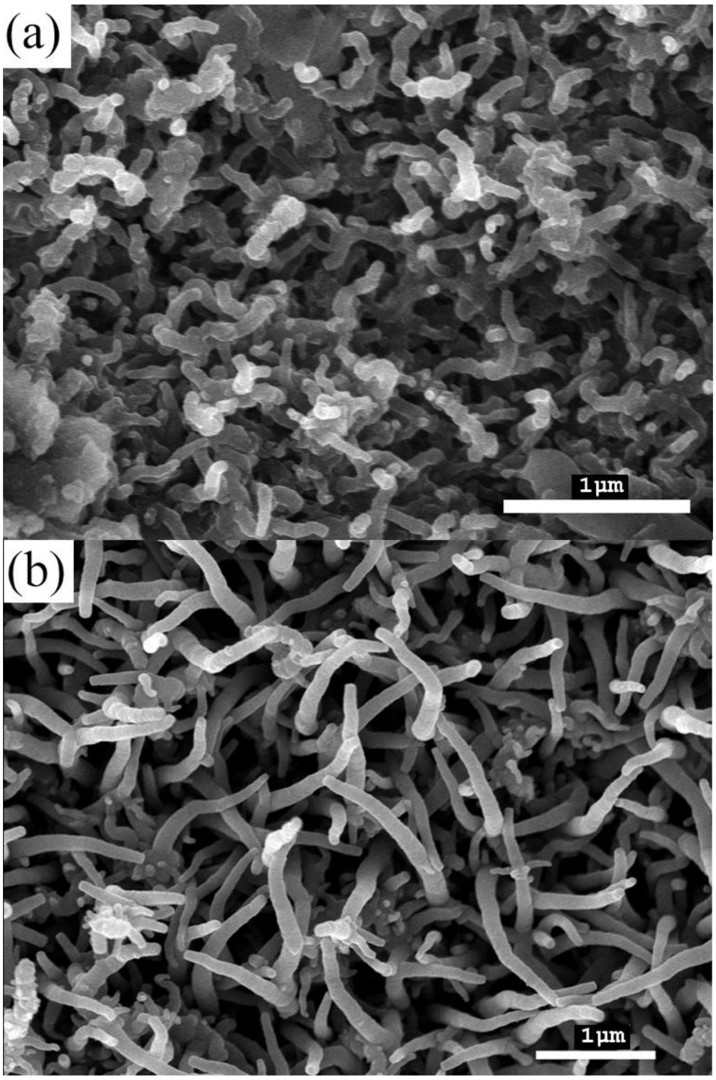

Figure 4.45: FESEM images of (a) CV-(rGO-AgNPs-2)/PpyNFs and (b) AMP-(rGO-AgNPs-2)/PpyNFs.

4.5.4. Cyclic voltammetry (CV)

To investigate the volume of drop cast, five volumes of GO-AgNPs were tested. Figure 4.46 shows that 20 µL is the optimum volume for dropping as recorded the highest current under the presence of hydrogen peroxide.

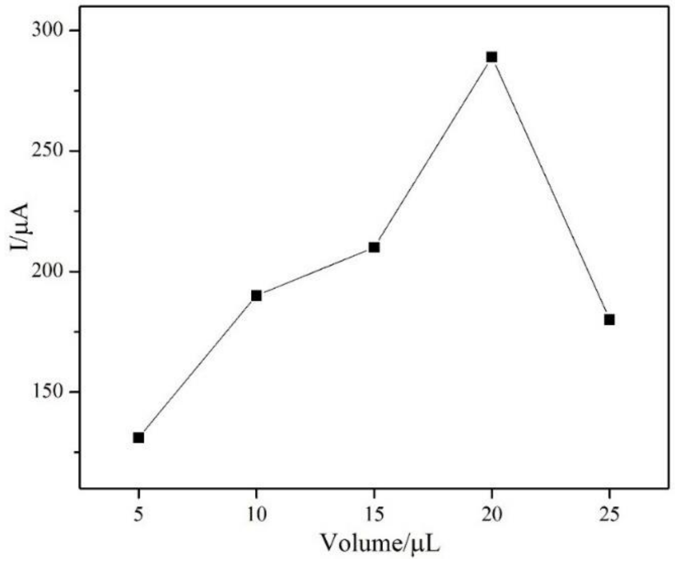

Figure 4.46: The current response affected by applied potential in the presence of 1 mM H_2O_2 on the GO-AgNPs coated GCE in 0.1 M phosphate buffer solution (pH 6.5).

Electrocatalytic reduction of AMP-(rGO-AgNPs-1, 2, 3) and AMP-(rGO-AgNPs-4) are shown in Figure 4.47. The catalytic activities of almost all AMP-(rGO-AgNPs) electrodes are markedly better than (rGO-AgNPs)-4. The comparison between AMP-(rGO-AgNPs-1), AMP-(rGO-AgNPs-2) and AMP-(rGO-AgNPs-3) which were synthesized in the $Ag(NH_3)_2OH$ solution, shows that the AMP-(rGO-AgNPs-2) has the highest electrocatalytic activity which is mainly due to higher available surface area. In comparison with AMP-(rGO-AgNPs-1), the particle density of AMP-(rGO-AgNPs-2) is higher, but it is lower as compared to AMP-(rGO-AgNPs-3) which is presumably due to bigger particle size of AgNPs that led to lower surface area. FESEM (Figure 4.44) images approved the results of CVs.

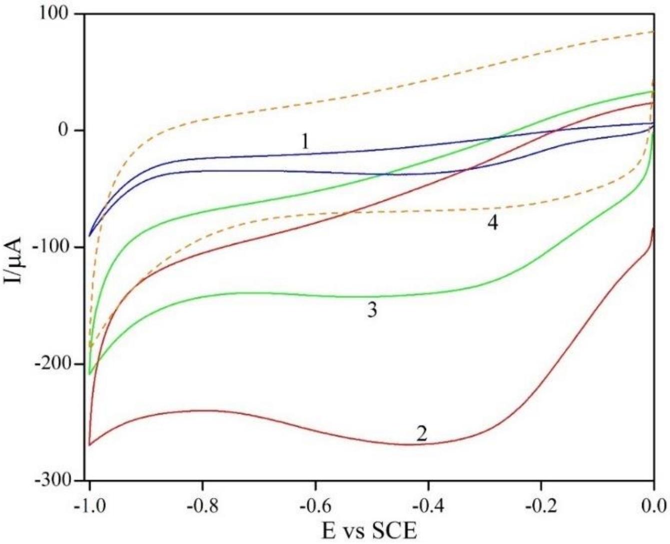

Figure 4.47: CVs of different modified electrodes: (1) (rGO-AgNPs-1), (2) (rGO-AgNPs-2), (3) (rGO-AgNPs-3) and (4) (rGO-AgNPs-4) in 0.1 M PBS (pH 6.5) with adding 1 mM H_2O_2.

In amperometry method, GO-AgNPs is reduced in different potentials. Fig. 4.48 shows the maximum electrocatalytic reduction peak of H_2O_2 for different reduction potentials. As can be seen, -1.5 V *vs*. SCE is the best potential for reducing GO in amperometry method. Below -1.5 V, potential is not enough for reducing all the oxygen-containing groups and in the case of higher potential, it contributed to detachment of GO-AgNPs from GCE.

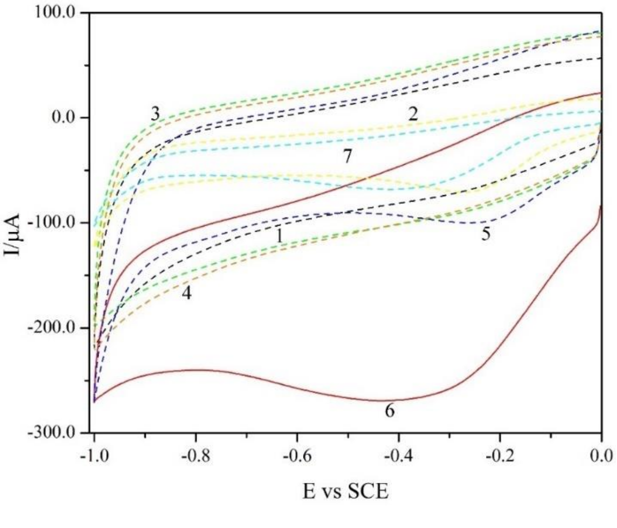

Figure 4.48: CVs of (rGO-AgNPs-2) in 0.1 M PBS (pH 6.5) in the presence of 1.0 mM H_2O_2 at different applied potential at scan rate of 50 mVs^{-1}.

Figure 4.49 represents that the electropolymerization of polypyrrole nanofibers on the surface of AgNPs-GO (CV-(rGO-AgNPs)/PpyNFs) dramatically increases the catalytic activity in the presence of 1 mM H_2O_2 (pH 6.5).

The comparison between CV-(rGO-AgNPs-2)/PpyNFs and AMP-(rGO-AgNPs-2) confirms that Ppy and GO are electropolymerized and reduced, respectively, in one-step process. Figure 4.49 also confirms that synthesis of polypyrrole and reduction of GO in one-step process shows better catalytic activity toward H_2O_2, mainly because of simultaneous effect of PpyNFs, AgNPs and rGO.

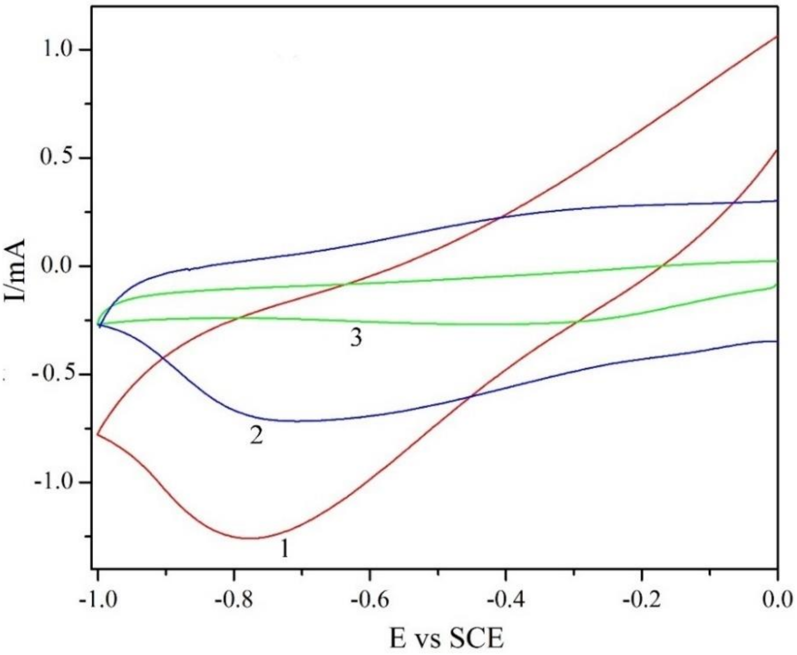

Figure 4.49: Cyclic voltammograms of (1) AMP-(rGO-AgNPs-2), (2) CV-(rGO-AgNPs-2)/PpyNFs and (3) AMP-(rGO-AgNPs-2)/PpyNFs in the presence of 1 mM H_2O_2 in phosphate buffer solution (pH 6.5) at scan rate of 50 mVs^{-1}.

By using amperometry method for reduction of GO and polymerization of PpyNFs, catalytic activity towards H_2O_2 exhibits a notable cathodic peak mainly because of full reduction and polymerization of GO and PpyNFs, respectively (AMP-(rGO-AgNPs)/PpyNFs). As shown previously, electropolymerization of polypyrrole with amperometry method caused to having enlarged nanofibers and consequently higher surface area and this phenomenon means that H_2O_2 has wider choice to be reduced. The polypyrrole in the nanofiber form provides remarkable high surface area for reduction of H_2O_2. During reduction of H_2O_2, the polypyrrole can undergo the over-oxidation, and as previously shown, H_2O_2 directly is reduced in the vicinity of PpyNFs (1 and 2) (Flätgen *et al.*, 1999; Mahmoudian *et al.*, 2013; Mahmoudian *et al.*, 2012). With increasing the surface area of the PPy, the reduction of H_2O_2 could be increased as well:

$$2\mathrm{PpyNFs}_{(s)} + \mathrm{H_2O_2}_{(l)} \rightarrow 2\mathrm{PpyNFs}^{+}_{(s)} + 2\mathrm{OH}^{-}_{(aq)} \qquad \text{(Eq. 4.9)}$$

$$\mathrm{PpyNFs}^{+}_{(s)} + e^{-} \text{ (applied potential)} \rightarrow \mathrm{PpyNFs}_{(s)} \qquad \text{(Eq. 4.10)}$$

4.5.5. Electrochemical Impedance Spectroscopy (EIS)

Figure 4.50 represents the results of EIS for the bare GCE and three modified electrodes in the solution containing $[Fe(CN)_6]^{3-/4-}$ (1:1). Charge transfer resistance (R_{ct}) of the bare GCE is almost 83 kΩ (Figure 4.50(1)). After modifying GCE with AgNPs-GO-2, Nyquist plot shows two different R_{ct}, the first semicircle with lower diameter due to the Ag particles and the bigger semicircle due to GO which increase the resistance (Figure 4.50(2)).

After converting (GO-AgNPs) to (rGO-AgNPs) through amperometry method at -1.5 V *vs*. SCE, the semicircle dramatically decreased due to smaller band gap of rGO compared with GO. In the low frequency region, the AMP-(rGO-AgNPs-2) shows Warburg impedance meaning that the process is under the control of diffusion. Semicircle diameter totally decreased after deposition of PpyNFs signifying that PpyNFs improves the conductivity of modified electrode.

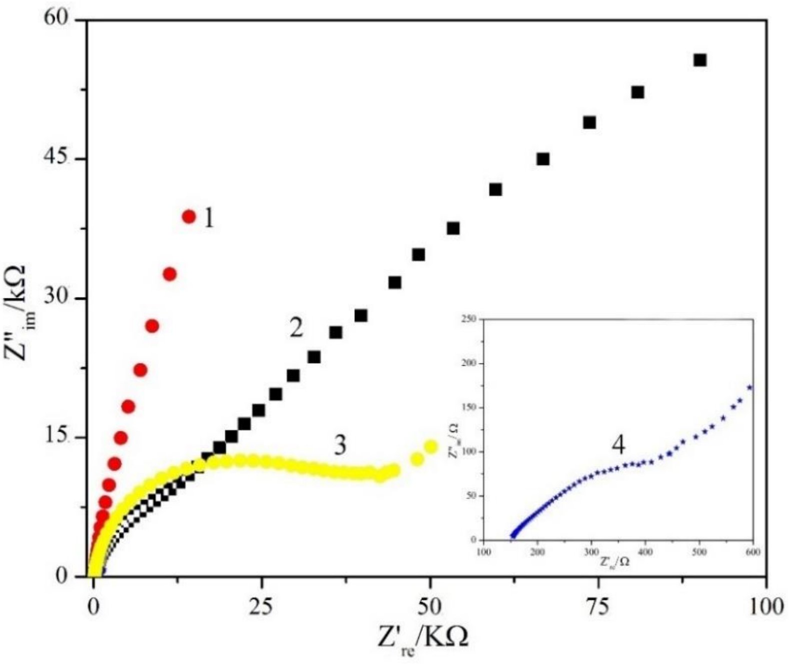

Figure 4.50: Nyquist diagrams of (1) GCE, (2) AgNPs-GO-2/GCE, (3) AMP-(rGO-AgNPs-2) and (4) AMP-(rGO-AgNPs-2)/PpyNFs in 0.1 M KCl solution containing 1 mM $Fe(CN)_6^{3-/4-}$(1:1).

Table 4.10: EIS parameters achieved by equivalent circuits of bare electrode, AgNPs-GO, AMP-(rGO-AgNPs-2) and AMP-(rGO-AgNPs-2)/PpyNFs in 0.1 M KCl solution containing 1 mM $Fe(CN)_6^{3-/4-}$ (1:1).

Electrode	**R_s (Ω)**	**R_{ct1} (Ω)**	**Q_1 (nMho)**	**W (µMho)**	**R_{ct2} (Ω)**	**Q_2 (nMho)**	**n**
Bare	148	82770	290	-	-	-	0.88
AgNPs-GO-2	145	12102	998	-	375×10^3	12.8×10^3	0.84
AMP-(rGO-AgNPs-2)	149	30181	332	33	-	-	0.87
AMP-(rGO-AgNPs-2)/PpyNFs	149	394	629×10^3	4.89	-	-	-

4.5.6. Sensor optimization

The mentioned experimental results confirm that H_2O_2 can electrochemically be reduced in the presence of AMP-(rGO-AgNPs-2)/PpyNFs on the surface of GCE. To develop the performance of the sensor, various factors influencing the current response of the sensor were investigated. Figure 4.51 shows the influence of operating potential on the amperometric response of the AMP-(rGO-AgNPs-2)/PpyNFs and the reduction current studied under batch conditions ranging -0.7 to -0.9 V *vs*. SCE in a solution containing 1 mM H_2O_2 in 0.1 M phosphate buffer solution (pH 6.5). As can be seen in Figure 4.51, the potential value of -0.75 V was determined as the operating potential.

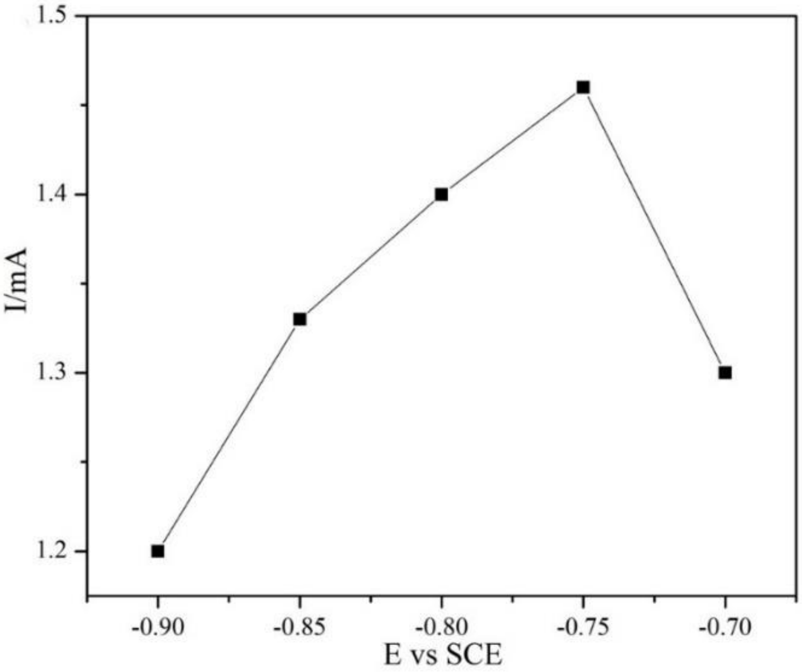

Figure 4.51: Effect of the applied potential on the current response of 1 mM H_2O_2 on the AMP-(rGO-AgNPs-2)/PpyNFs in 0.1 M PBS (pH 6.5).

4.5.6.1. Amperometric detection of H_2O_2

Figure 4.52 displays the current response of AMP-(rGO-AgNPs-2)/PpyNFs with successive addition of H_2O_2 into PBS at pH 6.5 under the applied potential of -0.75 V in the stirring condition (2000 rpm). The response time was fast (less than 3 s) and with increasing the concentration of H_2O_2 from 0.1 mM to 90 mM, the current increased linearly.

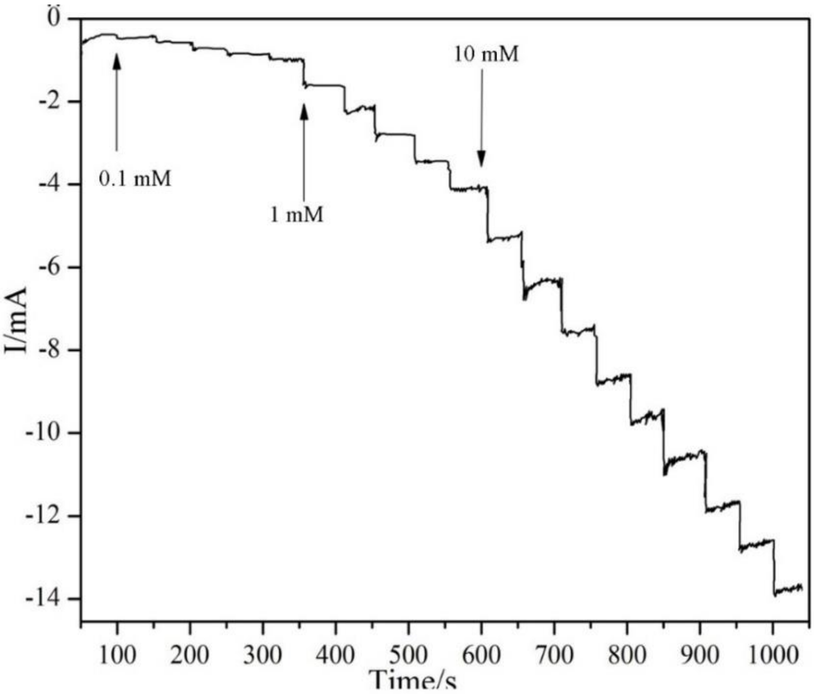

Figure 4.52: Current–time responses of AMP-(rGO-AgNPs-2)/PpyNFs with the subsequent addition of H_2O_2 into 0.1 M PBS (pH 6.5) at −0.75 V.

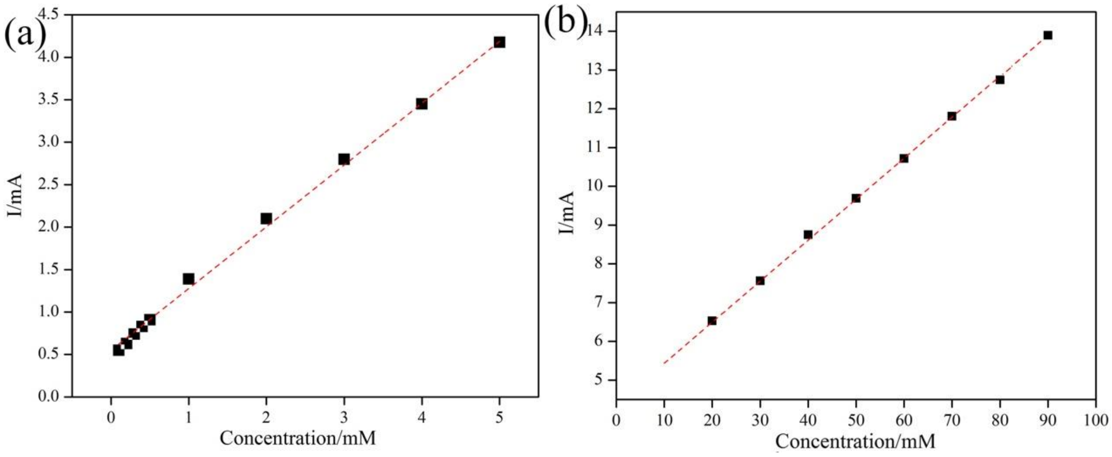

Figure 4.53: Calibration curve of (a) lower (0.1–5 mM) and (b) higher (10–90 mM) concentration range of AMP-(rGO-AgNPs-2)/PpyNFs.

In calibration curve, the sensor shows two linear sections for the response to H_2O_2. Based on the first linear section, the linear regression equation of I = 0.7367 (µA.mM^{-1}) + 0.5423 (R^2= 0.997) is determined, increasing from 0.1 mM to 5 mM (Figure 4.53(a)) while, in a higher concentration of H_2O_2, the second linear section raised up to 90 mM (Figure 4.53(b)) with a linear equation of $I = 9.4395\ (\mu A.mM^{-1}) + 41.277\ (R^2 = 0.999)$. For two linear parts, the LOD and LOQ (S/N=3) are calculated to be 1.099 µM, 3.665 µM and 0.085 µM, 0.286 µM, respectively. As listed in Table 4.11, the detection limit and the linear range of AMP-(rGO-AgNPs-2)-PpyNFs are better and wider than other modified electrodes based on polypyrrole, silver and reduced graphene oxide (Moradi *et al*., 2013; Zhong *et al*., 2013; Li *et al*., 2010; Liu *et al*., 2011; Liu *et al*., 2013; Mahmoudian *et al*., 2013; Kaniyankandy *et al*., 2007; Luo *et al*., 2011).

Table 4.11: Comparison between LOD and linear range of different non-enzymatic H_2O_2 sensors with AMP-(rGO-AgNPs-2)-PpyNFs.

Modify electrode	**Performance**		**Ref.**
	LOD (µmol.L^{-1})	**Liner range** (mmol.L^{-1})	
Ag NPs-NFs/GCE	62	0.1–80	(Tian *et al*., 2010)
AgNP/rGO-benzylamine	31.3	0.1–100	(Liu *et al*., 2011)
ERGO-Ag/GCE	1.6	0.1–100	(Moradi *et al*., 2013)
PPy/Mn NWs	2.12	0.005–0.09	(Mahmoudian *et al*., 2013)
GO/MnO_2	0.8	5-600 µM	(Li *et al*., 2010)
Graphene–AgNPLs	3	0.02–10	(Zhong *et al*., 2013)
PDDA-rGO/AgNPs/GCE	35	0.1–41	(Liu *et al*., 2013)
AgNP-CPNBs	0.9	0.1-70	(Luo *et al*., 2011)
(rGO-AgNPs)/PpyNFs	1.099 0.085	0.1-5 10-90	This work

4.5.6.2. Repeatability, reproducibility and stability

The repeatability, reproducibility and stability of the prepared sensor were studied. Five modified electrodes were prepared under the same condition and relative standard deviation (RSD) of the current response toward 1 mM H_2O_2 was found to be 2.14%, confirming that the results can be reproducible.

The repeatability of one sensor to determine 1 mM H_2O_2 was fairly good. The RSD was 1.22% for 10 successive assays. In order to investigate the stability of AMP-(rGO-AgNPs-2)/PpyNFs electrode, the modified electrode was stored in ambient condition and the current was periodically monitored for 21 days (Figure 4.54).

The current response did not have considerable decrease by the first week, the sensor retains around 86.3% of its initial response after three weeks (I_0 and I are the response current in the first and following days, respectively).

The overall performance concluded that AMP-(rGO-AgNPs-2)/PpyNFs shows a good repeatability, reproducibility and stability.

4.5.6.3. Interference study

The effect of electroactive interfering species on modified electrode was evaluated. Figure 4.54(inset) shows the amperometric response of the AMP-(rGO-AgNPs-2)/PpyNFs towards the successive addition of 1 mM H_2O_2 and this is followed by glucose, ascorbic acid, ethanol and uric acid into 0.1 M PBS at pH 6.5.

As can be seen, the current response of the mentioned electroactive interfering species is quite negligible which confirms that AMP-(rGO-AgNPs-2)/PpyNFs has a superior selectivity towards H_2O_2.

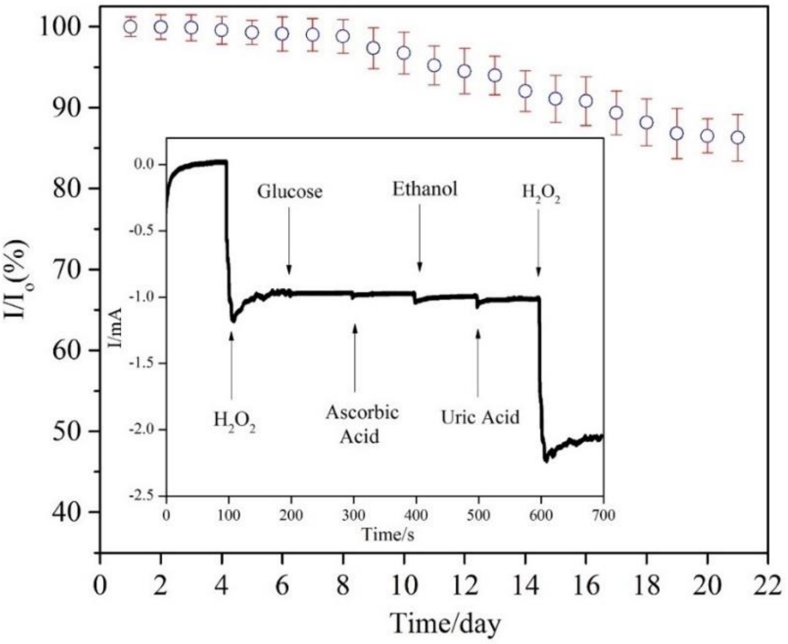

Figure 4.54: Long term stability of the AMP-(rGO-AgNPs-2)/PpyNFs studied in three weeks.

Table 4.12: H_2O_2 determination in real samples by using AMP-(rGO-AgNPs-2)-PpyNFs.

Sample	**Added (mM)**	**RSD%**	**Measured by sensor (mM)**	**Recovery%**
1	0.1	0.810	0.097	97.45
2	1	1.655	0.964	96.48
3	5	6.296	5.129	102.58
4	10	1.890	9.605	96.05
5	50	1.517	48.628	97.25

Cyclic voltammetry was carried out to study the performance of AMP-(rGO-AgNPs-2)-PpyNFs electrode towards glucose. As can be seen from Figure 4.55, the prepared nanocomposite presented a broad peak which is mainly due to oxidation of polypyrrole. This finding indicates that AMP-(rGO-AgNPs-2)-PpyNFs nanocomposite is not suitable to be used for dual analytes detection.

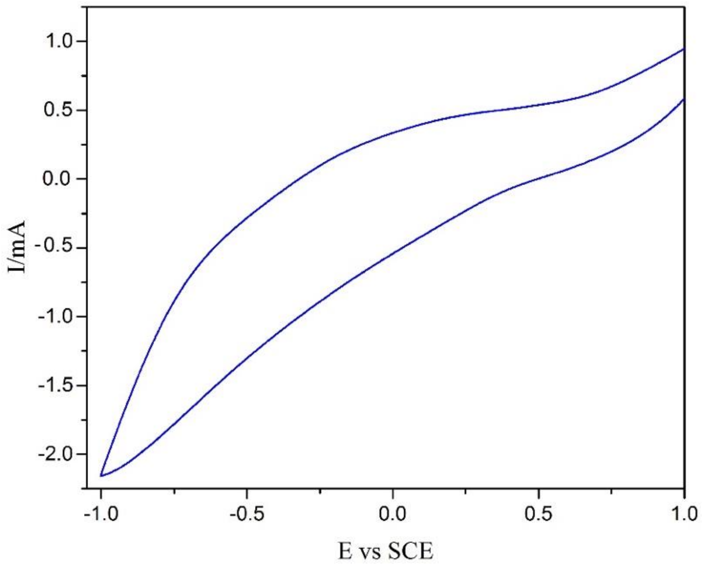

Figure 4.55: CV of AMP-(rGO-AgNPs-2)-PpyNFs electrode in a 0.1 M phosphate buffer solution (pH 7.2) and 1 mM glucose, scanned at 50 mVs^{-1} scan rate.

4.6. PpyNFs/AgNPs composite

4.6.1. X-ray Diffraction (XRD)

Figure 4.56(inset) shows the X-ray Diffractions of PpyNFs/AgNPs deposited on GCE. As can be seen, a broad peak exists at 24–27°, due to the periodically aligned polypyrrole chains (Zha *et al.*, 2013). The intense peaks at 38.3°, 44.2°, 64.4°, and 77.5° correspond to (111), (200) and (220) planes of cubic phase of silver, respectively (Moradi *et al.*, 2013; Panigrahi *et al.*, 2015). The diffractograms of PpyNFs/AgNPs composites presented the peaks due to the existence of PpyNFs and silver nanoparticles.

4.6.2. Energy-dispersive X-ray Spectroscopy (EDX)

EDX analysis was employed to prove the elemental composition of Ag nanoparticles on the surface of Ppy. Figure 4.56 displays the EDX spectra of

PpyNFs/AgNPs-1. Elemental Ag is detected in PpyNFs/AgNPs. This supports the point that Ag was able to be successfully deposited onto PPy nanofibers.

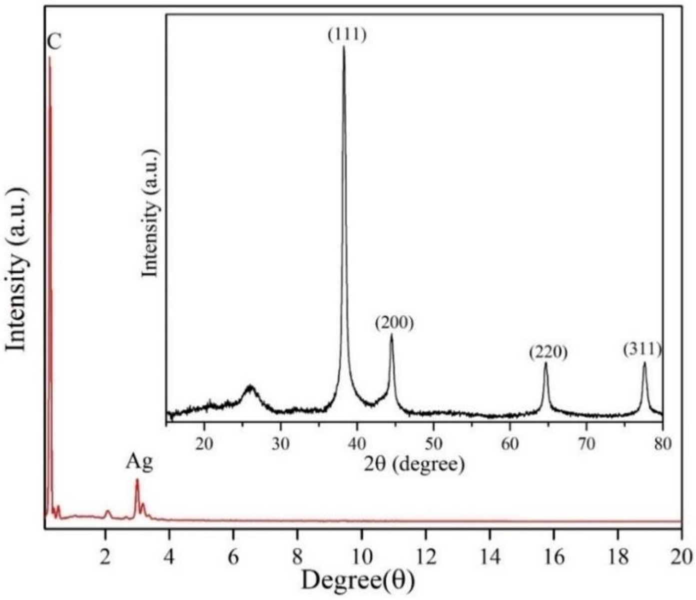

Figure 4.56: EDX spectra of AgNPs-1-PPy/GCE and (inset) XRD spectrum of PpyNFs/AgNPs-1.

4.6.3. Field Emission Scanning Electron Microscopy (FESEM)

FESEM images and particle size distribution of all modified electrodes are shown in Figure 4.57. As depicted in Figure 4.57(a, b), the AgNPs with an average size of 25 nm and particle size with a narrow distribution have been decorated, uniformly dispersed on the polypyrrole surface and anchored on most parts of the polypyrrole surface. As can be seen in Figure 4.57(c–f), as the concentration of $Ag(NH_3)_2OH$ increased, the average size of particles increased and consequently the particle size distribution of deposited Ag widened. The size and coverage density of electrodeposited silver nanoparticles on the polypyrrole surface are affected by the types of Ag precursors (Moradi *et al.*, 2013). The average particle size increased to 725 nm and the particle size distribution widened, when $AgNO_3$ was used as a precursor of Ag as shown in Figure 4.57(g) and h. The plausible reason is that $Ag(NH_3)_2OH$ has a higher stability than $AgNO_3$ and has resistance to reduction, preventing the growth of Ag into large particles (Moradi *et al.*, 2013; Kaniyankandy *et al*., 2007).

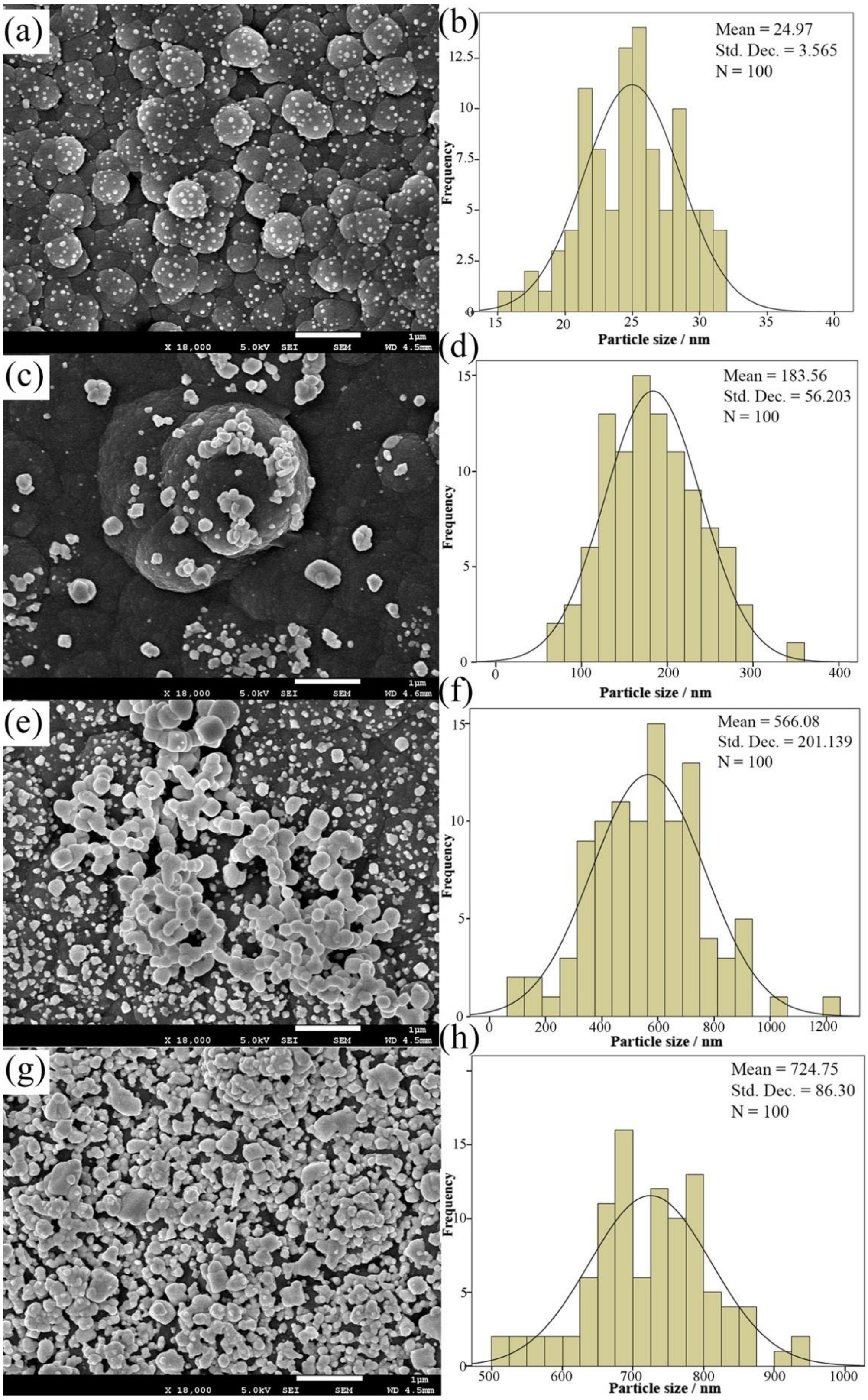

Figure 4.57: FESEM images and particle size distribution of (a, b) PpyNFs/AgNPs-1, (c, d) PpyNFs/AgNPs-2, (e, f) PpyNFs/AgNPs-3 and (g, h) PpyNFs/AgNPs-4.

4.6.4. Cyclic voltammetry (CV)

High electrocatalytic activity for the reduction of H_2O_2 is one of the most promising characteristics of AgNPs. In order to investigate the electrochemical performance of non-enzymatic AgNPs electrodeposited on the surface of polypyrrole, CV of all PpyNFs/AgNPs electrodes was carried out in a 0.1 M phosphate buffer solution (PBS) at pH 6.5 in the presence and absence of 1 mM hydrogen peroxide. For the Ppy/GC electrode (Figure 4.58(e)), no electrochemical activity was recorded under the presence of hydrogen peroxide at the selected potential range. When silver nanoparticles are electrodeposited on the surface of Ppy, the modified electrodes show a remarkable electrocatalytic behavior toward H_2O_2 reduction. PpyNFs decorated with AgNPs is different from individual Ppy, not only in the synergistic amplification effect between Ppy and AgNPs but also in the electrocatalytic reduction effect of Ag toward hydrogen peroxide.

Figure 4.58(a, d) shows the CVs of PpyNFs/AgNPs-1 electrode in the presence and absence of 1 mM H_2O_2 at a scan rate of 50 mVs^{-1}. In the absence of H_2O_2, a little reduction peak occurred at about 0.15 V at PpyNFs/AgNPs-1 electrode (Figure 4.58(d)). When H_2O_2 was added in the solution, the reduction peak increased dramatically, suggesting that PpyNFs/AgNPs-1 exhibited high electrocatalytic activity toward the reduction of H_2O_2. Therefore, a highly increased reduction peak at PpyNFs/AgNPs-1 electrode in the presence of H_2O_2 revealed the synergistic effect of Ag and polypyrrole which can greatly improve the electrocatalytic reduction of H_2O_2.

With increasing the concentration of $Ag(NH_3)_2OH$ solution, the particle size increased and consequently the agglomeration takes place which causes to reduce the reduction of H_2O_2.

Finally, it can be concluded that after addition of H_2O_2 to the solution, silver nanoparticles which are decorated on the surface of the Ppy surface react chemically with H_2O_2 according to the following equations:

$$\mathrm{2Ppy - AgNPs(0) + \ H_2O_2 \ \rightarrow 2Ppy - AgNPs(I) - OH} \qquad \text{(Eq. 4.11)}$$

$$\mathrm{2Ppy - AgNPs(I) - OH + \ 2H^+ \ + \ 2e^- \ \rightarrow 2Ppy - AgNPs(0) + \ 2H_2O} \qquad \text{(Eq. 4.12)}$$

In the phosphate buffer solution, the H_2O_2 was reduced via following mechanism:

$$\mathrm{H_2O_2 + e^- \leftrightarrow \ OH + OH^-} \qquad \text{(Eq. 4.13)}$$

$$\mathrm{OH + e^- \leftrightarrow \ OH^-} \qquad \text{(Eq. 4.14)}$$

$$\mathrm{2OH^- + 2H^+ \leftrightarrow \ 2H_2O} \qquad \text{(Eq. 4.15)}$$

After electrodepositing of the AgNPs on the surface of PpyNFs, as shown below, the reduction of H_2O_2 becomes more irreversible:

$$\mathrm{H_2O_2 \overset{Ag}{\rightarrow} \frac{1}{2} O_2 \ + H_2O} \qquad \text{(Eq. 4.16)}$$

$$\mathrm{O_2 \ + 2e^- \ + 2H^+ \xrightarrow{Electrode} \ H_2O_2} \qquad \text{(Eq. 4.17)}$$

Then, the generated O_2 would turn into the detection signal on electrode suggesting that the electrochemical reduction of O_2 on the electrode occurs (Šljukić *et al.*, 2005; Zhao *et al.*, 2009). Due to a low applied potential, the background current decreased, which can minimize the response of common interference species and reduce the O_2 reduction current (Zhao *et al.*, 2009).

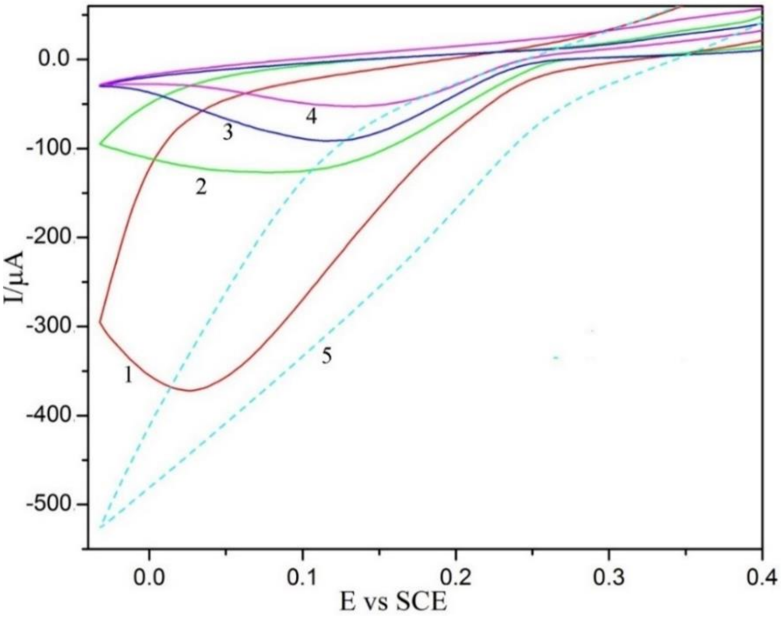

Figure 4.58: Cyclic voltammograms of (1) PpyNFs/AgNPs-1, (2) PpyNFs/AgNPs-2, (3) PpyNFs/AgNPs-3, (4) PpyNFs/AgNPs-4 in the presence of 1 mM H_2O_2 in phosphate buffer solution (pH 6.5) at scan rates of 50 mVs^{-1} and (5) Ppy/GCE.

4.6.5. Electrochemical Impedance Spectroscopy (EIS)

In order to analyze the impedance changes of the modified electrode, electrochemical impedance spectroscopy was employed. Figure 4.59(a) depicts the Nyquist plots in 0.1 M KCl solution containing 1 mM $\mathrm{Fe(CN)}_6^{-3/-4}$ (1:1). The Nyquist plot of impedance spectra consists of semicircle portion which at higher frequencies correlates to the electron transfer limited process, while on the other hands, a linear portion at lower frequencies correlates to the diffusion process. The electron transfer resistance (R_{ct}) can be evaluated by using the diameter of the semicircle diameter. As previously discussed, with increasing the concentration of $Ag(NH_3)_2OH$ solution, the size of the electrodeposited AgNPs increased and consequently, agglomeration takes place. Moreover, with increasing the density of electrodeposited AgNPs, the charge transfer resistance (R_{ct}) of the modified electrodes decreases. This can be attributed to the low resistance properties of AgNPs. The comparison between the semicircle diameters from the Nyquist diagrams of AgNPs-1-Ppy (1423 Ω), AgNPs-2-Ppy (689 Ω) and AgNPs-3-Ppy (140 Ω) shows the direction of R_{ct}:

GCE > PpyNFs/AgNPs-1 > PpyNFs/AgNPs-2 > PpyNFs/AgNPs-3

The $R_s(CPE[R_{ct}W])$ equivalent circuit model was employed in the simulation of the impedance behavior of all the modified electrodes, from the experimentally gained impedance data.

By exploiting the series components, the model was developed. The first component is ohmic resistance of the solutions (R_s) and the second one is a set of constant phase elements (CPE) and the resistance of layer (R_{ct}). R_{ct} indicates the conductivity of the samples that are in the parallel position with CPE.

Additionally, from the diffusion impedance, W, which stands for the Warburg element, is a series connection to R_{ct}. Figure 4.59(b) shows the phase plot that is in agreement with the results obtained from Nyquist plot.

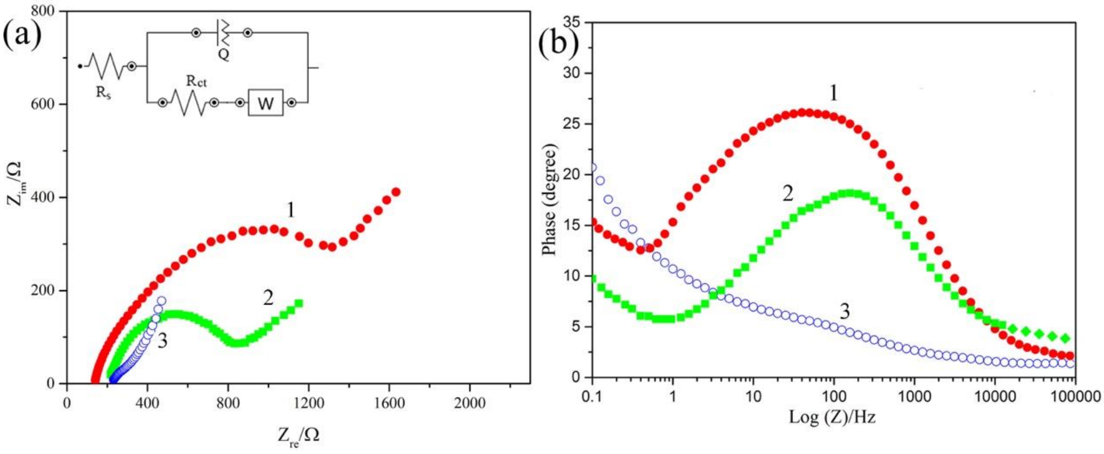

Figure 4.59: (a) Nyquist plots of (1) PpyNFs/AgNPs-1, (2) PpyNFs/AgNPs-2, (3) PpyNFs/AgNPs-3 and (inset) equivalents circuits. (b) Bode plats of (1) PpyNFs/AgNPs-1, (2) PpyNFs/AgNPs-2, (3) PpyNFs/AgNPs-3.

Table 4.13: EIS parameters achieved by equivalent circuits modified electrodes in 0.1 M KCl solution containing 1 mM $Fe(CN)_6^{3-/4-}$ (1:1).

Electrode	R_s (Ω)	R_{ct} (Ω)	Q (μMho)	W (mMho)	n
PpyNFs/AgNPs-1	185	1423	130	3.35	0.53
PpyNFs/AgNPs-2	199	689	84	6.32	0.55
PpyNFs/AgNPs-3	210	140	1.01e+03	4.08	0.45

4.6.6. Sensor optimization

The mentioned experimental results confirm that H_2O_2 can electrochemically be reduced in the presence of PpyNFs/AgNPs-1 on the surface of GCE. To develop the performance of the sensor, various factors influencing the current response of the sensor were investigated. Figure 4.60 (inset) shows the influence of operating potential on the amperometric response of the PpyNFs/AgNPs-1 and the reduction current studied under batch conditions ranging from 0.0 to 0.1 V *vs*. SCE in a solution containing 1 mM H_2O_2 in 0.1 M phosphate buffer solution (pH 6.5). As can be seen, the potential value of 0.025 V was determined as the operating potential.

4.6.6.1. Amperometric detection of H_2O_2

Amperometric i–t curve is the regularly utilized technique to assess the electrocatalytic activities of electrochemical sensors. Figure 4.60 shows the amperometric responses of the PpyNFs/AgNPs-1 electrode at 0.025 V versus SCE as a result of the successive addition of H_2O_2 to the continuously stirred 0.1 M phosphate buffer solution (pH 6.5) at 25 °C. The experiments were carried out with freshly prepared electrode. As shown in Figure 4.60(a), the PpyNFs/AgNPs-1 was very sensitive to the changes in the concentration of H_2O_2 and responded rapidly. The response time was fast (less than 2 s) and with increasing the concentration of H_2O_2 from 0.1 mM to 120 mM, the current increased linearly. In calibration curve, the sensor shows two linear sections for the response to H_2O_2. Based on the first linear section, the linear regression equation of I = 62.6 (µA.mM^{-1}) + 260.6 (R^2= 0.999) is determined, increasing from 0.1 mM to 5 mM (Figure 4.61 (a)), while in a higher concentration of H_2O_2, the second linear section raised up to 120 mM (Figure 4.61(b)) with a linear equation of I = 28.1 (µA.mM^{-1}) + 402.7 (R^2= 0.999). The limit of quantification (LOQ) and the limit of detection (LOD) of PpyNFs/AgNPs-1 were determined by Eq. 4.3 and Eq. 4.4. In Figure 4.61 (a, b) for two linear parts, the LOD and LOQ (S/N=3) were calculated to be 0.115, 0.383 µM and 0.256, 0.854 µM, respectively.

As listed in Table 4.14, the detection limit and the linear range of PpyNFs/AgNPs-1 are better and wider than other modified electrodes based on polypyrrole and silver nanoparticles.

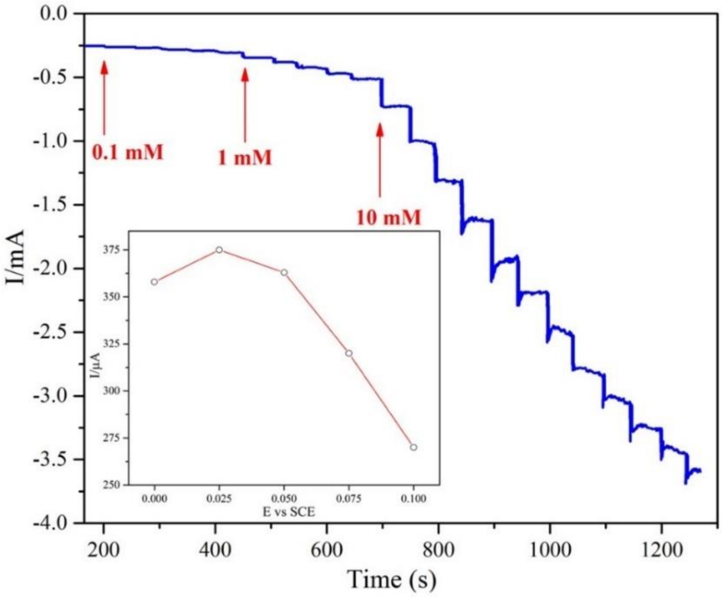

Figure 4.60: Current–time responses of PpyNFs/AgNPs-1 with the subsequent addition of H_2O_2 into 0.1 M PBS (pH 6.5) at 0.025 V *vs*. SCE. (Inset) Effect of the applied potential on the current response of 1 mM H_2O_2 on the PpyNFs/AgNPs-1 in 0.1 M PBS (pH 6.5).

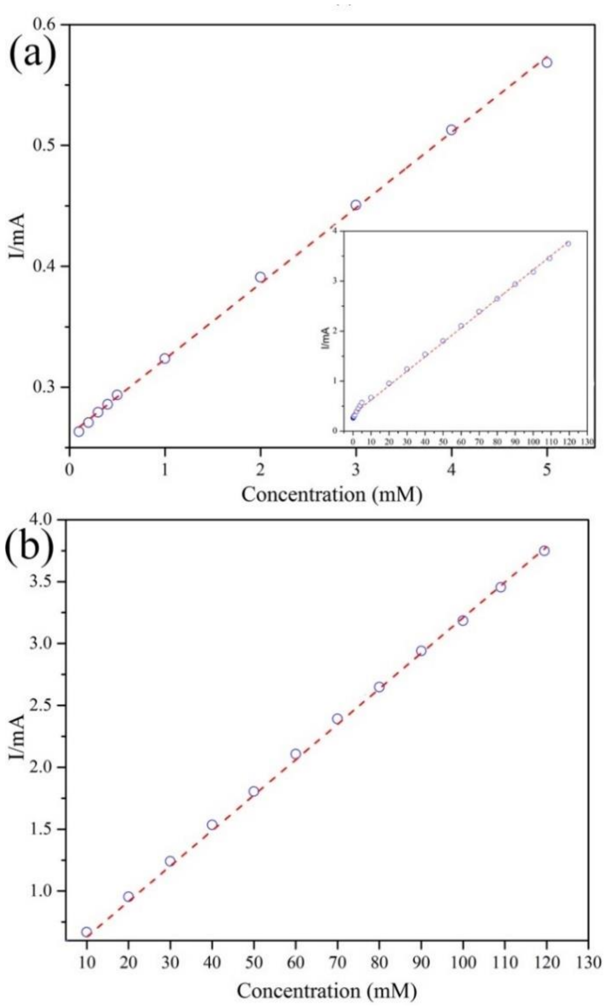

Figure 4.61: Calibration curve of (c) lower (0.1–5 mM) and (inset: calibration curve) and (d) higher (10–120 mM) concentration range.

4.6.6.2. Repeatability, reproducibility and stability

The repeatability, reproducibility and stability of the prepared sensor were studied. Five modified electrodes were prepared under the same condition and relative standard deviation (RSD) of the current response toward 1 mM H_2O_2 was found to be 3.5%, confirming that the results can be reproducible. The repeatability of one sensor to determine 1 mM H_2O_2 was fairly good. The RSD was 4.23% for 10 successive assays. In order to investigate the stability of PpyNFs/AgNPs-1 electrode, the modified electrode was stored in ambient condition and the current was periodically monitored for 21 days (Figure 4.62). The current response did not have considerable decrease by the first week, and as can be seen from Figure 4.62, the sensor retains around 89% of its initial response after 3 weeks (I_0 and I are the response current in the first and following days, respectively). The overall performance concluded that PpyNFs/AgNPs-1 shows a good repeatability, reproducibility and stability.

Table 4.14: Comparison between LOD and linear range of different non-enzymatic H_2O_2 sensors with PpyNFs/AgNPs-1.

Modified electrode	Performance		Ref.
	LOD (μmol.L^{-1})	**Liner range** (mmol.L^{-1})	
Ag NPs-NFs/GCE	62	0.1–80	(Tian *et al.*, 2010)
AgNP/rGO-benzylamine	31.3	0.1–100	(Liu *et al.*, 2011)
ERGO-Ag/GCE	1.6	0.1–100	(Moradi *et al.*, 2013)
PPy/Mn NWs	2.12	0.005–0.09	(Mahmoudian *et al.*, 2013)
Ag NPs-MWCNT/Au	0.5	0.05–17	(Zhao *et al.*, 2009)
PQ11-AgNPs/GCE	33.9	0.1–180	(Lu *et al.*, 2011)
Graphene–AgNPLs	3	0.02–10	(Zhong *et al.*, 2013)
Ag NPs/PPy/Fe3O4/GCE	1.7	0.005–11.5	(Qi *et al.*, 2015)
PDDA-rGO/AgNPs/GCE	35	0.1–41	(Liu *et al.*, 2013)
AgNP-CPNBs	0.9	0.1-70	(Luo *et al.*, 2011)
PpyNFs/AgNPs-1	0.115 0.256	0.1-5 10-120	This work

4.6.6.3. Interference study

Figure 4.62(inset) demonstrates the selectivity and anti-interference advantages by comparing the amperometric responses of relevant electroactive species. The amperometric response of the PpyNFs/AgNPs-1 towards the successive addition of 1 mM H_2O_2 was measured and this is followed by glucose, ascorbic acid, ethanol and uric acid into 0.1 M PBS at pH 6.5 at a working potential of 0.025 V *vs*. SCE. As can be seen, the current response of the mentioned electroactive interfering species is quite negligible which confirms that PpyNFs/AgNPs-1 has a superior selectivity towards H_2O_2. The good ability of anti-interference is largely attributed to the low working potential of 0.025 V used in the determination of H_2O_2 (Wang, 2010).

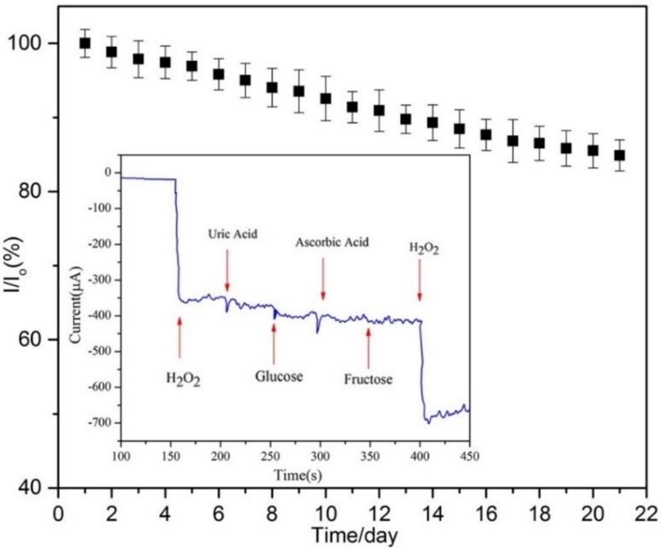

Figure 4.62: Long term stability of the PpyNFs/AgNPs-1 studied in three weeks, and (inset) shows amperometric response of PpyNFs/AgNPs-1 upon the successive addition of 1 mM uric acid, glucose, ascorbic acid and fructose into 0.1 M PBS (pH 6.5) with an applied potential +0.025 V.

All the measurements were carried out four times. Table 4.15 lists the average recoveries. Considering the relative standard deviation (RSD) values and calculated recovery, it can be observed that the developed sensor holds possible applications for evaluating specific concentration range of H_2O_2.

Table 4.15: H_2O_2 determination in real samples using PpyNFs/AgNPs-1.

Sample	Added (mM)	RSD%	Measured by sensor (mM)	Recovery%
1	0.1	0.810	0.097	97.45
2	1	1.655	0.964	96.48
3	5	6.296	5.129	102.58
4	10	1.890	9.605	96.05
5	50	1.517	48.628	97.25

Cyclic voltammetry was conducted to study the performance of PpyNFs/AgNPs-1electrode towards glucose. As can be seen from Figure 4.63, although the current significantly increased by altering the voltage, the prepared nanocomposite did not show distinct peak at the presence of glucose, suggesting that in this potential window, PpyNFs/AgNPs-1 nanocomposite cannot be used as sensor for GLC detection.

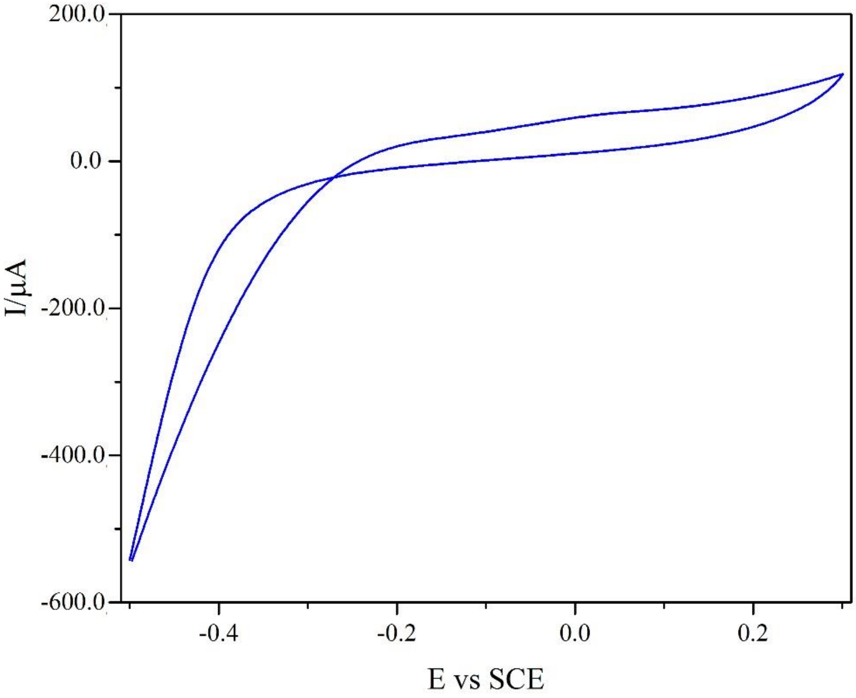

Figure 4.63. CV of PpyNFs/AgNPs-1 electrode in a 0.1 M phosphate buffer solution (pH 7.2) and 1 mM glucose, scanned at 50 mVs^{-1} scan rate.

4.7. PpyMTs-CuNPs composite

In order to evaluate the effect of counter ion concentration and its nature, polypyrrole was electropolymerized using four types of electrolytes: $LiClO_4$, SDS, PTSA, and $CuCl_2$, in different concentrations ranging from 1 to 10 mM, while the concentration of pyrrole monomer was fixed at 0.1 M.

The electrochemical impedance investigations revealed the effect of counter ion size on the conductivity of the synthesized polypyrrole. Figure 4.64(a) shows that with increasing the counter ion size, conductivity of the synthesized polypyrrole decreased which is in good agreement with previous findings (Wood & Iroh, 1996; Yamaura *et al*., 1988). Figure 4.64(b) shows the effect of type and concentration (1, 5 and 10 mM) of counter ion toward H_2O_2 detection in phosphate buffer solution (pH 6.5).

As can be seen (Figure 4.64b), Ppy synthesized in 10 mM $CuCl_2$ solution shows the highest current peak toward H_2O_2. The chemical nature of the counter ion not only affects the electroactivity of the synthesized polypyrrole, but also influences the bulk structure and surface characteristics. Additionally, the size of counter ions can adjust the surface structural properties and electrical conductivities, but counter ions with larger size can alter the density of polymer (leading to larger or smaller holes in the polymer structure which depends on the anion properties in specific size) (Abd-Elwahed & Holze, 2002) and more dramatically affect the properties such as physical handling and surface topography (Guimard *et al*., 2007).

The effect of the anion type during the electropolymerization has been reported by several groups (Abd-Elwahed & Holze, 2002; Eftekhari *et al*., 2006; Eftekhari *et al*., 2006).

During the doping and dedoping process, the polypyrrole goes through considerable volume changes. The type of anion has also an influence on the surface appearance (smooth or rough surface).

As it was discussed by many researchers, anions can be classified into two main categories; Class 1 anions including perchlorate, which develops a compact structure and Class 2 anions including sulphate and chloride leading to an open structure (Abd-Elwahed & Holze, 2002).

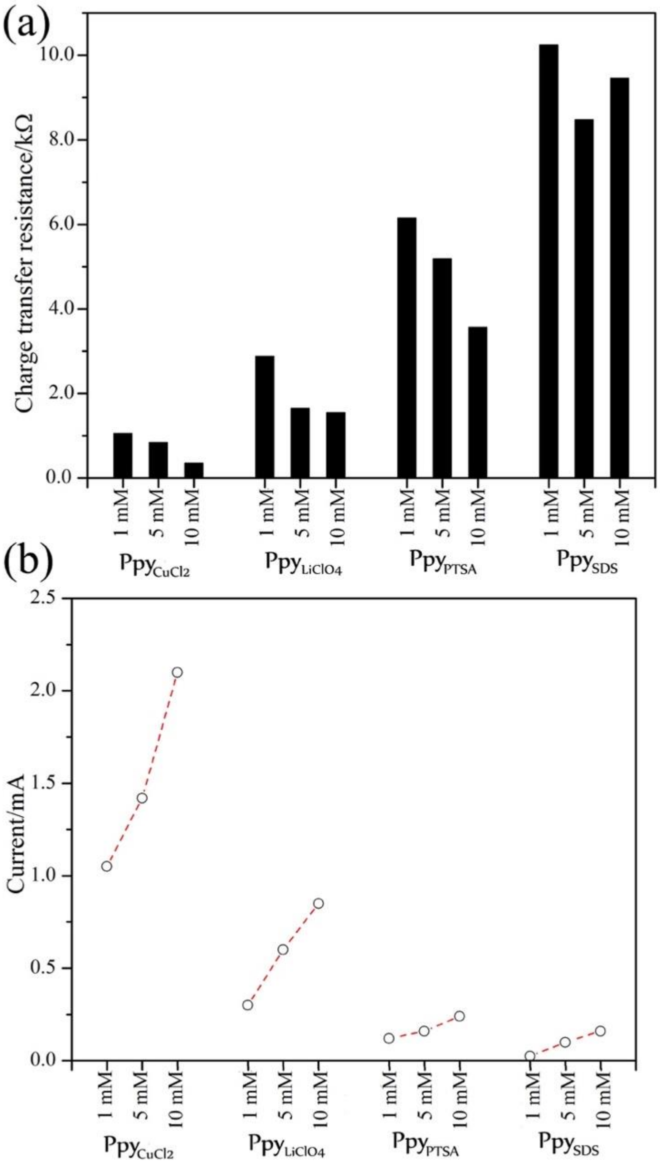

Figure 4.64: (a) Impedance value at different concentrations of $CuCl_2$, $LiClO_4$, PTSA and SDS in $Fe(CN)_6^{-3/-4}$ solution; (b) The effect of concentration and type of dopants on the current response for 1 mM H_2O_2 in phosphate buffer solution (pH 6.5).

4.7.1. X-ray Diffraction (XRD)

The Cu nanoparticles were examined by using powder XRD (Figure 4.65). Three main peaks at 43°, 51°, and 74° ranging from 10° to 80° are clearly presented in the diffraction pattern, which can be attributed to the diffraction from the (111), (200) and (220) planes, respectively.

The peak positions were in great agreement with literature values of fcc Cu (Wu & Chen, 2004). The XRD data obviously shows that the Cu nanoparticles were decorated on polypyrrole micro trunk-like surface by electrodeposition process. Further peaks of Cu or other impurities and oxidation of Cu_2O/CuO were not seen (Kang *et al.*, 2007; Yang *et al.*, 2010).

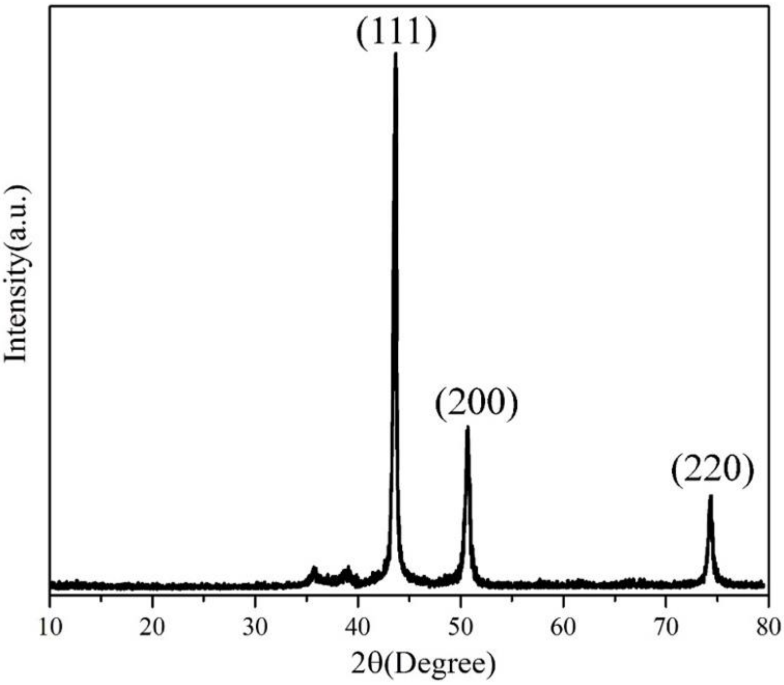

Figure 4.65: XRD spectrum of CV-Ppy_{CuCl2}MTs-CuNPs.

4.7.2. Energy-dispersive X-ray Spectroscopy (EDX)

EDX analysis was performed to approve the elemental compositions. Figure 4.66 presents the EDX spectra of PpyMTs-CuNPs. Cu element can be observed in the PpyMTs-CuNPs. This confirmed that CuNPs has been successfully deposited onto the surface micro trunk-like polypyrrole.

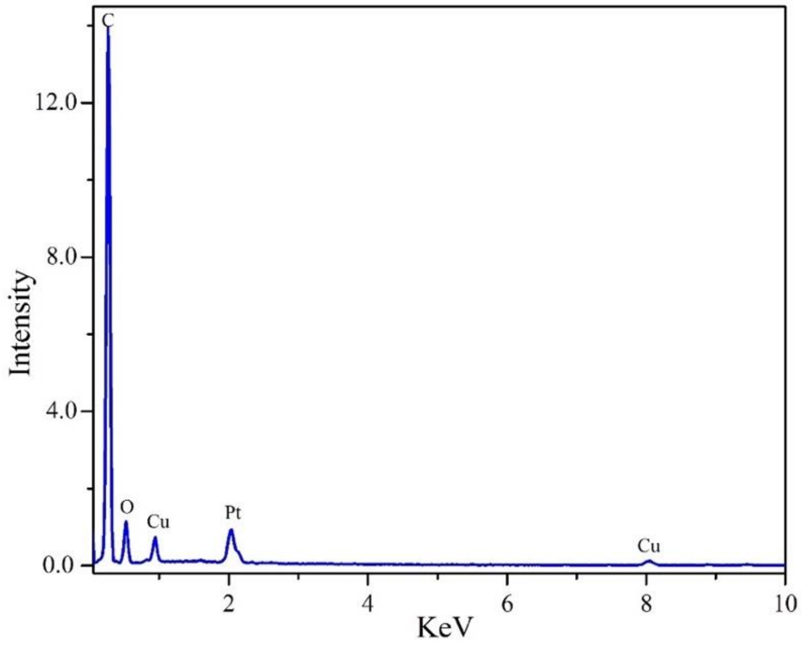

Figure 4.66: EDX spectra of CV-Ppy$_{CuCl2}$MTs-CuNPs and (inset)

4.7.3. Field Emission Scanning Electron Microscopy (FESEM)

Figure 4.67 shows the morphology of different polypyrroles, which were synthesized with four kinds of electrolyte. As can be seen, electropolymerization with SDS counter ion (Figure 4.67(a)) resulted in an unshaped polypyrrole with several holes in diameter around 500 nm. Large size of counter ion is responsible for formation of these holes. By changing the counter ion to $LiClO_4$, polypyrrole formed a semi micro fiber with 1 µm in diameter (Figure 4.67(b)). In contrast, clean and relatively smooth polypyrrole with the diameter of 100 nm has been obtained by using PTSA (Figure 4.67(c)). The Ppy$_{PTSA}$ nanowires film has a well-ordered polymer chain structure with a very high surface-to-volume ratio (Meng *et al.,* 2013). Figure 4.67(d, e) shows prepared polypyrroles $CuCl_2$ as a counter ion through amperometry and cyclic voltammetry method, respectively. As can be seen, amperometry method led to packed polypyrrole fibers with the diameter less than 1 µm. By utilizing CV method, along with the formation of micro trunk-like polypyrrole with the diameter more than 1 µm, deposition of well-defined copper nanoparticles occurred. Except for copper nanoparticles with around 30 nm in diameter, each micro trunk-like polypyrrole has a hole on the tip of itself with a diameter of around 100 nm which could improve incorporation of analytes and provide a great surface-to-volume ratio that is useful for reduction of H_2O_2 (Meng *et al.*, 2013). It is seen as an ideal interface that can be attempted in the use of electrochemical sensor.

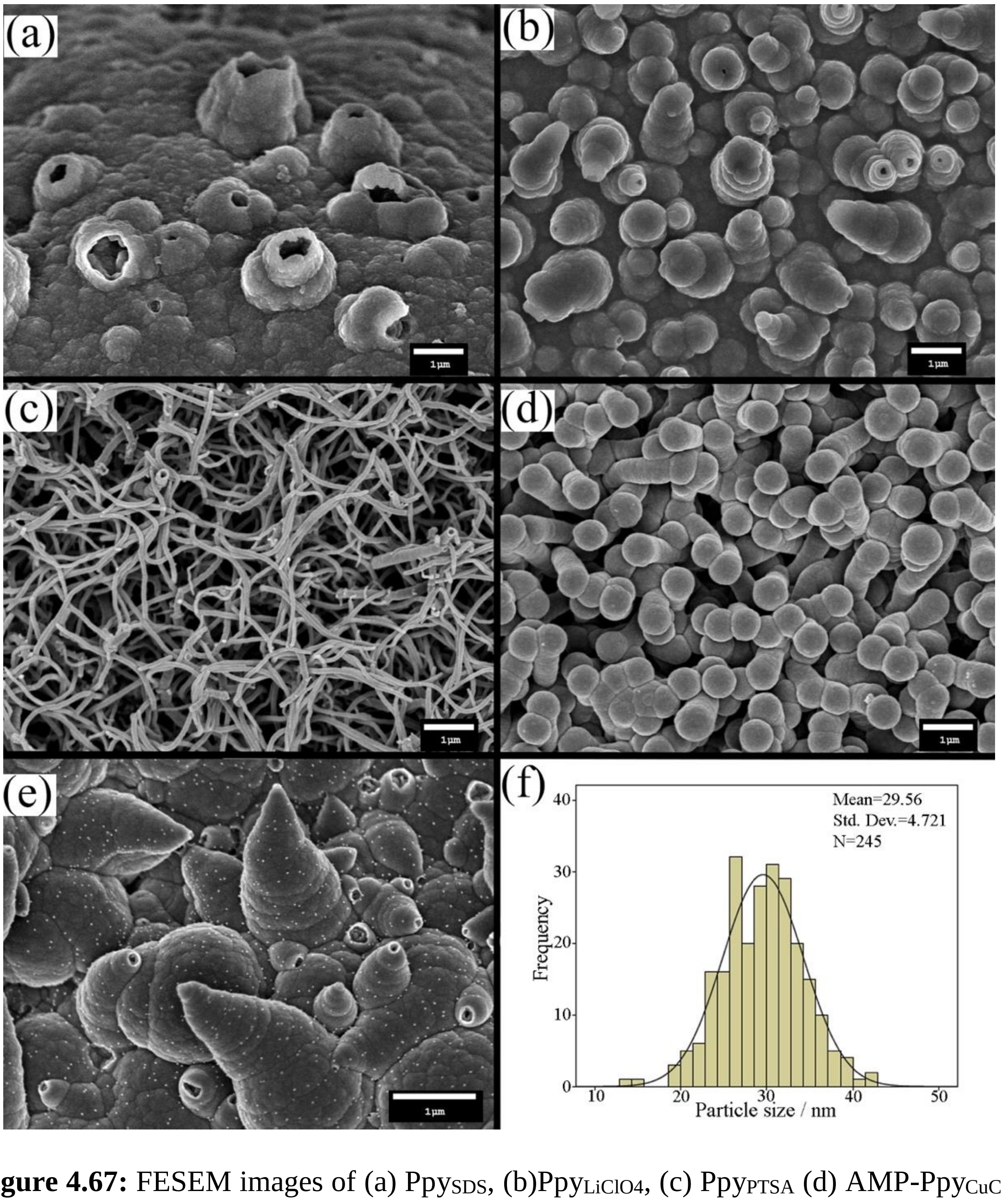

Figure 4.67: FESEM images of (a) Ppy$_{SDS}$, (b)Ppy$_{LiClO4}$, (c) Ppy$_{PTSA}$ (d) AMP-Ppy$_{CuCl2}$, (e) CV-Ppy$_{CuCl2}$MTs-CuNPs and (f) particle size distribution of copper nanoparticles.

4.7.4. Cyclic voltammetry (CV)

Figure 4.68 shows the electrocatalytic activity of all modified electrodes towards H_2O_2 in 0.1 M phosphate buffer solution (PBS) at pH 6.5.

Figure 4.68 presents that polypyrroles, which were synthesized with SDS, PTSA and $LiClO_4$ show weak peaks as compare with AMP-Ppy_{CuCl2} and CV-PpyMTs-CuNPs. This is primarily due to the incorporation of copper particles inside the polymer.

As can be seen, CV-Ppy_{CuCl2}MTs-CuNPs shows two distinct peaks. In compare with polypyrrole synthesized with copper chloride through amperometry method, CV-Ppy_{CuCl2}MTs-CuNPs shows higher catalytic peak.

It can be concluded that copper ion in the CV-Ppy_{CuCl2}MTs-CuNPs nanocomposite is in charge of the higher reduction of H_2O_2.

In a possible electrocatalytic mechanism for the H_2O_2 reduction, Cu(II) was first electrochemically reduced to Cu(I), reacting chemically with H_2O_2 and resulting in the conversion of H_2O_2 into OH^- and regeneration of the catalyst, as shown in the following equations (Mahmoudian *et al*., 2014; Zhang *et al*., 2008):

$$\mathrm{PPyMTs - CuNPs\ (II) + e^{-} \rightarrow PPyMTs - CuNPs\ (I)} \qquad \text{(Eq. 4.18)}$$

$$\mathrm{PPyMTs - CuNPs\ (I) + 1/2\ H_2O_2 \rightarrow PPyMTs - CuNPs(II) + OH^{-}} \qquad \text{(Eq. 4.19)}$$

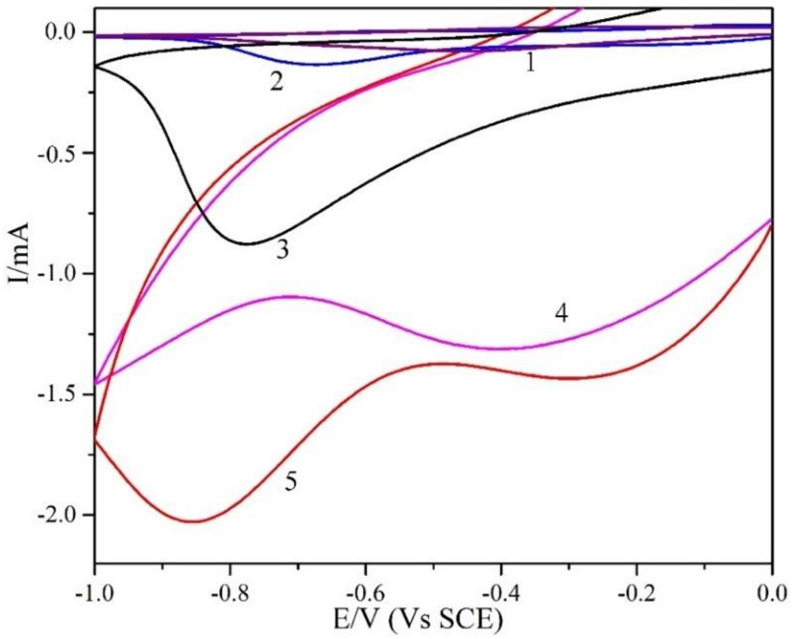

Figure 4.68. Cyclic voltammograms of (1) Ppy_{SDS}, (2) Ppy_{PTSA}, (3) Ppy_{LiClO4}, (4) AMP-Ppy_{CuCl2} and (5) CV-Ppy_{CuCl2}MTs-CuNPs in the presence of 1 mM H_2O_2 in phosphate buffer solution (pH 6.5) at scan rates of 50 mVs^{-1}.

4.7.5. Electrochemical Impedance Spectroscopy (EIS)

The Nyquist plots of Ppy_{SDS}, Ppy_{PTSA}, Ppy_{LiClO_4}, AMP-Ppy_{CuCl_2} and CV-Ppy_{CuCl2}MTs-CuNPs electrodes in the solution containing $\mathrm{Fe(CN)}_6^{-3/-4}$ are presented in Figure 4.69.

Meaningful differences in the impedance data were seen. The impedance data of modified electrodes included a semicircle part observed at higher frequency range and a linear segment at lower frequencies representing the electron transfer limited process and the diffusion-limited process, respectively.

The semicircle diameter is equal to the electron transfer resistance (R_{ct}) reflecting the conductivity. As can be seen, semicircle diameter, which indicates the film conductivity, decreases by using smaller counter ion. The following trend was observed in the modified electrodes:

R_{ct}: Ppy_{SDS} > Ppy_{PTSA} > Ppy_{LiClO_4} > AMP-Ppy_{CuCl_2} > CV-Ppy_{CuCl2}MTs-CuNPs

Counter ion size: SDS > PTSA>$LiClO_4$> $CuCl_2$

The polypyrrole synthesized through amperometric and cyclic voltammetry method showed two different behaviors. In the amperometry method, synthesized polymer with copper chloride counter ion shows a smaller semicircle than other modified electrode, which confirms the synergetic effect of copper and polypyrrole. Electropolymerization through cyclic voltammetry method leads to two semicircles with different diameters.

As can be seen from Figure 4.69, the smaller diameter is attributed to the copper nanoparticles whereas bigger semicircle is due to polypyrrole film. Figure 4.70 shows the equivalent circuits for all modified electrodes. Table 4.16 shows the EIS parameters achieved by equivalent circuits of modified electrodes.

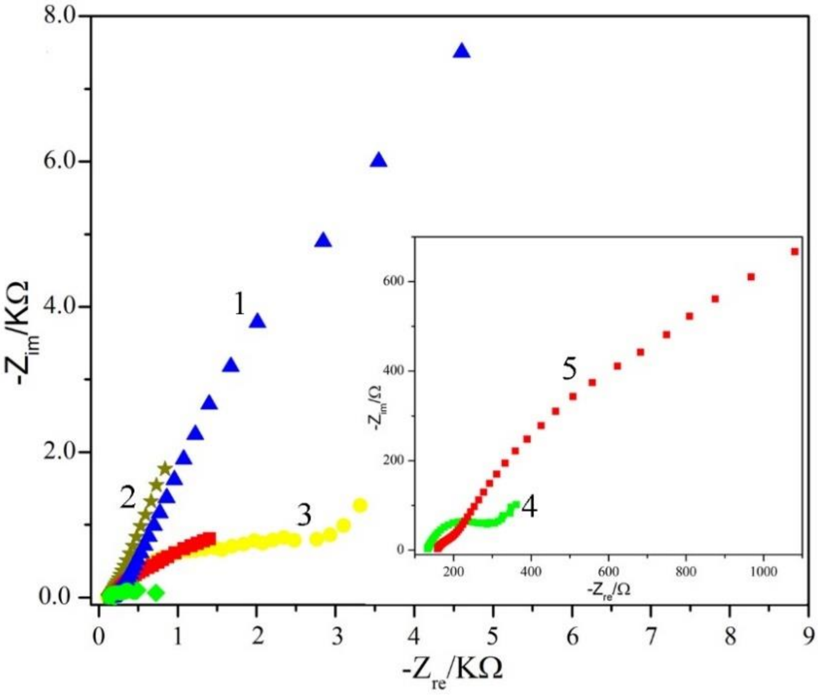

Figure 4.69: Nyquist diagrams of (1) Ppy_{SDS}, (2) Ppy_{PTSA}, (3) AMP-$Ppy_{CuCl2,}$ (4) CV-Ppy_{CuCl2}MTs-CuNPs and (5) AMP-Ppy_{CuCl2}MTs-CuNPs in 0.1 M KCl solution containing 1 mM $[Fe(CN)]_6^{(-3/-4)}$ (1:1).

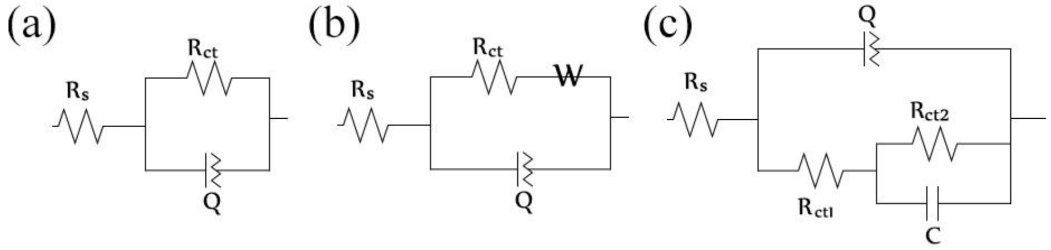

Figure 4.70: Equivalent circuits of modified electrodes.

Table 4.16: EIS parameters achieved by equivalent circuits of bare electrode, Ppy_{SDS}, Ppy_{LiClO4}, Ppy_{PTSA}, AMP-Ppy_{CuCl2} and CV-Ppy_{CuCl2}MTs-CuNPs in 0.1 M KCl solution containing 1 mM $[Fe(CN)]_6^{(-3/-4)}$ (1:1).

Electrode	**R_s (Ω)**	**R_{ct1} (Ω)**	**Q (µMho)**	**W (µMho)**	**R_{ct2} (Ω)**	**C (µF)**	**n**
Ppy_{SDS}	148	97658	162	-	-	-	0.87
Ppy_{PTSA}	154	5251	216	-	-	-	0.96
Ppy_{LiClO4}	151	2851	284	1086	-	-	0.66
AMP-Ppy_{CuCl2}	148	278	315	9349	-	-	0.78
CV-Ppy_{CuCl2}MTs-CuNPs	158	155	570	-	4412	26.4	0.58

4.7.6. Sensor optimization

To develop the performance of the H_2O_2 sensor, various factors influencing the current response of the sensor were investigated.

Figure 4.671(a) shows the influence of operating potential on the amperometric response of the CV-Ppy_{Cucl2}MTs-CuNPs and the reduction current studied under batch conditions ranging from −0.6 to −0.8 V *vs*. SCE in a solution containing 1 mM H_2O_2 in 0.1 M phosphate buffer solution (pH 6.5).

As can be seen in Figure 4. 71(a), the potential value of −0.85 V was determined as the operating potential. Figure 4.71(b) indicates the effect of the pH value of phosphate buffer solution on the reduction current of H_2O_2 on CV-Ppy$_{CuCl2}$MTs-CuNPs electrode. The current response dramatically increased with the pH changes from 4.5 to 6.5 and gradually decreased at pH higher than 6.5. It is recommended that pH 6.5 is the optimized pH for the electrochemical reduction of H_2O_2.

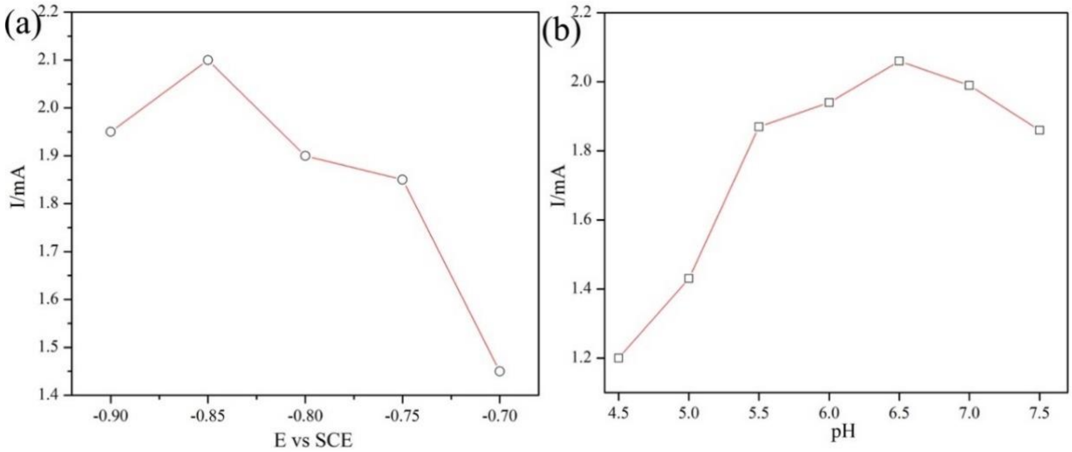

Figure 4.71: (a) Effect of the applied potential on the current response of 1 mM H_2O_2 on the CV-Ppy$_{CuCl2}$MFs-CuNPs in 0.1 M PBS (pH 6.5); (b) The effect of pH of PBS on the current response for 1 mM H_2O_2 at CV-Ppy$_{CuCl2}$MFs-CuNPs electrode.

4.7.6.1. Amperometric detection of H_2O_2

Figure 4.72 displays the current response of CV-Ppy$_{CuCl2}$MTs-CuNPs with successive addition of H_2O_2 into PBS at pH 6.5 under the applied potential of −0.85 V in the stirring condition (2000 rpm).

The response time was fast (less than 3 s) and as the concentration of H_2O_2 increases from 0.2 to 110 mM, the current increased linearly.

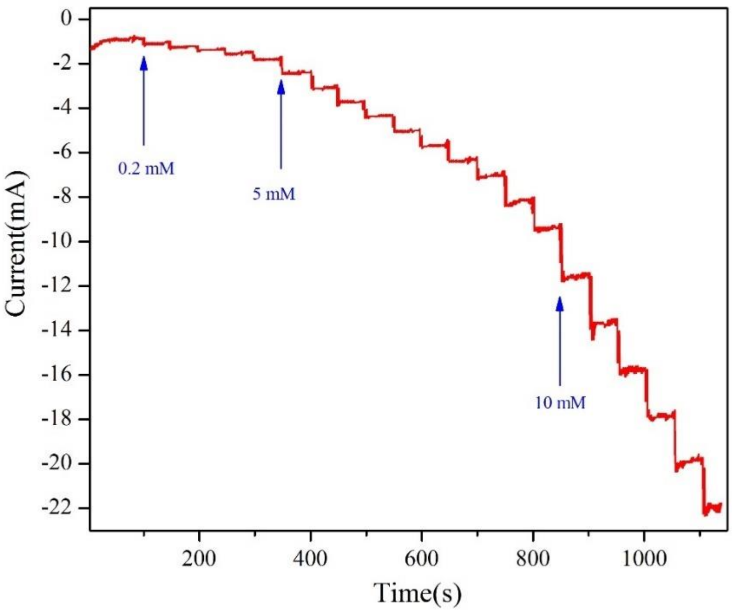

Figure 4.72: Current-time responses of CV-Ppy$_{CuCl2}$MTs-CuNPs with the subsequent addition of H_2O_2 into 0.1 M PBS (pH 6.5) at -0.85V *vs.* SCE.

In calibration curve, the sensor shows two linear sections for the response to H_2O_2. Based on the first linear section, the linear regression equation of I = 0.9 (μA.mM^{-1}) + 0.88 (R^2= 0.987) is determined, increasing from 0.2 to 1 mM (Figure 4.73 (a)), while in a higher concentration of H_2O_2, the second linear section raised up to 110 mM with a linear equation of I = 0.184 (μA.mM^{-1}) + 0.6939 (R^2= 0.995) (Figure 4.73(b)).

For the two linear parts, the LOD and LOQ (S/N = 3) are calculated to be 0.9, 3 and 4.39, 14.64 μM, respectively.

As listed in Table 4.17, the detection limit and the linear range of CV-Ppy$_{Cucl2}$MTs-CuNPs are better and wider than most of the other modified electrodes based on polypyrrole and copper.

Table 4.17: Comparison between LOD and linear range of different non-enzymatic H_2O_2 sensors with CV-Ppy$_{Cucl2}$MTs-CuNPs.

Modified electrode	**Performance**		**Ref**
	LOD (µmol.L^{-1})	**Liner range** (mmol.L^{-1})	
PPy/Mn NWs	2.2	0.005-0.09	(Mahmoudian *et al.*, 2013)
PPy NWs-Co NC	2.3	0.007-4.3	(Zhang *et al.*, 2008)
Cu/PSi-CPE	0.27	0.5–3780	(Ensafi *et al.*, 2014)
PPy-Pt	1.17	0.035-9.9	(Li *et al.*, 2010)
CuO/MWCNTs/OPpy	5 0.05	Up to 10 Up to 0.002	(Yu *et al.*, 2015)
Cu-MWCNTs	1	Up to 7.5	(Yang *et al.*, 2010)
Ag NPs/PPy/Fe_3O_4/GCE	1.7	0.005–11.5	(Qi *et al.*, 2015)
PPyNT/rGO FET-type sensor	0. 1	0.1 nM to 100 nM	(Park *et al.*, 2014)
PPy/Fe3O4 NBs	0.4715 1.5719	10-50 50-100	(Mahmoudian *et al.*, 2014)
CV-Ppy$_{Cucl2}$MTs-CuNPs	0.9 4.39	0.2-1 2-110	This work

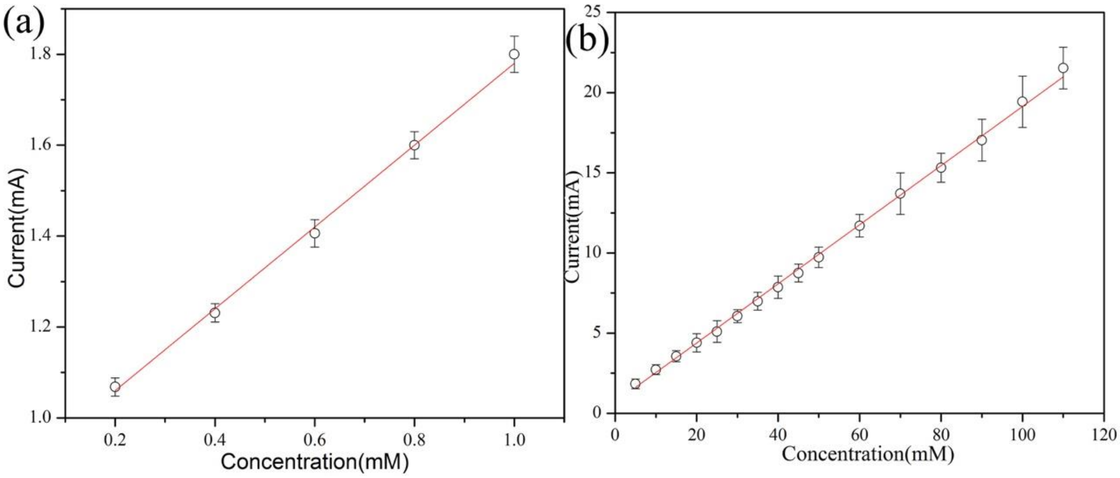

Figure 4.73: (a) Calibration curve of lower (1.0 mM) and (b) higher (110 mM) concentration range of CV-Ppy$_{CuCl2}$MTs-CuNP.

4.7.6.2. Repeatability, reproducibility and stability

The repeatability, reproducibility and stability of the prepared sensor were studied. Five modified electrodes were prepared under the same condition and relative standard deviation (RSD) of the current response toward 1 mM H_2O_2 was found to be 2.03%, confirming that the results can be reproducible.

The repeatability of the sensor to determine 1 mM H_2O_2 was fairly good. The RSD was 1.85% for 10 successive assays. In order to investigate the stability of CV-Ppy_{Cucl2}MTs-CuNPs electrode, the modified electrode was stored in the ambient condition and the current was periodically monitored for 21 days (Figure 4.74).

The current response considerably decreases by the first 10 days, and as can be seen from Figure 4.74, the sensor retains around 74% of its initial response after 3 weeks (I_0 and I are the response current in the first and following days, respectively). The main reason for this dramatic decrease during 21 days is that a passive layer could be easily formed on the surface of the copper electrode and reduces its activity (Xu *et al.*, 2006). The overall performance concluded that CV-Ppy_{Cucl2}MTs-CuNPs shows a good repeatability, reproducibility and stability.

4.7.6.3. Interference study

The effect of electroactive interfering species on modified electrode was evaluated. Figure 4.74(inset) shows the amperometric response of the CV-Ppy_{Cucl2}MTs-CuNPs towards the successive addition of 1 mM H_2O_2 and this is followed by glucose, ascorbic acid, fructose, uric acid and lactose into 0.1 M PBS at pH 6.5.

As can be seen, the current response of the mentioned electroactive interfering species is quite negligible, which confirms that CV-Ppy$_{CuCl2}$MTs-CuNPs has a superior selectivity towards H_2O_2. To prove the accuracy of the sensor, a lens-cleaning solution was used for performing the detection of H_2O_2. The H_2O_2 determination in the samples of the mentioned solution was carried out on the modified sensor employing standard addition method. The dilution of samples has been done through using phosphate buffer solution (pH 6.5) prior to determining the current response. Later, H_2O_2 solutions were successively added to the system in order to determine the current response through standard addition method. All the measurements were carried out four times.

Table 4.18 lists the average recoveries. By considering the relative standard deviation (RSD%) values and calculated recovery, it can be observed that the developed sensor holds possible applications for evaluating specific concentration range of H_2O_2.

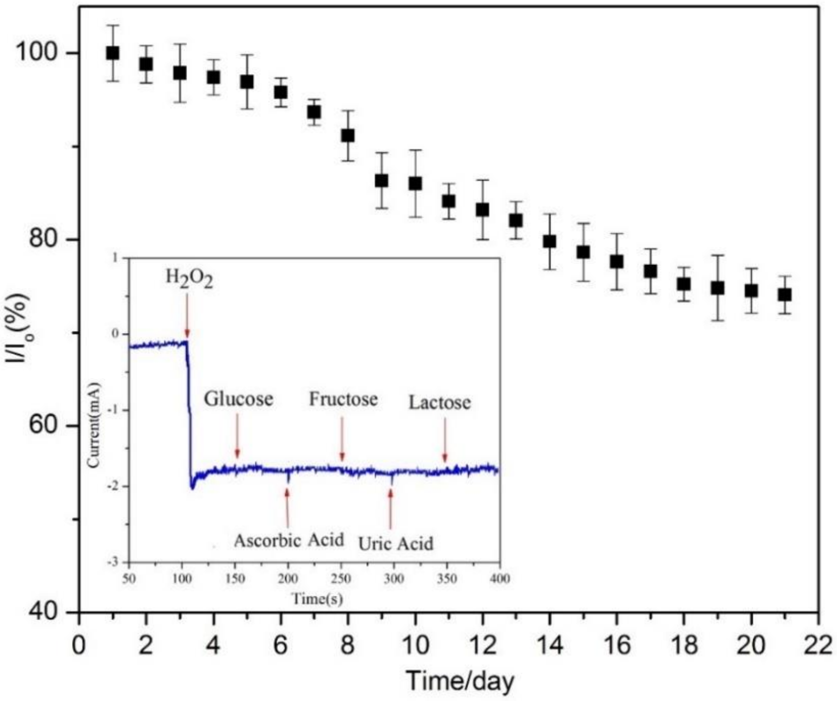

Figure 4.74: Long term stability of the CV-Ppy$_{CuCl2}$MTs-CuNPs studied in three weeks and (inset) amperometric response of CV-Ppy$_{CuCl2}$MTs-CuNPs upon the successive addition of 1 mM H_2O_2, glucose, ascorbic acid, fructose, uric acid and lactose into 0.1 M PBS (pH 6.5) with an applied potential -0.85 V *vs*. SCE.

Table 4.18: H_2O_2 determination in real samples by using CV-Ppy$_{CuCl2}$MTs-CuNPs.

Sample	Added (mM)	RSD%	Measured by sensor (mM)	Recovery%
1	0.2	6.129	0.206	103.4
2	1	1.647	0.96	96
3	10	1.561	10.114	101.14
4	50	0.907	49.392	98.78

Cyclic voltammetry was used to study the performance of modified electrode towards glucose. As can be seen from Figure 4.75, the prepared nanocomposite did not show oxidation peak at the presence of glucose, which suggesting that in this potential window, nanocomposite cannot be used as sensor for GLC detection.

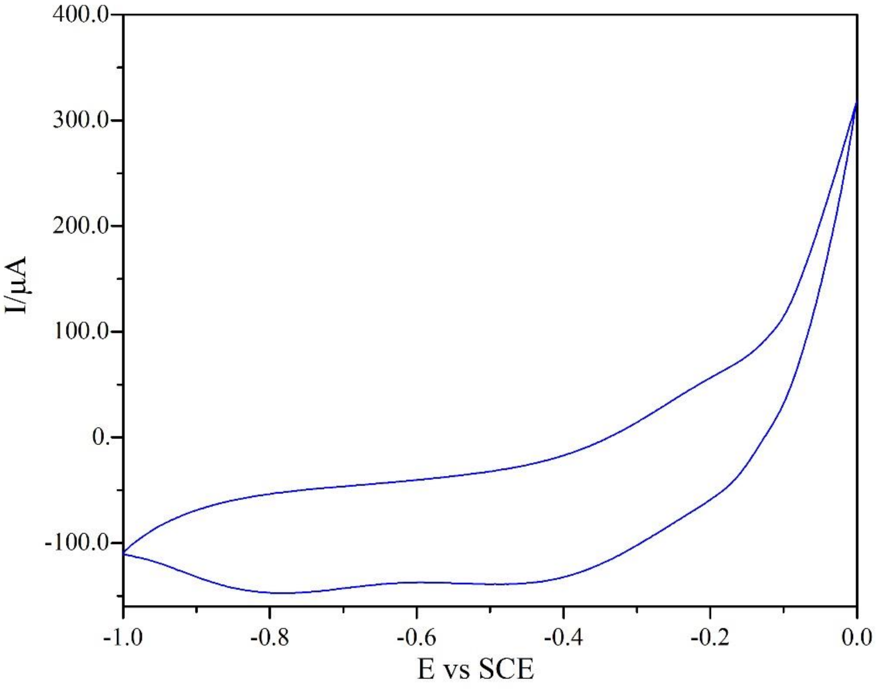

Figure 4.75: CV of CV-Ppy$_{CuCl2}$MTs-CuNPs electrode in a 0.1 M phosphate buffer solution (pH 7.2) and 1 mM glucose, scanned at 50 mVs^{-1} scan rate.

CHAPTER 5: CONCLUSION & RECOMMENDATIONS

The goal for this work was to design highly sensitive and selective non-enzymatic H_2O_2 and glucose sensor. To address this, seven modified electrodes were prepared based on combination of metal nanoparticles (CuNPs and AgNPs), polypyrrole and reduced graphene oxide.

Copper and silver nanoparticles as selected nanometals showed good detection ability towards hydrogen peroxide concentrations. Role of reduced graphene oxide in improving the sensing performance of selected nanoparticles was tested.

The enhanced electrocatalytic ability of CuNPs, AgNPs and rGO modified electrode is considered to be the result of a large surface area and high conductivity as well as fast electron transfer provided by graphene sheets, confirming its important role of graphene sheets. The electroactivity of CuNPs and AgNPs nanoparticles modified by Ppy were investigated and the finding showed the considerable improvement in H_2O_2 sensing after modification. These modified electrodes were stable enough in electrochemical measurements which possibly due to supporting matrix of Ppy. All enzyme-free H_2O_2 sensors showed good repeatability, reproducibility and selectivity towards H_2O_2 detection. There were no significant changes of current response during the detection of 1.0 mM H_2O_2 in the presence of normal physiological interferents such as ascorbic acid and uric acid and other selected sugars. All the fabricated sensors were further evaluated their performance in the determination of H_2O_2 in real samples where the results indicated the low RSD values which confirmed high possibility to use the presented nanocomposites in future for clinical diagnostics. Compared to graphene sheets, Ppy revealed better influence electrical conductivity.

Table 5.1 shows the performance of all prepared modified electrodes in H_2O_2 detection.

Table 5.1: Sensor performance comparison between all the fabricated nanocomposites.

No	**Modified electrode**	**Performance**		**Applied potential**
		LOD (µmol.L^{-1})	**Linear range** (mmol.L^{-1})	
1	rGO-CuNPs	0.601	0.1-18	-0.2
2	rGO-AgNPs	0.016	0.1-24	-0.05
3	(rGO-AgNPs)-PpyNFs	1.099 0.085	0.1-5 10-90	-0.75
4	rGO/Ppy/AgNPs	Unsatisfactory		
5	rGO/PpyNFs/Cu_xO	0.03	0.1-100	+0.2 (GLC response)
	rGO/PpyNFs/Cu_xO	0.036	0.12	-0.5 (H_2O_2 response)
6	PpyMTs-CuNPs	0.9 4.39	0.2-1 2-110	-0.85
7	PpyNFs/AgNPs	0.115 0.256	0.1-5 10-120	0.025

Compared to graphene sheets, Ppy revealed better influence electrical conductivity. Among all the prepared nanocomposites, rGO/PpyNFs/Cu_xO nanoparticles displayed the highest H_2O_2 sensing performance among the other fabricated sensors with a low detection limit of 0.3 µM and excellent sensitivity value with linear concentration range of 0.1-100 mM. In order to investigate the potential of rGO/PpyNFs/Cu_xO

nanocomposite to be applied in dual-analyte detection, this modified electrode was examined towards glucose. It showed high glucose sensing performance as well, with a low detection limit of 0.036 μM and excellent sensitivity value with linear concentration range of 0.1-100 mM.

Based on this work, future development should concentrate on further applications of this nanocomposite in other diagnostic purposes. The synergetic effect of rGO, PpyNPs and metal nanoparticles and providing high surface area and high conductivity as well as fast electron transfer of the materials are main factors which increased the performance of the electrode towards H_2O_2 and glucose. It showed the high glucose sensing performance with a low detection limit of 0.036 μM and excellent sensitivity value with linear concentration range of 0.1-100 mM.

Based on this work, further studies should concentrate on advance applications of this nanocomposite in other diagnostic purposes. Other recommendations may include:

- Applying two different noble metals at the same time with any mentioned nanocomposites matrix as an approach to further enhance the performance of the H_2O_2 sensor.
- Modify the rGO to be functionalized with any other functional groups to achieve better dispersion and less agglomeration of composite components.
- Blending two different kinds of conducting polymers in same electrode to observe the changes in term of electron transfer effect that may improve the H_2O_2 sensing performances.

References

Abd-Elwahed, A., & Holze, R. (2002). Ion size and size memory effects with electropolymerized polyaniline. *Synthetic Metals*, *131*(1–3), 61–70.

An, C. Y., Zhuo, K., Kim, W. J., & Chung, C. H. (2015). A dendritic palladium electrode for a hydrogen peroxide sensor fabricated by electrodeposition on a dynamic hydrogen-bubble template and dealloying. *Sensors and Actuators, B: Chemical*, *213*, 329–333.

An, S. J., Zhu, Y., Lee, S. H., Stoller, M. D., Emilsson, T., Park, S., Ruoff, R. S. (2010). Thin film fabrication and simultaneous anodic reduction of deposited graphene oxide platelets by electrophoretic deposition. *Journal of Physical Chemistry Letters*, *1*(8), 1259–1263.

Annamalai, S. K., Palani, B., & Chandrasekara Pillai, K. (2012). Highly stable and redox active nano copper species stabilized functionalized-multiwalled carbon nanotube/chitosan modified electrode for efficient hydrogen peroxide detection. *Colloids and Surfaces A: Physicochemical and Engineering Aspects*, *395*, 207–216.

Aradilla, D., Estrany, F., Casellas, F., Iribarren, J. I., & Alemán, C. (2014). All-polythiophene rechargeable batteries. *Organic Electronics: Physics, Materials, Applications*, *15*(1), 40–46.

Ashok Kumar, S., Lo, P.-H., & Chen, S.-M. (2009). Electrochemical Analysis of H_2O_2 and Nitrite Using Copper Nanoparticles/Poly(o-phenylenediamine) Film Modified Glassy Carbon Electrode. *Journal of The Electrochemical Society*, *156*(7), E118.

Astruc, D. (2008). Transition-metal Nanoparticles in Catalysis: From Historical Background to the State-of-the Art. *Nanoparticles and Catalysis, 16,* 1–48.

Badhulika, S., Myung, N. V., & Mulchandani, A. (2014). Conducting polymer coated single-walled carbon nanotube gas sensors for the detection of volatile organic compounds. *Talanta*, *123*, 109–114.

Bai, L., Yuan, R., Chai, Y., Yuan, Y., Mao, L., & Zhuo, Y. (2011). Highly sensitive electrochemical label-free aptasensor based on dual electrocatalytic amplification of Pt-AuNPs and HRP. *The Analyst*, *136*(9), 1840–5.

Bai, Y. H., Du, Y., Xu, J. J., & Chen, H. Y. (2007). Choline biosensors based on a bi-electrocatalytic property of MnO_2 nanoparticles modified electrodes to H_2O_2. *Electrochemistry Communications*, *9*(10), 2611–2616.

Balamurugan, A., & Chen, S. M. (2009). Silver nanograins incorporated PEDOT modified electrode for electrocatalytic sensing of hydrogen peroxide. *Electroanalysis*, *21*(12), 1419–1423.

Balandin, A. A., Ghosh, S., Bao, W., Calizo, I., Teweldebrhan, D., Miao, F., & Lau, C. N. (2008). Superior thermal conductivity of single-layer graphene. *Nano Letters*, *8*(3), 902–907.

Banks, C. E., & Compton, R. G. (2005). Exploring the electrocatalytic sites of carbon nanotubes for NADH detection: an edge plane pyrolytic graphite electrode study. *The Analyst*, *130*(9), 1232–1239.

Banks, C. E., Davies, T. J., Wildgoose, G. G., & Compton, R. G. (2005). Electrocatalysis at graphite and carbon nanotube modified electrodes: edge-plane sites and tube ends are the reactive sites. *Chemical Communications*, *7*, 829–841.

Banks, C. E., Moore, R. R., Davies, T. J., Compton, R. G., & Road, S. P. (2004). Investigation of modified basal plane pyrolytic graphite electrodes: definitive evidence for the electrocatalytic properties of the ends of carbon nanotubes. *Chemical Communications*, *2*(16), 1804–1805.

Barbero, C.A. (2005). Ion exchange at the electrode/electrolyte interface studied by probe beam deflection techniques. *Physical Chemistry Chemical Physics*, *7*(9), 1885–99.

Basirun, W. J., Sookhakian, M., Baradaran, S., Mahmoudian, M. R., & Ebadi, M. (2013). Solid-phase electrochemical reduction of graphene oxide films in alkaline solution. *Nanoscale Research Letters*, *8*(1), 397.

Becerril, H. A., Mao, J., Liu, Z., Stoltenberg, R. M., Bao, Z., & Chen, Y. (2008). Evaluation of solution-processed reduced graphene oxide films as transparent conductors. *ACS Nano*, *2*(3), 463–470.

Bidan, G., Billon, M., Livache, T., Mathis, G., Roget, A., & Torres-Rodriguez, L. M. (1999). Conducting polymers as a link between biomolecules and microelectronics. *Synthetic Metals*, *102*(1–3), 1363–1365.

Bolotin, K. I., Sikes, K. J., Jiang, Z., Klima, M., Fudenberg, G., Hone, J., Stormer, H. L. (2008). Ultrahigh electron mobility in suspended graphene. *Solid State Communications*, *146*(9–10), 351–355.

Brânzoi, V., Pilan, L., Ioniţă, M., Brânzoi, F., Branzoi, V., Pilan, L., Branzoi, F. (2004). Electropolymerization Mechanism and Electrochemical Properties of Polypyrrole Film Doped with a Large Anion. *Molecular Crystals and Liquid Crystals*, *416*(1), 73–83.

Brodie, B. C. (1859). On the Atomic Weight of Graphite. *Philosophical Transactions of the Royal Society of London*, *149*(9), 249–259.

Buck, R. P., Lindner, E., Kutner, W., & Inzelt, G. (2004). Piezoelectric chemical sensors. *Pure and Applied Chemistry*, *76*(6), 1139–1160.

Bui, M. N., Pham, X., Nam, K., Ai, C., Shin, Y., Hun, G., Seong, G. H. (2010). Electrocatalytic reduction of hydrogen peroxide by silver particles patterned on single-walled carbon nanotubes. *Sensors and Actuators B: Chemical*, *150*(1), 436–441.

Cai, W., Piner, R. D., Stadermann, F. J., Park, S., Shaibat, M. A., Ishii, Y., Ruoff, R. S. (2008). Synthesis and solid-state NMR structural characterization of 13C-labeled graphite oxide. *Scienc*, *321*(5897), 1815–7.

Campbell, F. W., & Compton, R. G. (2010). The use of nanoparticles in electroanalysis: An updated review. *Analytical and Bioanalytical Chemistry*, *396*(1), 241–259.

Cao, F., & Gong, J. (2012). Nonenzymatic glucose sensor based on CuO microfibers composed of CuO nanoparticles. *Analytica Chimica Acta*, *723*, 39–44.

Carothers, W., & Flory, P. (2008). Conducting Polymers, *Electrochimica Acta*, *1834*, 265–268.

Chandra, M., & Xu, Q. (2007). Room temperature hydrogen generation from aqueous ammonia-borane using noble metal nano-clusters as highly active catalysts. *Journal of Power Sources*, *168*(1), 135–142.

Chang, S. H., Yeh, M. H., Rick, J., Su, W. N., Liu, D. G., Lee, J. F., Hwang, B. J. (2014). Bimetallic catalyst of PtIr nanoparticles with high electrocatalytic ability for hydrogen peroxide oxidation. *Sensors and Actuators, B: Chemical*, *190*, 55–60.

Chen, H., Wang, X., Liu, G., Lin, A., Wen, Y., & Yang, H. (2015). Electrochemical construction of porous gold nanostructures on DVD substrate and its application as nonenzymatic hydrogen peroxide sensor. *Science China Chemistry*, *58*(10), 1585–1592.

Chen, H., Zhang, Z., Cai, D., Zhang, S., Zhang, B., Tang, J., & Wu, Z. (2011). A hydrogen peroxide sensor based on Ag nanoparticles electrodeposited on natural nano-structure attapulgite modified glassy carbon electrode. *Talanta*, *86*(1), 266–270.

Chen, K. J., Chandrasekara Pillai, K., Rick, J., Pan, C. J., Wang, S. H., Liu, C. C., & Hwang, B. J. (2012). Bimetallic PtM nanoparticle decorated multi-walled carbon nanotube enzyme-free, mediator-less amperometric sensor for H_2O_2. *Biosensors and Bioelectronics*, *33*(1), 120–127.

Chen, K. J., Lee, C. F., Rick, J., Wang, S. H., Liu, C. C., & Hwang, B. J. (2012). Fabrication and application of amperometric glucose biosensor based on a novel PtPd bimetallic nanoparticle decorated multi-walled carbon nanotube catalyst. *Biosensors and Bioelectronics*, *33*(1), 75–81.

Chen, L., Tang, Y., Wang, K., Liu, C., & Luo, S. (2011). Direct electrodeposition of reduced graphene oxide on glassy carbon electrode and its electrochemical application. *Electrochemistry Communications*, *13*(2), 133–137.

Chen, S., Yuan, R., Chai, Y., & Hu, F. (2013). Electrochemical sensing of hydrogen peroxide using metal nanoparticles: A review. *Microchimica Acta*, *180*(1–2), 15–32.

Chen, W., Cai, S., Ren, Q.-Q., Wen, W., & Zhao, Y.-D. (2012). Recent advances in electrochemical sensing for hydrogen peroxide: a review. *The Analyst*, *137*(1), 49.

Cheng, C., Nie, S., Li, S., Peng, H., Yang, H., Ma, L., Zhao, C. (2013). Biopolymer functionalized reduced graphene oxide with enhanced biocompatibility via mussel inspired coatings/anchors. *Journal of Materials Chemistry B*, *1*(3), 265–275.

Cherevko, S., & Chung, C. H. (2010). The porous CuO electrode fabricated by hydrogen bubble evolution and its application to highly sensitive non-enzymatic glucose detection. *Talanta*, *80*(3), 1371–1377.

Chirizzi, D., Guascito, M. R., Filippo, E., Malitesta, C., & Tepore, A. (2016). A novel nonenzymatic amperometric hydrogen peroxide sensor based on CuO@Cu_2O nanowires embedded into poly(vinyl alcohol). *Talanta*, *147*, 124–131.

Cinti, S., Arduini, F., Moscone, D., Palleschi, G., & Killard, A. J. (2014). Development of a hydrogen peroxide sensor based on screen-printed electrodes modified with inkjet-printed Prussian blue nanoparticles. *Sensor*, *14*(8), 14222–14234.

Clark, L. C., & Lyons, C. (1962). Electrode Systems for Continuous Monitoring in Cardiovascular Surgery. *Annals of the New York Academy of Sciences*, *102*(1), 29–45.

Clarke, W.L., & Santiago, J.V. (1977). The characteristics of a new glucose sensor for use in an artificial pancreatic beta cell. *Artificial Organs*, *1*(2), 78–82.

Clergereaux, R., Séguy, I., Jolinat, P., Farenc, J., & Destruel, P. (2000). Electronic conduction in electropolymerized carbazole thin films. *Journal of Physics D: Applied Physics*, *33*(16), 1947–1952.

Comba, F. N., Rubianes, M. D., Cabrera, L., Gutiérrez, S., Herrasti, P., & Rivas, G. A. (2010). Highly Sensitive and selective glucose biosensing at carbon paste electrodes modified with electrogenerated magnetite nanoparticles and glucose oxidase. *Electroanalysis*, *22*(14), 1566–1572.

Compton, O. C., & Nguyen, S. T. (2010). Graphene oxide, highly reduced graphene oxide, and graphene: Versatile building blocks for carbon-based materials. *Small*, *6*(6), 711–723.

Contractor, A. Q., Sureshkumar, T. N., Narayanan, R., Sukeerthi, S., Lal, R., & Srinivasa, R. S. (1994). Conducting polymer-based biosensors. *Electrochimica Acta*, *39*(8–9), 1321–1324.

Cosnier, S., & Karyakin, A. (2010). *Electropolymerization: Concepts, Materials and Applications*. Berlin: Springer Verlag.

Cui, X., Wu, S., Li, Y., & Wan, G. G. (2015). Sensing hydrogen peroxide using a glassy carbon electrode modified with in-situ electrodeposited platinum-gold bimetallic nanoclusters on a graphene surface. *Microchimica Acta*, *182*(1–2), 265–272.

Dai, L. (2004). *Intelligent Macromolecules for Smart Devices*. London: Structure.

Das, A., Chakraborty, B., & Sood, A. K. (2008). Raman spectroscopy of graphene on different substrates and influence of defects. *Bulletin of Materials Science*, *31*(3), 579–584.

Das, T. K., & Prusty, S. (2013). Graphene-Based Polymer Composites and Their

Applications. *Polymer-Plastics Technology and Engineering*, *52*(4), 319-331.

De Surville, R., Jozefowicz, M., Yu, L. T., Pepichon, J., & Buvet, R. (1968). Electrochemical chains using protolytic organic semiconductors. *Electrochimica Acta, 13*(6), 1451–1458.

Deng, S.-Y., Zhang, G.-Y., Shan, D., Liu, Y.-H., Wang, K., & Zhang, X.-J. (2015). Pyrocatechol violet-assisted in situ growth of copper nanoparticles on carbon nanotubes: The synergic effect for electrochemical sensing of hydrogen peroxide. *Electrochimica Acta*, *155,* 78–84.

Deshpande, P. P., Jadhav, N. G., Gelling, V. J., & Sazou, D. (2014). Conducting polymers for corrosion protection: A review. *Journal of Coatings Technology Research*, *11*(4), 473–494.

Diaz, A. F., Kanazawa, K. K., & Gardini, G. P. (1979). Electrochemical polymerization of pyrrole. *Journal of the Chemical Society, Chemical Communications,* (14), 635-636.

Diaz, A. F., & Logan, J. A. (1980). Electroactive polyaniline films. *Journal of Electroanalytical Chemistry*, *111*(1), 111–114.

Dobson, P. J., (2011). *Handbook of Biosensors and Biosensor Kinetics*. The Netherlands: Elsevier.

Dung, N. Q., Patil, D., Duong, T., Jung, H., Kim, D., & Yoon, S.-G. (2012). An amperometric glucose biosensor based on a GOx-entrapped TiO_2–SWCNT composite. *Sensors and Actuators B: Chemical, 166–167,* 103–109.

Eda, G., & Chhowalla, M. (2010). Chemically derived graphene oxide: Towards large-area thin-film electronics and optoelectronics. *Advanced Materials, 2*(22), 2392–2415.

Eftekhari, A., Harati, M., & Pazouki, M. (2006). Electrochemical synthesis of polypyrrole macro-tubes on aluminum substrate. *Synthetic Metals*, *156*(9–10), 643–647.

Eftekhari, A., Kazemzad, M., & Keyanpour-Rad, M. (2006). Significant Effect of Dopant Size on Nanoscale Fractal Structure of Polypyrrole Film. *Polymer Journal, 38*(8), 781-785.

Elzanowska, H., Abu-Irhayem, E., Skrzynecka, B., & Birss, V. I. (2004). Hydrogen peroxide detection at electrochemically and sol-gel derived Ir oxide films. *Electroanalysis*, *16*(6), 478–490.

Ensafi, A. A., Abarghoui, M. M., & Rezaei, B. (2014). Electrochemical determination of hydrogen peroxide using copper/porous silicon based non-enzymatic sensor. *Sensors and Actuators, B: Chemical*, *196,* 398–405.

Farmer, J. A., & Campbell, C. T. (2010). Ceria Maintains Smaller Metal Catalyst Particles by Strong Metal-Support Bonding. *Science*, *329*(5994), 933–936.

Fauvarque, J. F., Petit, M. A., Pfluger, F., Jutand, A., Chevrot, C., & Troupel, M. (1983).

Preparation of poly(1,4-phenylene) by nickel(0) complex catalyzed electropolymerization. *Die Makromolekulare Chemie Rapid Communications*, *4*(7), 455–457.

Fernández-Blanco, C., Colina, Á., & Heras, A. (2013). UV/Vis spectroelectrochemistry as a tool for monitoring the fabrication of sensors based on silver nanoparticle modified electrodes. *Sensors*, *13*(5), 5700–5711.

Ferrari, A. C. (2007). Raman spectroscopy of graphene and graphite: Disorder, electron-phonon coupling, doping and nonadiabatic effects. *Solid State Communications*, *143*(1–2), 47–57.

Ferrari, A. C., & Robertson, J. (2000). Interpretation of Raman spectra of disordered and amorphous carbon. *Physical Review B*, *61*(20), 14095–14107.

Flätgen, G., Wasle, S., Lübke, M., Eickes, C., Radhakrishnan, G., Doblhofer, K., & Ertl, G. (1999). Autocatalytic mechanism of H_2O_2 reduction on Ag electrodes in acidic electrolyte: experiments and simulations. *Electrochimica Acta*, *44*(25), 4499–4506.

Fridman. (1974). Simultaneous polymerization and formation of polyacetylene film on the surface of concentrated soluble Zieglertype catalyst solution. *Journal of Polymer Science - Polymer Chemistry Edition*, *12*(1), 11–20.

Fridman. (1977). Synthesis of electrically conducting organic polymers: halogen derivatives of polyacetylene, (CH). *Journal of the Chemical Society, Chemical Communications*, (16), 578–580.

Gangopadhyay, R., & De, A. (2000). Conducting polymer nanocomposites: A brief overview. *Chemistry of Materials*, *12*(3), 608–622.

Gao, P., & Liu, D. (2015). Facile synthesis of copper oxide nanostructures and their application in non-enzymatic hydrogen peroxide sensing. *Sensors and Actuators, B: Chemical*, *208*, 346–354.

Gao, R., Hu, N., Yang, Z., Zhu, Q., Chai, J., Su, Y., Zhang, Y. (2013). Paper-like graphene-Ag composite films with enhanced mechanical and electrical properties. *Nanoscale Research Letters*, *8*(1), 32.

Gao, W. (2015). The chemistry of graphene oxide. *Graphene Oxide, Springer International Publishing*, *39*(1), 61–95.

Gao, W., Alemany, L. B., Ci, L., & Ajayan, P. M. (2009). New insights into the structure and reduction of graphite oxide . *Nature Chemistry*, *1*(5), 403–408.

Gatselou, V. A., Giokas, D. L., Vlessidis, A. G., & Prodromidis, M. I. (2015). Rhodium nanoparticle-modified screen-printed graphite electrodes for the determination of hydrogen peroxide in tea extracts in the presence of oxygen. *Talanta*, *134*, 482–487.

Ge, D., Mu, J., Huang, S., Liang, P., Gcilitshana, O. U., Ji, S., Shi, W. (2011). Electrochemical synthesis of polypyrrole nanowires in the presence of gelatin. *Synthetic Metals*, *161*(1–2), 166–172.

Geim, A. K., & Novoselov, K. S. (2007). The rise of graphene. *Nature Mater.*, *6*(3), 183–191.

Geiszt, M., & Leto, T. L. (2004). The Nox family of NAD(P)H oxidases: Host defense and beyond. *Journal of Biological Chemistry, 279*(50), 51715–51718.

Gerard, M., Chaubey, A., & Malhotra, B. D. (2002). Application of conducting polymers to biosensors. *Biosensors and Bioelectronics, 17*(5), 345–359.

Gomes, A., Fernandes, E., & Lima, J. L. F. C. (2005). Fluorescence probes used for detection of reactive oxygen species. *Journal of Biochemical and Biophysical Method*, *65*(2-3), 45-80.

Gómez-Navarro, C., Meyer, J. C., Sundaram, R. S., Chuvilin, A., Kurasch, S., Burghard, M., Kaiser, U. (2010). Atomic structure of reduced graphene oxide. *Nano Letters*, *10*(4), 1144–1148.

Gómez-Navarro, C., Weitz, R. T., Bittner, A. M., Scolari, M., Mews, A., Burghard, M., & Kern, K. (2007). Electronic transport properties of individual chemically reduced graphene oxide sheets. *Nano Letters*, *7*(11), 3499–3503.

Goncalves, R. L. S., Rothschild, D. E., Quinlan, C. L., Scott, G. K., Benz, C. C., & Brand, M. D. (2014). Sources of superoxide/H_2O_2 during mitochondrial proline oxidation. *Redox Biology*, *2*(1), 901–909.

Greene, R. L., Street, G. B., & Suter, L. J. (1975). Superconductivity in polysulfur nitride $(SN)_X$. *Physical Review Letters, 34*(10), 577–579.

Guerfi, A., Trottier, J., Boyano, I., De Meatza, I., Blazquez, J. A., Brewer, S., Zaghib, K. (2014). High cycling stability of zinc-anode/conducting polymer rechargeable battery with non-aqueous electrolyte. *Journal of Power Sources, 248*, 1099–1104.

Guilbault, G. G., & Lubrano, G. J. (1973). An enzyme electrode for the amperometric determination of glucose. *Analytica Chimica Acta*, *64*(3), 439–455.

Guimard, N. K., Guimard, N. K., Gomez, N., Gomez, N., Schmidt, C. E., & Schmidt, C. E. (2007). Conducting polymers in biomedical engineering. *Progress in Polymer Science*, *32*(8–9), 876–921.

Guo, H., Wang, X.-F., Qian, Q., Wang, F., & Xia, X. (2009). A Green Approach to the Synthesis of Graphene Nanosheets. *ACS Nano*, *3*(9), 2653–2659.

Guo, S., Li, J., Ren, W., Wen, D., Dong, S., & Wang, E. (2009). Carbon nanotube/silica coaxial nanocable as a three-dimensional support for loading diverse ultra-high-density metal nanostructures: Facile preparation and use as enhanced materials for electrochemical devices and SERS. *Chemistry of Materials*, *21*(11), 2247–2257.

Guo, S., Wen, D., Dong, S., & Wang, E. (2009). Gold nanowire assembling architecture for H_2O_2 electrochemical sensor. *Talanta*, *77*(4), 1510–1517.

Ghadimi, H., Nasiri-Tabrizi, B., Moozarm Nia, P., Basirun, W.J., Tehrani, R.A., & Lorestani, F. (2015). Nanocomposites of nitrogen-doped graphene decorated with a palladium silver bimetallic alloy for use as a biosensor for methotrexate detection. *RSC Adv.*, *5*(120), 99555–99565.

Ghadimi, H., Mahmoudian, M.R., & Basirun, W.J. (2015). A sensitive dopamine biosensor based on ultra-thin polypyrrole nanosheets decorated with Pt nanoparticles. *RSC Adv.*, *5*(49), 39366–39374.

Habibi, B., Jahanbakhshi, M., & Pournaghi-Azar, M. H. (2012). Voltammetric and amperometric determination of hydrogen peroxide using a carbon-ceramic electrode modified with a nanohybrid composite made from single-walled carbon nanotubes and silver nanoparticles. *Microchimica Acta*, *177*(1–2), 185–193.

He, H., Klinowski, J., Forster, M., & Lerf, A. (1998). A new structural model for graphite oxide. *Chemical Physics Letters*, *287*(1–2), 53–56.

He, P., Liu, H., Li, Z., Liu, Y., Xu, X., & Li, J. (2004). Electrochemical deposition of silver in room-temperature ionic liquids and its surface-enhanced Raman scattering effect. *Langmuir*, *20*(23), 10260–10267.

He, X., Hu, C., Liu, H., Du, G., Xi, Y., & Jiang, Y. (2010). Building Ag nanoparticle 3D catalyst via $Na_2Ti_3O_7$ nanowires for the detection of hydrogen peroxide. *Sensors and Actuators, B: Chemical*, *144*(1), 289–294.

Heinze, J., Frontana-Uribe, B. A., & Ludwigs, S. (2010). Electrochemistry of conducting polymers-persistent models and new concepts. *Chemical Reviews*, *110*(8), 4724–4771.

Hirata, M., Gotou, T., Horiuchi, S., Fujiwara, M., & Ohba, M. (2004). Thin-film particles of graphite oxide 1: High-yield synthesis and flexibility of the particles. *Carbon*, *42*(14), 2929–2937.

Holze, R., & Wu, Y. P. (2014). Intrinsically conducting polymers in electrochemical energy technology: Trends and progress. *Electrochimica Acta*, *122*, 93–107.

Hrapovic, S., Liu, Y., Male, K. B., & Luong, J. H. T. (2004). Electrochemical Biosensing Platforms Using Platinum Nanoparticles and Carbon Nanotubes. *Analytical Chemistry*, *76*(4), 1083–1088.

Huang, J. Y., Wang, K., & Wei, Z. X. (2010). Conducting polymer nanowire arrays with enhanced electrochemical performance. *Journal of Materials Chemistry*, *20*(6), 1117–1121.

Huang, J., & Yang, Z. (2014). Synthesis of ZnO/polypyrrole composites and an application in Zn/Ni rechargeable batteries. *RSC Advances*, *4*(37), 19205–19209.

Huang, N. M., Lim, H. N., Chia, C. H., Yarmo, M. A., & Muhamad, M. R. (2011). Simple room-temperature preparation of high-yield large-area graphene oxide. *International Journal of Nanomedicine*, *6*, 3443–3448.

Hummers, W. S., & Offeman, R. E. (1958). Preparation of Graphitic Oxide. *Journal of the American Chemical Society*, *80*(6), 1339–1339.

Inzelt, G. (2011). Rise and rise of conducting polymers. *Journal of Solid State Electrochemistry*, *15*(7–8), 1711–1718.

Ishpal, & Kaur, A. (2013). Spectroscopic and electrical sensing mechanism in oxidant-mediated polypyrrole nanofibers/nanoparticles for ammonia gas. *Journal of Nanoparticle Research*, *15*(5), 1637.

Ivory, D. M., Miller, G. G., Sowa, J. M., Shacklette, L. W., Chance, R. R., & Baughman, R. H. (1979). Highly conducting charge-transfer complexes of poly(p-phenylene). *The Journal of Chemical Physics*, *71*(1979), 1506-1507.

Jakubec, P., Urbanová, V., Marková, Z., & Zbořil, R. (2015). Novel Fe@FeO@Ag nanocomposite for efficient non-enzymatic sensing of hydrogen peroxide. *Electrochimica Acta*, *153*, 62–67.

Jang, H. D., Kim, S. K., Chang, H., Choi, J. W., & Huang, J. X. (2013). Synthesis of graphene based noble metal composites for glucose biosensor. *Materials Letters*, *106*, 277–280.

Jang, J. (2006). Conducting polymer nanomaterials and their applications. *Advances in Polymer Science*, *199*(1), 189-260.

Jang, J., & Oh, J. H. (2005). Fabrication of a highly transparent conductive thin film from polypyrrole/poly(methyl methacrylate) core/shell nanospheres. *Advanced Functional Materials*, *15*(3), 494–502.

Jia, J., Kato, D., Kurita, R., Sato, Y., Maruyama, K., Suzuki, K., Niwa, O. (2007). Structure and electrochemical properties of carbon films prepared by a electron cyclotron resonance sputtering method. *Analytical Chemistry*, *79*(1), 98–105.

Jiang, L. C., & Zhang, W. D. (2009). Electrodeposition of TiO_2 nanoparticles on multiwalled carbon nanotube arrays for hydrogen peroxide sensing. *Electroanalysis*, *21*(8), 988–993.

Jiang, B. Bin, Wei, X. W., Wu, F. H., Wu, K. L., Chen, L., Yuan, G. Z., Ye, Y. (2014). A non-enzymatic hydrogen peroxide sensor based on a glassy carbon electrode modified with cuprous oxide and nitrogen-doped graphene in a nafion matrix. *Microchimica Acta*, *181*(11–12), 1463–1470.

Kaiser, A. B. (2001). Electronic transport properties of conducting polymers and carbon nanotubes. *Reports on Progress in Physics*, *64*(1), 1–49.

Kanazawa, K. K., Diaz, A. F., Geiss, R. H., Gill, W. D., Kwak, J. F., Logan, J. A., Street, G. B. (1979). “Organic metals”: polypyrrole, a stable synthetic “metallic” polymer. *J. Chem. Soc., Chem. Commun.*, (19), 854–855.

Kang, Q., Yang, L., & Cai, Q. (2008). An electro-catalytic biosensor fabricated with Pt-Au nanoparticle-decorated titania nanotube array. *Bioelectrochemistry*, *74*(1), 62–65.

Kang, X., Mai, Z., Zou, X., Cai, P., & Mo, J. (2007). A sensitive nonenzymatic glucose sensor in alkaline media with a copper nanocluster/multiwall carbon nanotube-modified glassy carbon electrode. *Analytical Biochemistry, 363*(1), 143–150.

Kaniyankandy, S., Nuwad, J., Thinaharan, C., Dey, G. K., & Pillai, C. G. S. (2007). Electrodeposition of silver nanodendrites. *Nanotechnology*, *18*(12), 125610.

Karami, H., & Nezhad, A. R. (2013). Investigation of pulse-electropolymerization of conductive polypyrrole nanostructures. *International Journal of Electrochemical Science*, *8*(6), 8905–8921.

Kathuroju, P. K., & Jampana, N. (2012). Growth of polypyrrole-horseradish peroxidase microstructures for H_2O_2 biosensor. *IEEE Transactions on Instrumentation and Measurement*, *61*(9), 2339–2345.

Khalkhali, R. A. (2005). Electrochemical synthesis and characterization of electroactive conducting polypyrrole polymers. *Russian Journal of Electrochemistry*, *41*(9), 950–955.

Koné, A., Dieng, M. M., Aaron, J. J., Lazerges, M., Jouini, M., Aeiyach, S., & Lacaze, P. C. (2005). AOT reverse micelle, a new organized medium for the electrosynthesis of polyaromatic hydrocarbons; Application to the electropolymerization of biphenyl. *Synthetic Metals*, *150*(3), 227–239.

Kopecká, J., Kopecký, D., Vrňata, M., Fitl, P., Stejskal, J., Trchová, M., Sapurina, I. (2014). Polypyrrole nanotubes: mechanism of formation. *RSC Adv.*, *4*(4), 1551–1558.

Kopelevich, Y., & Esquinazi, P. (2007). Graphene Physics in Graphite. *Advance Materials*, *19*, 9.

Kovtyukhova, N. I., Ollivier, P. J., Martin, B. R., Mallouk, T. E., Chizhik, S. a., Buzaneva, E. V., & Gorchinskiy, A. D. (1999). Layer-by-Layer Assembly of Ultrathin Composite Films from Micron-Sized Graphite Oxide Sheets and Polycations. *Chemistry of Materials*, *11*(3), 771–778.

Kudin, K. N., Ozbas, B., Schniepp, H. C., Prud'homme, R. K., Aksay, I. A., & Car, R. (2008). Raman spectra of graphite oxide and functionalized graphene sheets. *Nano Letters*, *8*(1), 36–41.

Laloi, C., Apel, K., & Danon, A. (2004). Reactive oxygen signalling: The latest news. *Current Opinion in Plant Biology*, *7*(3), 323–328.

Láng, G. G., Ujvári, M., Rokob, T. a., & Inzelt, G. (2006). The brush model of the polymer films-analysis of the impedance spectra of Au,Pt|poly(o-phenylenediamine) electrodes. *Electrochimica Acta*, *51*(8–9), 1680–1694.

Le, W. Z., & Liu, Y. Q. (2009). Preparation of nano-copper oxide modified glassy carbon electrode by a novel film plating/potential cycling method and its characterization. *Sensors and Actuators, B: Chemical*, *141*(1), 147–153.

Lee, C., Wei, X., Kysar, J. W., & Hone, J. (2008). Measurement of the elastic properties and intrinsic strength of monolayer graphene. *Science*, *321*(5887), 385–388.

Lee, J. H., Tang, I. N., & Weinstein-Lloyd, J. B. (1990). A non-enzymatic method for the determination of hydrogen peroxide in atmospheric samples. *Analytical Chemistry*, *62*(21), 2381–2384.

Leonardi, S. G., Aloisio, D., Donato, N., Russo, P. A., Ferro, M. C., Pinna, N., & Neri, G. (2014). Amperometric Sensing of H_2O_2 using Pt-TiO_2/Reduced Graphene Oxide Nanocomposites. *ChemElectroChem*, *1*(3), 617–624.

Lerf, A., He, H., Forster, M., & Klinowski, J. (1998). Structure of Graphite Oxide Revisited. *Journal of Physical Chemistry B*, *102*(23), 4477–4482.

Li, J., Qiu, J. D., Xu, J. J., Chen, H. Y., & Xia, X. H. (2007). The synergistic effect of prussian-blue-grafted carbon nanotube/ poly(4-vinylpyridine) composites for amperometric sensing. *Advanced Functional Materials*, *17*(9), 1574–1580.

Li, J., Yuan, R., Chai, Y., Zhang, T., & Che, X. (2010). Direct electrocatalytic reduction of hydrogen peroxide at a glassy carbon electrode modified with polypyrrole nanowires and platinum hollow nanospheres. *Microchimica Acta*, *171*(1), 125–131.

Li, L., Du, Z., Liu, S., Hao, Q., Wang, Y., Li, Q., & Wang, T. (2010). A novel nonenzymatic hydrogen peroxide sensor based on MnO_2/graphene oxide nanocomposite. *Talanta*, *82*(5), 1637–1641.

Li, M., Yan, W., Zhu, H., Xia, S., Wu, H., & Tang, Z. (2015). Synthesis and gas sensing properties of biomorphic SnO_2 derived from loofah sponge and eggshell membrane. *Journal of Materials Science: Materials in Electronics*, *26*(12), 9561–9570.

Li, M., Zhu, H., Mao, X., Xiao, W., & Wang, D. (2013). Electropolymerization of polypyrrole at the three-phase interline: Influence of polymerization conditions. *Electrochimica Acta*, *92*(0), 108–116.

Li, X., Wang, L., Wu, Q., Chen, Z., & Lin, X. (2014). A nonenzymatic hydrogen peroxide sensor based on Au-Ag nanotubes and chitosan film. *Journal of Electroanalytical Chemistry*, *735*, 19–23.

Li, Z. F., Zhang, H., Liu, Q., Liu, Y., Stanciu, L., & Xie, J. (2014). Novel pyrolyzed polyaniline-grafted silicon nanoparticles encapsulated in graphene sheets as Li-ion battery anodes. *ACS Applied Materials and Interfaces*, *6*(8), 5996–6002.

Li, Z., He, Y., Ke, X., Gan, L., Zhao, J., Cui, G., & Wu, G. (2015). Three-dimensional nanoporous gold-cobalt oxide electrode for high-performance electroreduction of hydrogen peroxide in alkaline medium. *Journal of Power Sources*, *294*, 136–140.

Lim, C. S., Sofer, Z., Toh, R. J., Eng, A. Y. S., Luxa, J., & Pumera, M. (2015). Iridium- and Osmium-decorated Reduced Graphenes as Promising Catalysts for Hydrogen Evolution. *ChemPhysChem*, *16*(9), 1898–1905.

Lima, L. R., Moraes, M. L., Nigoghossian, K., Peres, M. F. S., & Ribeiro, S. J. L. (2016). Silk fibroin-antigenic peptides-YVO_4:Eu^{3+} nanostructured thin films as sensors for hepatitis C. *Journal of Luminescence*, *170*, 375–379.

Lin, C. Y., Lai, Y. H., Balamurugan, A., Vittal, R., Lin, C. W., & Ho, K. C. (2010).

Electrode modified with a composite film of ZnO nanorods and Ag nanoparticles as a sensor for hydrogen peroxide. *Talanta*, *82*(1), 340–347.

Lin, M. S., & Leu, H. J. (2005). A Fe_3O_4-based chemical sensor for cathodic determination of hydrogen peroxide. *Electroanalysis*, *17*(22), 2068–2073.

Lin, W. J., Liao, C. S., Jhang, J. H., & Tsai, Y. C. (2009). Graphene modified basal and edge plane pyrolytic graphite electrodes for electrocatalytic oxidation of hydrogen peroxide and nicotinamide adenine dinucleotide. *Electrochemistry Communications*, *11*(11), 2153–2156.

Lin, Y., Li, L., Hu, L., Liu, K., & Xu, Y. (2014). Multifunctional poly(dopamine)-assisted synthesis of silver nano particles/carbon nanotubes nanocomposite: Toward electrochemical sensing of hydrogen peroxide with enhanced sensitivity. *Sensors and Actuators, B: Chemical*, *202*, 527–535.

Lin, W. De, Chang, H. M., & Wu, R. J. (2013). Applied novel sensing material graphene/polypyrrole for humidity sensor. *Sensors and Actuators, B: Chemical*, *181*, 326–331.

Liu, A., Geng, H., Xu, C., & Qiu, H. (2011). A three-dimensional hierarchical nanoporous PdCu alloy for enhanced electrocatalysis and biosensing. *Analytica Chimica Acta*, *703*(2), 172–178.

Liu, C., Wang, K., Luo, S., Tang, Y., & Chen, L. (2011). Direct electrodeposition of graphene enabling the one-step synthesis of graphene-metal nanocomposite films. *Small*, *7*(9), 1203–1206.

Liu, S., Tian, J., Wang, L., Li, H., Zhang, Y., & Sun, X. (2010). Stable aqueous dispersion of graphene nanosheets: Noncovalent functionalization by a polymeric reducing agent and their subsequent decoration with Ag nanoparticles for enzymeless hydrogen peroxide detection. *Macromolecules*, *43*(23), 10078–10083.

Liu, S., Tian, J., Wang, L., & Sun, X. (2011). A method for the production of reduced graphene oxide using benzylamine as a reducing and stabilizing agent and its subsequent decoration with Ag nanoparticles for enzymeless hydrogen peroxide detection. *Carbon*, *49*(10), 3158–3164.

Liu, X. X., Xu, X. W., Zhu, H., & Yang, X. R. (2013). Synthesis of graphene nanosheets with incorporated silver nanoparticles for enzymeless hydrogen peroxide detection. *Analytical Methods*, *5*(9), 2298–2304.

Liu, Y., Zhang, B. H., Xiao, S. Y., Liu, L. L., Wen, Z. B., & Wu, Y. P. (2014). A nanocomposite of MoO_3 coated with PPy as an anode material for aqueous sodium rechargeable batteries with excellent electrochemical performance. *Electrochimica Acta*, *116*, 512–517.

Lorestani, F., Shahnavaz, Z., Mn, P., Alias, Y., & Manan, N. S. A. (2015). One-step hydrothermal green synthesis of silver nanoparticle-carbon nanotube reduced-graphene oxide composite and its application as hydrogen peroxide sensor. *Sensors and Actuators, B: Chemical*, *208*(0), 389–398.

Lorestani, F., Shahnavaz, Z., Nia, P. M., Alias, Y., & Manan, N. S. A. (2015). One-step preparation of silver-polyaniline nanotube composite for non-enzymatic hydrogen peroxide detection. *Applied Surface Science*, *347,* 816–823.

Lorestani, F., Moozarm Nia P., Alias, Y., & Manan, N.S.A. (2015). One-Step Synthesis of Different Silver-Polyaniline Composite Morphologies for Enzymless Hydrogen Peroxide Detection. *Journal of the Electrochemical Society*, *162*(7), B193–B200.

Lu, J., Do, I., Drzal, L. T., Worden, R. M., & Lee, I. (2008). Nanometal-decorated exfoliated graphite nanoplatelet based glucose biosensors with high sensitivity and fast response. *ACS Nano*, *2*(9), 1825–1832.

Lu, W., Liao, F., Luo, Y., Chang, G., & Sun, X. (2011). Hydrothermal synthesis of well-stable silver nanoparticles and their application for enzymeless hydrogen peroxide detection. *Electrochimica Acta*, *56*(5), 2295–2298.

Lu, W., Luo, Y., Chang, G., Asiri, A. M., Al-Youbi, A. O., & Sun, X. (2012). Supramolecular microfibrils of o-phenylenediamine dimers: Oxidation-induced formation of Au nanoparticle-decorated nanoplates for H_2O_2 detection. *Current Nanoscience*, *8*(2), 221–225.

Lui, C. H., Liu, L., Mak, K. F., Flynn, G. W., & Heinz, T. F. (2009). Ultraflat graphene. *Nature*, *462*(7271), 339–341.

Luo, B., Li, X., Yang, J., Li, X., Xue, L., Li, X., Jiang, L. (2014). Non-enzymatic electrochemical sensors for the detection of hydrogen peroxide based on Cu_2O/Cu nanocomposites. *Analytical Methods*, *6*(4), 1114–1120.

Luo, J., Jiang, S., Zhang, H., Jiang, J., & Liu, X. (2012). A novel non-enzymatic glucose sensor based on Cu nanoparticle modified graphene sheets electrode. *Analytica Chimica Acta*, *709*, 47–53.

Luo, J., Zhang, H., Jiang, S., Jiang, J., & Liu, X. (2012). Facile one-step electrochemical fabrication of a non-enzymatic glucose-selective glassy carbon electrode modified with copper nanoparticles and graphene. *Microchimica Acta*, *177*(3–4), 485–490.

Luo, Y., Lu, W., Chang, G., Liao, F., & Sun, X. (2011). One-step preparation of Ag nanoparticle-decorated coordination polymer nanobelts and their application for enzymeless H_2O_2 detection. *Electrochimica Acta*, *56*(24), 8371–8374.

Luque, G. L., Rodríguez, M. C., & Rivas, G. A. (2005). Glucose biosensors based on the immobilization of copper oxide and glucose oxidase within a carbon paste matrix. *Talanta*, *66*(2), 467–471.

Ma, P., Zhu, H., Wei, J., & Zhang, M. (2015). Facile Fabrication of Au Nanoparticles Immobilized on Polyaniline Nanofibers: High Sensitive Nonenzymatic Hydrogen Peroxide Sensor. *Nanoscience and Nanotechnology Letters*, *7*(2), 127–133.

Mabrook, M., & Zeze, D. (2015). Editorial: Graphene electronics. *IET Circuits, Devices & Systems*, *9*(1), 2–3.

Mahmood, N., Zhang, C., Yin, H., & Hou, Y. (2014). Graphene-based nanocomposites for energy storage and conversion in lithium batteries, supercapacitors and fuel cells. *Journal of Materials Chemistry A*, *2*(1), 15–32.

Mahmoudian, M.R., Alias, Y., Basirun, W.J., Woi, P.M., & Yousefi, R. (2014). Synthesis of Polypyrrole Coated Silver Nanostrip Bundles and Their Application for Detection of Hydrogen Peroxide. *Journal of the Electrochemical Society, 161*(9), H487–H492.

Mahmoudian, M. R., Alias, Y., & Basirun, W. J. (2012). The electrical properties of a sandwich of electrodeposited polypyrrole nanofibers between two layers of reduced graphene oxide nanosheets. *Electrochimica Acta*, *72*, 53–60.

Mahmoudian, M. R., Alias, Y., Basirun, W. J., & Ebadi, M. (2012). Preparation of ultra-thin polypyrrole nanosheets decorated with Ag nanoparticles and their application in hydrogen peroxide detection. *Electrochimica Acta*, *72*, 46–52.

Mahmoudian, M. R., Alias, Y., Basirun, W. J., Moradi Golsheikh, A., & Jamali-Sheini, F. (2013). Synthesis of polypyrrole coated manganese nanowires and their application in hydrogen peroxide detection. *Materials Chemistry and Physics*, *141*(1), 298–303.

Mahmoudian, M. R., Alias, Y., Basirun, W. J., Woi, P. M., Baradaran, S., & Sookhakian, M. (2014). Synthesis, characterization, and sensing applications of polypyrrole coated Fe_3O_4 nanostrip bundles. *Ceramics International*, *40*(7 Part A), 9265–9272.

Mahmoudian, M. R., Alias, Y., Basirun, W. J., Woi, P. M., & Sookhakian, M. (2014). Facile preparation of MnO_2 nanotubes/reduced graphene oxide nanocomposite for electrochemical sensing of hydrogen peroxide. *Sensors and Actuators, B: Chemical*, *201*, 526–534.

Malhotra, B. D., Chaubey, A., & Singh, S. P. (2006). Prospects of conducting polymers in biosensors. *Analytica Chimica Acta*, *578*(1), 59–74.

Mani, V., Devasenathipathy, R., Chen, S. M., Wang, S. F., Devi, P., & Tai, Y. (2015). Electrodeposition of copper nanoparticles using pectin scaffold at graphene nanosheets for electrochemical sensing of glucose and hydrogen peroxide. *Electrochimica Acta*, *176*, 804–810.

Manivannan, S., & Ramaraj, R. (2009). Core-shell Au/Ag nanoparticles embedded in silicate sol-gel network for sensor application towards hydrogen peroxide. *Journal of Chemical Sciences*, *121*(5), 735–743.

Mayavan, S., Sim, J.-B., & Choi, S.-M. (2012). Simultaneous reduction, exfoliation and functionalization of graphite oxide into a graphene-platinum nanoparticle hybrid for methanol oxidation. *Journal of Materials Chemistry*, *22*(2), 6953.

McAllister, M. J., Li, J. L., Adamson, D. H., Schniepp, H. C., Abdala, A. A., Liu, J., Aksay, I. A. (2007). Single sheet functionalized graphene by oxidation and thermal expansion of graphite. *Chemistry of Materials*, *19*(18), 4396–4404.

McCreery, R. L. (2008). Advanced carbon electrode materials for molecular electrochemistry. *Chemical Reviews*, *108*(7), 2646–2687.

Meher, S. K., & Rao, G. R. (2013). Archetypal sandwich-structured CuO for high performance non-enzymatic sensing of glucose. *Nanoscale*, *5*(5), 2089–99.

Meng, F., Shi, W., Sun, Y., Zhu, X., Wu, G., Ruan, C., Ge, D. (2013). Nonenzymatic biosensor based on Cu_xO nanoparticles deposited on polypyrrole nanowires for improving detection range. *Biosensors and Bioelectronics*, *42*(1), 141–147.

Meng, F., Yan, X., Liu, J., Gu, J., & Zou, Z. (2011). Nanoporous gold as non-enzymatic sensor for hydrogen peroxide. *Electrochimica Acta*, *56*(12), 4657–4662.

Miao, X. M., Yuan, R., Chai, Y. Q., Shi, Y. T., & Yuan, Y. Y. (2008). Direct electrocatalytic reduction of hydrogen peroxide based on Nafion and copper oxide nanoparticles modified Pt electrode. *Journal of Electroanalytical Chemistry*, *612*(2), 157–163.

Mikat, J., Orgzall, I., & Hochheimer, H. D. (2001). Optical absorption and vibrational spectroscopy of conducting polypyrrole under pressure. *Synthetic Metals*, *116*(1–3), 167–170.

Mkhoyan, K. A., Contryman, A. W., Silcox, J., Stewart, D. A., Eda, G., Mattevi, C., Chhowalla, M. (2009). Atomic and electronic structure of graphene-oxide. *Nano Letters*, *9*(3), 1058–1063.

Molapo, K.M., Ndangili, P.M., Ajayi, R.F., Mbambisa, G., Mailu, S.M., Njomo, N., Iwuoha, E.I. (2012). Electronics of Conjugated Polymers (I): Polyaniline. *International Journal of Electrochemical Science*, *7*(12), 11859–11875.

Momeni, S., & Nabipour, I. (2015). A Simple Green Synthesis of Palladium Nanoparticles with Sargassum Alga and Their Electrocatalytic Activities Towards Hydrogen Peroxide. *Applied Biochemistry and Biotechnology*, *176*(7), 1937–1949.

Moradi Golsheikh, A., Huang, N. M., Lim, H. N., Zakaria, R., & Yin, C. Y. (2013). One-step electrodeposition synthesis of silver-nanoparticle-decorated graphene on indium-tin-oxide for enzymeless hydrogen peroxide detection. *Carbon*, *62*, 405–412.

Mu, S. (2011). The electrocatalytic oxidative polymerization of o-phenylenediamine by reduced graphene oxide and properties of poly(o-phenylenediamine). *Electrochimica Acta*, *56*(11), 3764–3772.

Niu, X., Chen, C., Zhao, H., Chai, Y., & Lan, M. (2012). Novel snowflake-like Pt-Pd bimetallic clusters on screen-printed gold nanofilm electrode for H_2O_2 and glucose sensing. *Biosensors and Bioelectronics*, *36*(1), 262–266.

Niwa, O., Jia, J., Sato, Y., Kato, D., Kurita, R., Maruyama, K., Hirono, S. (2006). Electrochemical performance of angstrom level flat sputtered carbon film consisting of sp^2 and sp^3 mixed bonds. *Journal of the American Chemical Society*, *128*(22), 7144–7145.

Nogueira, R. F. P., Oliveira, M. C., & Paterlini, W. C. (2005). Simple and fast spectrophotometric determination of H_2O_2 in photo-Fenton reactions using metavanadate. *Talanta*, *66*(1), 86–91.

Novoselov, K. S., Geim, A. K., Morozov, S. V, Jiang, D., Zhang, Y., Dubonos, S. V, Firsov, A. A. (2004). Electric Field Effect in Atomically Thin Carbon Films. *Science*, *306*(5696), 666–669.

Novoselov, K. S., Jiang, Z., Zhang, Y., Morozov, S. V., Stormer, H. L., Zeitler, U., Geim, A. K. (2007). Room-Temperature Quantum Hall Effect in Graphene. *Science*, *315*(5817), 1379–1379.

Okawa, Y., Yokoyama, N., Sakai, Y., & Shiba, F. (2015). Direct electron transfer biosensor for hydrogen peroxide carrying nanocomplex composed of horseradish peroxidase and Au-nanoparticle – Characterization and application to bienzyme systems. *Analytical Chemistry Research*, *5*, 1–8.

Okumura, M., Akita, T., Haruta, M., Wang, X., Kajikawa, O., & Okada, O. (2003). Multi-component noble metal catalysts prepared by sequential deposition precipitation for low temperature decomposition of dioxin. *Applied Catalysis B: Environmental*, *41*(1–2), 43–52.

Orlita, M., Faugeras, C., Plochocka, P., Neugebauer, P., Martinez, G., Maude, D. K., Potemski, M. (2008). Approaching the dirac point in high-mobility multilayer epitaxial graphene. *Physical Review Letters*, *101*(26), 267601.

Palanisamy, S., Chen, S. M., & Sarawathi, R. (2012). A novel nonenzymatic hydrogen peroxide sensor based on reduced graphene oxide/ZnO composite modified electrode. *Sensors and Actuators, B: Chemical*, *166–167*, 372–377.

Pandey, D., Reifenberger, R., & Piner, R. (2008). Scanning probe microscopy study of exfoliated oxidized graphene sheets. *Surface Science*, *602*(9), 1607–1613.

Paneri, A., Heo, Y., Ehlert, G., Cottrill, A., Sodano, H., Pintauro, P., & Moghaddam, S. (2014). Proton selective ionic graphene-based membrane for high concentration direct methanol fuel cells. *Journal of Membrane Science*, *467*, 217–225.

Panigrahi, R., & Srivastava, S. K. (2015). Trapping of microwave radiation in hollow polypyrrole microsphere through enhanced internal reflection: a novel approach. *Scientific Reports*, *5*, 7638.

Parades, J. I., Villar-Rodil, S., Martínez-Alonso, A., & Tascón, J. M. D. (2008). Graphene oxide dispersions in organic solvents. *Langmuir*, *24*(19), 10560–10564.

Paredes, J. I., Villar-Rodil, S., Solís-Fernández, P., Martínez-Alonso, A., & Tascón, J. M. D. (2009). Atomic force and scanning tunneling microscopy imaging of graphene nanosheets derived from graphite oxide. *Langmuir*, *25*(10), 5957–5968.

Park, J. W., Park, S. J., Kwon, O. S., Lee, C., & Jang, J. (2014). Polypyrrole nanotube embedded reduced graphene oxide transducer for field-effect transistor-type H_2O_2 biosensor. *Analytical Chemistry*, *86*(3), 1822–1828.

Park, S., Dikin, D. A., Nguyen, S. T., & Ruoff, R. S. (2009). Graphene oxide sheets chemically cross-linked by polyallylamine. *Journal of Physical Chemistry C*, *113*(36), 15801–15804.

Parnell, C. M., Watanabe, F., Nasini, U. B., Berry, B. C., Mitchell, T., Shaikh, A. U., & Ghosh, A. (2015). Electrochemical sensing of hydrogen peroxide using a cobalt(III) complex supported on carbonaceous nanomaterials. *Journal of Electroanalytical Chemistry*, *740*, 37–44.

Pei, S., & Cheng, H. M. (2012). The reduction of graphene oxide. *Carbon, 50*(9), 3210–3228.

Pham, V. H., Cuong, T. V., Hur, S. H., Oh, E., Kim, E. J., Shin, E. W., & Chung, J. S. (2011). Chemical functionalization of graphene sheets by solvothermal reduction of a graphene oxide suspension in N-methyl-2-pyrrolidone. *Journal of Materials Chemistry*, *21*(10), 3371.

Qi, C. & Zheng, J. (2015). Novel nonenzymatic hydrogen peroxide sensor based on Fe_3O_4/PPy/Ag nanocomposites. *Journal of Electroanalytical Chemistry*, *747*, 53–58.

Qiu, R., Cha, H. G., Noh, H. B., Shim, Y. B., Zhang, X. L., Qiao, R., Kang, Y. S. (2009). Preparation of dendritic copper nanostructures and their characterization for electroreduction. *Journal of Physical Chemistry C, 113*(36), 15891–15896.

Rabolt, J. F., Clarke, T. C., Kanazawa, K. K., Reynolds, J. R., & Street, G. B. (1980). Organic metals: poly-(p-phenylene sulphide) hexafluoroarsenate. *Journal of the Chemical Society, Chemical Communications*, (8), 347.

Rajkumar, M., Thiagarajan, S., & Chen, S. M. (2011). Electrochemical fabrication of Rh-Pd particles and electrocatalytic applications. *Journal of Applied Electrochemistry*, *41*(6), 663–668.

Ramanathan, K., Pandey, S. S., Kumar, R., Gulati, A., Surya, A., Murthy, N., & Malhotra, B. D. (2000). Covalent immobilization of glucose oxidase to poly(o-amino benzoic acid) for application to glucose biosensor. *Journal of Applied Polymer Science*, *78*(3), 662–667.

Ramanathan, K., Ram, M. K., Malhotra, B. D., & Murthy, A. S. N. (1995). Application of polyaniline-Langmuir-Blodgett films as a glucose biosensor. *Materials Science and Engineering C, 3*(3–4), 159–163.

Ramesha, G. K., & Sampath, N. S. (2009). Electrochemical reduction of oriented Graphene oxide films: An in situ Raman spectroelectrochemical study. *Journal of Physical Chemistry C, 113*(19), 7985–7989.

Rao, C. N. R., Kulkarni, G. U., Govindaraj, A., Satishkumar, B. C., & Thomas, P. J. (2000). Metal nanoparticles, nanowires, and carbon nanotubes. *Pure and Applied Chemistry*, *72*(1–2).

Rao, C. N. R., Sood, A. K., Subrahmanyam, K. S., & Govindaraj, A. (2009). Graphene: The new two-dimensional nanomaterial. *Angewandte Chemie - International Edition*, *48*(42), 7752–7777.

Rubinson, J., & Kayinamura, Y. (2009). Charge transport in conducting polymers: insights from impedance spectroscopy. *Chemical Society Review.*, *38*(12), 3339–

3347.

Ruoff, R. (2014). High Surface Area Graphene-Based Materials for Electrochemical Energy Storage. *225th ECS Meeting (May 11-15, 2014).*

Sahoo, S., Dhibar, S. & Das, C.K. (2012). Facile Synthesis of PolyPyrrole Nano Fiber and its Enhanced Electrochemical performances in different Electrolytes. *Synthesis*, *6*(12), 1–16.

Sabouraud, G., Sadki, S., & Brodie, N. (2000). The mechanisms of pyrrole electropolymerization. *Chemical Society Reviews*, *29*(5), 283–293.

Safavi, A., Maleki, N., & Farjami, E. (2009). Electrodeposited silver nanoparticles on carbon ionic liquid electrode for electrocatalytic sensing of hydrogen peroxide. *Electroanalysis*, *21*(13), 1533–1538.

Schab-balcerzak, E. (2011). Electropolymerization, Croatia: InTech.

Schafhaeutl, C. (1840). On the combinations of carbon with silicon and iron, and other metals, forming the different species of cast iron, steel, and malleable iron. *Philosophical Magazine Series 3*, *16*(104), 426–434.

Schniepp, H. C., Li, J. L., McAllister, M. J., Sai, H., Herrera-Alonson, M., Adamson, D. H., Aksay, I. A. (2006). Functionalized single graphene sheets derived from splitting graphite oxide. *Journal of Physical Chemistry B*, *110*(17), 8535–8539.

Sekkarapatti Ramasamy, M., Nikolakapoulou, A., Raptis, D., Dracopoulos, V., Paterakis, G., & Lianos, P. (2015). Reduced graphene oxide/polypyrrole/PEDOT composite films as efficient Pt-free counter electrode for dye-sensitized solar cells. *Electrochimica Acta*, *173*, 276–281.

Selvaraju, T., & Ramaraj, R. (2009). Electrocatalytic reduction of hydrogen peroxide at nanostructured copper modified electrode. *Journal of Applied Electrochemistry*, *39*(3), 321–327.

Şenel, M., & Nergiz, C. (2012). Novel amperometric glucose biosensor based on covalent immobilization of glucose oxidase on poly(pyrrole propylic acid)/Au nanocomposite. *Current Applied Physics*, *12*(4), 1118–1124.

Seyfoddin, A., Chan, A., Chen, W. T., Rupenthal, I. D., Waterhouse, G. I. N., & Svirskis, D. (2015). Electro-responsive macroporous polypyrrole scaffolds for triggered dexamethasone delivery. *European Journal of Pharmaceutics and Biopharmaceutics*, *94*, 419–426.

Shahnavaz, Z., Lorestani, F., Alias, Y., & Woi, P. M. (2014). Polypyrrole-$ZnFe_2O_4$ magnetic nano-composite with core-shell structure for glucose sensing. *Applied Surface Science*, *317*(0), 622–629.

Shan, C., Yang, H., Han, D., Zhang, Q., Ivaska, A., & Niu, L. (2010). Graphene/AuNPs/chitosan nanocomposites film for glucose biosensing. *Biosensors and Bioelectronics*, *25*(5), 1070–1074.

Shan, C., Yang, H., Song, J., Han, D., Ivaska, A., & Niu, L. (2009). Direct Electrochemistry of Glucose Oxidase and Biosensing for Glucose Based on Graphene Direct Electrochemistry of Glucose Oxidase and Biosensing for Glucose Based on Graphene. *Analytical Chemistry*, *81*(6), 2378–2382.

Shang, N. G., Papakonstantinou, P., McMullan, M., Chu, M., Stamboulis, A., Potenza, A., Marchetto, H. (2008). Catalyst-free efficient growth, orientation and biosensing properties of multilayer graphene nanoflake films with sharp edge planes. *Advanced Functional Materials*, *18*(21), 3506–3514.

Shao, Y., El-Kady, M. F., Wang, L. J., Zhang, Q., Li, Y., Wang, H., Kaner, R. B. (2015). Graphene-based materials for flexible supercapacitors. *Chemical Society Reviews.*, *44*(11), 3639–3665.

Shao, Y., Wang, J., Wu, H., Liu, J., Aksay, I. A., & Lin, Y. (2010). Graphene based electrochemical sensors and biosensors: A review. *Electroanalysis*, *22*(10), 1027-1036.

Shen, G., Chen, P.-C., Ryu, K., & Zhou, C. (2009). Devices and chemical sensing applications of metal oxide nanowires. *Journal of Materials Chemistry*, *19*(October 2008), 828–839.

Shin, Y. J., & Kameoka, J. (2012). Amperometric cholesterol biosensor using layer-by-layer adsorption technique onto electrospun polyaniline nanofibers. *Journal of Industrial and Engineering Chemistry*, *18*(1), 193–197.

Shin, Y. J., Kim, S. H., Yang, D. H., Kwon, H., & Shin, J. S. (2010). Amperometric glucose biosensor by means of electrostatic layer-by-layer adsorption onto polyaniline-coated polyester films. *Journal of Industrial and Engineering Chemistry*, *182*(7–8), 1543–1549.

Shirakawa, H. (2001). The discovery of polyacetylene film - The dawning of an era of conducting polymers. *Current Applied Physics*, *1*(4–5), 281–286.

Shukla, V. K., Yadav, R. S., Yadav, P., & Pandey, A. C. (2012). Green synthesis of nanosilver as a sensor for detection of hydrogen peroxide in water. *Journal of Hazardous Materials*, *213–214*, 161–166.

Si, Y., & Samulski, E. T. (2008). Synthesis of water soluble graphene. *Nano Letters*, *8*(6), 1679–1682.

Singh, R. P., & Pandey, A. C. (2011). Silver nanosieve using 1,2-benzenedicarboxylic acid: a sensor for detection of hydrogen peroxide. *Analytical Methods*, *3*(3), 586.

Šljukić, B., Banks, C. E., & Compton, R. G. (2005). An Overview of the Electrochemical Reduction of Oxygen at Carbon-Based Modified Electrodes. *Journal of the Iranian Chemical Society*, *2*(1), 1-25.

Song, H., Ma, C., You, L., Cheng, Z., Zhang, X., Yin, B., Zhang, K. (2015). Electrochemical hydrogen peroxide sensor based on a glassy carbon electrode modified with nanosheets of copper-doped copper(II) oxide. *Microchimica Acta*, *182*(7–8), 1543–1549.

Stankovich, S., Dikin, D. A., Dommett, G. H. B., Kohlhaas, K. M., Zimney, E. J., Stach, E. A., Ruoff, R. S. (2006). Graphene-based composite materials. *Nature, 442*(7100), 282–286.

Stankovich, S., Dikin, D. A., Piner, R. D., Kohlhaas, K. A., Kleinhammes, A., Jia, Y., Ruoff, R. S. (2007). Synthesis of graphene-based nanosheets via chemical reduction of exfoliated graphite oxide. *Carbon*, *45*(7), 1558–1565.

Stejskal, J., & Sapurina, I. (2005). Polyaniline: Thin films and colloidal dispersions. *Pure and Applied Chemistry*, *77*(5), 815–826.

Stolyarova, E., Rim, K. T., Ryu, S., Maultzsch, J., Kim, P., Brus, L. E., Flynn, G. W. (2007). High-resolution scanning tunneling microscopy imaging of mesoscopic graphene sheets on an insulating surface. *Sciences*, *104*(22), 1–4.

Sun, F., Zhu, R., Jiang, H., Huang, H., Liu, P., & Zheng, Y. (2015). Synthesis of Novel CuO Nanosheets with Porous Structure and Their Non-Enzymatic Glucose Sensing Applications. *Electroanalysis*, *27*(5), 1238–1244.

Szabó, T., Berkesi, O., Forgó, P., Josepovits, K., Sanakis, Y., Petridis, D., & Dékány, I. (2006). Evolution of Surface Functional Groups in a Series of Progressively Oxidized Graphite Oxides Evolution of Surface Functional Groups in a Series of Progressively Oxidized Graphite Oxides. *Chemistry of Materials*, *18*(11), 2740–2749.

Tajabadi, M. T., Basirun, W. J., Lorestani, F., Zakaria, R., Baradaran, S., Amin, Y. M., Sookhakian, M. (2015). Nitrogen-doped graphene-silver nanodendrites for the non-enzymatic detection of hydrogen peroxide. *Electrochimica Acta*, *151*, 126–133.

Takahashi, S., Abiko, N., & Anzai, J. I. (2013). Redox response of reduced graphene oxide-modified glassy carbon electrodes to hydrogen peroxide and hydrazine. *Materials*, *6*(5), 1840–1850.

Tamburri, E., Orlanducci, S., Toschi, F., Terranova, M. L., & Passeri, D. (2009). Growth mechanisms, morphology, and electroactivity of PEDOT layers produced by electrochemical routes in aqueous medium. *Synthetic Metals, 159*(5–6), 406–414.

Tang, L., Wang, Y., Li, Y., Feng, H., Lu, J., & Li, J. (2009). Preparation, structure, and electrochemical properties of reduced graphene sheet films. *Advanced Functional Materials*, *19*(17), 2782–2789.

Teo, P. S., Lim, H. N., Huang, N. M., Chia, C. H., & Harrison, I. (2012). Room temperature in situ chemical synthesis of Fe_3O_4/graphene. *Ceramics International*, *38*(8), 6411–6416.

Tian, J., Liu, S., & Sun, X. (2010). Supramolecular microfibrils of o-phenylenediamine dimers: Oxidation-induced morphology change and the spontaneous formation of Ag nanoparticle decorated nanofibers. *Langmuir, 26*(19), 15112–15116.

Tian, J., Luo, Y., Li, H., Lu, W., Chang, G., Qin, X., & Sun, X. (2011). Ag@poly(m-phenylenediamine)-Ag core–shell nanoparticles: one-step preparation, characterization, and their application for H_2O_2 detection. *Catalysis Science &*

Technology, *1*(8), 1393.

Tsai, T.-H., Chen, T.-W., Chen, S.-M., & Lin, K. C. (2011). Copper nanoparticles with copper hexacyanoferrate and poly (3, 4-ethylenedioxythiophene) hybrid film modified electrode for hydrogen peroxide detection. *International Journal of Electrochemical Science*, *6*, 4628–4637.

Tsai, T.-H., Thiagarajan, S., & Chen, S.-M. (2010). Green synthesized Au–Ag bimetallic nanoparticles modified electrodes for the amperometric detection of hydrogen peroxide. *Journal of Applied Electrochemistry*, *40*(12), 2071–2076.

Tsiafoulis, C. G., Trikalitis, P. N., & Prodromidis, M. I. (2005). Synthesis, characterization and performance of vanadium hexacyanoferrate as electrocatalyst of H_2O_2. *Electrochemistry Communications*, *7*(12), 1398–1404.

Tung, V. C., Allen, M. J., Yang, Y., & Kaner, R. B. (2009). High-throughput solution processing of large-scale graphene. *Nature Nanotechnology*, *4*(1), 25–29.

Turkmen, E., Bas, S. Z., Gulce, H., & Yildiz, S. (2014). Glucose biosensor based on immobilization of glucose oxidase in electropolymerized poly(o-phenylenediamine) film on platinum nanoparticles-polyvinylferrocenium modified electrode. *Electrochimica Acta*, *123*, 93–102.

Uzunoglu, A., Scherbarth, A. D., & Stanciu, L. A. (2015). Bimetallic PdCu/SPCE non-enzymatic hydrogen peroxide sensors. *Sensors and Actuators, B: Chemical*, *220*, 968–976.

Varghese, O. K., & Grimes, C. a. (2003). Metal Oxide Nanoarchitectures for Environmental Sensing. *Journal of Nanoscience and Nanotechnology*, *3*(4), 277–293.

Wang, A. J., Liao, Q. C., Feng, J. J., Yan, Z. Z., & Chen, J. R. (2012). In situ synthesis of polydopamine-Ag hollow microspheres for hydrogen peroxide sensing. *Electrochimica Acta*, *61*, 31–35.

Wang, J. (2005). Carbon-nanotube based electrochemical biosensors: A review. *Electroanalysis*, *17*(1), 7–14.

Wang, J. (2005). Nanomaterial-based electrochemical biosensors. *The Analyst*, *130*(4), 421.

Wang, J. (2006). Electrochemical biosensors: Towards point-of-care cancer diagnostics. *Biosensors and Bioelectronics*, *21*(10), 1887–1892.

Wang, J. (2008). Electrochemical glucose biosensors. *Electrochemical Sensors, Biosensors and Their Biomedical Applications*, *108*(2), 57–69.

Wang, J., & Lin, Y. (2008). Functionalized carbon nanotubes and nanofibers for biosensing applications. *Trends in Analytical Chemistry*, *27*(7), 619–626.

Wang, J., Xu, Y., Zhu, J., & Ren, P. (2012). Electrochemical in situ polymerization of reduced graphene oxide/polypyrrole composite with high power density. *Journal of*

Power Sources, *208*, 138–143.

Wang, J., Yang, S., Guo, D., Yu, P., Li, D., Ye, J., & Mao, L. (2009). Comparative studies on electrochemical activity of graphene nanosheets and carbon nanotubes. *Electrochemistry Communications*, *11*(10), 1892–1895.

Wang, L., Wang, F., Shang, L., Zhu, C., Ren, W., & Dong, S. (2010). AuAg bimetallic nanoparticles film fabricated based on H_2O_2-mediated silver reduction and its application. *Talanta*, *82*(1), 113–117.

Wang, L., Zhu, H., Hou, H., Zhang, Z., Xiao, X., & Song, Y. (2012). A novel hydrogen peroxide sensor based on Ag nanoparticles electrodeposited on chitosan-graphene oxide/cysteamine-modified gold electrode. *Journal of Solid State Electrochemistry*, *16*(4), 1693–1700.

Wang, L., Zhu, H., Song, Y., Liu, L., He, Z., Wan, L., Chen, J. (2012). Architecture of poly(o-phenylenediamine)-Ag nanoparticle composites for a hydrogen peroxide sensor. *Electrochimica Acta*, *60*, 314–320.

Wang, Q., & Zheng, J. (2010). Electrodeposition of silver nanoparticles on a zinc oxide film: Improvement of amperometric sensing sensitivity and stability for hydrogen peroxide determination. *Microchimica Acta*, *169*(3), 361–365.

Wang, S., Han, Z., Li, Y., Peng, R., & Feng, B. (2015). An electrochemical sensor based on reduced graphene oxide and copper sulfide hollow nanospheres. *RSC Adv.*, *5*(130), 107318–107325.

Wang, W., Xie, Y., Xia, C., Du, H., & Tian, F. (2014). Titanium dioxide nanotube arrays modified with a nanocomposite of silver nanoparticles and reduced graphene oxide for electrochemical sensing. *Microchimica Acta*, *181*(11–12), 1325–1331.

Wang, Y., Wei, W., Zeng, J., Liu, X., & Zeng, X. (2008). Fabrication of a copper nanoparticle/chitosan/carbon nanotube-modified glassy carbon electrode for electrochemical sensing of hydrogen peroxide and glucose. *Microchimica Acta*, *160*(1–2), 253–260.

Wiley, B., Sun, Y., & Xia, Y. (2007). Synthesis of silver nanostructures with controlled shapes and properties. *Accounts of Chemical Research*, *40*(10), 1067–1076.

Wood, G. A., & Iroh, J. O. (1996). Efficiency of electropolymerization of pyrrole onto carbon fibers. *Synthetic Metals*, *80*(1), 73–82.

Wu, S., Ge, R., Lu, M., Xu, R., & Zhang, Z. (2015). Graphene-based nano-materials for lithium-sulfur battery and sodium-ion battery. *Nano Energy*, *15*, 379–405.

Wu, S. H., & Chen, D. H. (2004). Synthesis of high-concentration Cu nanoparticles in aqueous CTAB solutions. *Journal of Colloid and Interface Science*, *273*(1), 165–169.

Wu, S., Zhao, H., Ju, H., Shi, C., & Zhao, J. (2006). Electrodeposition of silver-DNA hybrid nanoparticles for electrochemical sensing of hydrogen peroxide and glucose. *Electrochemistry Communications*, *8*(8), 1197–1203.

Wu, Z. S., Ren, W., Gao, L., Liu, B., Jiang, C., & Cheng, H. M. (2009). Synthesis of high-quality graphene with a pre-determined number of layers. *Carbon*, *47*(2), 493–499.

Xie, G., Cheng, J., Li, Y., Xi, P., Chen, F., Liu, H., Zeng, Z. (2012). Fluorescent graphene oxide composites synthesis and its biocompatibility study. *Journal of Materials Chemistry*, *22*(18), 9308.

Xu, B., Ye, M. L., Yu, Y. X., & Zhang, W. De. (2010). A highly sensitive hydrogen peroxide amperometric sensor based on MnO_2-modified vertically aligned multiwalled carbon nanotubes. *Analytica Chimica Acta*, *674*(1), 20–26.

Xu, Q., Zhao, Y., Xu, J. Z., & Zhu, J. J. (2006). Preparation of functionalized copper nanoparticles and fabrication of a glucose sensor. *Sensors and Actuators, B: Chemical*, *114*(1), 379–386.

Yamaura, M., Hagiwara, T., & Iwata, K. (1988). Enhancement of electrical conductivity of polypyrrole film by stretching: Counter ion effect. *Synthetic Metals*, *26*(3), 209–224.

Yang, J., Zhang, W. De, & Gunasekaran, S. (2010). An amperometric non-enzymatic glucose sensor by electrodepositing copper nanocubes onto vertically well-aligned multi-walled carbon nanotube arrays. *Biosensors and Bioelectronics*, *26*(1), 279–284.

Yang, S., Guo, D., Su, L., Yu, P., Li, D., Ye, J., & Mao, L. (2009). A facile method for preparation of graphene film electrodes with tailor-made dimensions with Vaseline as the insulating binder. *Electrochemistry Communications*, *11*(10), 1912–1915.

Yang, Y. J., Li, W., & Wu, X. (2014). Copper sulfide|reduced graphene oxide nanocomposite for detection of hydrazine and hydrogen peroxide at low potential in neutral medium. *Electrochimica Acta*, *123*, 260–267.

Yao, L., Yang, W., Yang, J., He, L., Sun, J., Song, R., Huang, W. (2011). Preparation and catalytic ability to reduce hydrogen peroxide of Ag nanoparticles highly dispersed via hyperbranched copolymer. *Nanoscale*, *3*(3), 916–8.

Yao, S., Xu, J., Wang, Y., Chen, X., Xu, Y., & Hu, S. (2006). A highly sensitive hydrogen peroxide amperometric sensor based on MnO_2 nanoparticles and dihexadecyl hydrogen phosphate composite film. *Analytica Chimica Acta*, *557*(1–2), 78–84.

Ye, J. S., Cui, H. F., Liu, X., Lim, T. M., Zhang, W. De, & Sheu, F. S. (2005). Preparation and characterization of aligned carbon nanotube-ruthenium oxide nanocomposites for supercapacitors. *Small*, *1*(5), 560–565.

Yi, Q., Niu, F., Li, L., Du, R., Zhou, Z., & Liu, X. (2011). Novel nanoporous silver particles for electro-reduction of hydrogen peroxide in alkaline media. *Journal of Electroanalytical Chemistry*, *654*(1–2), 60–65.

Yin, Z., Zhu, J., He, Q., Cao, X., Tan, C., Chen, H., Zhang, H. (2014). Graphene-Based materials for solar cell applications. *Advanced Energy Materials*, *4*(1).

Yu, H., Jian, X., Jin, J., Zheng, X. C., Liu, R. T., & Qi, G. C. (2015). Nonenzymatic sensing of glucose using a carbon ceramic electrode modified with a composite film made from copper oxide, overoxidized polypyrrole and multi-walled carbon nanotubes. *Microchimica Acta*, *182*(1–2), 157–165.

Yu, Y., Sun, Q., Liu, X., Wu, H., Zhou, T., & Shi, G. (2011). Size-controllable gold-platinum alloy nanoparticles on nine functionalized ionic-liquid surfaces and their application as electrocatalysts for hydrogen peroxide reduction. *Chemistry - A European Journal*, *17*(40), 11314–11323.

Yuan, B., Xu, C., Liu, L., Zhang, Q., Ji, S., Pi, L., Huo, Q. (2013). Cu_2O/NiO_x/graphene oxide modified glassy carbon electrode for the enhanced electrochemical oxidation of reduced glutathione and nonenzyme glucose sensor. *Electrochimica Acta*, *104*, 78–83.

Zainy, M., Huang, N. M., Vijay Kumar, S., Lim, H. N., Chia, C. H., & Harrison, I. (2012). Simple and scalable preparation of reduced graphene oxide-silver nanocomposites via rapid thermal treatment. *Materials Letters, 89*, 180–183.

Zha, Z., Wang, J., Qu, E., Zhang, S., Jin, Y., Wang, S., & Dai, Z. (2013). Polypyrrole hollow microspheres as echogenic photothermal agent for ultrasound imaging guided tumor ablation. *Scientific Reports, 3*, 2360.

Zhai, X., & Gao, Z. (2010). Prussian blue electrodeposited on nano Ag-coated multiwalled carbon nanotubes composite for the determination of hydrogen peroxide. *Analytical Sciences : The International Journal of the Japan Society for Analytical Chemistry, 26*(3), 343–7.

Zhang, D., Fang, Y., Miao, Z., Ma, M., Du, X., Takahashi, S., Chen, Q. (2013). Direct electrodeposion of reduced graphene oxide and dendritic copper nanoclusters on glassy carbon electrode for electrochemical detection of nitrite. *Electrochimica Acta, 107*, 656–663.

Zhang, K., Zhang, L. L., Zhao, X. S., & Wu, J. (2010). Graphene/polyaniline nanofiber composites as supercapacitor electrodes. *Chemistry of Materials, 22*(4), 1392–1401.

Zhang, T., Yuan, R., Chai, Y., Li, W., & Ling, S. (2008). A novel nonenzymatic hydrogen peroxide sensor based on a polypyrrole nanowire-copper nanocomposite modified gold electrode. *Sensors*, *8*(8), 5141–5152.

Zhang, X., Gu, A., Wang, G., Huang, Y., Ji, H., & Fang, B. (2011). Porous Cu–NiO modified glass carbon electrode enhanced nonenzymatic glucose electrochemical sensors. *The Analyst*, *136*(24), 5175.

Zhang, Y., Sun, Y., Liu, Z., Xu, F., Cui, K., Shi, Y., Li, Z. (2011). Au nanocages for highly sensitive and selective detection of H_2O_2. *Journal of Electroanalytical Chemistry*, *656*(1–2), 23–28.

Zhang, Y., Wang, Y., Jia, J., & Wang, J. (2012). Nonenzymatic glucose sensor based on graphene oxide and electrospun NiO nanofibers. *Sensors and Actuators, B: Chemical*, *171–172*(0), 580–587.

Zhang, Y., Zhang, C., Zhang, D., Ma, M., Wang, W., & Chen, Q. (2016). Nanoassemblies consisting of Pd/Pt nanodendrites and poly (diallyldimethylammonium chloride)-coated reduced graphene oxide on glassy carbon electrode for hydrogen peroxide sensors. *Materials Science and Engineering C*, *58*, 1246–1254.

Zhao, J., Pei, S., Ren, W., Gao, L., & Cheng, H. M. (2010). Efficient preparation of large-area graphene oxide sheets for transparent conductive films. *ACS Nano*, *4*(9), 5245–5252.

Zhao, W., Wang, H., Qin, X., Wang, X., Zhao, Z., Miao, Z., Chen, Q. (2009). A novel nonenzymatic hydrogen peroxide sensor based on multi-wall carbon nanotube/silver nanoparticle nanohybrids modified gold electrode. *Talanta*, *80*(2), 1029–1033.

Zhong, L., Gan, S., Fu, X., Li, F., Han, D., Guo, L., & Niu, L. (2013). Electrochemically controlled growth of silver nanocrystals on graphene thin film and applications for efficient nonenzymatic H_2O_2 biosensor. *Electrochimica Acta*, *89*, 222–228.

Zhou, M., Wang, Y., Zhai, Y., Zhai, J., Ren, W., Wang, F., & Dong, S. (2009). Controlled synthesis of large-area and patterned electrochemically reduced graphene oxide films. *Chemistry - A European Journal*, *15*(25), 6116–6120.

Zhou, M., Zhai, Y., & Dong, S. (2009). Electrochemical sensing and biosensing platform based on chemically reduced graphene oxide. *Analytical Chemistry*, *81*(14), 5603–5613.

Zhou, Y.-G., Chen, J.-J., Wang, F.-B., Sheng, Z.-H., & Xia, X.-H. (2010). A facile approach to the synthesis of highly electroactive Pt nanoparticles on graphene as an anode catalyst for direct methanol fuel cellsw. *Chemical Communications*, *46*(32), 5951–5953.

Zhu, Y., Murali, S., Cai, W., Li, X., Suk, J. W., Potts, J. R., & Ruoff, R. S. (2010). Graphene and graphene oxide: Synthesis, properties, and applications. *Advanced Materials*, *22*(35), 3906–3924.

Appendix

This section provides a list of publications in ISI journals during the current PhD research and conferences/seminars attended along the candidature.

List of Publication (Published/Accepted)

Corresponding Authors and First Authors:

Pooria Moozarm Nia, Woi, P.M., Lorestani, F., Mahmoudian, M.R., Alias Y. (2015). Electrodeposition of copper oxide/polypyrrole/reduced graphene oxide as a nonenzymatic glucose biosensor. **Sensors and Actuators B: Chemical**, *209, 100-108* **(Journal Impact Factor: 4.758)**.

Pooria Moozarm Nia, Lorestani, F., Woi, P.M., Alias, Y. (2015). A novel non-enzymatic H_2O_2 sensor based on polypyrrole nanofibers–silver nanoparticles decorated reduced graphene oxide nano composites, **Applied Surface Science**, *332 648-656* **(Journal Impact Factor: 3.150)**.

Pooria Moozarm Nia, Woi, P.M., Alias, Y. (2016). One-Step Electrodeposition of Polypyrrole-Copper Nano Particles for H_2O_2 Detection, **Journal of The Electrochemical Society**, *163, B8-B14* **(Journal Impact Factor: 3.266)**.

Pooria Moozarm Nia, Woi, P.M., Alias, Y. (2015). Hydrogen peroxide sensor: Uniformly decorated silver nanoparticles on polypyrrole for wide detection range, **Applied Surface Science**, *332 (2015) 648-656* **(Journal Impact Factor: 3.150)**.

Pooria Moozarm Nia, Woi, P.M., Alias. Y. (2016). Facile one-step electrochemical deposition of copper nanoparticles and reduced graphene oxide as nonenzymatic hydrogen peroxide sensor. **Applied surface science**, *(under review)* **(Journal Impact Factor: 3.150)**.

B8 Journal of The Electrochemical Society, 163 (3) B8-B14 (2016)
0013-4651/2016/163(3)/B8/7/$33.00 © The Electrochemical Society

One-Step Electrodeposition of Polypyrrole-Copper Nano Particles for H_2O_2 Detection

Pooria Moozarm Nia,[z] **Woi Pei Meng, and Y. Alias**[z]

Department of Chemistry, University of Malaya, Kuala Lumpur 50603, Malaysia

A straightforward and novel one-step technique for electrochemical synthesis of polypyrrole micro trunk-like shape decorated with copper nanoparticles (PpyMTs-CuNPs) is presented. The technique is based on electropolymerization and copper electrodeposition in the one-pot aqueous solution. The electrodeposited CuNPs with 30 nm in diameter have embedded on the polypyrrole micro trunk-like (PpyMTs). The synthesized PpyMTs-CuNPs were characterized by field emission scanning electron microscopy (FESEM), X-ray photoelectron spectroscopy (XRD) and electrochemical methods. The chemical structures, morphology, catalytic and electrochemical properties of the synthesized PpyMTs-CuNPs toward H_2O_2 were examined. The prepared PpyMTs–CuNPs increased electrocatalytic activity toward reduction of hydrogen peroxide (H_2O_2) and can be employed as an inexpensive and novel sensor for determination of H_2O_2. The initial linear part was observed ranging from 0.2 mM to 1 mM with a limit of detection of 0.9 μm and the next linear part increased to 110 mM, having a limit of detection of 4.39 μm (S/N of 3). Additionally, the sensor exhibited remarkable reproducibility, stability and selectivity that make PpyMTs-CuNPs a good nonenzymatic H_2O_2 sensor.
[DOI: 10.1149/2.0481603jes]

Manuscript submitted August 13, 2015; revised manuscript received October 14, 2015. Published December 18, 2015.

Electropolymerization is a simple method for synthesizing conducting polymers (CPs), especially due to its relatively straightforward procedure.[1–4] Electropolymerization of conducting polymers dates back to 1968 when "pyrrole black" was made on a platinum electrode by exposing an aqueous solution of sulfuric acid and pyrrole monomer to an oxidative potential.[5] Recently, electropolymerization is carried out by utilizing a three-electrode cell which includes reference, working and counter electrodes in a solution of the monomer, proper solvent and electrolyte (counter ion).[6] At the surface of the working electrode, monomers are exposed to oxidation potential to generate radical cations. Then, the radical cations react with other radical cations or monomers to form insoluble polymer chains on the surface of electrode.[5]

High electron affinities and the presence of conjugated double bonds together with low oxidation potentials are fundamental prerequisites for the unique electrical characteristics of Ppy. The electrical conductivity of Ppy can be increased by a doping-dedoping process.[7,8] Particular properties of conducting polymers, like nonlinear optical and electrical features which are innate in metal or other semi-conductors along with the mechanical characteristics create new potentials for technological usages such as gas sensor,[9,10] supercapacitors,[11–13] rechargeable batteries,[14–16] drug-releasing agents,[17] transistors,[18] chemical or biochemical sensors.[19–24] Excellent redox properties, ease of synthesis, high conductivity ($2 \times 10^2\ \Omega^{-1}\text{cm}^{-1}$) and good environmental stability make the polypyrrole (Ppy) as one of the most promising conducting polymers.[19,25,26]

CPs have also been employed as adaptable matrices for dispersing or embedding metal nanoparticles to form nanocomposite materials which possess characteristics of the singular components with a synergistic effect.[27–30] The combination of CPs with metal nanoparticles suggests a compelling way to strengthen the polymer along with introducing electrical characteristics based on morphological modification or electronic interaction between the two components.[23,31,32] The metal–polymer composite properties totally increased when the size of material is reduced to the nanoscale.[20,33–35] Nanoscale composites have drawn huge attention, not only due to their potential performances in various fields such as electronics, chemistry, physics, optics, biomedical science and material science, but also due to their innate characteristics fundamental interest.[36,37]

Generally, the frequently used methods employed for the synthesis of conducting polymer–metal composites include chemical, electrochemical and electrospinning techniques.[38–43] A multistep electropolymerization of conducting polymer composites generally includes electrodeposition of metal particles on the as-prepared polymer surface.[27,28] The electrochemical methods based on one-step processes are not frequently applied for synthesizing the conducting polymer-metal composites.

In the current study, the electrochemical synthesis of polypyrrole microtrunks-copper nanoparticles (PpyMTs-CuNPs) composites with increased sensing toward hydrogen peroxide is presented. Current investigation has been carried out by using and comparing four kinds of doping agents: lithium perchlorate ($LiClO_4$), sodium dodecyl sulfate (SDS), p-toluene sulfonate acid (PTSA) and copper chloride ($CuCl_2$). The morphological properties of different formed structures have been cautiously evaluated by using field-emission scanning electron microscopy (FESEM). Through combining the cathodic codeposition of PpyMTs-CuNPs nanoparticles composite, a novel modified electrode based on conducting polymer – metal nanoparticles with intricate structure was formed. The morphology, electrochemical properties, chemical composition and electrocatalytic activity of the prepared micro trunk-like polypyrrole decorated with Cu nanoparticles were studied in details.

Experimental

Materials.—All of the materials including potassium hydrogen phosphate (99%), lithium perchlorate (99%), pyrrole (99.5%), potassium dihydrogen phosphate (99%) and copper(II) chloride dehydrate (99%) were purchased from Sigma–Aldrich and were used in the form in which they were received.

Instruments.—Electrochemical measurements including electrochemical impedance spectroscopy (EIS), chronoamperometry and cyclic voltammetry (CV) were carried out by using a potentiostat/galvanostat model PGSTAT-302N from the Autolab controlled by Nova 1.11 software. A counter electrode, a reference electrode and a working electrode formed a three-electrode compartment cell. A saturated calomel electrode (SCE) was the reference electrode for all the potentials. X-ray powder diffraction (XRD, Philips X'pert system using Cu Kα radiation) was used for characterizing the crystal phase. For morphologies comparison, the field emission scanning electron microscopy (FESEM) images were taken by using FESEM, FEI Nova Nano-SEM 400 operated at 10.0 kV.

Preparation of the nonenzymatic H_2O_2 sensor.—Glassy carbon electrode (GCE) was used to act as the base electrode, in order to fabricate the nonenzymatic sensor. The clean GCE was polished to a mirror by using alumina (under 1, 0.1 and 0.05 mm diameter) slurries in the pre-experiment preparations and was subsequently washed by double distilled water and ultrasonicated in a mixture of distilled water and ethanol for 10 min. To be ready for use, it was dried under high purity N_2 gas flow.

---

[z] E-mail: poorianm@yahoo.com; perwei@um.edu.my; yatimah70@um.edu.my

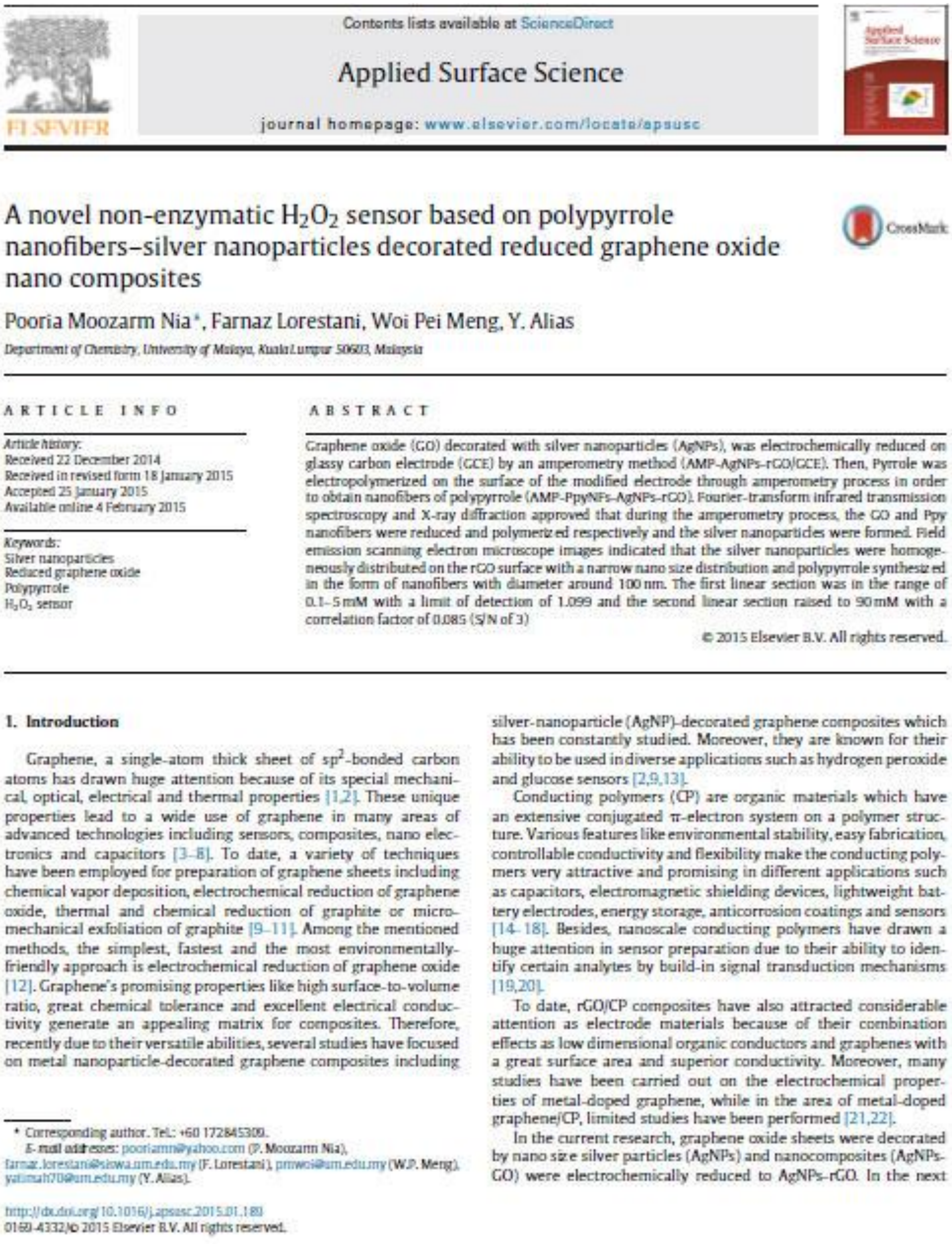

Contents lists available at ScienceDirect

Applied Surface Science

journal homepage: www.elsevier.com/locate/apsusc

A novel non-enzymatic H_2O_2 sensor based on polypyrrole nanofibers–silver nanoparticles decorated reduced graphene oxide nano composites

Pooria Moozarm Nia*, Farnaz Lorestani, Woi Pei Meng, Y. Alias

Department of Chemistry, University of Malaya, Kuala Lumpur 50603, Malaysia

ARTICLE INFO

Article history:
Received 22 December 2014
Received in revised form 18 January 2015
Accepted 25 January 2015
Available online 4 February 2015

Keywords:
Silver nanoparticles
Reduced graphene oxide
Polypyrrole
H_2O_2 sensor

ABSTRACT

Graphene oxide (GO) decorated with silver nanoparticles (AgNPs), was electrochemically reduced on glassy carbon electrode (GCE) by an amperometry method (AMP-AgNPs-rGO/GCE). Then, Pyrrole was electropolymerized on the surface of the modified electrode through amperometry process in order to obtain nanofibers of polypyrrole (AMP-PpyNFs-AgNPs-rGO). Fourier-transform infrared transmission spectroscopy and X-ray diffraction approved that during the amperometry process, the GO and Ppy nanofibers were reduced and polymerized respectively and the silver nanoparticles were formed. Field emission scanning electron microscope images indicated that the silver nanoparticles were homogeneously distributed on the rGO surface with a narrow nano size distribution and polypyrrole synthesized in the form of nanofibers with diameter around 100 nm. The first linear section was in the range of 0.1–5 mM with a limit of detection of 1.099 and the second linear section raised to 90 mM with a correlation factor of 0.085 (S/N of 3)

1. Introduction

Graphene, a single-atom thick sheet of sp^2-bonded carbon atoms has drawn huge attention because of its special mechanical, optical, electrical and thermal properties [1,2]. These unique properties lead to a wide use of graphene in many areas of advanced technologies including sensors, composites, nano electronics and capacitors [3–8]. To date, a variety of techniques have been employed for preparation of graphene sheets including chemical vapor deposition, electrochemical reduction of graphene oxide, thermal and chemical reduction of graphite or micromechanical exfoliation of graphite [9–11]. Among the mentioned methods, the simplest, fastest and the most environmentally-friendly approach is electrochemical reduction of graphene oxide [12]. Graphene's promising properties like high surface-to-volume ratio, great chemical tolerance and excellent electrical conductivity generate an appealing matrix for composites. Therefore, recently due to their versatile abilities, several studies have focused on metal nanoparticle-decorated graphene composites including silver-nanoparticle (AgNP)-decorated graphene composites which has been constantly studied. Moreover, they are known for their ability to be used in diverse applications such as hydrogen peroxide and glucose sensors [2,9,13].

Conducting polymers (CP) are organic materials which have an extensive conjugated π-electron system on a polymer structure. Various features like environmental stability, easy fabrication, controllable conductivity and flexibility make the conducting polymers very attractive and promising in different applications such as capacitors, electromagnetic shielding devices, lightweight battery electrodes, energy storage, anticorrosion coatings and sensors [14–18]. Besides, nanoscale conducting polymers have drawn a huge attention in sensor preparation due to their ability to identify certain analytes by build-in signal transduction mechanisms [19,20].

To date, rGO/CP composites have also attracted considerable attention as electrode materials because of their combination effects as low dimensional organic conductors and graphenes with a great surface area and superior conductivity. Moreover, many studies have been carried out on the electrochemical properties of metal-doped graphene, while in the area of metal-doped graphene/CP, limited studies have been performed [21,22].

In the current research, graphene oxide sheets were decorated by nano size silver particles (AgNPs) and nanocomposites (AgNPs-GO) were electrochemically reduced to AgNPs-rGO. In the next

---

* Corresponding author. Tel.: +60 172845309.
E-mail addresses: pooriamn@yahoo.com (P. Moozarm Nia), farnaz.lorestani@siswa.um.edu.my (F. Lorestani), pmwoi@um.edu.my (W.P. Meng), yatimah70@um.edu.my (Y. Alias).

http://dx.doi.org/10.1016/j.apsusc.2015.01.180

Contents lists available at ScienceDirect

Sensors and Actuators B: Chemical

journal homepage: www.elsevier.com/locate/snb

Electrodeposition of copper oxide/polypyrrole/reduced graphene oxide as a nonenzymatic glucose biosensor

Pooria Moozarm Nia[a,*], Woi Pei Meng[a], Farnaz Lorestani[a], M.R. Mahmoudian[b], Y. Alias[a]

[a] Department of Chemistry, University of Malaya, Kuala Lumpur 50603, Malaysia
[b] Department of Chemistry, Shahid Sharafat, University of Farhangian, 15916 Tehran, Iran

ARTICLE INFO

Article history:
Received 22 September 2014
Received in revised form 3 November 2014
Accepted 12 November 2014
Available online 20 November 2014

Keywords:
Copper oxide
Polypyrrole
Reduced graphene oxide
Glucose
Nonenzymatic biosensor

ABSTRACT

We report the synthesis and application of copper oxide/polypyrrole nanofiber/reduced graphene oxide nanocomposite (Cu_2O/Ppy/rGO/GCE) for the detection of glucose (GLC). Cu_2O, Ppy and rGO were synthesized via electrodeposition process. The formation of the rGO and Ppy were approved by Fourier Transform Infrared Spectroscopy (FT-IR). Energy-dispersive X-ray spectroscopy (EDX) and X-ray diffraction (XRD) confirmed the formation of copper oxide. The field emission scanning electron microscopy (FESEM) images depicted the existence of wrinkle rGO, Ppy nanofibers with diameter around 100 nm and the uniformity of the Cu_2O particles deposited on the Ppy nanofibers. Electrochemical impedance spectroscopy (EIS) data also indicated the charge transfer of each layer decreased compared to the underneath layer. By using cyclic voltammetry (CV) and chronoamperometry under pH 7.2, the electrocatalytic activity of Cu_2O/Ppy/rGO/GCE toward GLC was explored. The sensor presented a linear range of 0.1–100 mM (R^2 = 0.991) of GLC, that is higher than most of the present nonenzymatic glucose biosensors based on Cu_2O, Ppy and rGO. The limit of detection (LOD) reaches 0.03 μM (at S/N = 3). Additionally, the sensor exhibited remarkable reproducibility, stability and selectivity properties which make Cu_2O/Ppy/ rGO/GCE a good nonenzymatic GLC sensor.

1. Introduction

More than 220 million of people around the world are suffering from diabetes which is a highly extensive disease bringing about metabolic disorders. Testing the blood glucose (GLC) is very crucial for diabetic patients and helps to evade the clustering of blood GLC (in the range of 4.4–6.6 mM). Therefore it is of high significance to establish straightforward system with high sensitivity, selectivity and stability in order to distinguish GLC levels [1–3].

Graphite oxide was primarily recorded 150 years ago and reappeared tremendously in the studies due to the low cost and volume production of graphene-based materials. The layered structure of graphite oxide is similar to graphite's structure but in graphite oxide, the sheet of carbon atoms is densely decorated by groups which contain oxygen, which besides increasing the interlayer distance, it makes the atomic-thick layers hydrophilic. Therefore, this resulted to the exfoliation of oxidized layers in water under moderate ultra-sonication [4–9]. It also should be mentioned that the most interesting feature of GO is being partly reduced to graphene-like sheets through the removal of the groups which contain oxygen with the recovery of a conjugated structure [7,8,10–12].

In 1977, Shirakawa et al. [13] reported electrical conductivity in a conjugated polymer and since then conducting polymers have been largely explored due to their unique electrical characteristics. Polypyrrole, among the conducting polymers is specifically advantageous for its different financial applications like chemical sensors [14,15], supercapacitors [15–17], biosensors [2,6,7,18,19], gas sensors [20] and corrosion protection [21–23] because of being environmentally stable, electrically conductive and flexible. Recently a huge attempt has been made to expand polypyrrole nanostructures which exhibit unique physical and chemical characteristics preferable to their bulky counterpart and that is due to an expanding need for conducting polymers in the field of nanoscience and technology [24–27]. Electrochemical polymerization provides a one-step procedure and offers precise control of the thickness and the structure of the resulting film [28].

Transition metal oxides, like Cu_2O are drawing a huge attention as sensors for detection of glucose because of their good characteristics such as low cost, ease of synthesis and post synthesis

---

* Corresponding author. Tel.: +60 379676774; fax: +60 379674188.
E-mail addresses: pooriamn@yahoo.com (P. Moozarm Nia), pmwoi@um.edu.my (W.P. Meng), farnaz.lorestani@siswa.um.edu.my (F. Lorestani), M_R_mahmoudian@yahoo.com (M.R. Mahmoudian), yatimah70@um.edu.my (Y. Alias).

http://dx.doi.org/10.1016/j.snb.2014.11.072

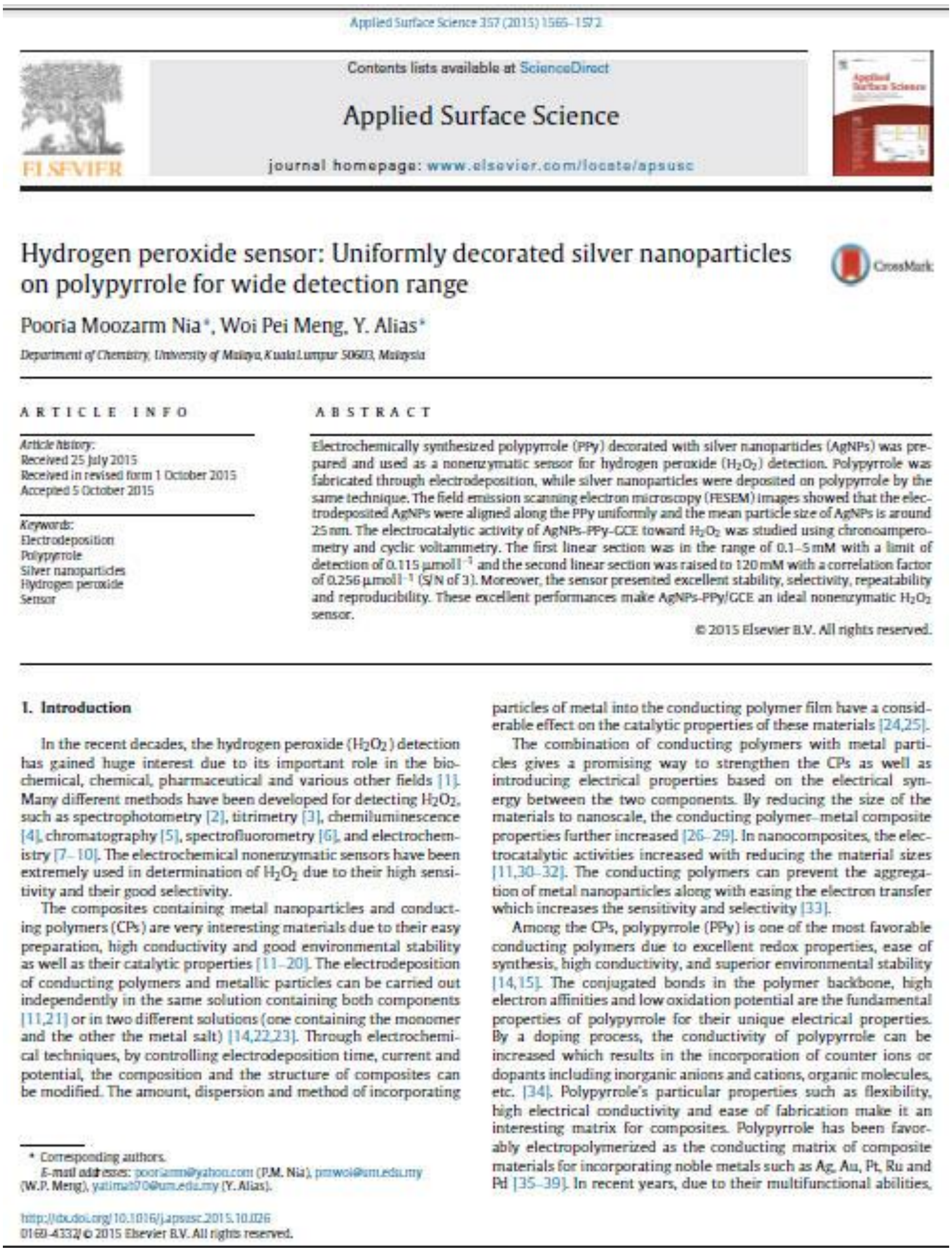

Applied Surface Science 357 (2015) 1565–1572

Contents lists available at ScienceDirect

Applied Surface Science

journal homepage: www.elsevier.com/locate/apsusc

Hydrogen peroxide sensor: Uniformly decorated silver nanoparticles on polypyrrole for wide detection range

Pooria Moozarm Nia*, Woi Pei Meng, Y. Alias*

Department of Chemistry, University of Malaya, Kuala Lumpur 50603, Malaysia

ARTICLE INFO

Article history:
Received 25 July 2015
Received in revised form 1 October 2015
Accepted 5 October 2015

Keywords:
Electrodeposition
Polypyrrole
Silver nanoparticles
Hydrogen peroxide
Sensor

ABSTRACT

Electrochemically synthesized polypyrrole (PPy) decorated with silver nanoparticles (AgNPs) was prepared and used as a nonenzymatic sensor for hydrogen peroxide (H_2O_2) detection. Polypyrrole was fabricated through electrodeposition, while silver nanoparticles were deposited on polypyrrole by the same technique. The field emission scanning electron microscopy (FESEM) images showed that the electrodeposited AgNPs were aligned along the PPy uniformly and the mean particle size of AgNPs is around 25 nm. The electrocatalytic activity of AgNPs-PPy-GCE toward H_2O_2 was studied using chronoamperometry and cyclic voltammetry. The first linear section was in the range of 0.1–5 mM with a limit of detection of 0.115 μmol l^{-1} and the second linear section was raised to 120 mM with a correlation factor of 0.256 μmol l^{-1} (S/N of 3). Moreover, the sensor presented excellent stability, selectivity, repeatability and reproducibility. These excellent performances make AgNPs-PPy/GCE an ideal nonenzymatic H_2O_2 sensor.

1. Introduction

In the recent decades, the hydrogen peroxide (H_2O_2) detection has gained huge interest due to its important role in the biochemical, chemical, pharmaceutical and various other fields [1]. Many different methods have been developed for detecting H_2O_2, such as spectrophotometry [2], titrimetry [3], chemiluminescence [4], chromatography [5], spectrofluorometry [6], and electrochemistry [7–10]. The electrochemical nonenzymatic sensors have been extremely used in determination of H_2O_2 due to their high sensitivity and their good selectivity.

The composites containing metal nanoparticles and conducting polymers (CPs) are very interesting materials due to their easy preparation, high conductivity and good environmental stability as well as their catalytic properties [11–20]. The electrodeposition of conducting polymers and metallic particles can be carried out independently in the same solution containing both components [11,21] or in two different solutions (one containing the monomer and the other the metal salt) [14,22,23]. Through electrochemical techniques, by controlling electrodeposition time, current and potential, the composition and the structure of composites can be modified. The amount, dispersion and method of incorporating particles of metal into the conducting polymer film have a considerable effect on the catalytic properties of these materials [24,25].

The combination of conducting polymers with metal particles gives a promising way to strengthen the CPs as well as introducing electrical properties based on the electrical synergy between the two components. By reducing the size of the materials to nanoscale, the conducting polymer–metal composite properties further increased [26–29]. In nanocomposites, the electrocatalytic activities increased with reducing the material sizes [11,30–32]. The conducting polymers can prevent the aggregation of metal nanoparticles along with easing the electron transfer which increases the sensitivity and selectivity [33].

Among the CPs, polypyrrole (PPy) is one of the most favorable conducting polymers due to excellent redox properties, ease of synthesis, high conductivity, and superior environmental stability [14,15]. The conjugated bonds in the polymer backbone, high electron affinities and low oxidation potential are the fundamental properties of polypyrrole for their unique electrical properties. By a doping process, the conductivity of polypyrrole can be increased which results in the incorporation of counter ions or dopants including inorganic anions and cations, organic molecules, etc. [34]. Polypyrrole's particular properties such as flexibility, high electrical conductivity and ease of fabrication make it an interesting matrix for composites. Polypyrrole has been favorably electropolymerized as the conducting matrix of composite materials for incorporating noble metals such as Ag, Au, Pt, Ru and Pd [35–39]. In recent years, due to their multifunctional abilities,

---

* Corresponding authors.
E-mail addresses: pooriamn@yahoo.com (P.M. Nia), pmwoi@um.edu.my (W.P. Meng), yatimah70@um.edu.my (Y. Alias).

http://dx.doi.org/10.1016/j.apsusc.2015.10.026

List of conferences/seminars attended:

- **Facile one-step Electrochemical Deposition of Polypyrrole-copper Nanoparticles for Detection Hydrogen Peroxide**, *8th International Scientific Conference on Applied Sciences and Engineering conference (ISCASE-15)*, kuala Lumpur, Malaysia, April 2016, Oral Presenter.

- **Course on UHR Fiwld Emision Scanning Electron Microscope, STEM, EDS & Sample Preparations**, *Chemistry department, University of Malaya*, Kuala Lumpur, Malaysia, July 2016, Oral Presenter.

- **Facile one-step electrochemical deposition of copper nanoparticles and reduced graphene oxide as nonenzymatic hydrogen peroxide sensor**, *International Conference and Exhibition on Nanomedicine and Nanotechnology*, Baltimore, USA, August 2016, Poster Presenter.